Effect of particle morphology on film morphology and properties

Elodie Limousin

Supervised by: N. Ballard and J.M. Asua

Chemical Engineering Group
University of the Basque Country UPV/EHU
Donostia-San Sebastián

(2019)

Content

Chapter 1. Introduction and objectives

1.1 Motivations

One of the greatest challenges facing modern society is the reduction of climate change and the development of sustainable materials. With this in mind, the production of protective and decorative coatings, which has traditionally been dominated by solvent based products, is gradually being shifted towards the use of waterborne dispersions. Such coatings imply the formation of a film which often needs to satisfy several seemingly contradictory requirements with regards to mechanical properties. One common example is the necessity for outdoor coatings to be both capable of forming a film at relatively low temperatures whilst being hard at the same temperature. Solvent based coatings easily fulfill these requirements. Matching their performance with waterborne coatings is not trivial and often potentially toxic additives, such as coalescing agents, have to be added to the formulation. Efforts are now devoted to synthesize latexes presenting good properties whilst adding a minimum of additives. One way to do this is through the use of a blend of two latexes with different glass transition temperatures (T_{gs}). One latex with a low T_g to form a film at low temperature and the other one with a higher T_g, to provide film hardness. However, blending leads to non homogenous films and the properties of the film are affected.[1] A more uniform distribution of the two phases in the film can be obtained by using heterogeneous polymer particles (also called hybrid particles). In this case, two different polymers are present in the same particle which offers the opportunity to combine the

positive properties of their constituents. Although such polymers are typically incompatible, their phase separation during film formation can be controlled by grafting reactions.[2–6]

Recent works showed that controlling the morphology of hybrid particles is not trivial.[1,7–13] Interestingly, much less attention has been paid to the fact that application properties are really determined by the film morphology and that the relationship between the particle morphology and the film morphology is not evident. The goal of this PhD Thesis is to shed some light on this relationship. Therefore, as it is expected that the film morphology is affected by the particle morphology and the film formation process, the knowledge available about these aspects will be summarized in the next sections.

1.2 Synthesis of hybrid particles

A variety of chemical and physical methods exists for the synthesis of structured polymer particles with different morphologies. Of these, emulsion polymerization is the most common for the synthesis of waterborne polymer-polymer hybrids due to its versatility to control the properties of the final product. Miniemulsion polymerization is more adequate when hydrophobic monomers, preformed polymers and inorganic particles should be included in the polymer particles.[14–19]

1.2.1 Emulsion polymerization

Emulsion polymerization is a technique that leads to colloidal polymer particles dispersed in water with an average particle size that usually is in the range 80 - 300 nm. These polymeric dispersions, often called latexes, are produced by free radical polymerization. Properties of the final latex are determined during polymerization through the formulation (monomers, stabilizer, initiator, crosslinkers) and the process variables (type of reactor, temperature, feeding strategies). Commercial latexes are mostly prepared in stirred tank reactors operated semicontinuously, whereas batch processes are only used to polymerize monomers with similar reactivities and low heat of polymerization. However, this process will be discussed first in order to outline the fundamental basis of emulsion polymerization.

1.2.1.1 Batch emulsion polymerization

In a batch emulsion polymerization, all the compounds of the formulation, except the initiator, are charged into the reactor. The monomers are dispersed in the water phase forming monomer droplets stabilized by a surfactant. Depending on the formulation, surfactant micelles may also be present, with some surfactant also free in the aqueous phase. The reactor is heated to the reaction temperature and usually a water-soluble initiator (aqueous phase) is added as a shot (thermal initiator) or fed during a part of the reaction time (redox initiator). Then, polymerization proceeds in three intervals in series (see Figure 1-1).[20,21]

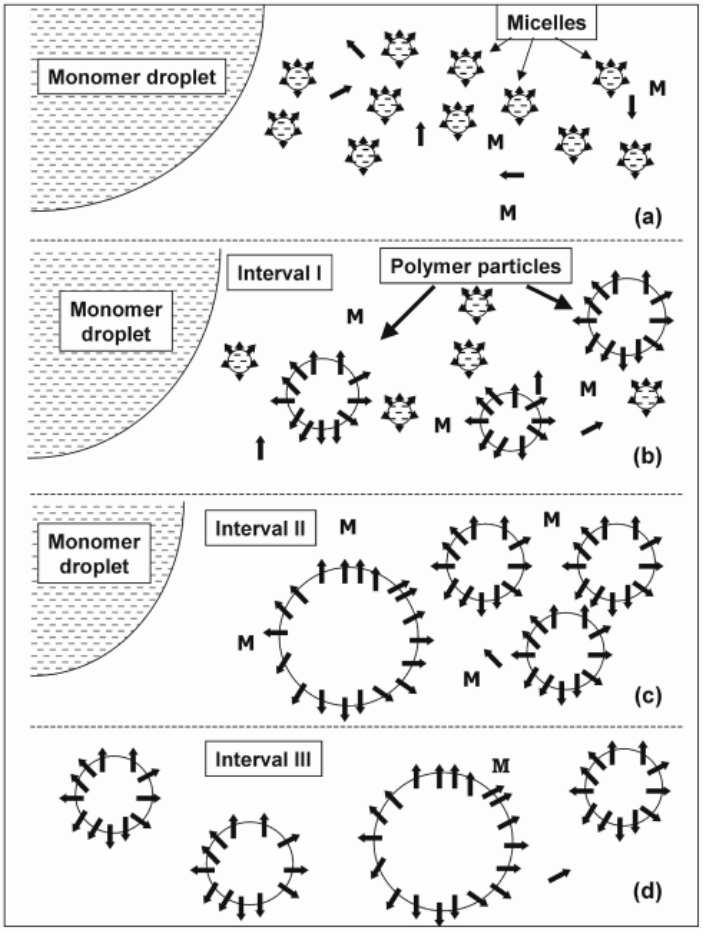

Figure 1-1: Intervals in the batch emulsion polymerization.[22] Reproduced with permission from John Wiley and Sons

Interval I: Particle nucleation. Once the initiator is in the reaction medium, radicals are formed. Typically, radicals formed in the aqueous phase are too hydrophilic to directly enter into the organic phase and therefore, they propagate with monomer dissolved in the aqueous phase. After adding some monomer units, the oligoradicals become hydrophobic enough to enter into the micelles. A polymer chain is formed by propagation of the oligoradical in monomer swollen micelle. A micelle containing at least one polymer chain is called a polymer particle. This process is called heterogeneous nucleation.[20,21] The oligoradicals that do not enter into micelles will continue to grow in the aqueous phase until reaching a critical length at which they are too hydrophobic and precipitate. The precipitated chain is stabilized by the surfactant present in the aqueous phase and monomer diffuses into the new polymer particle. This second process is called homogenous nucleation.[23] Additionally, a third nucleation process known as droplet nucleation can occur by radical entry directly into the monomer droplets, although due to the very low surface area of the droplets compared to micelles this process is extremely unlikely in a typical emulsion polymerization. The end of this interval occurs when all the particles are formed, for a monomer conversion of 5-10% (depending on surfactant/monomer ratio). Due to the increase of the number of particles, the polymerization rate increases in this interval.

Interval II: In this interval, monomer droplets and polymer particles coexist. Polymer particles are the main loci of polymerization. The monomer consumed in the polymer particles are replaced by monomer which diffuses from the droplets to the polymer particles, namely the monomer should diffuse through the aqueous phase. This may be a problem for highly water

insoluble monomers. If the rate of monomer transport is fast enough, the monomer concentration in the polymer particles remains constant in this stage meaning that the polymerization rate is almost constant during this interval. Particle size increases in this interval which ends when the monomer droplets disappear. This interval finishes at a conversion about 25-40%, depending on the extent to which polymer particles are swollen by the monomer.

Interval III: The monomer partitions between the polymer particles (main locus) and the aqueous phase. Monomer is mainly consumed by polymerization in the polymer particles and the concentration of monomer in the polymer particles decreases in this interval. As the number of particle remains constant, the polymerization rate decreases (although a gel effect may cause an increase in the polymerization rate).

1.2.1.2 Semicontinuous emulsion polymerization

In semi-continuous reactors, monomers, surfactant, initiator and water are continuously fed into the reactor. In continuous stirred tank reactors, the whole formulation is continuously fed into the reactor and the product continuously withdrawn. In seeded semi-continuous emulsion polymerization, the initial charge contains a pre-formed latex, called the “seed”, and some fraction of the formulation (monomers, emulsifier, initiator or water). In this system, emulsion polymerization does not follow the intervals described above and is typically in a steady state with the number of particles remaining constant and the monomer consumed by polymerization being replaced by monomer fed into the system. Having said that, nucleation of

new particles may still occur when there is enough emulsifier available to stabilize the oligoradicals, which precipitate in the aqueous phase (homogeneous nucleation). The likelihood of homogeneous nucleation increases with the water solubility of the monomers. Secondary particles may be desirable when bimodal particle size distributions are sought. In this case, heterogeneous nucleation is provoked by adding enough surfactant to form micelles. This is more likely to occur when mobile surfactant are used.[24] Feeding the monomer faster than it is consumed by the reaction should be avoided because the polymer particles become saturated with monomer leading to the formation of monomer droplets which leads to problems in controlling the polymer properties.[25] In addition, an excess of free monomer may jeopardize the safety of the operation.[25] Because reproducibility of particle nucleation in emulsion polymerization is limited, seeded semicontinuous emulsion polymerization is often used to overcome this issue. Since the polymer particles in the seed latex have a high surface area, they efficiently capture radicals from the aqueous phase and thus nucleation of new particles is minimized, leading to better reproducibility. By varying the composition and amount of the initial charge and the composition and flow rates of the feeds, copolymer composition[26–28], molecular weight distribution[29–31], particle size distribution[32,33] and particles morphology[9,11,34] can be controlled. To form hybrid particles, a first polymer is used as a seed for the seeded emulsion polymerization of a monomer giving a second polymer. The particle morphologies that can be obtained by emulsion polymerization will be detailed in Section 1.3.1.

Although emulsion polymerization is highly efficient process for the synthesis of many polymers, it presents certain limitations in the synthesis of hybrid particles. Particle growth implies that the monomer has to be transported from the monomer droplets to the polymer

particles by diffusion through the aqueous phase. In addition, the transport of inorganic filler or preformed polymer is impossible. To overcome this issue, droplet nucleation should be favored while other nucleation mechanisms (micellar and homogeneous nucleation) should be minimized or avoided. The direct nucleation of the monomer droplets can be enhanced if the droplet size is reduced and the surface area of the droplets is large compared to the micelles. This can be achieved by generating an initial emulsion containing droplets on the order of 50 - 500 nm and this process is known as miniemulsion polymerization.

1.2.2 Miniemulsion polymerization

The main difference between miniemulsion polymerization[35–43] and conventional emulsion polymerization is particle nucleation. In miniemulsion polymerization, the droplet size of the initial emulsions is made sufficiently small such that the nucleation occurs mainly in the droplets.

Miniemulsions are submicron (droplet diameter ≈ 50 - 500 nm) oil-in-water dispersions which are stable for a period sufficient to allow polymerization. In miniemulsion polymerization, the monomers are dispersed in an aqueous solution of surfactant. A costabilizer (a hydrophobic, low molecular weight compound) is added to stabilize the miniemulsion against diffusional degradation (Ostwald-ripening).[44] No micelles are present in the system because the surfactant is used to stabilize the large surface area of the droplets. Therefore, when

radicals are formed in the system, they enter into the droplets forming polymer particles, which makes droplet nucleation the main mechanism to form polymer particles.

Formation of droplets in the region of 50 - 500 nm is the result of two consecutive processes: droplet break-up and coagulation.[40,45] Generating small droplets requires substantial mechanical energy and several devices can be used to obtain the monomer-water dispersions including rotor-stators[46,47], membranes[48], static mixers[49], sonifiers[50] and high pressure homogenizers[45,51]. These devices rely on mechanical shear forces and/or cavitation to break the oil phase into submicron size droplets. High-pressure homogenization allows obtaining high-solids content dispersions of nanodroplets even for systems dealing with highly viscous organic phases.[45,52] At the lab scale the most common technique is sonication. Usually, the surfactant is dissolved in the water and the oil phase is composed of the costabilizer dissolved in the monomers. Then, the oil phase is added to the water phase under vigorous agitation and the coarse emulsion is subjected to sonication under agitation. The sonifier tip produces ultrasound waves that cause the molecules to oscillate about their main position as the waves propagates. During the compression cycle, the average distance between the molecules decreases, whilst during rarefaction the distance increases. The rarefaction results in a negative pressure that may cause formation of voids or cavities (cavitation bubbles) that may grow in size. In the succeeding compression cycle of wave, the bubbles are forced to contract and may even disappear totally. The shock waves produced on the total collapse of the bubbles cause the break-up of the surrounding monomer droplets.[53] During the miniemulsification, agitation is required to ensure that all parts of the coarse emulsion pass through the small region below the sonifier tip that is affected by the ultrasound

waves. Therefore the quality of the miniemulsion depends on the flow pattern in the flask, the power applied and the sonication time.[54] Droplet size decreases with the sonication time until a plateau is reached.

As a result of nucleation predominantly occurring directly in the miniemulsion droplets, the diffusion limitations encountered in conventional emulsion polymerization can be overcome and the synthesis of polymer-polymer and polymer-inorganic colloidal materials with complex morphologies is possible. For example, for polymer-polymer hybrid, Mehravar *et al.*[19] synthesized comb-like acrylic-based polymer latexes containing nano-sized crystallizable domains. A seed was prepared by miniemulsion polymerization of stearyl acrylate which led to the formation of crystalline domains. Then, acrylic monomers were fed or added as a shot in order to obtain different hybrid particles which different degrees of crystallinity. Another example is the synthesize of acrylic-polyurethane hybrid by Lopez *et al.* in order to improve the cohesive strength of adhesive.[13] By addition of MMA in the acrylic polymer they obtained hemispherical particle morphology which led to an improvement of the properties of the polymer film (see Figure 1-2). Li *et al*.[16] synthesized polyurethane / acrylic hybrid by redox-initiated miniemulsion and a relatively small amount of surfactant. Particles with a diameter of 50 nm were obtained. However, particle size increased with aging time due to the flocculation of the particles resulting from the chain extension reaction of NCO groups with water. Bisphenol A was used as chain extender to avoid this flocculation. Tsavalas *et al.*[3] synthesized acrylic / epoxy resin core-shell particles (Figure 1-3). Latexes were obtained in which the polyester resin was grafted to the acrylic polymer, forming a water-based crosslinkable coating.

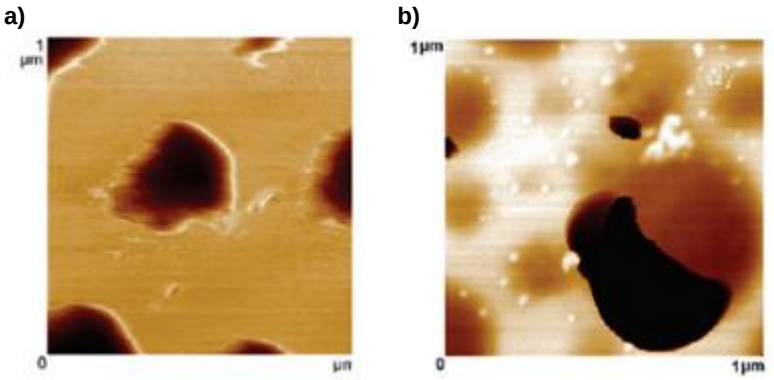

Figure 1-2: AFM images of individual particles of the hybrid latex a) without and b) containing MMA on a mica substrate.[13] Reproduced with permission from American Chemical Society

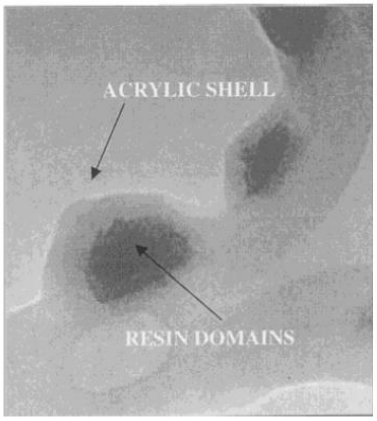

Figure 1-3: TEM images of particles morphology of acrylic / epoxy resin particles latex.[3] Reproduced with permission from John Wiley and Sons

Miniemulsion is also used in the synthesis of polymer-inorganic material hybrid because no transport through the water phase is needed. Aguirre *et. al.* incorporated cerium oxide (CeO_2) in acrylate latex particles hybrid by semi-batch emulsion polymerization.[55,56] The seed was produced by miniemulsion polymerization containing the whole load of the metal oxide. It was found that the nanoparticles were preferentially located at the surface of the seed particles. They obtained a single aggregate of CeO_2 particles per polymer particle due to the incompatibility between the CeO_2 and the polymer (see Figure 1-4 a)). The hybrid dispersion led to UV protective coatings. Another example is the work of de San Luis *et al*.[57]. They used miniemulsion to encapsulate quantum dots into acrylic particles. This hybrid system can be used to improve the electronic transmission in electronic devices such as light emission diodes or solar cells.[58–60] They showed that inefficient encapsulation led to a loss of fluorescent intensity of the quantum dots. This issue was solved by formation of cross-linked core/shell particles composed by a core of cross-linked polystyrene and quantum dots and a shell of cross-linked polymethyl methacrylate produced by seeded semi-batch miniemulsion polymerization (Figure 1-4 b)). Sun *et al.*[15] encapsulated Laponite clay into polystyrene particles. Hydrophobicity of the clay is the key point for the success of the encapsulation and the stability of the latex. A quaternary ammonium salt was mixed with the clay in the monomer phase in order to disintegrate the agglomerates in the clay under sonication. Then, the miniemulsion was prepared by ultrasonication. The salt helped to stabilize the system with a nonionic surfactant. Gong *et al.*[61] encapsulated magnetite into cross linked PS latex particles. After optimization of the formulation (surfactant and crosslinker amount), a homogeneous distribution of the magnetite in the particles was obtained (see Figure 1-4 c)). The magnetic

hybrid nanospheres being superparamagnetic are excellent candidates for biomedical applications after suitable surface modification.

Miniemulsion is also employed to replace surfactant by solid particles in the so-called Pickering (mini)emulsion.[62–67] For example, Gonzalez-Matheus *et al*.[66] synthesized high solids content Pickering stabilized latexes using silica (see Figure 1-4 d)). The silica was modified with alkoxysilanes to make it less hydrophilic and maintain it stable in the aqueous medium. In her work, González *et al.*[67] used surface modified titanium oxide as Pickering stabilizer in the miniemulsion polymerization of methyl methacrylate with butyl acrylate for self-cleaning coatings (see Figure 1-4 e)).

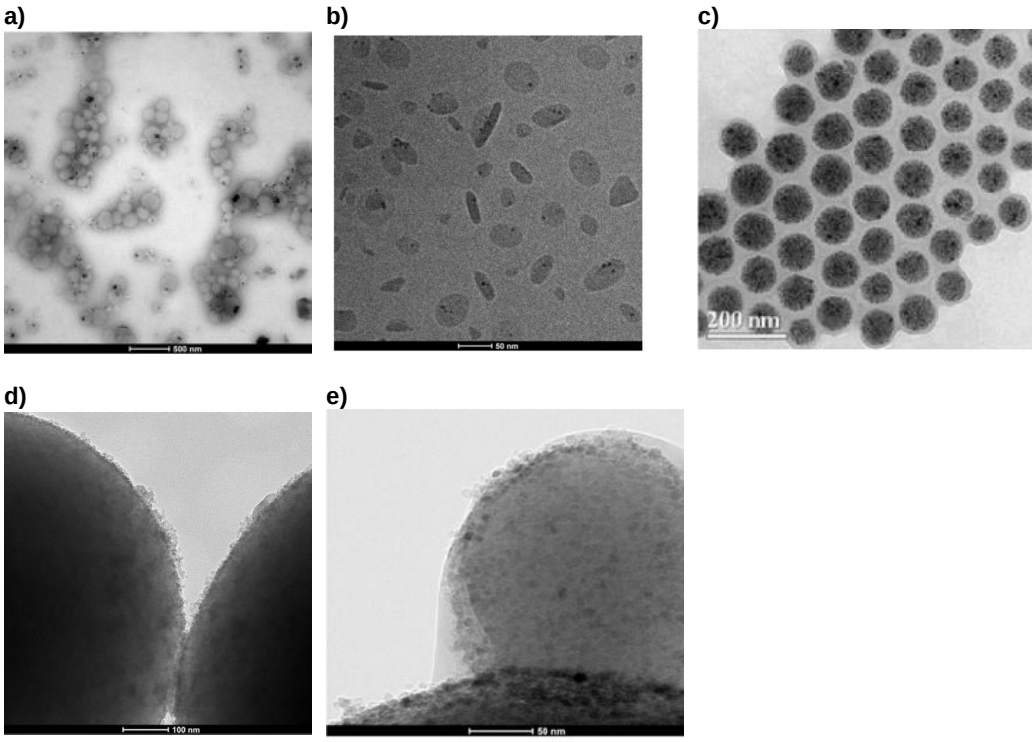

Figure 1-4: a) TEM image of poly MMA/BA/AA latex synthesized with 2 wt% of CeO_2 nanoparticles synthesized by miniemulsion,[56] b) Cryo-TEM micrograph of styrene/DVB monomer miniemulsion droplets containing QDs (0.32 wbm%),[57] c) HR–TEM images of magnetic latexes synthesized,[61] d) TEM image of the surface of the silica stabilized polymer particles synthesized by miniemulsion[66] and e) TEM image of poly MMA/BA latex synthesized with 10 wbm% of TiO_2.[67] All reproduced with permission from Elsevier

1.3 Particle morphology

Particle morphology is the result of the synthesis of particles containing two immiscible phases within the same particle. The incompatibility between the two phases leads to formation of structured particles in which particle morphology is determined by both kinetic and thermodynamic factors. Two important hybrid systems can be identified: polymer-polymer systems and polymer-inorganic material systems.

1.3.1 Polymer-polymer systems

Polymer-polymer hybrid particles can be produced by both emulsion and miniemulsion polymerization. In emulsion polymerization, particles of a given polymer (Polymer 1) are used as a seed for the seeded emulsion polymerization of monomer giving a different polymer (Polymer 2). In miniemulsion polymerization, one of the polymer phases is a preformed polymer that is dissolved in the monomer mixture. In both cases, monomers are polymerized in the presence of a preformed polymer and during polymerization of the monomers, phase separation occurs. Figure 1-5 shows the evolution of the particle morphology for a two-phase system. Before the addition of the initiator, the preformed polymer, which may be one of a variety of materials such as polystyrene,[68] poly(acrylates),[9,69] alkyd[1], polyurethanes[70], epoxy resins[71] and polysiloxanes[72] is swollen by monomers. After initiation of the polymerization, polymer chains are formed inside the preformed polymer matrix. When the concentration of new polymer chains increased, phase separation occurs and clusters are formed. These

clusters can grow due to polymerization within the clusters, by diffusion of polymer formed through the matrix and by coagulation with other clusters. In addition, clusters migrate toward the equilibrium morphology, which is determined by the interfacial tension between the various phases.[34] However, the final morphology strongly depends on the kinetics of cluster migration. When the movement of the phases is not hindered, equilibrium morphologies are reached. Otherwise, non-equilibrium particle morphologies result from the hindered movement of the clusters due to the high internal viscosity of the particles. In this case, different particles morphologies can be formed such as: raspberry-like[73,74] or occluded[75,76] (see Figure 1-6). Occluded particles are formed when the second stage monomer polymerizes within the matrix formed by the first stage polymer and the viscosity of the matrix is high. Raspberry and multi-lobed morphologies can result from the high viscosity of the second polymer which forms the lobes.[74] This can be achieved by using polymers which are not soluble in their monomers such as polyacrylonitrile.[74] Multi-lobed morphology can be form by a hard seed and a hydrophobic second monomer using water soluble initiator.[75]

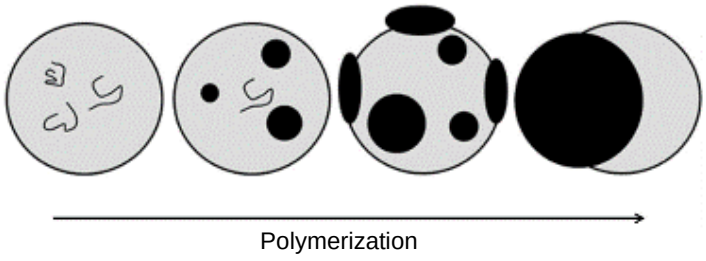

Figure 1-5: Particle morphology development[25] Reproduced with permission from John Wiley and Sons

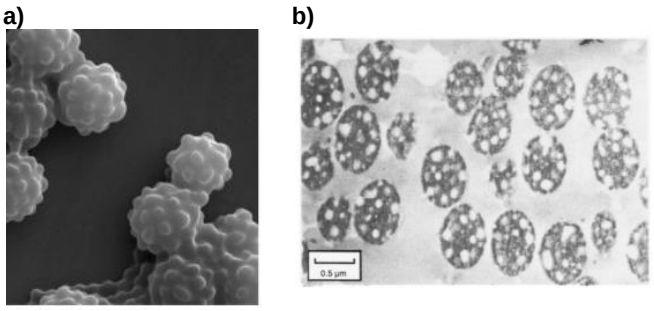

Figure 1-6: Illustrative examples of non-equilibrium morphologies: a) raspberry-like,[73] reproduced with permission of Springer Nature and b) occluded[76] reproduced with permission of American Chemical Society

The final morphology of hybrid particles is therefore controlled by both thermodynamics and kinetics. For two-phase polymer-polymer systems, the thermodynamic equilibrium morphology corresponds to the minimum overall surface energy, which depends on the interfacial areas and interfacial tensions between the polymer phases (γ_{12}), and between each polymer phase and the aqueous medium (γ_{13}, γ_{23}).[77]. The calculation of the minimum overall surface energy is facilitated by the limited number of possible equilibrium morphologies achievable (core-shell, inverted core-shell and hemispherical) (see Figure 1-7). Figure 1-8 displays examples of these morphologies. Inverted core-shell particles are obtained when the second stage polymer is more hydrophobic than the first stage one and the phases are not cross-linked.[78] Hemispherical morphologies are formed when the two polymers have similar hydrophilicities and a relatively high polymer-polymer interfacial tension.

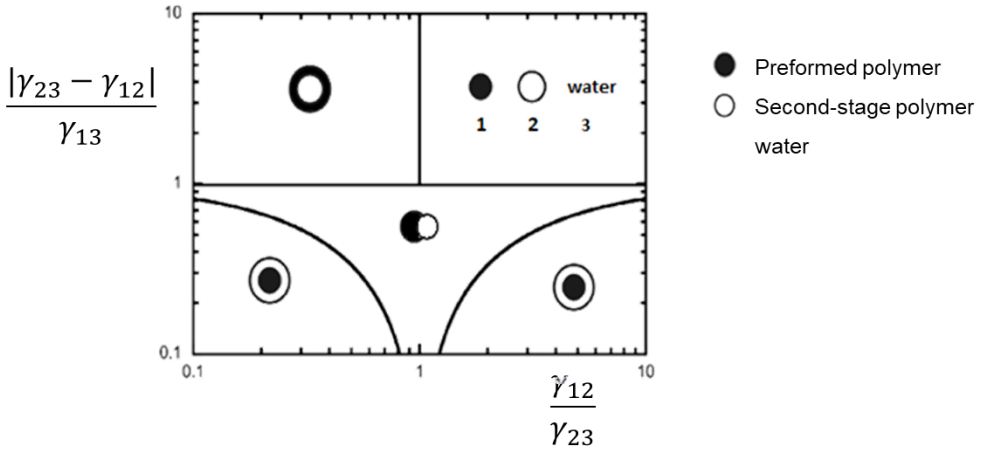

Figure 1-7: Diagram of thermodynamic equilibrium morphologies for polymer-polymer systems.[34] Reproduced with permission from American Chemical Society

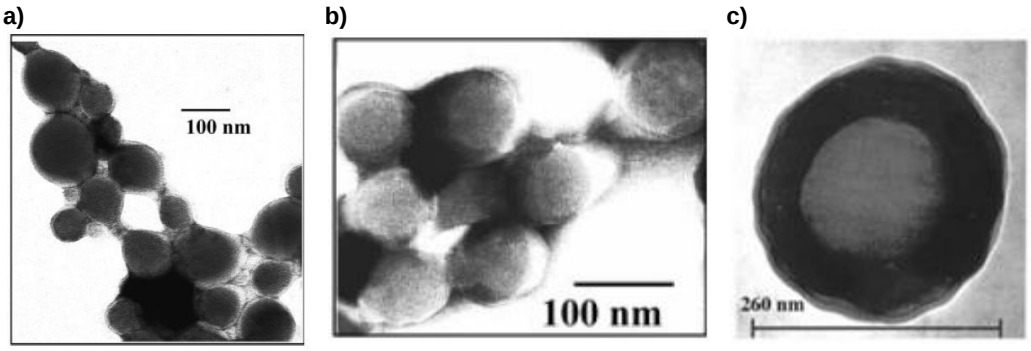

Figure 1-8: TEM images of thermodynamic equilibrium morphologies: a) core-shell[11], b) hemispherical[11] and c) inverted core-shell.[78] Reproduced with permission from a) and b)John Wiley and Sons and c) American Chemical Society

1.3.2 Polymer-inorganic systems

By combining polymers and inorganic materials in a same particle, a large range of particle morphologies can be obtained leading to a broad diversity of applications. Such polymer-inorganic hybrids can be applied in medicine for drug delivery systems[79], prostheses and implants[80], medical diagnostic[81], automotive coatings[82], tooth paste[83] and energy storage[84].

Polymer-inorganic systems can be synthesized by sol-gel process[85], self-assembly techniques such as heterocoagulation[86] or layer-by-layer assembly[87], and in-situ polymerization[88]. However, (mini)emulsion polymerization is the most versatile technique for the synthesis of hybrid materials. Miniemulsion is used for encapsulation of inorganic material because no transport through the water phase is needed and the inorganic material can be relatively easily encapsulated.[89] Pickering-stabilized systems (see Figure 1-9), in which the solid inorganic material resides at the latex particle surface, can be synthesized by both emulsion[62,88,90–92] and miniemulsion[40,64,66] but miniemulsion is favored because it allows to achieve higher solids content with a higher incorporation of the inorganic particles.[66,93]

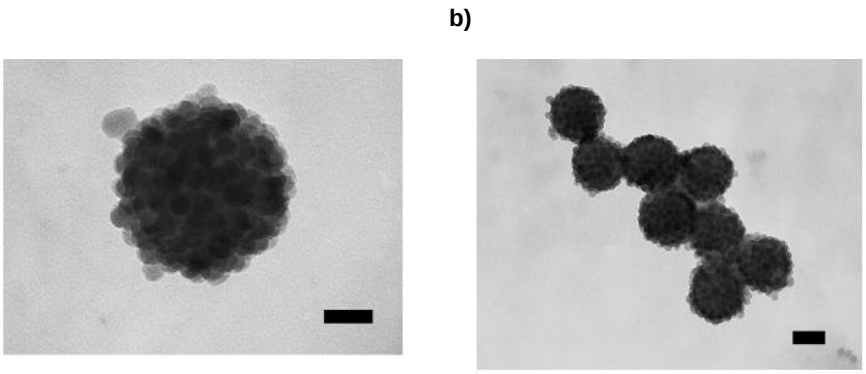

Figure 1-9: TEM images of colloidal silica armored polystyrene latex particles. Scale bars: a) 50 nm and b) 100 nm.[64] Reproduced with permission from American Chemical Society

In polymer-inorganic systems, particle morphology is also the result of the interplay between kinetics and thermodynamics. The equilibrium morphology is, as in polymer-polymer system, the one that minimizes the surface energy of the system, which for a polymer-inorganic system is:

$$E = A_{PW}\gamma_{PW} + A_{IW}\gamma_{IW} + A_{IP}\gamma_{IP} + A_{II}\gamma_{II} \quad \textbf{(1-1)}$$

where A_{ij} and γ_{ij} are the interfacial area and interfacial tension, respectively between phases *i* and j, where *P*, *I* and *W* represent polymer, inorganic material, and aqueous phase.[94] Equation (1-1) includes the energy associated to the interaction between inorganic particles. In most of the cases, the inorganic material is surface-modified in order to make it hydrophobic and more

compatible with the monomers. This means that the interfacial tension γ_{II} can be negligible because when the surface-modified inorganic particles come into contact, the contact occurs between surfaces that are modified with the same material. With this assumption, Equation (1-1) reduces to an equation that has the same mathematical form as the equation used to calculate the equilibrium morphologies for polymer-polymer systems.[95] The minimization of the surface energy gives the map of morphologies (see Figure 1-10, the dark phase corresponds to the inorganic material and the clear one to the polymer). As in polymer-polymer hybrid, the final morphology depends on the kinetics of the inorganic material migration. Non-equilibrium particle morphologies may result from the hindered movement of the cluster due to the high viscosity of the particles.

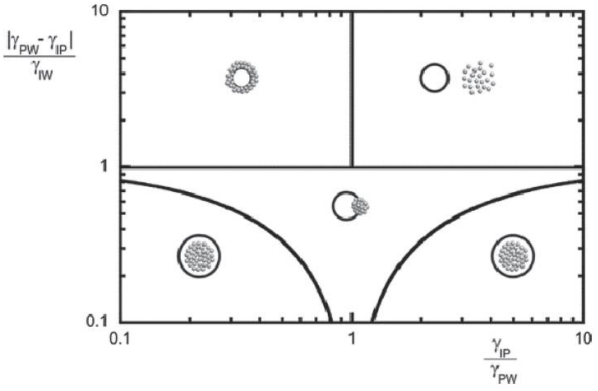

Figure 1-10: Diagram of thermodynamic equilibrium morphologies for polymer-inorganic systems[94] Reproduced with permission of John Wiley and Sons

1.4 Film formation of homogeneous particles latex

"Latex film formation" is the process by which an aqueous dispersion of polymer particles is transformed into a continuous film. For latexes composed of homogenous particles, the film formation process is well established.[96–103] The process can be split into three steps: (a) evaporation of water and particle ordering, (b) particle deformation and (c) interdiffusion of polymers across particle-particle borders (see Figure 1-11).[96] These steps can overlap in time. The film formation process can result in differences in the final film morphology and therefore will directly affect the final film properties.

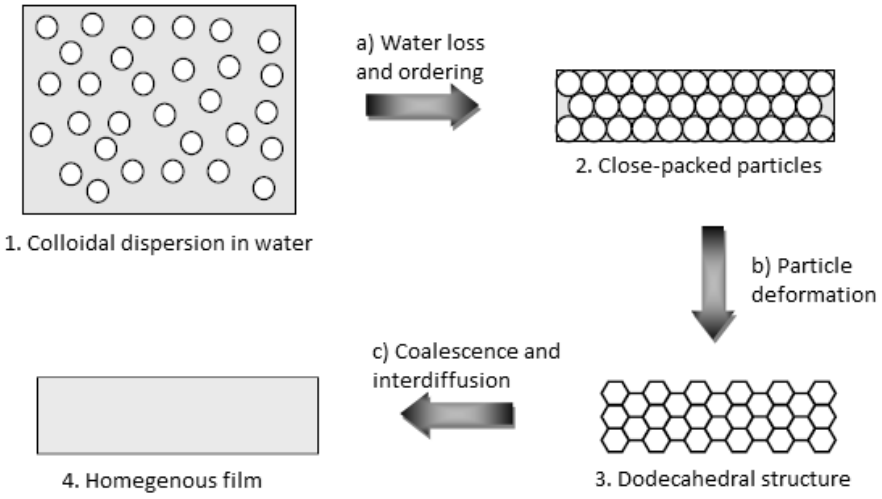

Figure 1-11: Schematic representation of film formation[104]

Stage a: Evaporation of water and particle ordering

The first stage involves removal of excess water by evaporation to achieve close-packing of particles. This drying stage is an important step that significantly influences the distribution of particles in the latex film. Non uniform drying in both horizontal[103,105–107] and vertical[103,106,108,109] directions are observed.

Vertical drying

To understand the process of vertical drying, two timescales have to be taken in account: the one associated with the time required for the water to evaporate in a wet film, and the one corresponding to the time needed for a particle to diffuse from the top to the bottom of the film. The time for evaporation is *H* (wet thickness – dry thickness) divided by the evaporation rate *E* (expressed as a velocity):

$$t_{evap} \sim \frac{H}{E} \qquad \textbf{(1-2)}$$

The time for diffusion of a particle for the distance *H* from the top to the bottom of the film is inversely related to the diffusion coefficient of the particles D_0:

$$t_{diff} \sim \frac{H^2}{D_0} \qquad \textbf{(1-3)}$$

A comparison of the two times is given by the dimensionless Peclet number, P_e as:

$$P_e = \frac{t_{diff}}{t_{evap}} \sim \frac{HE}{D_0} = \frac{6\pi\mu RHE}{kT} \quad \textbf{(1-4)}$$

Equation (1-4) uses the Stokes-Einstein relation for the particle diffusion coefficient:

$$D_0 = \frac{kT}{6\pi\mu R} \quad \textbf{(1-5)}$$

With kT being the thermal energy, μ the viscosity of the aqueous phase and R the particle radius (assuming that they are spherical).

For P_e >>1, diffusion is relatively slow, and therefore a layer of close-packed particles accumulate at the top surface during water evaporation. In Figure 1-12, Ma *et al.* show the accumulation of particles at the air-film interface during film formation.[107] If the particles deform and coalesce, a skin layer may be formed and the evaporation rate will decrease considerably.[110,111] This will have an impact on the properties like cohesion and barrier resistance. Substrate corrosion and poor adhesion to the substrate can also result. For P_e <<1, the particles are predicted to remain dispersed uniformly in the film. The particles order themselves fast enough to avoid being captured at the air-film surface. Moreover, Equation (1-4) shows that uniform drying can be achieved with slow evaporation rates and thin films.

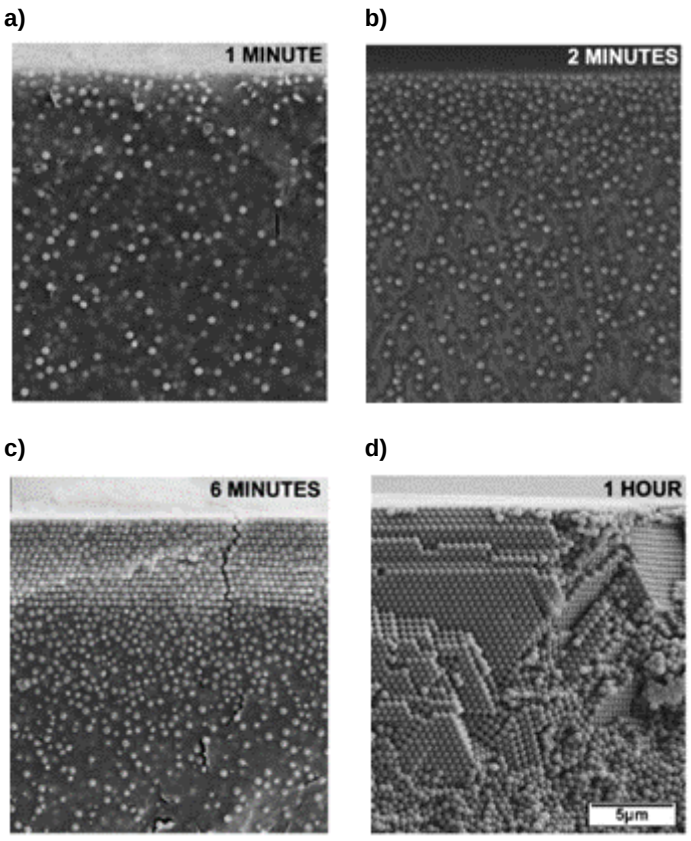

Figure 1-12: Freeze fracture SEM image of cross-sections views a drying film cast from a PS latex after different times of casting: a) 1 minute, b) 2 minutes, c) 6 minutes and d) 1 hour.[107] Reproduced with permission from Elsevier

Horizontal packing and drying fronts

In addition to non-uniform drying in the vertical direction, latex films do not dry uniformly in the horizontal direction.[96,101,105–107,112] The film presents different fronts of different appearances while the film is drying (see Figure 1-13). At least two different fronts can be described. The boundary between a dilute dispersion and the packed particles (where water started to evaporate) is called the “particle front”. In a packed particle bed, a boundary is formed between the wet and dry region, which is called the “drying front”. These fronts are schematically described in Figure 1-14. It has to be point out that these results are only representative for dilute dispersion, commercial latexes are concentrated and may behave differently.

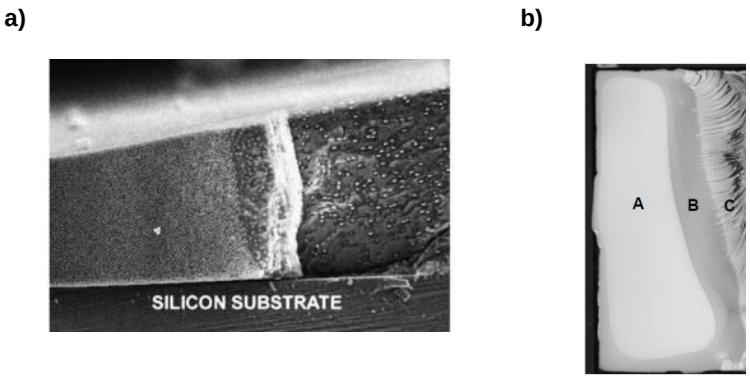

Figure 1-13: a) Formation and progression of lateral consolidation fronts[107] and b) top view of film drying presenting horizontal drying fronts. Region “A” of the film is still fluid. Region “B” presents close packed particles and is saturated in water. Region “C” is dried.[106] Reproduced with permission from Elsevier

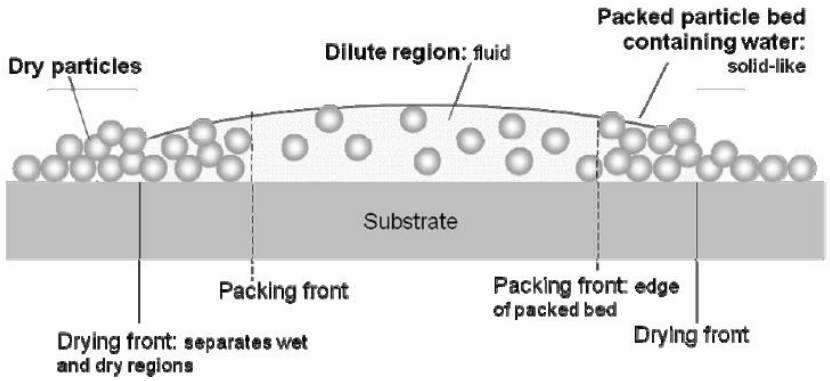

Figure 1-14: Schematic diagram showing the two different types of horizontal front.[103] Reproduced with permission from Springer Nature

While the water evaporates, the particles become arranged in a close-packed form. This ordering can be random and the evaporation rate, controlled by temperature and humidity, has an impact on the particle ordering. Indeed, a fast evaporation prevents the formation of a crystal-like structure. On the other hand, crystal-like structures can be formed from monodispersed particles with a slow evaporation. In that case, crystals tend toward face-centered cubic (FCC) packing.[96]

Stage b: Particle deformation

After close packing of the latex during the first stage, the particles usually start to deform. This is the second stage of film formation. The ideal result for the deformation is a structure without voids. The compaction and deformation of particles in a FCC configuration

leads to rhombic dodecahedral structure (see Figure 1-15). This configuration can be reach for bimodal systems if the size of the small particles allow them to fill the voids left by the big ones during particle ordering.[113] If the small particles are softer than the big ones, their size does not need to be well-defined as they will deform more easily. The development of microscopy techniques has allowed the particle deformation stage to be observed and described. In 1952, Bradford observed that in optically-transparent and continuous films, there is significant particle deformation at the particle surface.[114] This particle deformation is a result of several forces that begin to act upon the particles during drying. The dominant driving force for particle deformation is a reduction in the surface free energy which is balanced by the viscoelastic nature of the polymer. Therefore, interfacial tension between the latex polymer and either water or air have a decisive role in particle deformation.[103] For polymeric materials, the response strongly depends on the viscoelasticity of the particles. Experimental observations pointed out that different deformation mechanisms occurred which are summarized in Figure 1-16 and will be discussed below.

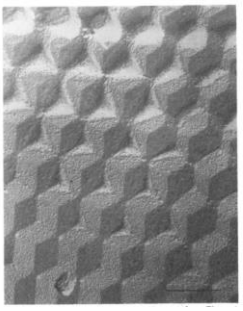

Figure 1-15: TEM image of a carbon replica of a fractured latex films presenting particles in an FCC array which deformed into rhombic dodecahedra.[115] Reproduced with permission from American Chemical Society

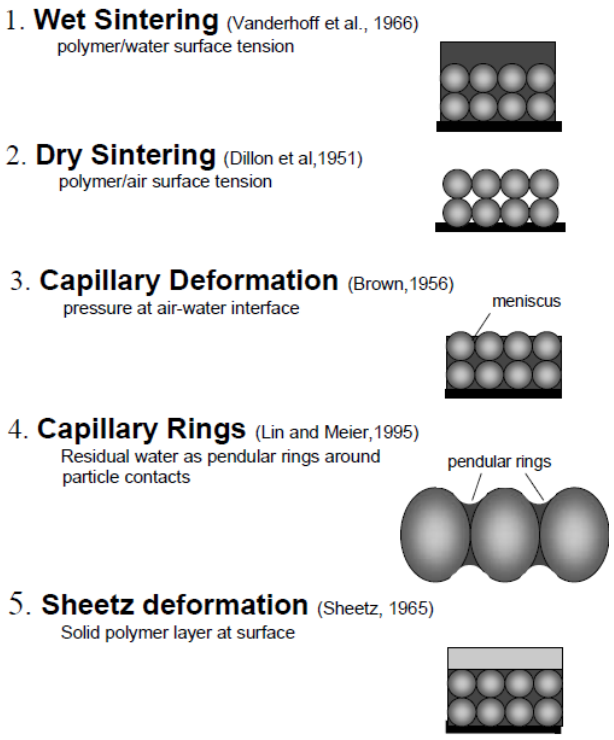

Figure 1-16: Possible mechanisms for particle deformation.[103] Reproduced with permission from Springer Nature

Wet sintering

Wet sintering involves the deformation of particles in presence of water (see Figure 1-16.1). The driving force in that case is the interfacial tension between the particles and the water. If the particles fused together in water, the interfacial area between them is eliminated and the interfacial free energy is decreased. Dobler *et al.*[116] observed particle deformation and compaction only due to the polymer-water interfacial tension. However, the rate of compaction under standard conditions is slow compared to the evaporation of water, so, under common conditions, wet sintering is not a dominant mechanism for film formation.[66,69,82]

Dry sintering

Dry sintering occurs when particles are deformed in the absence of water (see Figure 1-16.2). It is a common mechanism in ceramic made from oxide powders.[118] In the case of latex films, it is driven by the surface tension between the polymer and the air. To observe dry sintering, the water has to evaporate completely before significant particle deformation occurs, which in practice implies that the film is dried at a temperature under the polymer glass transition temperature, to avoid particle deformation. Then the temperature is raised in order to deform the particles.[119] Sperry *et al*. compared a film form an acrylic latex (T_g = 50ºC) dried under these conditions and compare it with one dried under usual conditions. They observed that the minimum film formation temperature (MFFT) was the same in both cases, meaning that for that case, water was not relevant in the deformation of acrylic latex particles films at low temperature.[104,120,121]

Capillary deformation

At a wet film surface, the water between particles forms a meniscus, which is a curved interface between air and water (see Figure 1-16.3). The radius of curvature depends on the wetting of the particles (given by the water contact angle on the polymer surface). The curvature of the air-water interface creates a negative pressure in the fluid, called the "capillary pressure" which compresses the particles below, as hypothesized by Brown. Under this compression the particles deform. The maximum pressure available, with a water-air surface tension of γ_{wa}, can be estimated geometrically as 12.9 γ_{wa} / R_o assuming a spherical meniscus within a triangular array of particle with initial radius R_o. The deformation is dependent on the polymer rheology. Brown assumed that particles were elastic with a shear rate G, and determined the pressure needed to achieve complete compaction of particles as 0.37G. He predicted that film formation occurred when the criterion $G < 35\ \gamma_{wa} / R_o$ holds true. Therefore the particle radius has to be below a critical size in order for film formation to occur. A key point is that the pressure difference across the meniscus is inversely proportional to its radius of curvature. Thus, a more tightly curved water surface will create a greater capillary pressure.[104,122,123]

Receding water front

Capillary rings or receding water front is an inhomogeneous regime (see Figure 1-16.4).[124] Deformation occurs initially by capillary deformation but residual water remains as pendular rings between the particles. The capillary pressure exerted by the pendular rings is similar than in capillary deformation.[104]

Sheetz deformation

Sheetz noticed that film formation is often vertically inhomogeneous, with a skin of dried polymer covering a fluid dispersion below (see Figure 1-16.5).[100] The polymer skin significantly decreases the evaporation rate. Therefore, particles accumulated at the top surface and they have time to sinter by the wet sintering mechanism.[104,117]

Figure 1-17 shows the map developed by Routh and Russel to determine the dominant mechanism for particular latex and drying conditions. This map can be used to tune the parameters such as the evaporation rate or the film thickness and its influence on the particle deformation mechanism. This deformation map depends on two dimensionless control parameters: λ and the Peclet number (*Pe*) (see Equation 1-4). The parameter λ is defined as the ratio between the time required for film compaction (which mean for complete particle deformation t_{def}) and the characteristic time for the evaporation of water t_{evap}, considering that the polymer is viscous. The control parameter is written as

$$\lambda = \frac{t_{def}}{t_{evap}} = \frac{\eta_0 R_0 / \gamma_{wa}}{H/E} = \frac{\eta_0 R_0 E}{\gamma_{wa} H} \qquad \textbf{(1-6)}$$

where η_0 is the low shear viscosity of the polymer, and γ_{wa} is the water-air interfacial tension. A high λ value means that the time required for particle deformation is longer that the evaporation time of water. This implies that the deformation occurs when the water is gone, namely, by a dry sintering mechanism. On the other hand, if λ is low, the time for water to evaporate is higher that the deformation time of the particles meaning that the deformation occurs by a wet sintering mechanism.

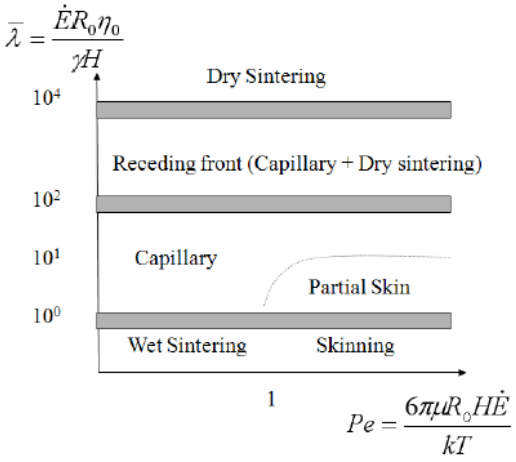

Figure 1-17: Routh-Russel deformation map for latex film formation.[104] Reproduced with permission from American Chemical Society

Stage c: Diffusion across particle/particle boundaries

The last stage involves interdiffusion of the polymer across particle interfaces to fuse the particles boundaries (see Figure 1-18). Interdiffusion of polymer chains occurs at temperature above their glass transition temperature and it is driven by Brownian motion.[125,126] Good cohesion of a latex film is achieved when the polymer chains from different particles have interdiffused between them. The development of techniques of neutron scattering and non-

radiative energy transfer have shown that interdiffusion of polymer chains does indeed occur in homogenous latex particles.[125,127–132]

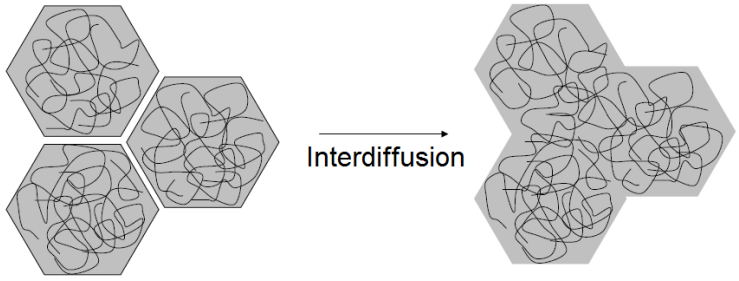

Figure 1-18: Schematic representation of polymer interdiffusion in a latex film.[103] Reproduced with permission from Springer Nature

Several factors affect polymer interdiffusion in latex films of which the molecular weight of the polymer chains and the difference of temperature between the T_g of the polymer and the temperature of film formation are the most important.

Tomba *et al*.[131,132] studied the impact of blending two latexes presenting a high and low molecular weight on polymer interdiffusion. They found that better diffusion of the chains occurred between long and small chains than between two long chains. The chains having different molecular weights present different T_g and the low molecular weight polymer (Mn = 6.4 kg/mol) serves as a plasticizer for the higher molecular weight polymer. In a more general way, the interdiffusion is proportional to the inverse of the square of the molecular weight of the polymer.[125]

Wu *et al.*[130] investigated the temperature dependence of polymer diffusion. They used a latex with a T_g = 28 ºC and measured the polymer diffusion by fluorescence resonance energy transfer. For this technique, two near identical latexes are labeled with fluorescent dyes; one with a donor dye and the other one with an acceptor dye. The two latexes were blended and their film formation studied. When the polymers diffuse, the donor and acceptor come closer and an increase in the extent of energy transfer is measured. Fluorescence decay profiles are measured and the quantum efficiency of energy transfer related to the fraction of molecular mixing is calculated from the changes in the area under the decay profiles. The extent of mixing of the polymer chains is determined with the parameter $f_m(t)$ which gives the extent of mixing of polymer chains after annealing of the film for a time t. Figure 1-19 shows the value of the extent of mixing for different annealing temperature and times. They showed that by increasing the temperature of film formation polymer, diffusion was faster.

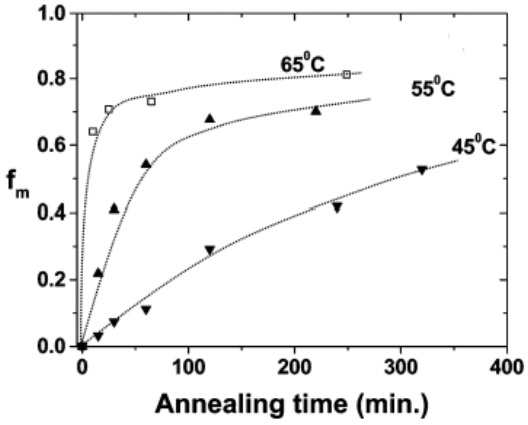

Figure 1-19: Plot of the extent of mixing vs annealing time.[130] Reproduced with permission from American Chemical Society

1.5 Film formation of heterogeneous particles latex

As highlighted in the motivations, one way to satisfy conflicting application requirements is by using a blend of two latexes with different T_{gs}.[113,132–138] The soft polymer helps to form a coherent film under ambient conditions, leading to a continuous film with a dispersed phase of hard polymer, which enhances the mechanical properties.[137] For example, Geurts et al.[137] have shown that through a clever choice of the components of the blend the development of high performance volatile organic compound (VOC)-free paints is possible. This was achieved by using a blend of large soft and small hard particles and adjusting the relative stability of the two dispersions. The resulting film presented an internal structure of connected hard polymer domains embedded in a matrix of soft polymer (a honeycomb structure of hard small particles in a soft polymer was used to illustrate the film structure in Figure 1-20).[11]

A substantial amount of research has been conducted to correlate the characteristics of the blend (composition of the latexes, particles size, ratio between the two latexes, etc.) to the film morphology and properties.[113,124,134,136,137,139–143] Indeed, film formation process of a latex blend is not trivial and stratification can often occur.[142,144–147] Makepeace *et al.*[142] showed that stratification occurred for blends of large soft particles and small hard ones for high size ratio and/or high volume fraction of small particles (Figure 1-21). While in certain cases stratification can be attractive, such as in the production of multilayer coatings,[148] in most cases, homogeneous films are desired and phase separation can lead to an unwanted decrease in the physical properties of the resulting films.[143,149,150]

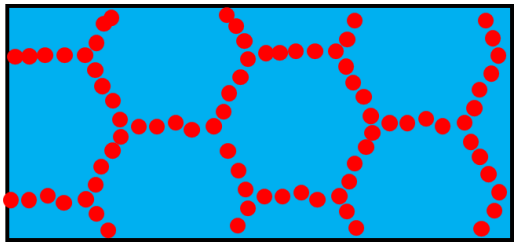

Figure 1-20: a) Model image of a film morphology which enhance the mechanical properties (blue corresponds to soft polymer and red to hard polymer)[137]

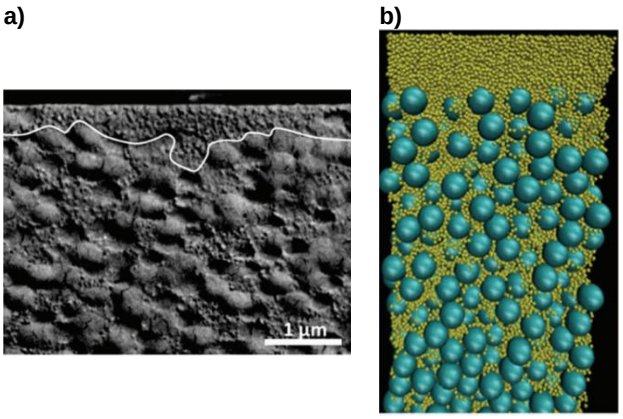

Figure 1-21: a) SEM image of cryo-fractured cross-sections of dried films with a large:small size ratio = 7, a volume fraction of small particles = 0.2 and a total initial volume fraction of particles = 0.4, and b) Cross-sectional visualisation of the results of a Langevin dynamics simulations. The small particles are shown in yellow.[142] Reproduced with permission from The Royal Society of Chemistry

Multiphase acrylic particles show great potential to overcome the issues that arise when using latex blends, as there is a homogeneous distribution of the two phases throughout the polymer film.[151] Moreover, the film morphology discussed by Geurts *et al*. can be translated to hybrid particles containing a soft core and a hard shell. At first sight, one would expect that such particles would be resistant to the deformation needed to undergo film formation, and indeed it has been shown that poly(butyl acrylate) core - poly(methyl methacrylate) shell particles with the same amount of polymer in core and shell do not form film at room temperature.[2] However, it has been reported that under conditions that either reduce the resistance to deformation (thinner and lower T_g shells) or that increase the driving force for deformation (smaller particles), films can be formed from VOC-free soft core-hard shell particles. Thus, using poly(butyl acrylate) core- poly(methyl methacrylate) shell particles Dos Santos and Leibler found that macroscopically homogeneous and transparent films could be obtained by limiting the PMMA contents to 30 wt%.[69,152] TEM images show that they obtained the morphology described by Geurts *et al*. (Figure 1-22). Although the films were ductile, resisting deformations up to 150%, perhaps due to the soft core, the yield stress was limited to 2 MPa. Price *et al*.[153] used a $T_g \approx 3$ ºC core and a $T_g \approx 60$ ºC shell and found that MFFT increased from < 0 ºC for 75/25 wt/wt core/shell particles to 20 ºC for 65/35 and to 35 ºC for 50/50 particles. However, both 65/35 and 50/50 gave poor films when formulated as paints. In addition, the increase of the core T_g forced the decrease of the amount of shell. Using a beam bending technique, they showed that films cast using particles with a thicker hard shell tend to crack during drying due to the restricted deformation and limited strength development in the particle network. On the other hand, Heuts et al. reported that MFFT and Konig hardness were determined by the ratio between soft (T_g = 5 ºC) and hard (T_g = 60 ºC) phases with almost no

effect of the particle morphology (soft core-hard shell vs. hard core-soft shell). Unfortunately, film morphology that might have helped to understand this result was not studied. In addition, a relatively low value of the yield stress was obtained (≈ 3 MPa). A common characteristic of these works is that a very soft polymer is used for the core, which leads to relatively low yield stress and puts a limit on their practical application.

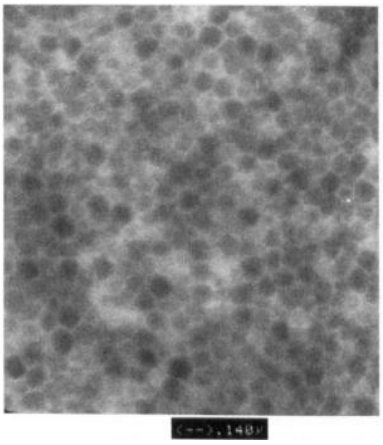

Figure 1-22: TEM image of a film from PBA/PMMA particles in a ratio 80/20 stained with RuO_4.[152] Reproduced with permission from John Wiley and Sons

Homogenous transparent films can be obtained with the hard phase located in the seed polymer. Film formation from particle dispersions with different morphologies (at thermodynamic equilibrium or not) have also been studied. Hagen *et al*.[68] synthesized

hemispherical particles with a hard seed (PS) and a soft second-stage polymer (styrene /butadiene: 50/50 wt/wt). A core-shell morphology was obtained for a pure PS seed and more irregular core was obtained with a PS core cross-linked using divinyl benzene (DVB). The latex formed a continuous film by visual inspection. Figure 1-23 presents the TEM images of the polymer particles and the cross-section of the film with the DVB in the core of the particles. It shows that no large phase separation occurred during film formation. Moreover the latex with the crosslinked PS core particle led to a more reinforced film than the pure PS core particles latex. Schuler *et al*.[9] synthesized different particles with non-equilibrium morphologies by varying the relative amounts soft (BA/MMA/AA: 65.7/32.8/1.5) and hard polymer (MMA/AA: 98.5/1.5) phases in the composite latex. They showed that particle morphology was maintained during film formation without phase migration (see Figure 1-24). As may be expected, it was observed that tensile strength increased and elongation at break decreased with the increase of hard phase in the system but due to the different hard/soft ratios, it was not possible to isolate the effect of particle morphology on mechanical properties.

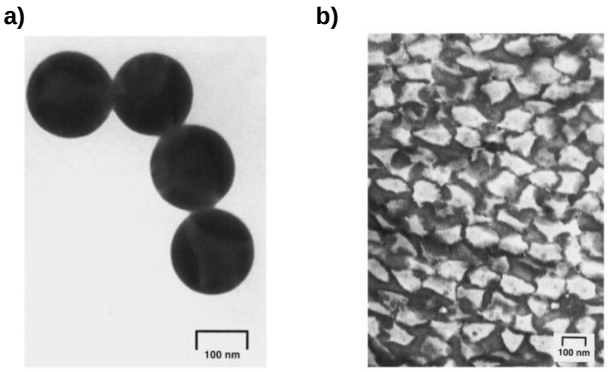

Figure 1-23: a) TEM image of a latex particles with DVB in the seed and a ratio soft/hard: 50/50 b) TEM image of a cross-section of a film cast from the same latex.[68] Reproduced with permission from John Wiley and Sons

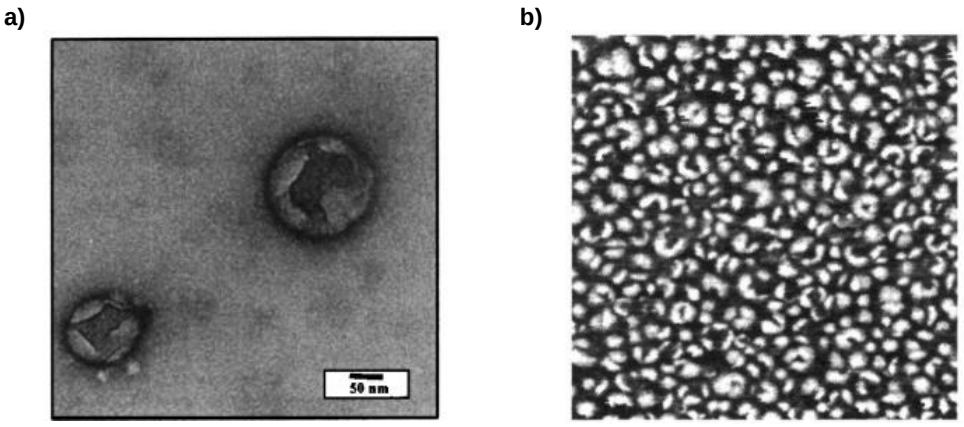

Figure 1-24: a) TEM image of a latex particles with a ratio soft/hard: 65/35 b) AFM phase image (2 μm x 2 μm) of air-film interface from the same latex.[9] Reproduced with permission from Elsevier

Yuan *et al*.[154] synthesized hemispherical particles with a hard seed (T_g = 74 ºC) and a soft second-phase polymer (T_g = 23.2 ºC) with a 50/50 wt/wt ratio between the two phases. They cast a film from this latex at 25 ºC for 2h and then annealed the film at different temperatures (40, 60, 80, 90, 100 and 120 ºC). Figure 1-25 shows the SEM images of the fractured films. The film dried at 25 ºC showed cracks because the drying temperature was too close to the T_g of the soft phase to allow sufficient particle deformation. Moreover, the hard phase of the particle did not deform. With annealing at 80ºC, a more homogeneous film was obtained without cracks due to the good interdiffusion of the soft polymer chains, but the hard phase remained undeformed. When the annealing temperature was above the T_{gs} of both polymers, sufficient mobility of both phases led to phase separation. Phase separation was confirmed by a decrease of the film transparency. Water resistance of the films was improved increasing the annealing temperature until 100ºC due to the formation of micro-pinholes and cracks at the surface of the film above this temperature. This work showed that film morphology (and so, film properties) can be tuned by varying the drying conditions.

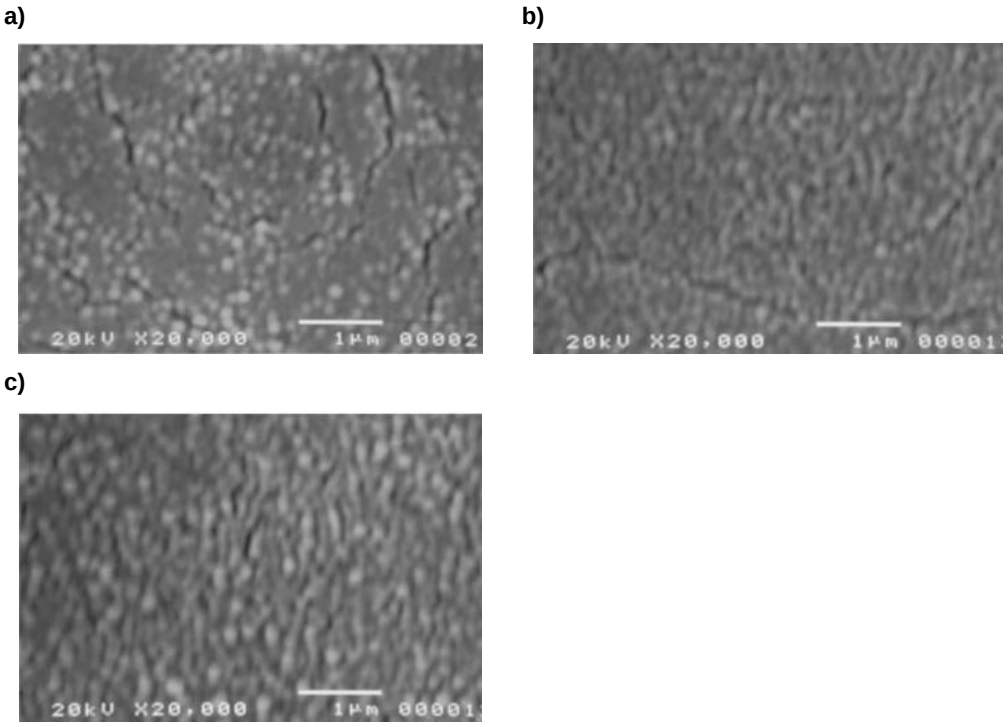

Figure 1-25: SEM cross-section images of hemispherical particles latex films for a film annealed for 120 min at a) 25 ºC, b) 80 ºC and c) 120 ºC.[154] Reproduced with permission from Elsevier

Lee[155] studied core-shell particles with PMMA core and PS shell synthesized by surfactant-free emulsion polymerization with a ratio PMMA/PS: 1/2. A film was cast at 180 ºC and film morphology and properties were measured after different annealing times up 180 min. After 90 min of annealing, movement of the phases gave a film with a PS continuous phase and PMMA clusters dispersed in the PS phase showing some connectivity between them. This

morphology led to an increase of the film tensile strength. After 180 min of thermal annealing, large clusters of PMMA were formed leading to a decrease of film properties.

In the case of film formation from polymer – inorganic hybrid particles latexes two main film morphologies can be obtained depending on the location of the inorganic material in the particle. On one hand, the inorganic material can surround the particles, acting as stabilizer. Common inorganic materials used as stabilizers are: clay[4,156–159], titanium dioxide[17,67] or silica[62,160–162]. Honeycomb-like structure are mainly obtained from this particle morphology, the inorganic material acting as a barrier between the polymer chains contained in each particle.[159–161] Gonzalez-Matheus *et al.*[161] synthesized latex particles stabilized by silica by miniemulsion polymerization. They showed that, surprisingly, this film morphology led to an increase in Young's modulus and stress at break maintaining the elongation. Moreover, as temperature increased during film formation, an increasing number of these barriers were broken allowing interpenetration of the polymer from different particles (Figure 1-26). Ruggerone *et al.*[157] synthesized polystyrene particles with laponite platelets bounded to the particle surface. This particle morphology led to a film with a uniform dispersion of laponite in the polymer matrix (see Figure 1-27).

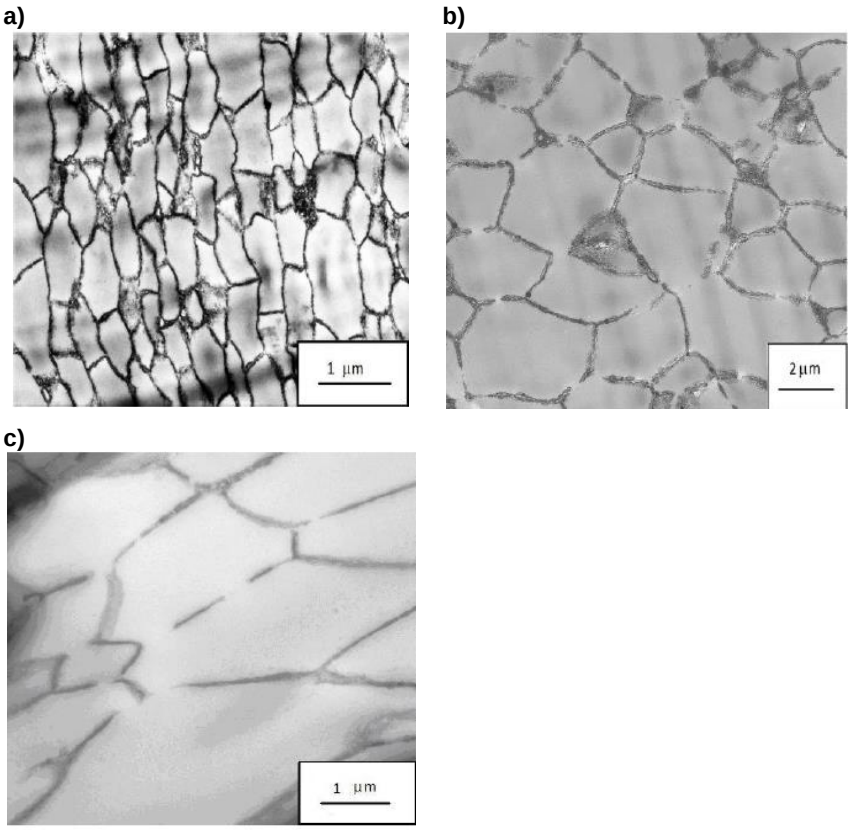

Figure 1-26: TEM image of a film prepared with a latex stabilized with 7.5 wt% of modified silica at a) 30 ºC, b) 60 ºC and c) 70 ºC.[161] Reproduced with permission from Elsevier

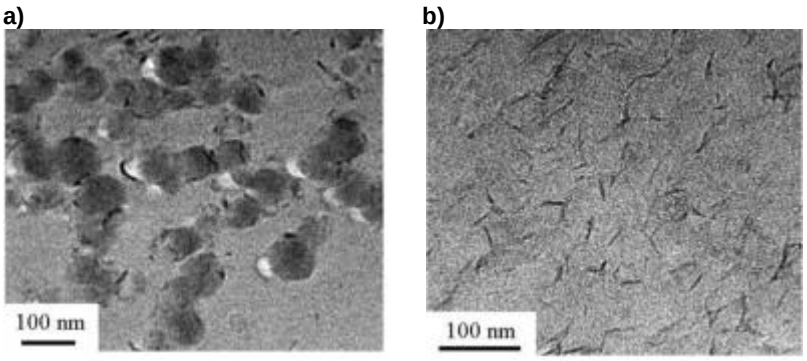

Figure 1-27: TEM images of a) polystyrene / laponite hybrid particles and b)the cross-section of a film cast from this latex.[157] Reproduced with permission from Elsevier

On the other hand, inorganic materials can be encapsulated inside the polymer particles. Quantum dots[57,163], cerium oxide[55,163] or silica[164,165] were successfully encapsulated and transparent films were obtained with the inorganic material dispersed homogeneously in the polymer matrix. Aguirre *et al.* synthesized by seeded semibatch emulsion polymerization 40 wt% solids content latexes with 0.5, 1 and 2 wt% of CeO_2 particles.[55,56] The seed containing all the inorganic particles was produced in situ by miniemulsion polymerization. It was found that at the end of the polymerization, CeO_2 particles were preferentially located at the particle – aqueous phase interface. In the subsequent seeded semibatch polymerization, the nanoparticles were encapsulated with poly(methyl methacrylate-*co*-butyl acrylate). Films casted from the hybrid latexes were transparent and good distribution of the CeO_2 was obtained (see Figure 1-28). Moreover the films showed substantially higher UV absorption than pure polymer films.

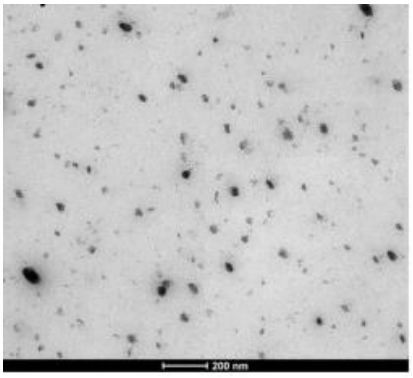

Figure 1-28: TEM image of a film cast from an acrylic/CeO_2 hybrid particles latex synthesized with 2 wt% of CeO_2.[56] Reproduced with permission from Elsevier

1.6 Objectives

The main goal of this thesis is to study how film morphology is influenced by the morphology of the waterborne particles from which the film is formed. Film morphology directly affects application properties and therefore, controlling film morphology would allow ultimately for control over the physical properties of the film. In all the examples given above a direct link between the morphology of the particle and the morphology of the film cast from the latex dispersion was not possible as a result of the often radical differences between polymer compositions when comparing different particle morphologies. Therefore, in this work, specific polymer-polymer hybrid systems are chosen that allow for the isolation of the potential effects of particle morphology on film morphologies and film properties.

1.7 Outline of the thesis

In **Chapter 2**, hybrid particles containing a hard, high T_g seed (Styrene(S)/Acrylamide(AM), T_g = 101 ºC) and a low T_g (Methyl Methacrylate(MMA)/Butyl Acrylate(BA)/Styrene(S), T_g = 13 ºC) second phase polymer were synthesized. Different particle morphologies were obtained by varying of the amount of AM in the seed and that of S in the second-stage polymer. Film morphologies and properties for films cast at 60 ºC were compared in order to find a link between particle morphology and film properties. Moreover, the effect of annealing temperature on film morphology was investigated.

In **Chapter 3**, soft core - hard shell latex particles synthesized by seeded semi-continuous emulsion polymerization are discussed. The aim is to maximize the interconnectivity of the hard phase in the resulting polymer film, thus generate films with improved mechanical properties. The soft core is comprised of a Styrene(S)-Butyl Acrylate(BA) copolymer with a T_g around room temperature. The composition of the second-stage polymer was varied (MMA/BA from 70/30 to 100/0) as well as the ratio between the core and the shell (from 40/60 to 90/10) in order to obtain particles with the same soft core with different hard shells. Films morphology and properties were measured. The effect of annealing temperature on film morphology and properties was also investigated.

In **Chapter 4**, the study the curing process of an alkyd resin in films cast from a hybrid acrylic/alkyd particles latex is discussed. First, the effect of catalysts on the curing of the alkyd in the polymeric film was explored using an AFM based nanomechanical mapping technique. The influence of the curing process on the film morphology and properties were investigated.

In **Chapter 5**, the synthesis, characterization and performance of waterborne acrylic / alkyd hybrid particles dispersions for coating applications are presented. Different particles morphologies were synthesized changing the alkyd resin used and the acrylic composition. These different latexes were used as binders in paints formulations and the main properties of the paints were studied and compared to paints prepared with binders composed of a homogeneous particles (namely, an alkyd dispersion) and also with a blend of acrylic particles and alkyd particles.

In **Chapter 6**, cellulose nanocrystal armored latex particles are discussed. Cellulose nanocrystals (CNCs) were used as Pickering stabilizer in emulsion polymerization process. A cationic initiator was used to ensure the adsorption of the negatively charged CNCs onto the latex particle surface. Films cast from the CNC armored latexes were studied by atomic force microscopy. The mechanical properties of the films were measured. Blends of the CNC armored particles with a regular latex were performed in order to explore the potential to produce mechanically tough polymer films for use in conventional coatings applications.

In **Chapter 7**, blends of acrylic polymer particles containing cationic surface charges with cellulose nanocrystals were studied. Interactions between the CNCs and the polymer particles led to specific film morphologies and properties. Moreover, blends of acrylic polymer particles with anionic surface charges were also blended with CNCs for comparison. The effect of the concentration of CNCs in these blends was studied on film morphology and properties.

In **Chapter 8**, the most significant conclusions of the thesis are presented.

In order to avoid repetition of the experimental and characterization techniques, a detailed description of the characterization methods is given in Appendix I. Finally the Abbreviations used in the thesis is listed.

1.8 References

(1) Goikoetxea, M.; Reyes, Y.; De Las Heras Alarcón, C. M.; Minari, R. J.; Beristain, I.; Paulis, M.; Barandiaran, M. J.; Keddie, J. L.; Asua, J. M. Transformation of waterborne hybrid polymer particles into films: Morphology development and modeling *Polymer* **2012**, *53*, 1098–1108.

(2) Rajatapiti, P.; Dimonie, V. L.; El-Aasser, M. S.; Vratsanos, M. S. Effects of compatibilizing agents in poly(n-butyl acrylate)/poly(methyl methacrylate) composite latexes *J. Appl. Polym. Sci.* **1997**, *63*, 205–219.

(3) Tsavalas, J. G.; Gooch, J. W.; Schork, F. J. Water-based crosslinkable coatings via miniemulsion polymerization of acrylic monomers in the presence of unsaturated polyester resin *J. Appl. Polym. Sci.* **2000**, *75*, 916–927.

(4) Negrete-Herrera, N.; Putaux, J.-L.; David, L.; Haas, F. De; Bourgeat-Lami, E. Polymer/Laponite Composite Latexes: Particle Morphology, Film Microstructure, and Properties *Macromol. Rapid Commun.* **2007**, *28*, 1567–1573.

(5) Goikoetxea, M.; Minari, R. J.; Beristain, I.; Paulis, M.; Barandiaran, M. J.; Asua, J. M. A new strategy to improve alkyd/acrylic compatibilization in waterborne hybrid dispersions *Polymer* **2010**, *51*, 5313–5317.

(6) Mehravar, S.; Ballard, N.; Agirre, A.; Tomovska, R.; Asua, J. M. Role of Grafting on Particle and Film Morphology and Film Properties of Zero VOC Polyurethane/Poly(meth)acrylate Hybrid Dispersions *Macromol. Mater. Eng.* **2018**, 1800532.

(7) Okubo, M.; Katsuta, Y.; Matsumoto, T. Studies on suspension and emulsion. Ii. peculiar morphology of composite polymer particles produced by seeded emulsion polymerization *J. Polym. Sci. Polym. Lett. Ed.* **1982**, *20*, 45–51.

(8) Sundberg, D. C.; Casassa, A. P.; Pantazopoulos, J.; Muscato, M. R.; Kronberg, B.; Berg, J. Morphology development of polymeric microparticles in aqueous dispersions. I. Thermodynamic considerations *J. Appl. Polym. Sci.* **1990**, *41*, 1425–1442.

(9) Schuler, B.; Baumstark, R.; Kirsch, S.; Pfau, A.; Sandor, M.; Zosel, A. Structure and properties of multiphase particles and their impact on the performance of architectural coatings *Prog. Org. Coatings* **2000**, *40*, 139–150.

(10) Sundberg, D. C.; Durant, Y. G. Latex Particle Morphology, Fundamental Aspects: A Review *Polym. React. Eng.* **2003**, *11*, 379–432.

(11) Herrera, V.; Pirri, R.; Asua, J. M.; Leiza, J. R. Morphology control in polystyrene/poly(methyl methacrylate) composite latex particles *J. Polym. Sci. Part A Polym. Chem.* **2007**, *45*, 2484–2493.

(12) Diaconu, G.; Paulis, M.; Leiza, J. R. High solids content waterborne acrylic/montmorillonite nanocomposites by miniemulsion polymerization *Macromol. React. Eng.* **2008**, *2*, 80–89.

(13) Lopez, A.; Degrandi-Contraires, E.; Canetta, E.; Creton, C.; Keddie, J. L.; Asua, J. M. Waterborne polyurethane-acrylic hybrid nanoparticles by miniemulsion polymerization: Applications in pressure-sensitive adhesives *Langmuir* **2011**, *27*, 3878–3888.

(14) Wu, X. Q.; Schork, F. J.; Gooch, J. W. Hybrid miniemulsion polymerization of acrylic/alkyd systems and characterization of the resulting polymers *J. Polym. Sci. Part A Polym. Chem.* **1999**, *37*, 4159–4168.

(15) Sun, Q.; Deng, Y.; Wang, Z. L. Synthesis and characterization of polystyrene-encapsulated laponite composites via miniemulsion polymerization *Macromol. Mater. Eng.* **2004**, *289*, 288–295.

(16) Li, M.; Daniels, E. S.; Dimonie, V.; David Sudol, E.; El-Aasser, M. S. Preparation of polyurethane/acrylic hybrid nanoparticles via a miniemulsion polymerization process *Macromolecules* **2005**, *38*, 4183–4192.

(17) Chen, T.; Colver, P. J.; Bon, S. A. F. Organic–Inorganic Hybrid Hollow Spheres Prepared from TiO2-Stabilized Pickering Emulsion Polymerization *Adv. Mater.* **2007**, *19*, 2286–2289.

(18) M. van Herk, A.; Landfester, K. *Hybrid Latex Particles Preparation with (Mini)emulsion Polymerization*; Springer Berlin Heidelberg, 2010.

(19) Mehravar, E.; Leiza, J. R.; Asua, J. M. Synthesis and characterization of comb-like acrylic-based polymer latexes containing nano-sized crystallizable domains *Polymer* **2016**, *84*, 167–177.

(20) Harkins, W. D. A General Theory of the Mechanism of Emulsion Polymerization *J. Am. Chem. Soc.* **1947**, *69*, 1428–1444.

(21) Smith, W. V.; Ewart, R. H. Kinetics of Emulsion Polymerization *J. Chem. Phys.* **1948**, *16*, 592.

(22) De La Cal, J. C.; Leiza, J. R.; Asua, J. M.; Butt, A.; Storti, G.; Morbidelli, M. In *Handbook of Polymer Reaction Engineering*; Wiley-VCH Verlag GmbH, 2008; pp. 249–322.

(23) Priest, W. J. Partice Growth in the Aqueous Polymerization of Vinyl Acetate *J. Phys. Chem.* **1952**, *56*, 1077–1082.

(24) Ballard, N.; Urrutia, J.; Eizagirre, S.; Schäfer, T.; Diaconu, G.; de la Cal, J. C.; Asua, J. M. Surfactant Kinetics and Their Importance in Nucleation Events in (Mini)emulsion Polymerization Revealed by Quartz Crystal Microbalance with Dissipation Monitoring *Langmuir* **2014**, *30*, 9053–9062.

(25) Asua, J. M. *Polymer Reaction Engineering*; Asua, J. M., Ed.; John Wiley and Sons, 2007.

(26) Gugliotta, L. M.; Arotçarena, M.; Leiza, J. R.; Asua, J. M. Estimation of conversion and copolymer composition in semicontinuous emulsion polymerization using calorimetric data *Polymer* **1995**, *36*, 2019–2023.

(27) Vicente, M.; Leiza, J. R.; Asua, J. M. Simultaneous control of copolymer composition and MWD in emulsion copolymerization *AIChE J.* **2001**, *47*, 1594–1606.

(28) Silvestri, D.; Gagliardi, M.; Cristallini, C.; Barbani, N.; Giusti, P. Different composition poly(methyl methacrylate-co-butyl methacrylate) copolymers through seeded semi-batch emulsion polymerization *Polym. Bull.* **2009**, *63*, 423–439.

(29) Plessis, C.; Arzamendi, G.; Leiza, J. R.; Schoonbrood, H. A. S.; Charmot, D.; Asua, J. M. Kinetics and polymer microstructure of the seeded semibatch emulsion copolymerization of n-butyl acrylate and styrene *Macromolecules* **2001**, *34*, 5147–5157.

(30) Elizalde, O.; Arzamendi, G.; Leiza, J. R.; Asua, J. M. Seeded Semibatch Emulsion

Copolymerization of n -Butyl Acrylate and Methyl Methacrylate *Ind. Eng. Chem. Res.* **2004**, *43*, 7401–7409.

(31) Díaz-Ponce, J. A.; Vazquez-Torres, H.; Martinez-Vera, C. Emulsion terpolymerization of St/MMA/BuA: Modeling of composition, number of particles and the influence of n-DDM on the molecular weights *Chem. Eng. Sci.* **2015**, *138*, 41–58.

(32) Meng, Y.; Weng, Z.; Shan, G.; Huang, Z.; Pan, Z. Particle size distribution and its formation mechanism of polysiloxane/acrylates core-shell composite particles *Acta Polym. Sin.* **2004**, *3*, 367–371.

(33) Mariz, I. de F. A.; de la Cal, J. C.; Leiza, J. R. Control of particle size distribution for the synthesis of small particle size high solids content latexes *Polymer* **2010**, *51*, 4044–4052.

(34) Gonzalez-Ortiz, L. J.; Asua, J. M. Development of Particle Morphology in Emulsion Polymerization. 1. Cluster Dynamics *Macromolecules* **1995**, *28*, 3135–3145.

(35) Ugelstad, J.; El-Aasser, M. S.; Vanderhoff, J. W. Emulsion polymerization: Initiation of polymerization in monomer droplets *J. Polym. Sci. Polym. Lett. Ed.* **1973**, *11*, 503–513.

(36) El-Aasser, M. S.; Miller, C. M. In *Polymeric Dispersions: Principles and Applications*; Springer Netherlands, 1997; pp. 109–126.

(37) Capek, I.; Chern, C. S. Radical polymerization in direct mini-emulsion systems *New Polym. Tech. Synth. Methodol.* **2001**, *155*, 101–165.

(38) Antonietti, M.; Landfester, K. Polyreactions in miniemulsions *Prog. Polym. Sci.* **2002**, *27*, 689–757.

(39) Asua, J. M. Miniemulsion polymerization *Prog. Polym. Sci.* **2002**, *27*, 1283–1346.

(40) Landfester, K. Miniemulsions for Nanoparticle Synthesis *Top Curr Chem* **2003**, *227*, 75–123.

(41) Schork, F. J.; Luo, Y.; Smulders, W.; Russum, J. P.; Butté, A.; Fontenot, K. Miniemulsion polymerization *Adv. Polym. Sci.* **2005**, *175*, 129–255.

(42) Herk, A. M. Van. In *Hybrid Latex Particles*; Springer Berlin Heidelberg, 2010; pp. 1–18.

(43) Asua, J. M. Challenges for industrialization of miniemulsion polymerization *Prog.*

Polym. Sci. **2014**, *39*, 1797–1826.

(44) Ugelstad, J.; Mórk, P. C. C.; Kaggerud, K. H. H.; Ellingsen, T.; Berge, A. Swelling of oligomer-polymer particles. New methods of preparation *Adv. Colloid Interface Sci.* **1980**, *13*, 101–140.

(45) Manea, M.; Chemtob, A.; Paulis, M.; De La Cal, J. C.; Barandiaran, M. J.; Asua, J. M. Miniemulsification in high-pressure homogenizers *AIChE J.* **2008**, *54*, 289–297.

(46) El-Jaby, U.; Cunningham, M. F.; Enright, T.; McKenna, T. F. L. Polymerisable miniemulsions using rotor-stator homogenisers *Macromol. React. Eng.* **2008**, *2*, 350–360.

(47) Ouzineb, K.; Lord, C.; Lesauze, N.; Graillat, C.; Tanguy, P. A.; McKenna, T. Homogenisation devices for the production of miniemulsions *Chem. Eng. Sci.* **2006**, *61*, 2994–3000.

(48) Liu, Z.; Lu, Y.; Zhang, M.; Wan, W.; Luo, G. Controllable preparation of uniform polystyrene nanospheres with premix membrane emulsification *J. Appl. Polym. Sci.* **2013**, *129*, 1202–1211.

(49) Farzi, G.; Bourgeat-Lami, E.; McKenna, T. F. L. Miniemulsions using static mixers: A feasibility study using simple in-line static mixers *J. Appl. Polym. Sci.* **2009**, *114*, 3875–3881.

(50) Behrend, O.; Ax, K.; Schubert, H. Influence of continuous phase viscosity on emulsification by ultrasound *Ultrason. Sonochem.* **2000**, *7*, 77–85.

(51) Amaral, M. Do; Asua, J. M. Synthesis of large, high-solid-content latexes by miniemulsion polymerization *J. Polym. Sci. Part A Polym. Chem.* **2004**, *42*, 4222–4227.

(52) López, A.; Chemtob, A.; Milton, J. L.; Manea, M.; Paulis, M.; Barandiaran, M. J.; Theisinger, S.; Landfester, K.; Hergeth, W. D.; Udagama, R.; McKenna, T.; Simal, F.; Asua, J. M. Miniemulsification of monomer-resin hybrid systems *Ind. Eng. Chem. Res.* **2008**, *47*, 6289–6297.

(53) Mason, T.; Peters, D. In *Practical Sonochemistry*; Wiley, 2002; pp. 1–48.

(54) Amaral, M. do; Arevalillo, A.; Santos, J. L.; Asua, J. M. Novel insight into the miniemulsification process: CFD applied to ultrasonication *Aqueous Polym. Dispersions* **2004**, 103–106.

(55) Aguirre, M.; Paulis, M.; Leiza, J. R. UV screening clear coats based on encapsulated CeO2 hybrid latexes *J. Mater. Chem. A* **2013**, *1*, 3155–3162.

(56) Aguirre, M.; Paulis, M.; Leiza, J. R. Particle nucleation and growth in seeded semibatch miniemulsion polymerization of hybrid CeO2/acrylic latexes *Polymer* **2014**, *55*, 752–761.

(57) De San Luis, A.; Bonnefond, A.; Barrado, M.; Guraya, T.; Iturrondobeitia, M.; Okariz, A.; Paulis, M.; Leiza, J. R. Toward the minimization of fluorescence loss in hybrid cross-linked core-shell PS/QD/PMMA nanoparticles: Effect of the shell thickness *Chem. Eng. J.* **2017**, *313*, 261–269.

(58) Zhao, J.; Bardecker, J. A.; Munro, A. M.; Liu, M. S.; Niu, Y.; Ding, I. K.; Luo, J.; Chen, B.; Jen, A. K. Y.; Ginger, D. S. Efficient CdSe/CdS quantum dot light-emitting diodes using a thermally polymerized hole transport layer *Nano Lett.* **2006**, *6*, 463–467.

(59) Caruge, J. M.; Halpert, J. E.; Wood, V.; Bulović, V.; Bawendi, M. G. Colloidal quantum-dot light-emitting diodes with metal-oxide charge transport layers *Nat. Photonics* **2008**, *2*, 247–250.

(60) Nam, M.; Kim, S.; Kim, S.; Kim, S.-W.; Lee, K. Efficient hybrid solar cells using PbSxSe1−x quantum dots and nanorods for broad-range photon absorption and well-assembled charge transfer networks *Nanoscale* **2013**, *5*, 8202–8209.

(61) Gong, T.; Yang, D.; Hu, J.; Yang, W.; Wang, C.; Lu, J. Q. Preparation of monodispersed hybrid nanospheres with high magnetite content from uniform Fe3O4 clusters *Colloids Surfaces A Physicochem. Eng. Asp.* **2009**, *339*, 232–239.

(62) Bon, S. A. F.; Chen, T. Pickering stabilization as a tool in the fabrication of complex nanopatterned silica microcapsules. *Langmuir* **2007**, *23*, 9527–9530.

(63) Dupin, D.; Schmidt, A.; Balmer, J. A.; Armes, S. P. Efficient synthesis of poly(2-vinylpyridine)-silica colloidal nanocomposite particles using a cationic azo initiator *Langmuir* **2007**, *23*, 11812–11818.

(64) Fortuna, S.; Colard, C. A. L.; Troisi, A.; Bon, S. A. F. Packing Patterns of Silica Nanoparticles on Surfaces of Armored Polystyrene Latex Particles *Langmuir* **2009**, *25*, 12399–12403.

(65) Schrade, A.; Mikhalevich, V.; Landfester, K.; Ziener, U. Synthesis and characterization of positively charged, alumina-coated silica/polystyrene hybrid nanoparticles via pickering miniemulsion polymerization *J. Polym. Sci. Part A Polym. Chem.* **2011**, *49*,

4735–4746.

(66) González-Matheus, K.; Leal, G. P.; Tollan, C.; Asua, J. M. High solids Pickering miniemulsion polymerization *Polymer* **2013**, *54*, 6314–6320.

(67) González, E.; Bonnefond, A.; Barrado, M.; Casado Barrasa, A. M.; Asua, J. M.; Leiza, J. R. Photoactive self-cleaning polymer coatings by TiO2 nanoparticle Pickering miniemulsion polymerization *Chem. Eng. J.* **2015**, *281*, 209–217.

(68) Hagen, R.; Salmén, L.; Karlsson, O.; Wesslén, B. Viscoelastic properties and film morphology of heterogeneous styrene-butadiene latexes *J. Appl. Polym. Sci.* **1996**, *62*, 1067–1078.

(69) Domingues Dos Santos, F.; Leibler, L. Large deformation of films from soft-core/hard-shell hydrophobic lattices *J. Polym. Sci. Part B Polym. Phys.* **2003**, *41*, 224–234.

(70) Martínez-Rugerio, G.; Alegría, Á.; Daniloska, V.; Tomovska, R.; Paulis, M.; Colmenero, J. Dielectric relaxations of Acrylic-Polyurethane hybrid materials *Polymer* **2015**, *74*, 21–29.

(71) Tang, E.; Bian, F.; Klein, A.; El-Aasser, M.; Liu, S.; Yuan, M.; Zhao, D. Fabrication of an epoxy graft poly(St-acrylate) composite latex and its functional properties as a steel coating *Prog. Org. Coatings* **2014**, *77*, 1854–1860.

(72) Zhang, Z.; Li, P. High solids content preparation of styrene-acrylate miniemulsion with PHMS as reactive costabilizer **2011**, *27*, 5–8.

(73) Ostovar, M.; Eslami, H. Synthesis of nanostructured confetti-like and mace-like particles via dispersion polymerization of alkyl methacrylates on polystyrene seeds *Colloid Polym. Sci.* **2016**, *294*, 1633–1642.

(74) Huang, H.; Liu, H. Synthesis of the raspberry-like PS/PAN particles with anisotropic properties via seeded emulsion polymerization initiated by X-ray radiation *J. Polym. Sci. Part A Polym. Chem.* **2010**, *48*, 5198–5205.

(75) Blenner, D.; Stubbs, J.; Sundberg, D. Multi-lobed composite polymer nanoparticles prepared by conventional emulsion polymerization *Polymer* **2017**, *114*, 54–63.

(76) Jonsson, J. E. L.; Hassander, H.; Jansson, L. H.; Tornell, B. Morphology of 2-Phase Polystyrene Poly(Methyl Methacrylate) Latex-Particles Prepared under Different Polymerization Conditions *Macromolecules* **1991**, *24*, 126–131.

(77) Torza, S.; Mason, S. . Three-phase interactions in shear and electrical fields *J. Colloid Interface Sci.* **1970**, *33*, 67–83.

(78) Kirsch, S.; Doerk, A.; Bartsch, E.; Sillescu, H.; Landfester, K.; Spiess, H. W.; Maechtle, W. Synthesis and characterization of highly cross-linked, monodisperse core-shell and inverted core-shell colloidal particles. Polystyrene/ poly(tert-butyl acrylate) core-shell and inverse core-shell particles *Macromolecules* **1999**, *32*, 4508–4518.

(79) Whitlow, J.; Pacelli, S.; Paul, A. Polymeric Nanohybrids as a New Class of Therapeutic Biotransporters *Macromol. Chem. Phys.* **2016**, *217*, 1245–1259.

(80) Catauro, M.; Bollino, F.; Papale, F.; Ferrara, C.; Mustarelli, P. Silica-polyethylene glycol hybrids synthesized by sol-gel: Biocompatibility improvement of titanium implants by coating *Mater. Sci. Eng. C* **2015**, *55*, 118–125.

(81) Kalia, S.; Kango, S.; Kumar, A.; Haldorai, Y.; Kumari, B.; Kumar, R. Magnetic polymer nanocomposites for environmental and biomedical applications *Colloid Polym. Sci.* **2014**, *292*, 2025–2052.

(82) Lionti, K.; Cui, L.; Volksen, W.; Dauskardt, R.; Dubois, G.; Toury, B. Independent control of adhesive and bulk properties of hybrid silica coatings on polycarbonate *ACS Appl. Mater. Interfaces* **2013**, *5*, 11276–11280.

(83) Sideridou, I. D.; Karabela, M. M.; Vouvoudi, E. C. Physical properties of current dental nanohybrid and nanofill light-cured resin composites *Dent. Mater.* **2011**, *27*, 598–607.

(84) Cho, E. S.; Coates, N. E.; Forster, J. D.; Ruminski, A. M.; Russ, B.; Sahu, A.; Su, N. C.; Yang, F.; Urban, J. J. Engineering Synergy: Energy and Mass Transport in Hybrid Nanomaterials *Adv. Mater.* **2015**, *27*, 5744–5752.

(85) Judeinstein, P.; Sanchez, C. Hybrid organic/inorganic materials: a land of multidisciplinarity *J. Mater. Chem.* **1996**, *6*, 511–525.

(86) Voorn, D. J.; Ming, W.; Van Herk, A. M.; Bomans, P. H. H. H.; Frederik, P. M.; Gasemjit, H. P.; Johanssmann, D. Controlled heterocoagulation of platelets and spheres *Langmuir* **2005**, *21*, 6950–6956.

(87) Yuan, J.; Zhou, S.; You, B.; Wu, L. Organic pigment particles coated with colloidal nano-silica particles via layer-by-layer assembly *Chem. Mater.* **2005**, *17*, 3587–3594.

(88) Bourgeat-lami, E.; Insulaire, M.; Reculusa, S.; Perro, A.; Ravaine, S.; Duguet, E. Nucleation of Polystyrene Latex Particles in the Presence of -Methacryloxypropyl-

trimethoxysilane : Functionalized Silica Particles *J. Nanosci. Nanotechnol.* **2006**, *6*, 432–444.

(89) Reculusa, S.; Poncet-Legrand, C.; Ravaine, S.; Mingotaud, C.; Duguet, E.; Bourgeat-Lami, E. Syntheses of raspberrylike silica/polystyrene materials *Chem. Mater.* **2002**, *14*, 2354–2359.

(90) Percy, M. J.; Michailidou, V.; Armes, S. P. Synthesis of Vinyl Polymer - Silica Colloidal Nanocomposites via Aqueous Dispersion Polymerization *Langmuir* **2003**, *19*, 2072–2079.

(91) Chen, M.; Wu, L.; Zhou, S.; You, B. Synthesis of raspberry-like PMMA/SiO2 nanocomposite particles via a surfactant-free method *Macromolecules* **2004**, *37*, 9613–9619.

(92) Bon, S. A. F. In *Encyclopedia of Polymeric Nanomaterials*; Kobayashi, S.; Müllen, K., Eds.; Springer Berlin Heidelberg, 2014; pp. 1–6.

(93) González-Matheus, K.; Leal, G. P.; Asua, J. M. Pickering-Stabilized Latexes with High Silica Incorporation and Improved Salt Stability *Part. Part. Syst. Charact.* **2014**, *31*, 94–100.

(94) Asua, J. M. Mapping the morphology of polymer-inorganic nanocomposites synthesized by miniemulsion polymerization *Macromol. Chem. Phys.* **2014**, *215*, 458–464.

(95) Chen, Y. C.; Dimonie, V.; El-Aasser, M. S. Effect of interfacial phenomena on the development of particle morphology in a polymer latex system *Macromolecules* **1991**, *24*, 3779–3787.

(96) Keddie, J. L. Film formation of latex *Mater. Sci. Eng. R Reports* **1997**, *21*, 101–170.

(97) Brown, G. L. Formation of films from polymer dispersions *J. Polym. Sci.* **1956**, *22*, 423–434.

(98) Henson, W.; Taber, D.; Bradford, E. Mechanism of film formation of latex paint *Ind. Eng. Chem.* **1953**, *45*, 735–739.

(99) Winnik, M. A. Latex film formation *Curr. Opin. Colloid Interface Sci.* **1997**, *2*, 192–199.

(100) Sheetz, D. P. Formation of films by drying of latex *J. Appl. Polym. Sci.* **1965**, *9*, 3759–3773.

(101) Hwa, J. C. H. Mechanism of film formation from latices. Phenomenon of flocculation *J. Polym. Sci. Part A Gen. Pap.* **1964**, *2*, 785–796.

(102) Wang, Y.; Juhué, D.; Winnik, M. A.; Leung, O. M.; Goh, M. C. Atomic force microscopy study of latex film formation *Langmuir* **1992**, *8*, 760–762.

(103) Keddie, J. L.; Routh, A. F. In *Fundamentals of Latex Film Formation*; Springer Netherlands, 2010.

(104) Routh, A. F.; Russel, W. B. Deformation Mechanisms during Latex Film Formation : Experimental Evidence *Ind. Eng. Chem. Res.* **2001**, *40*, 4302–4308.

(105) Routh, F.; Russel, W. B. Horizontal drying fronts during solvent evaporation from latex films *AIChE J.* **1998**, *44*, 2088–2098.

(106) Sutanto, E.; Ma, Y.; Davis, H. T.; Scriven, L. E. Cryogenic Scanning Electron Microscopy of Early Stages of Film Formation in Drying Latex Coatings *ACS Symp. Ser. Film Form. Coatings* **2001**, 174–192.

(107) Ma, Y.; Davis, H. T.; Scriven, L. E. Microstructure development in drying latex coatings *Prog. Org. Coatings* **2005**, *52*, 46–62.

(108) Salamanca, J. M.; Ciampi, E.; Faux, D. A.; Glover, P. M.; McDonald, P. J.; Routh, A. F.; Peters, A. C. I. A.; Satguru, R.; Keddie, J. L. Lateral drying in thick films of waterborne colloidal particles *Langmuir* **2001**, *17*, 3202–3207.

(109) Gorce, J.-P.; Bovey, D.; McDonald, P. J.; Palasz, P.; Taylor, D.; Keddie, J. L. Vertical water distribution during the drying of polymer films cast from aqueous emulsions. *Eur. Phys. J. E. Soft Matter* **2002**, *8*, 421–429.

(110) Mallégol, J.; Bennett, G.; Mcdonald, P. J.; Keddie, J. L.; Dupont, O.; Keddie, J. L. Skin Development During the Film Formation of Waterborne Acrylic Pressure-Sensitive Adhesives Containing Tackifying Resin *J. Adhes.* **2006**, *82*, 217–238.

(111) Vanderhoff, J. W.; Bradford, E. B.; Carrington, W. K. The transport of water through latex films *J. Polym. Sci. Polym. Symp.* **1973**, *41*, 155–174.

(112) Winnik, M. A.; Feng; J. Latex blends : an approach to zero VOC coatings *JCT, J. Coatings Technol.* **1996**, *68*, 39–50.

(113) Feng, J.; Winnik, M. A.; Shivers, R. R.; Clubb, B. Polymer Blend Latex Films: Morphology and Transparency *Macromolecules* **1995**, *28*, 7671–7682.

(114) Bradford, E. B. Electron microscope study of plasticized latices *J. Appl. Phys.* **1952**, *23*, 609–612.

(115) Wang, Y.; Kats, A.; Juhue, D.; Winnik, M. A.; Shivers, R. R.; Dinsdale, C. J. Freeze-fracture studies of latex films formed in the absence and presence of surfactant *Langmuir* **1992**, *8*, 1435–1442.

(116) Dobler, F.; Pith, T.; Holl, Y.; Lambla, M. Synthesis of model latices for the study of coalescence mechanisms *J. Appl. Polym. Sci.* **1992**, *44*, 1075–1086.

(117) Vanderhoff, J. W.; Tarkowski, H. L.; Jenkins, M. C.; Bradford, E. B. Theoretical Consideration of Interfacial Forces Involved in Coalescence of Latex Particles *Rubber Chem. Technol.* **1967**, *40*, 1246–1269.

(118) Bowen, P.; Carry, C. From powders to sintered pieces: Forming, transformations and sintering of nanostructured ceramic oxides *Powder Technol.* **2002**, *128*, 248–255.

(119) Sperry, P. R.; Snyder, B. S.; O'Dowd, M. L.; Lesko, P. M. Role of Water in Particle Deformation and Compaction in Latex Film Formation *Langmuir* **1994**, *10*, 2619–2628.

(120) Dillon, R. E.; Matheson, L. A.; Bradford, E. B. Sintering of synthetic latex particles *J. Colloid Sci.* **1951**, *6*, 108–117.

(121) Lin, F.; Meier, D. J. A study of latex film formation by atomic force microscopy .2. Film formation vs rheological properties: Theory and experiment *Langmuir* **1996**, *12*, 2774–2780.

(122) Mason, G. Formation of films from lattices a theoretical treatment *Br. Polym. J.* **1973**, *5*, 101–108.

(123) Eckersley, S. T.; Rudin, A. The film formation of acrylic latexes: A comprehensive model of film coalescence *J. Appl. Polym. Sci.* **1994**, *53*, 1139–1147.

(124) Keddie, J. L.; Meredith, P.; Jones, R. a. L.; Donald, a. M. Kinetics of Film Formation in Acrylic Latices Studied with Multiple-Angle-of-Incidence Ellipsometry and Environmental SEM *Macromolecules* **1995**, *28*, 2673–2682.

(125) Wang, Y.; Winnik, M. A. Polymer diffusion across interfaces in latex films *J. Phys. Chem.* **1993**, *97*, 2507–2515.

(126) Steward, P. A.; Hearn, J.; Wilkinson, M. C. Overview of polymer latex film formation and properties *Adv. Colloid Interface Sci.* **2000**, *86*, 195–267.

(127) Hahn, K.; Ley, G.; Oberthür, R. On particle coalescence in latex films (II) *Colloid Polym. Sci.* **1988**, *266*, 631–639.

(128) Feng, J.; Odrobina, E.; Winnik, M. A. Effect of Hard Polymer Filler Particles on Polymer Diffusion in a Low- T g Latex Film *Macromolecules* **1998**, *31*, 5290–5299.

(129) Liu, R.; Winnik, M. A.; Di Stefano, F.; Vanketessan, J. Interdiffusion vs cross-linking rates in isobutoxyacrylamide-containing latex coatings *Macromolecules* **2001**, *34*, 7306–7314.

(130) Wu, J.; Tomba, J. P.; Winnik, M. A.; Farwaha, R.; Rademacher, J. Temperature Dependence of Polymer Diffusion in Poly (vinyl acetate- co -dibutyl maleate) Latex Films *Macromolecules* **2004**, *37*, 2299–2306.

(131) Tomba, J. P.; Ye, X.; Li, F.; Winnik, M. A.; Lau, W. Polymer blend latex films: Miscibility and polymer diffusion studied by energy transfer *Polymer* **2008**, *49*, 2055–2064.

(132) Tomba, J. P.; Portinha, D.; Schroeder, W. F.; Winnik, M. A.; Lau, W. Polymer diffusion in high-M/low-M hard-soft latex blends *Colloid Polym. Sci.* **2009**, *287*, 367–378.

(133) Eckersley, S. T.; Helmer, B. J. Mechanistic considerations of particle size effects on film properties of hard/soft latex blends *J. Coatings Technol.* **1997**, *69*, 97–107.

(134) Spiro, J. G.; Farinha, J. P. S.; Winnik, M. A. Thermodynamics and morphology of latex blend films *Macromolecules* **2003**, *36*, 7791–7802.

(135) Singh, K. B.; Deoghare, G.; Tirumkudulu, M. S. Cracking in Soft−Hard Latex Blends: Theory and Experiments *Langmuir* **2009**, *25*, 751–760.

(136) Uğur, Ş.; Elaissari, A.; Holl, Y. Film formation from polystyrene–poly(butyl acrylate-co-methyl methacrylate) latex blends *Polym. Compos.* **2006**, *27*, 431–442.

(137) Geurts, J.; Bouman, J.; Overbeek, A. New waterborne acrylic binders for zero VOC paints *J. Coatings Technol. Res.* **2008**, *5*, 57–63.

(138) Colombini, D.; Hassander, H.; Karlsson, O. J.; Maurer, F. H. J. Influence of the particle size and particle size ratio on the morphology and viscoelastic properties of bimodal hard/soft latex blends *Macromolecules* **2004**, *37*, 6865–6873.

(139) Keddie, J. L.; Meredith, P.; Jones, R. a L.; Donald, A. M. Film formation of acrylic latices with varying concentrations of non-film-forming latex particles *Langmuir* **1996**, *12*, 3793–3801.

(140) Uğur, Ş.; Sunay, S.; Pekcan, Ö. Film formation of nano-sized hard latex (PS) in soft polymer matrix (PBA): An excimer study *Polym. Compos.* **2010**, *31*, 1611–1619.

(141) El-Aasser, M. S.; Tang, J.; Wang, X.; Daniels, E. S.; Dimonie, V. L.; Sudol, E. D. Advances in emulsion polymerization for coatings applications: Latex blends and reactive surfactants *J. Coatings Technol.* **2001**, *73*, 51–63.

(142) Makepeace, D. K.; Fortini, A.; Markov, A.; Locatelli, P.; Lindsay, C.; Moorhouse, S.; Lind, R.; Sear, R. P.; Keddie, J. L. Stratification in binary colloidal polymer films: experiment and simulations *Soft Matter* **2017**, *13*, 6969–6980.

(143) Uğur, Ş.; Sunay, M. S.; Elaissari, A.; Pekcan, Ö. Particle size effect on the film-forming process of PS/PBA composite latexes *Polym. Compos.* **2010**, *31*, 1637–1652.

(144) Kietzke, T.; Neher, D.; Kumke, M.; Ghazy, O.; Ziener, U.; Landfester, K. Phase separation of binary blends in polymer nanoparticles *Small* **2007**, *3*, 1041–1048.

(145) Spruijt, E.; Biesheuvel, P. M. Sedimentation dynamics and equilibrium profiles in multicomponent mixtures of colloidal particles *J. Phys. Condens. Matter* **2014**, *26*, 075101.

(146) Fortini, A.; Martín-Fabiani, I.; De La Haye, J. L.; Dugas, P. Y.; Lansalot, M.; D'Agosto, F.; Bourgeat-Lami, E.; Keddie, J. L.; Sear, R. P. Dynamic Stratification in Drying Films of Colloidal Mixtures *Phys. Rev. Lett.* **2016**, *116*, 118301.

(147) Schulz, M.; Keddie, J. L. A critical and quantitative review of the stratification of particles during the drying of colloidal films *Soft Matter* **2018**, *14*, 6181–6197.

(148) Bull, S. J.; Jones, A. M. Multilayer coatings for improved performance *Surf. Coatings Technol.* **1996**, *78*, 173–184.

(149) Tzitzinou, A.; Keddie, J. L.; Geurts, J. M.; Peters, A. C. I. A. I. A.; Satguru, R. Film formation of latex blends with bimodal particle size distributions: Consideration of particle deformability and continuity of the dispersed phase *Macromolecules* **2000**, *33*, 2695–2708.

(150) Ugur, S.; Holl, Y. Fluorescence study of film formation from hard/soft latex blends *E-Polymers* **2006**, *6*, 1–20.

(151) Chevalier, Y.; Hidalgo, M.; Cavaillé, J. Y.; Cabane, B. In *Progress in Organic Coatings*; Elsevier, 1997; Vol. 32, pp. 35–41.

(152) Domingues Dos Santos, F.; Fabre, P.; Drujon, X.; Meunier, G.; Leibler, L. Films from soft-core/hard-shell hydrophobic latexes: Structure and thermomechanical properties *J. Polym. Sci. Part B Polym. Phys.* **2000**, *38*, 2989–3000.

(153) Price, K.; Wu, W.; Wood, K.; Kong, S.; McCormick, A.; Francis, L. Stress development and film formation in multiphase composite latexes *J. Coatings Technol. Res.* **2014**, *11*, 827–839.

(154) Yuan, X.; Huo, D.; Qian, Q. Effect of annealing on the phase structure and the properties of the film formed from P(St-co-BA)/P(MMA-co-BA) composite latex *J. Colloid Interface Sci.* **2010**, *346*, 72–78.

(155) Lee, C. F. The properties of core-shell composite polymer latex. Effect of heating on the morphology and physical properties of PMMA/PS core-shell composite latex and the polymer blends *Polymer* **2000**, *41*, 1337–1344.

(156) Bon, S. A. F. F.; Colver, P. J. Pickering miniemulsion polymerization using laponite clay as a stabilizer *Langmuir* **2007**, *23*, 8316–8322.

(157) Ruggerone, R.; Plummer, C. J. G.; Negrete Herrera, N.; Bourgeat-Lami, E.; Månson, J. A. E. Fracture mechanisms in polystyrene/laponite nanocomposites prepared by emulsion polymerization *Eng. Fract. Mech.* **2009**, *76*, 2846–2855.

(158) Bonnefond, A.; Mičušík, M.; Paulis, M.; Leiza, J. R.; Teixeira, R. F. A.; Bon, S. A. F. Morphology and properties of waterborne adhesives made from hybrid polyacrylic/montmorillonite clay colloidal dispersions showing improved tack and shear resistance *Colloid Polym. Sci.* **2013**, *291*, 167–180.

(159) Delafresnaye, L.; Dugas, P.-Y.; Dufils, P.-E.; Chaduc, I.; Vinas, J.; Lansalot, M.; Bourgeat-Lami, E.; Laura Delafresnaye; Pierre-Yves Dugas; Pierre-Emmanuel Dufils; Isabelle Chaduc; Jérôme Vinas; Muriel Lansalot; Elodie Bourgeat-Lami. Synthesis of clay-armored poly(vinylidene chloride- co -methyl acrylate) latexes by Pickering emulsion polymerization and their film-forming properties *Polym. Chem.* **2017**, *8*, 6217–6232.

(160) Schmid, A.; Tonnar, J.; Armes, S. P. A new highly efficient route to polymer-silica colloidal nanocomposite particles *Adv. Mater.* **2008**, *20*, 3331–3336.

(161) González-Matheus, K.; Leal, G. P.; Asua, J. M. Film formation from Pickering stabilized waterborne polymer dispersions *Polymer* **2015**, *69*, 73–82.

(162) Schrade, A.; Landfester, K.; Ziener, U. Pickering-type stabilized nanoparticles by

heterophase polymerization *Chem. Soc. Rev.* **2013**, *42*, 6823.

(163) De San Luis, A.; Paulis, M.; Leiza, J. R. Co-encapsulation of CdSe/ZnS and CeO2nanoparticles in waterborne polymer dispersions: Enhancement of fluorescence emission under sunlight *Soft Matter* **2017**, *13*, 8039–8047.

(164) Espiard, P.; Guyot, A.; Perez, J.; Vigier, G.; David, L. Poly(ethyl acrylate) latexes encapsulating nanoparticles of silica: 3. Morphology and mechanical properties of reinforced films *Polymer* **1995**, *36*, 4397–4403.

(165) Bourgeat-Lami, E.; Lang, J. Encapsulation of Inorganic Particles by Dispersion Polymerization in Polar Media: 1. Silica Nanoparticles Encapsulated by Polystyrene *J. Colloid Interface Sci.* **1998**, *197*, 293–308.

Chapter 2. Influence of particle morphology on the structure and mechanical properties of films cast form polystyrene / poly (meth)acrylic hybrid latexes

2.1 Introduction

As pointed out in Chapter 1, the synthesis of polymer-polymer particles by emulsion polymerization to obtain different morphologies has been extensively studied.[1–9] However, it is not well known how the particle morphology influences the morphology and mechanical properties of films cast from such latexes. Therefore, the objective of this chapter is to see if film morphology can be engineered via the particle morphology to control mechanical properties. To this end, different particles morphologies with similar molecular weights and near identical formulations were targeted. We focused on pure acrylic latexes containing a hard seed (Styrene(S)/Acrylamide(AM), T_g = 101 ºC) and soft second stage polymer (Methyl Methacrylate (MMA)/Butyl Acrylate(BA)/Styrene(S), T_g = 16 ºC). The films morphologies and mechanical properties form the hybrid particles latexes were studied. In addition, a comparison with a blend of the two polymers with the same composition of the multiphase particles was performed to demonstrate the advantages of using multiphase particles rather than a blend.

The last part of this chapter is focused on the study of film morphologies obtained after thermal treatment of the films previously discussed.

2.2 Experimental part

2.2.1 Materials

Methyl methacrylate (MMA, technical grade, Quimidroga), butyl acrylate (BA, technical grade, Quimidroga), styrene (S, technical grade, Quimidroga) and acrylamide (AM, >98%, Sigma-Aldrich) were used as received. Potassium persulfate (KPS, >99%, Sigma-Aldrich) was used as thermal initiator. Sodium lauryl sulphate (SDS, >99%, Sigma-Aldrich) was used as conventional surfactant. GPC grade tetrahydrofuran (THF, Scharlau) was also used as received. Deionised water was used throughout the work.

2.2.2 Polymerizations

Latexes with very similar overall composition but different particle morphology were synthesized. For the first latex M1 a core-shell morphology was sought. A poly(styrene) (S) seed was prepared and a mixture of methyl methacrylate (MMA)/butyl acrylate (BA) (50/50 wt/wt) formed the second stage polymer in a seeded semicontinuous emulsion copolymerization. It was expected that the higher hydrophilicity of the second stage polymer led to a core-shell morphology. For the second latex, M2, a hemispherical morphology was

desired. For this, the hydrophilicity of the seed was increased by including some acrylamide(AM) (S/AM (with = 99.5/0.5 wt/wt) while maintaining the composition of the second stage polymer. M3 was synthesized increasing again the amount of acrylamide in the seed (S/AM: 98/2 wt/wt). Also aiming at hemispherical morphologies, a fourth system, M4, was synthesized with the same seed as M2 and including some styrene in the second stage polymer (MMA/BA/S = 45/50/5 wt/wt), which will increase the interfacial tension between the second stage polymer and water and decrease the interfacial tension between the two polymer phases. In all cases, the ratio between the seed and the second-stage polymer was 40/60 and the solids content was 50 wt %. The seeds were prepared using the formulations in Table 2-1. A solution composed of 1% of the total surfactant (sodium dodecyl sulfate, SDS) and 50% of the total water was charged into in a 1-L glass reactor equipped with a reflux condenser, a stainless steel anchor type stirrer, sampling device, and nitrogen inlet. The rest of the formulation was fed during 3 hours and afterwards the latex was left to react for another hour. Potassium persulfate (KPS) was used as thermal initiator. The reaction temperature was 70 ºC and the agitation rate was 150 rpm. The second stage polymer was obtained by seeded emulsion copolymerization carried out at 70 ºC using the formulations in Table 2-2. The seed latex was charged to the reaction and the rest of the chemicals were stirred to form a pre-emulsion. This pre-emulsion was then fed into the reactor for 3 hours and left to react in batch for another hour. Moreover, two single-phase latexes were synthesized at 70 ºC in the same manner as the seed latex using the formulations in Table 2-3. The formulations of these two latexes correspond to the two phases of the latex M4. Then, a blend (B4) was prepared with a ratio La/Lb: 40/60. The composition of the different systems are summarized in Table 2-4.Films were produced by casting 0.4g of latex (solids content 50%) in rectangular silicone molds (10

mm x 40 mm x 0.6 mm) and allowed them to dry at 60 ºC and 55% of relative humidity for 24 hours. Then, one sample of each film was annealed at 150 ºC for different times: 15 min, 4h and 20h.

Table 2-1: Formulation of the seed latex. T = 70 ºC

Compounds	S1 (g)	S2 (g)	S3 (g)
Water	135.1	135.1	135.1
SDS	3.9	3.9	3.9
KPS	1.04	1.04	1.04
AM	0	0.65	2.6
S	130	129.35	127.4

Table 2-2: Formulation of the semi-batch second stage polymerizations. T = 70 ºC

Compounds	M1 (g)	M2 (g)	M3 (g)	M4(g)
Seed	S1 270.04	S2 270.04	S3 270.04	S2**I** 270.04
Water	202.6	202.6	202.6	202.6
SDS	3.73	3.73	3.73	3.73
KPS	0.93	0.93	0.93	0.93
MMA	99	99	99	89.06
BA	99	99	99	98.95
S	0	0	0	9.9

Table 2-3: Formulation of the semi-batch polymerizations for the blend preparation. T = 70 ºC

Compounds	La (g)	Lb (g)
Water	202.72	202.72
SDS	5.85	5.85
KPS	1.56	1.56
AM	0.98	0
S	194.03	9.75
MMA	0	87.75
BA	0	97.5

Table 2-4: Composition of the different systems

	Core (S/AM)	Shell (MMA/BA/S)	Core / Shell (% wt/wt)
M1	100/0	50/50/0	40/60
M2	99.5/0.5	50/50/0	40/60
M3	98/2	50/50/0	40/60
M4	99.5/0.5	45/50/5	40/60
La	99.5/0.5	0	100/0
Lb	0	45/50/5	0/100

2.2.3 Characterizations

The particle size of the final latexes were measured by capillary hydrodynamic fractionation (CHDF). Residual monomers were measured by gas chromatography (GC). Solids content of the latexes was measured by gravimetry. Glass transition temperature, T_g, of the acrylic polymer was measured by differential scanning calorimetry (DSC). The gel content of the polymers was determined by Soxhlet extraction. The molecular weight distributions were determined by gel permeation chromatography (GPC). Particles and film morphologies were determined by transmission electron microscopy (TEM). The mechanical properties of the films cast from the synthesized latexes were determined by tensile test measurements. A detailed description of the characterization methods is provided in Appendix I.

2.3 Results and discussion

2.3.1 Latexes characterization and particle morphologies

Table 2-5 summarizes the results for the polymerizations for the seed latexes and the hybrid particles as well as the T_{gs} of the phases and the minimum film formation temperature (MFFT) of the films cast from the latex dispersions (see Table 2-4 for the compositions of the latexes). In all cases, conversion of the first stage polymer (seed) was high (X>95 %), although due to the glass effect some residual monomer was observed. For the final hybrid polymers, conversions greater than 99% were achieved in all cases. All the hybrid latexes presented

similar particle size, molecular weights, dispersities (***Đ***) and gel content with the exception of latex S3 which had 19% of gel content. This was most likely caused by physical interactions (hydrogen bonding) due to the acrylamide in the system rather than being a truly chemically cross-linked system. In addition, it is possible that the use of acrylamide may result in increased amount of intermolecular chain transfer to polymer which can lead to some chemically crosslinked material.[10]

Figure 2-1 presents the derivatives of the reversible heat flow measured by differential scanning calorimetry (DSC) of all samples for the first and second heating cycles. This gives information about the T_g of the phases as well as about the interaction between the two phases. For the current systems that have widely different T_{gs} any significant shift of the T_{gs} or the presence of peaks between the T_{gs} will indicate phase interpenetration.[11] The glass transition temperatures (measured in the second heating cycle) were almost identical in all systems. The first T_g (16 ºC) corresponds to the soft phase composed of MMA/BA/S and the second T_g = 103 ºC to the styrene-rich phase. Slightly higher T_{gs} were observed during the first scan for all hybrids and the blend. However, the differences were small and they did not indicate interpenetration between the two polymers as in this case, the T_{gs} should approach each other.[11]

Table 2-5: Results of the polymerization of the two acrylic hybrids latexes

Latex	Residual monomers (ppm) (Conversion (%))	Particle size (nm)	Gel content (%)	Mn (kg/mol)	Mw (kg/mol)	Đ	T_{gs} (°C)	MFFT (°C)
S1	25000 (96.7)	112	<2	168	679	4	93	> 90
M1	6150 (99.1)	130	<2	321	824	2.6	13 / 100	16
S2	28000 (96.4)	101	<2	190	596	3.1	90	> 90
M2	2500 (99.7)	120	<2	385	712	1.85	13 / 101	18
S3	23500 (97.1)	104	19	84	470	5.6	90	> 90
M3	2300 (99.8)	134	4.5	343	532	1.55	13 / 102	25
M4	8600 (97.8)	145	<2	344	623	1.8	13 / 101	17
La	10000 (96)	140	<2	110	525	4.8	88	> 90
Lb	850 (99.2)	112	<2	131	691	5.3	10	4
B4	/	/	/	/	/	/	10 / 101	< 6

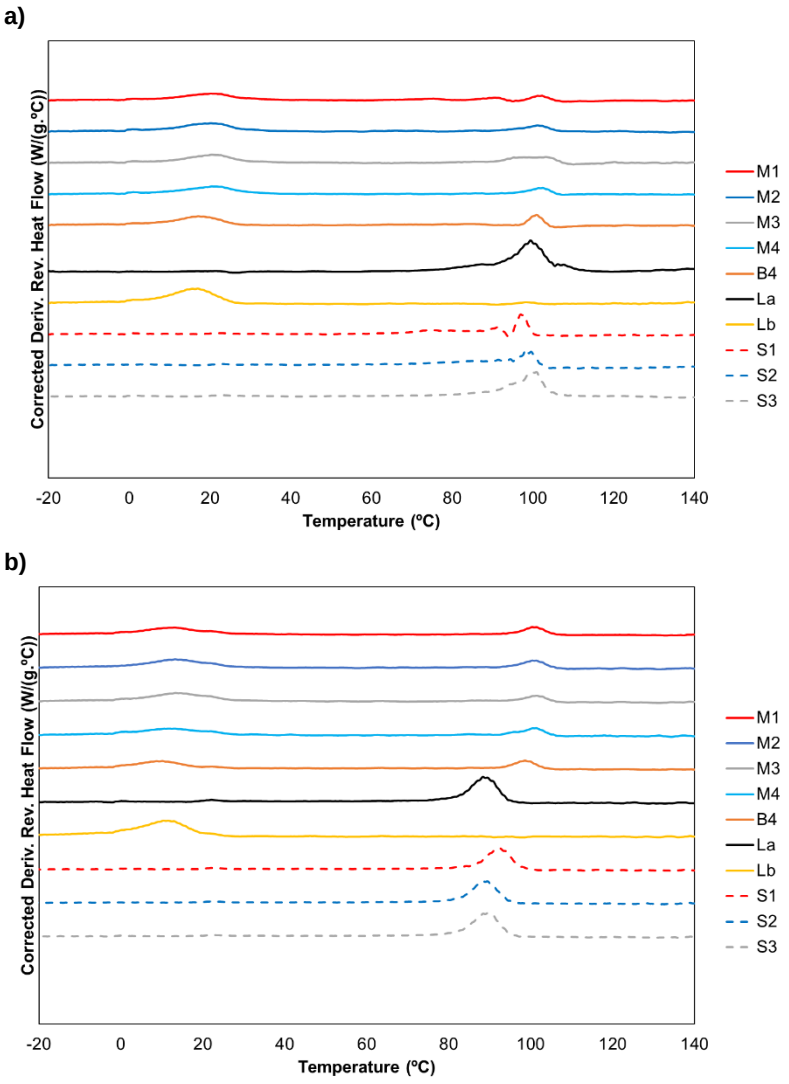

Figure 2-1: DSC curves during a) the first heating cycle and b) the second cycle

TEM images of the particles are given in Figure 2-3. These morphologies can be analyzed with the help of the map for equilibrium morphologies for two-phase polymer-polymer systems shown in Figure 2-2, as described by Gonzalez-Ortiz and Asua.[1,12] Latex M1 had a core-shell particle morphology, with the more hydrophobic styrene phase in the interior of the particle. For illustrative purposes, the approximate position of latex M1 in the morphology map is marked in Figure 2-2. Latex M2 presented a range of morphologies including core-shell and hemispherical morphologies. The approximate position of this latex is also marked in Figure 2-2. The difference of M2 with respect to M1 comes from the presence of acrylamide in the seed that reduced the interfacial tension between the seed and water (γ_{13}). Therefore, the position moved upwards in the morphology map and is at the borderline of a core-shell/hemispherical system. Addition of more AM in latex M3 caused a further decrease of γ_{13} likely crossing the border of the hemispherical morphology. However, the morphologies shown in Figure 2-3 c) are not equilibrium as many of the particles displayed two or more lobes, which is not a thermodynamically favorable state. This indicates that particle morphology was kinetically controlled due to the limited diffusion and coalescence of domains of the second stage polymer within the latex particle. This suggests that for latex M3 the driving force for phase migration was relatively weak due to the good compatibility between the two polymers, namely lower γ_{12}, which could be the result of some grafting of the second polymer to the acrylamide units of the first stage polymer. These units have a labile hydrogen that can be abstracted[10] and are likely to be located at the surface of the particles. Grafting may also be the reason for the presence of several lobes in these particles. However, the graft copolymer was not observed in the DSC curves, but this may be because its amount was low. In latex M4 a hemispherical equilibrium morphology was attempted using a poly(styrene) seed and increasing the interfacial tension

between the second stage polymer and water (γ_{23}) by including styrene in this copolymer. In addition, the presence of styrene in both phases also reduces the interfacial tension between them (γ_{12}). The position of M4 with respect M2 should be shifted to the left and upwards in the morphology map of Figure 2-2 and it was expected that this will lead to a hemispherical equilibrium morphology. However, Figure 2-3 d) shows that the morphology was at the border between core-shell and hemispherical and the observed morphology also seems to be a non-equilibrium one.

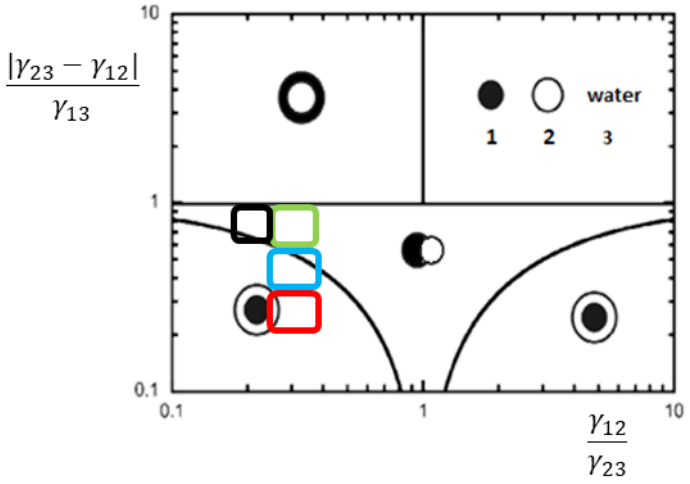

Figure 2-2: Diagram of thermodynamic equilibrium morphologies (M1: red, M2: blue, M3: green and M4: black) based on the work of Gonzalez-Ortiz and Asua[1]

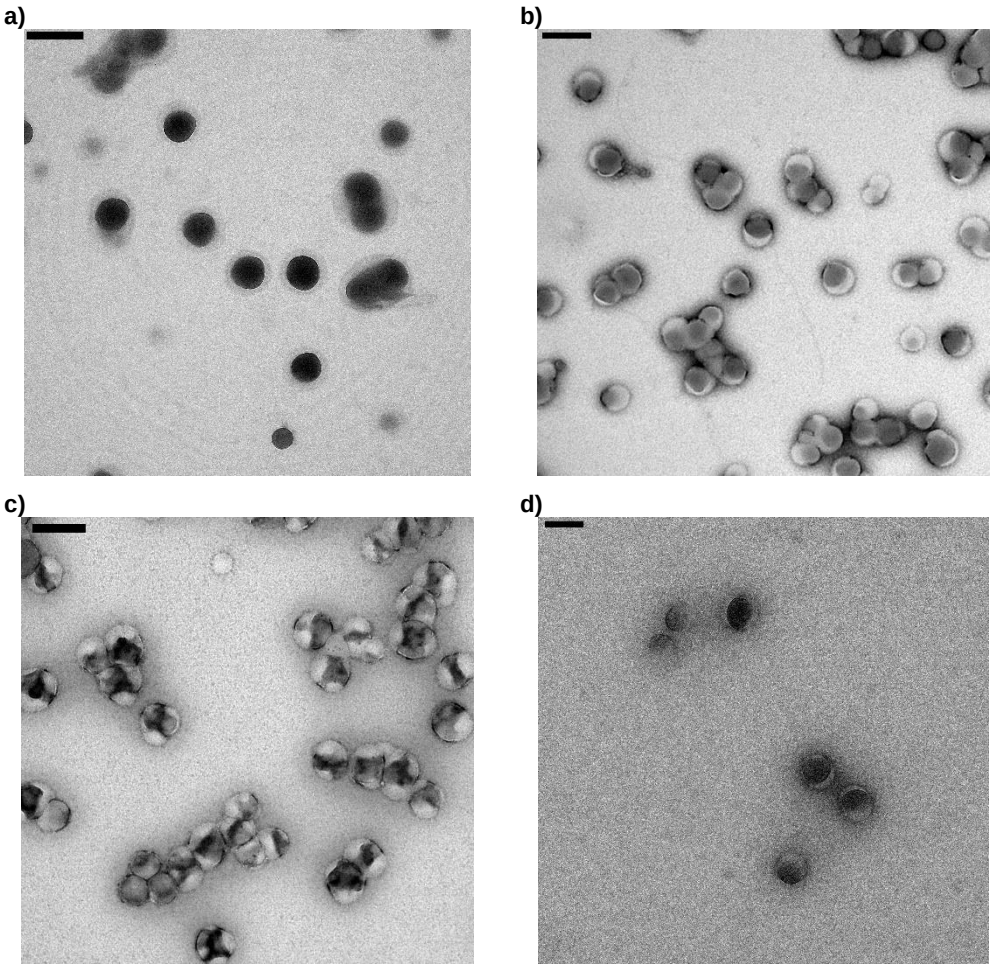

Figure 2-3: TEM images of the latex particles of a) M1, b) M2, c) M3 and d) M4 (scale bar: 200 nm)

The differences in particle morphologies affected the MFFT (see Table 2-5). M1, M2 and M4 presented MFFTs close to the T_g of the soft polymer, which indicates that the soft polymer formed a continuous structure. This result can be attributed to the predominance of the core-shell structure in these latexes. On the other hand, the MFFT of latex M3 was significantly higher (25 ºC) than the T_g of the soft phase (16 ºC). This suggests that the hard phase hindered the movement of the soft phase indirectly supporting the grafting hypothesis. The MFFT of the blend of hard and soft latexes was controlled by the T_g of the soft latex. In this case, the T_g as well as the MFFT of the comparative soft latex were slightly below those of the soft phase of the hybrid latex. This is likely the result of the small amounts of residual styrene from the first stage of the polymerization in the hybrid systems that are incorporated to the second stage soft polymer.

2.3.2 Films morphologies and properties

Figures 2-4 to 2-7 present TEM images of the cross sections of the films cast from the different hybrids at 60ºC (below the Tg of the hard phase) and then annealed at 150 ºC for different times. The dark areas correspond to the styrene rich domains (hard phase). It can be seen that the morphologies of the films cast at 60ºC are in good agreement with the particle morphologies. Films M1, M2 and M4 show well-defined styrene-rich domains (cores of the particles) dispersed in a continuous matrix of soft (shell) polymer. Film M3 shows some aggregation of hard non-spherical domains resulting from the statistical distribution of the hemispherical particles. These differences are in agreement with the differences in MFFT reported above. The film cast from the latex blend (Figure 2-8) shows aggregation of hard and soft domains that are a result of the statistical distribution of latex particles of different composition during the film formation process. This arrangement resulted in an opaque film due to the stronger light scattering (see Figure 2-9).

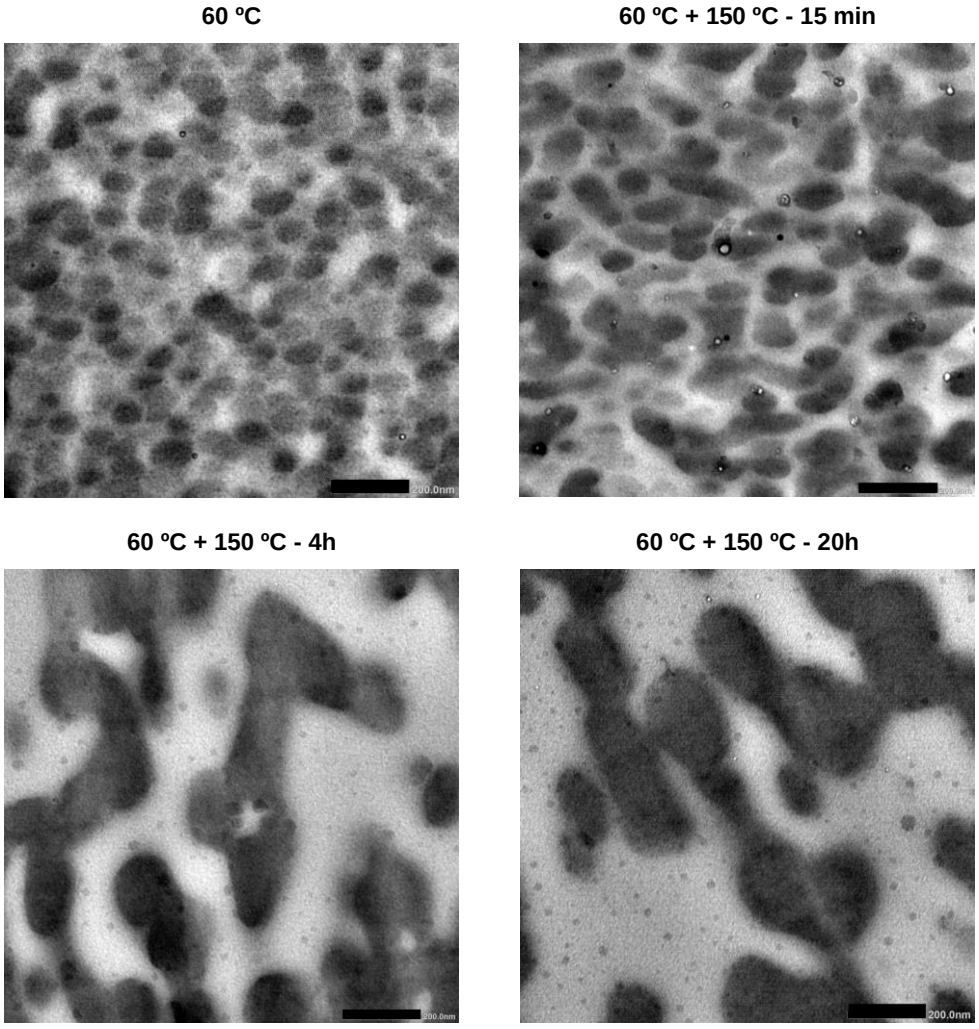

Figure 2-4: TEM images of the films from latex **M1** dried at 60 ºC and annealed at 150 ºC for different times (scale bar: 200 nm)

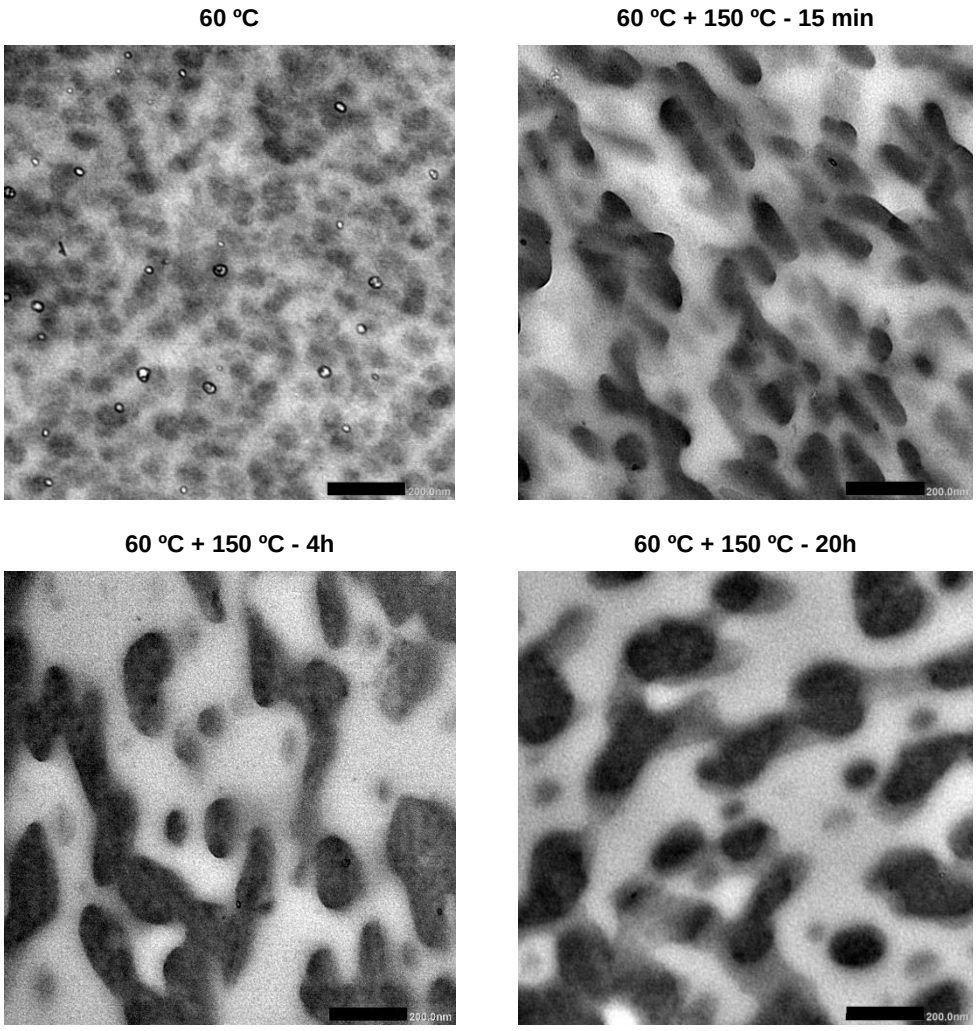

Figure 2-5: TEM images of the films from latex **M2** dried at 60 ºC and annealed at 150 ºC for different times (scale bar: 200 nm)

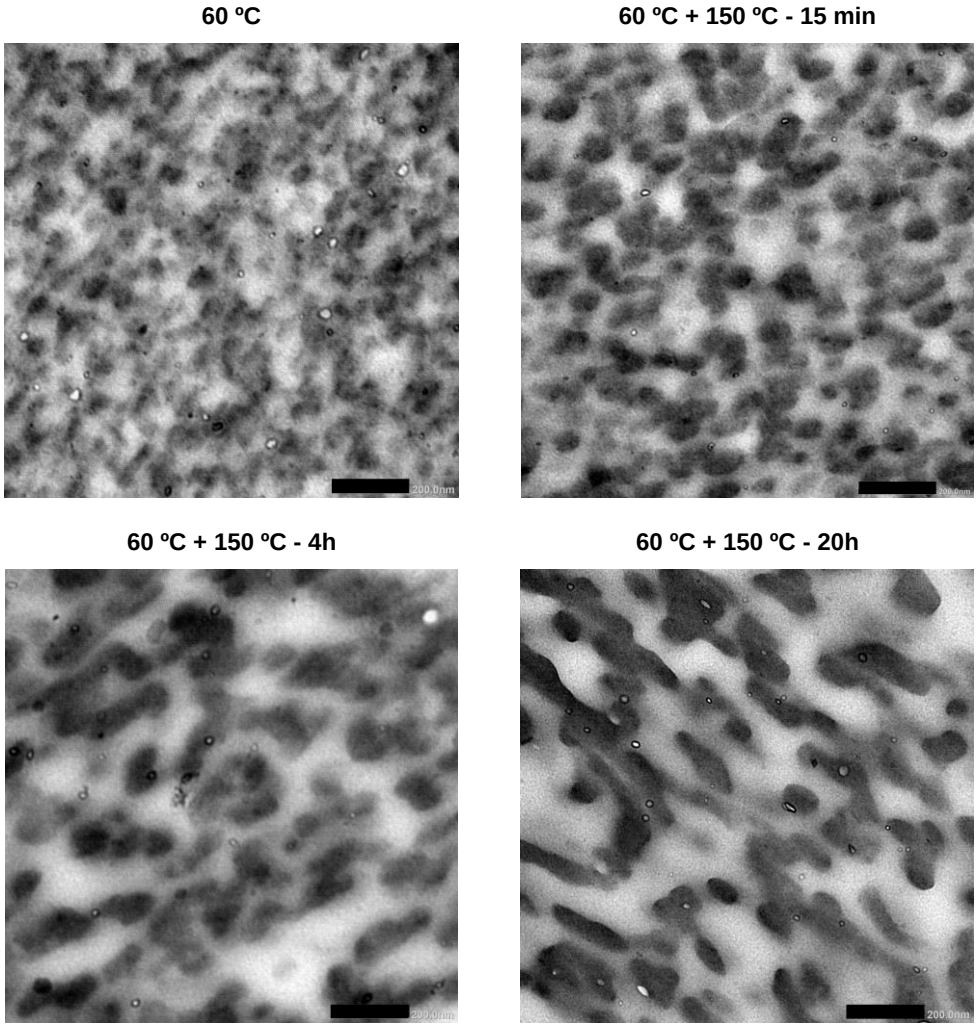

Figure 2-6: TEM images of the films from latex **M3** dried at 60 ºC and annealed at 150 ºC for different times (scale bar: 200 nm)

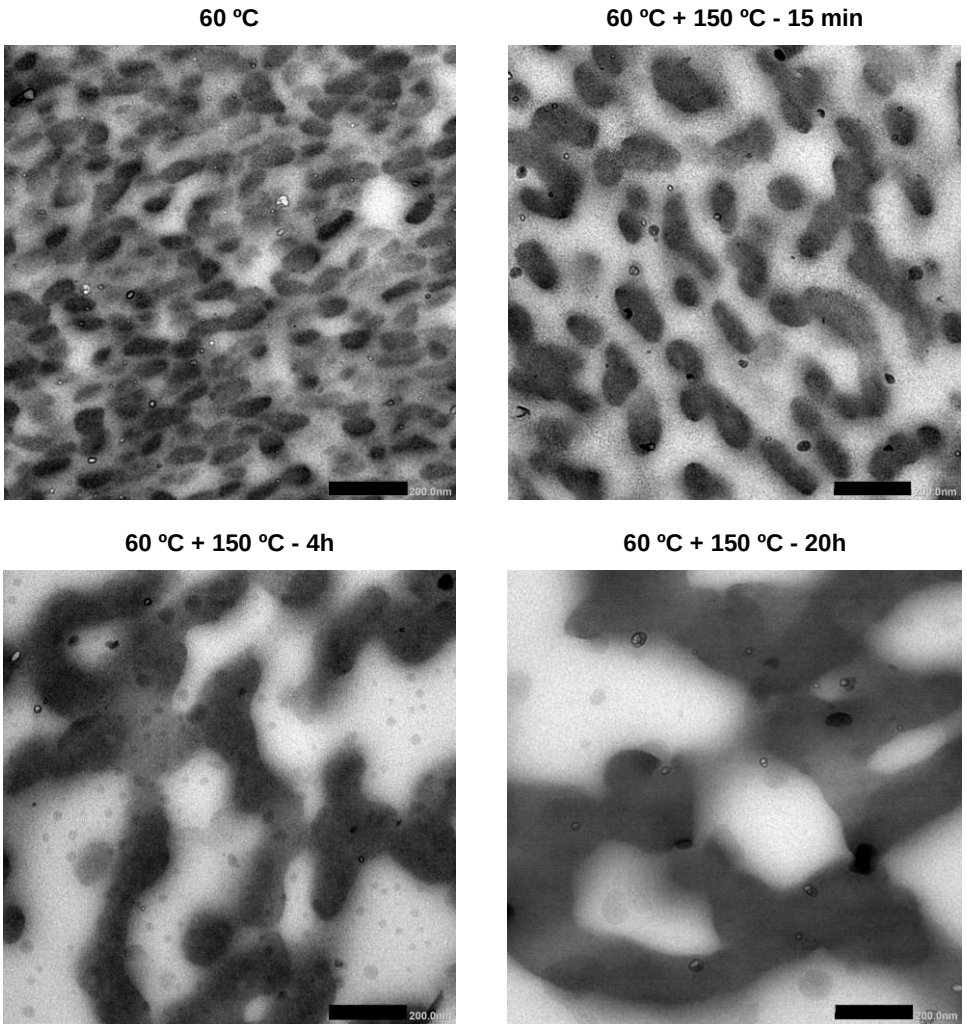

Figure 2-7: TEM images of the films from latex **M4** dried at 60 ºC and annealed at 150 ºC for different times (scale bar: 200 nm)

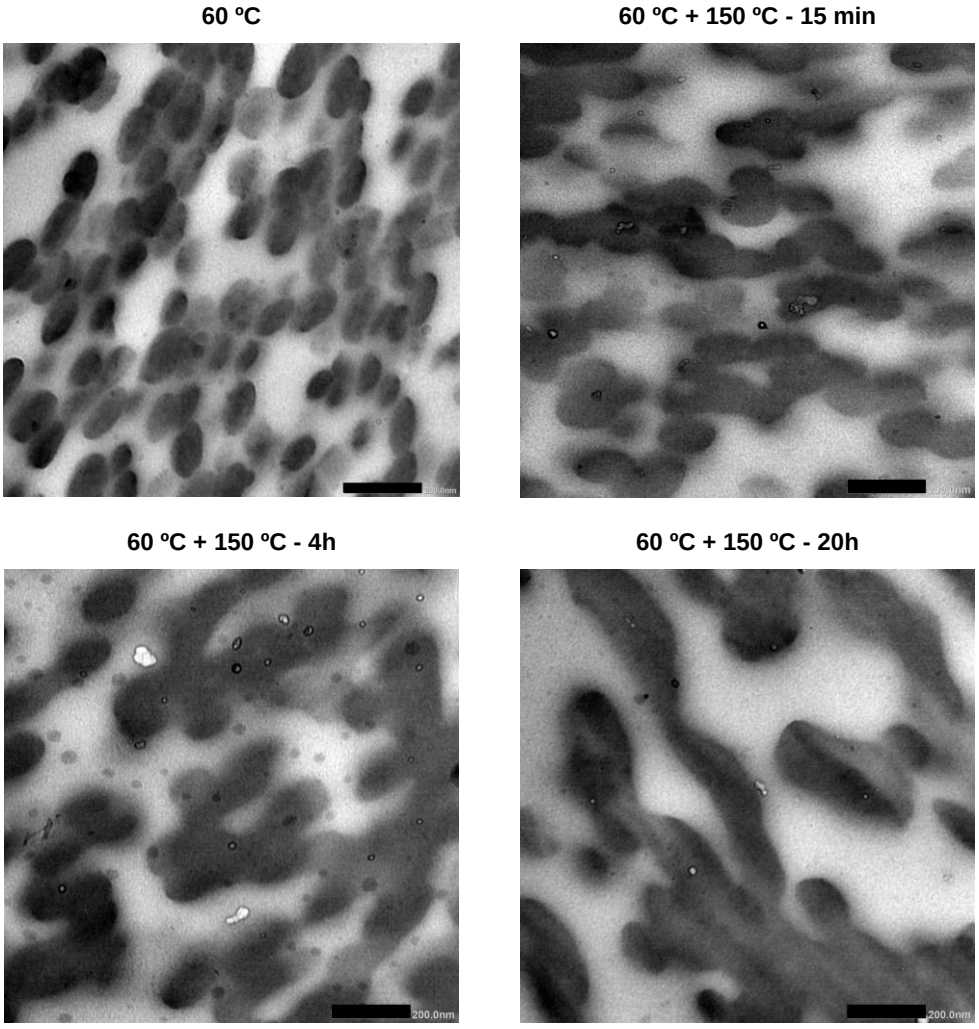

Figure 2-8: TEM images of the films from latex **B4** dried at 60 ºC and annealed at 150 ºC for different times (scale bar: 200 nm)

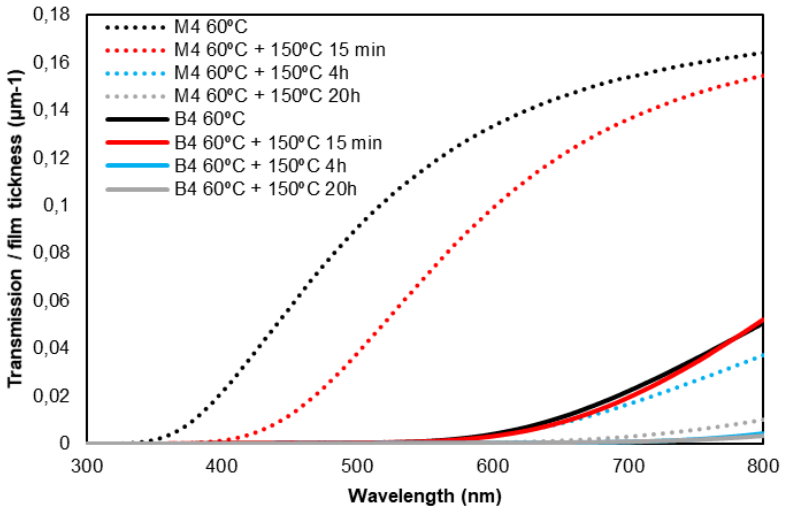

Figure 2-9: Light transmission of the films M4 and Its corresponding blend B4 dried at 60ºC and annealed at 150ºC for different times

The relationship between film structure and mechanical properties can be further elucidated from the behavior of the different films following thermal processing. Thermal treatment facilitates phase migration when the T_g of both phases is exceeded such that coalescence between domains can occur.[8,13] In such a case, just as in the development of latex particle morphology under kinetic control, the extent of phase migration is dependent on the rate of diffusion and coalescence of the different domains. Films were annealed at 150 ºC (temperature higher than the T_g of the hard phase) for 15 min, 4h and 20h. M1 suffered stronger phase separation with annealing time than M2, which in turn was more affected than M3. The reason for this observation can be related to the different values of polymer-polymer

interfacial tension, as the minimization of interfacial energy is the driving force for phase separation in these systems. M2 and M3 contain acrylamide and therefore polymer interfacial tension is lower and they evolve at a slower rate. The change in film morphology is also reflected in the light transmission of the films (see Figure 2-10), with those that undergo substantial phase migration to generate large domains leading to decreased transmission due to light scattering.

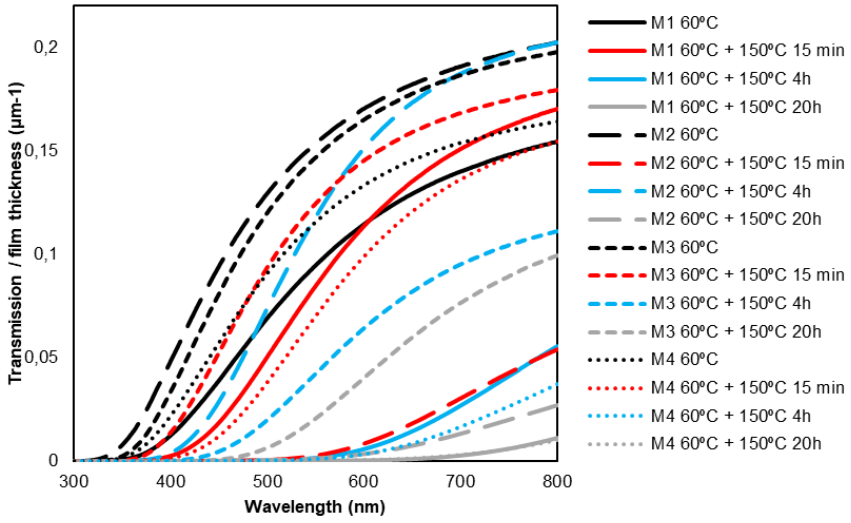

Figure 2-10: Light transmission of the different films dried at 60ºC and annealed at 150ºC for different times

Interestingly, in the case of latex M4 although the polymer-polymer interfacial tension is lower due to the inclusion of styrene in the second phase polymer resulting in a reduced driving

forces for phase migration, substantial phase migration can be seen to occur. Furthermore, unlike the other systems, annealing of M4 at 150ºC for 4h led to the formation of a connected network of the hard phase in the soft continuous phase rather than aggregated spherical inclusions. One potential reason for this may be the improved phase compatibility (lower interfacial tension), which in turn leads to a decreased driving force towards formation of spherical domains. Similarly, in the latex blend B4 the film evolved towards a co-continuous structure as a result of the low interfacial tension between the two polymer phases.

The mechanical properties of the films are shown in Figure 2-11 and Table 2-6. It can be observed that for the films cast at 60 ºC, samples M1, M2 and M4 have a similar Young´s modulus while that of M3 was substantially larger and had a much higher value of the yield stress compared to the other samples. All films showed a plastic deformation with some strain hardening. The stress at break was substantially higher for M4, and lower for latexes M2 and M3 that showed almost identical values and much lower for latex M1.

The higher Young modulus and higher yield stress of M3 was likely the result of a formation of aggregates of hard domains that formed structures that reinforced the film more than the isolated hard domains in latexes M1, M2 and M4. On the other hand, the high value of the stress at break for M4 was attributed to the better compatibility between the hard and soft polymers due to the presence of styrene in both phases. The higher stress at break of latexes M2 and M3 as compared to latex M1 suggests a better compatibility between the two polymers which further supports the hypothesis of grafting to the acrylamide present in the seeds of latexes M2 and M3.

The role of latex particle morphology on the mechanical properties of the film can therefore be observed as both direct and indirect effects. In the elastic (low strain) region the mechanical strength is related to the arrangement of the hard domains and thus the initial latex morphology impacts directly as this is what dictates the film structure. In the plastic region particle morphology has an indirect effect on film strength as the underlying features that lead to a given particle morphology (such as reducing polymer-polymer interfacial tension) also contribute to the strength of the polymer-polymer interface. The mechanical properties of the latex blend (B4) also showed substantial differences from that of the hybrid latex with a lower Young's modulus, as well as a higher strain at break. This was due to the differences in the film structure. As discussed before, the film cast from the blend at 60ºC shows a random arrangement of hard and soft domains resulting in a film where the mechanical properties were controlled by the soft phase.

Differences in the film morphology following thermal treatment were also observed in the tensile properties of the films The Young's modulus increased with the formation of hard clusters for films from M1 and M2. As the film from M1 suffered more of aggregation than M2, leading to formation of highly aspherical aggregates, the Young's modulus increased more. As the morphology of M3 was not strongly affected with annealing temperature, mechanical properties did not evolve significantly. The formation of a near percolating network after annealing for M4 led to an increase of the mechanical properties compared to M2 (higher Young's modulus, elongation at break and toughness). Similar behavior was obtained for B4 as thermal treatment led to a co-continuous film structure.

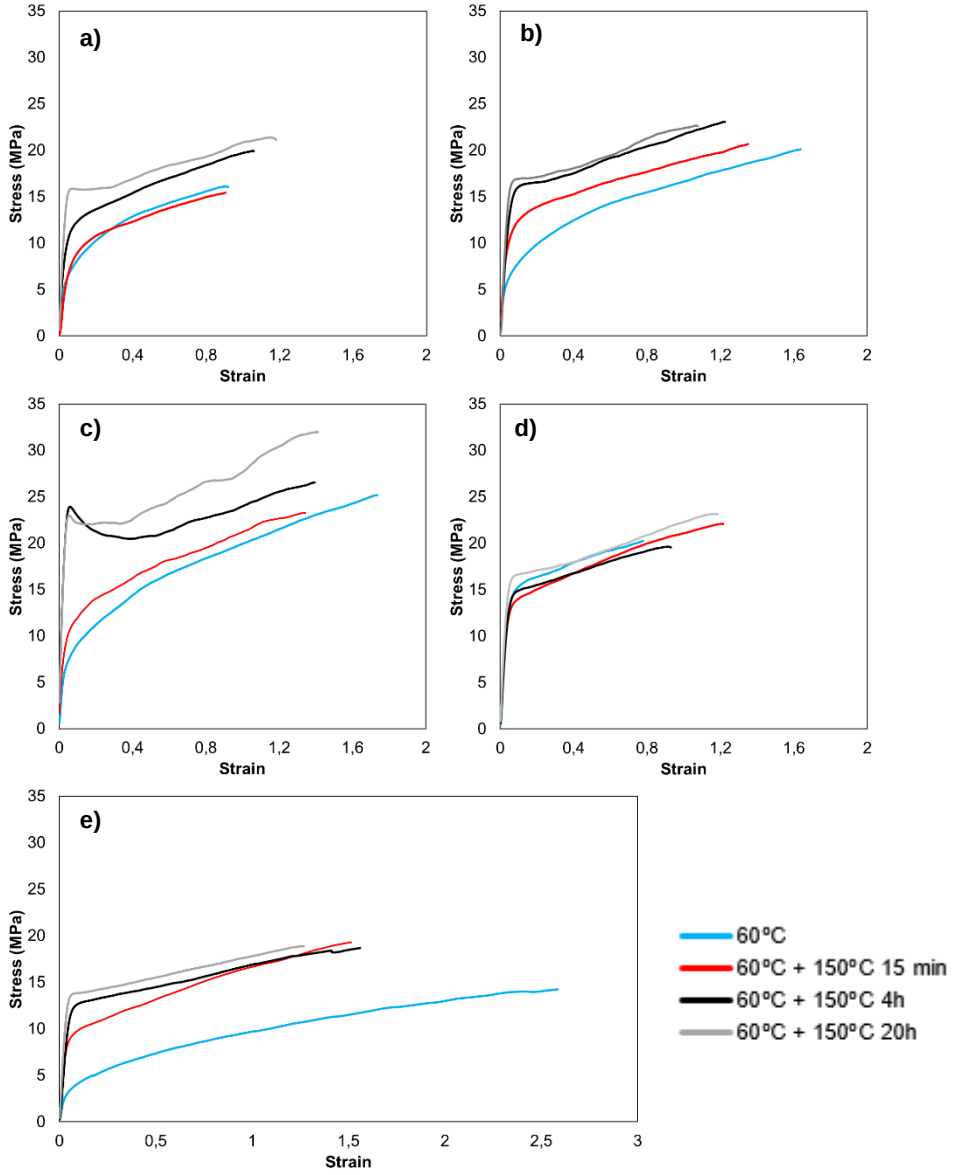

Figure 2-11: Stress-strain curves for the films from the latexes a) M1, b) M2, c) M3, d) M4 and e) B4

Table 2-6: Tensile test results for the different hybrids

	Young's modulus (MPa)	Elongation at break	Stress at break (MPa)	Toughness (MPa)
M1 – 60 ºC	268 ± 11	0.9 ± 0.1	16.1 ± 1	11.4 ± 2.7
M1 – 60 ºC + 150 ºC 15 min	225 ± 26	1.1 ± 0.2	17.2 ± 0.96	14.7 ± 3
M1 – 60 ºC + 150 ºC 4h	304 ± 6	1.1 ± 0.03	19.9 ± 2	16.9 ± 2
M1 – 60 ºC + 150 ºC 20h	407 ± 15	0.74 ± 0.35	19.7 ± 2.3	12.8 ± 4.5
M2 – 60 ºC	268 ± 33	1.65 ± 0.2	20.1 ± 0.8	24.6 ± 3.4
M2 – 60 ºC + 150 ºC 15 min	384 ± 22	1.4 ± 0.2	20.7 ± 3.3	22.5 ± 6
M2 – 60 ºC + 150 ºC 4h	371 ± 15	1.58 ± 0.32	25.0 ± 2.3	30.8 ± 3
M2 – 60 ºC + 150 ºC 20h	401 ± 5	1.10 ± 0.03	22.6 ± 1.8	20.1 ± 1.2
M3 – 60 ºC	390 ± 22	0.78 ± 0.09	20.2 ± 0.24	13.5 ± 1.1
M3 – 60 ºC + 150 ºC 15 min	363 ± 13	1.24 ± 0.08	22 ± 0.27	22.2 ± 0.14
M3 – 60 ºC + 150 ºC 4h	318 ± 34	1.22 ± 0.4	20.7 ± 1.2	21.0 ± 0.3
M3 – 60 ºC + 150 ºC 20h	384 ± 13	1.2 ± 0.2	23.1 ± 2.8	22.8 ± 0.6
M4 – 60 ºC	275 ± 4	1.73 ± 0.09	25.1 ± 0.48	31.2 ± 1.7
M4 – 60 ºC + 150 ºC 15 min	336 ± 15	1.34 ± 0.12	23.3 ± 1.1	24.1 ± 2.8
M4 – 60 ºC + 150 ºC 4h	535 ± 19	1.05 ± 0.29	24.3 ± 2.7	21.47 ± 2.2
M4 – 60 ºC + 150 ºC 20h	580 ± 12	1.4 ± 0.3	32.0 ± 0.6	35.9 ± 2.6
B4 – 60 ºC	141 ± 13	2.4 ± 0.7	18.1 ± 3	30.1 ± 3.3
B4 – 60 ºC + 150 ºC 15 min	246 ± 25	1.5 ± 0.5	19.3 ± 3.1	22.1 ± 4.2
B4 – 60 ºC +150 ºC 4h	263 ± 30	1.6 ± 0.2	18.7 ± 1.3	24.3 ± 3.7
B4 – 60 ºC + 150 ºC 20h	360 ± 40	1.3 ± 0.04	18.9 ± 1.9	20.2 ± 1

2.4 Conclusions

Latexes with almost identical overall composition and molecular weights and different particle morphology were synthesized using a hard seed (S/AM) and a soft second stage monomer (MMA/BA= 50/50 wt/wt). Through variation of the hydrophobicity of the seed and the second stage polymer core-shell and hemispherical morphologies were obtained. The films obtained with these latexes were compared with that of a blend of the same overall composition formed by hard and soft particles. It was observed that latex particle morphology influenced the mechanical properties of the film as a result of both direct and indirect effects. On the one hand, the morphology of the film is directly influenced by the initial particle morphology. Thus, compared to core-shell systems, hemispherical latex particles showed some domain aggregation in the final film, leading to higher MFFT and higher Young's modulus. On the other hand the features that lead to a given particle morphology, most critically the polymer-polymer interfacial tension, also play an important role in the mechanical properties. Thermal treatment at 150ºC led to a change in film morphology from evenly dispersed spherical domains to large non-spherical clusters, with the extent and rate of evolution being related to polymer-polymer interfacial tension. The formation of non-spherical clusters and in some cases a near percolating network of the hard phase resulted in an increased Young's modulus.

2.5 References

(1) Gonzalez-Ortiz, L. J.; Asua, J. M. Development of Particle Morphology in Emulsion Polymerization. 1. Cluster Dynamics *Macromolecules* **1995**, *28*, 3135–3145.

(2) Hagen, R.; Salmén, L.; Karlsson, O.; Wesslén, B. Viscoelastic properties and film morphology of heterogeneous styrene-butadiene latexes *J. Appl. Polym. Sci.* **1996**, *62*, 1067–1078.

(3) Schuler, B.; Baumstark, R.; Kirsch, S.; Pfau, A.; Sandor, M.; Zosel, A. Structure and properties of multiphase particles and their impact on the performance of architectural coatings *Prog. Org. Coatings* **2000**, *40*, 139–150.

(4) Domingues Dos Santos, F.; Fabre, P.; Drujon, X.; Meunier, G.; Leibler, L. Films from soft-core/hard-shell hydrophobic latexes: Structure and thermomechanical properties *J. Polym. Sci. Part B Polym. Phys.* **2000**, *38*, 2989–3000.

(5) Herrera, V.; Pirri, R.; Asua, J. M.; Leiza, J. R. Morphology control in polystyrene/poly(methyl methacrylate) composite latex particles *J. Polym. Sci. Part A Polym. Chem.* **2007**, *45*, 2484–2493.

(6) Stubbs, J. M.; Sundberg, D. C. The dynamics of morphology development in multiphase latex particles **2008**, *61*, 156–165.

(7) Stubbs, J.; Tsavalas, J.; Carrier, R.; Sundberg, D. The structural evolution of composite latex particles during starve-fed emulsion polymerization: Modeling and experiments for kinetically frozen morphologies *Macromol. React. Eng.* **2010**, *4*, 424–431.

(8) Yuan, X.; Huo, D.; Qian, Q. Effect of annealing on the phase structure and the properties of the film formed from P(St-co-BA)/P(MMA-co-BA) composite latex *J. Colloid Interface Sci.* **2010**, *346*, 72–78.

(9) Goikoetxea, M.; Reyes, Y.; De Las Heras Alarcón, C. M.; Minari, R. J.; Beristain, I.; Paulis, M.; Barandiaran, M. J.; Keddie, J. L.; Asua, J. M. Transformation of waterborne hybrid polymer particles into films: Morphology development and modeling *Polymer* **2012**, *53*, 1098–1108.

(10) González, G.; Ugalde, J. M.; De La Cal, J. C.; Asua, J. M. Synthesis of cationic polyelectrolytes by inverse microemulsion polymerization *Macromol. Rapid Commun.* **2009**, *30*, 2036–2041.

(11) Tripathi, A. K.; Tsavalas, J. G.; Sundberg, D. C. Quantitative measurements of the extent of phase separation duringand after polymerization in polymer composites using DSC *Thermochim. Acta* **2013**, *568*, 20–30.

(12) Torza, S.; Mason, S. . Three-phase interactions in shear and electrical fields *J. Colloid Interface Sci.* **1970**, *33*, 67–83.

(13) Lee, C. F. The properties of core-shell composite polymer latex. Effect of heating on the morphology and physical properties of PMMA/PS core-shell composite latex and the polymer blends *Polymer* **2000**, *41*, 1337–1344.

Chapter 3. Soft core-hard shell latex particles for mechanically strong VOC-free polymer films

3.1 Introduction

In Chapter 2, films cast from hybrid latexes with a hard seed and a soft second stage polymer to allow film formation at room temperature were studied. It was shown that the spherical hard domains were dispersed in the soft polymer matrix leading to a reinforcement of the films. As discussed in section 1.5 of Chapter 1, an alternative to this is to use core-shell particles with a soft core and hard shell.[1,2] At first sight this is surprising because one may expect that the hard shell prevents film formation. However, if the hard shell could be deformed the resulting film structure would be composed of a soft matrix reinforced by a honeycomb structure of hard material and has been shown to give mechanically strong polymer films.[1,3,4] In this chapter, the limits of this route with respect to the balance between mechanical strength and MFFT are explore. In order to achieve this, particles consisting of a soft core (S/BA, $T_g \approx$ 21 ºC) and a hard second stage polymer (MMA/BA) were synthesized and the effects on the film morphology and properties were studied. The polymer microstructure was modified by varying the MMA/BA proportion (70/30, 80/20, 100/0 wt/wt) in the shell and the ratio between the core and the second stage polymer ratios (90/10, 80/20, 60/40 wt/wt). The MFFT, film morphologies and properties were investigated. Finally, the effect of thermal processing on film morphologies is considered in the last part of the chapter.

3.2 Experimental part

3.2.1 Materials

Methyl methacrylate (MMA, Quimidroga, technical grade), butyl acrylate (BA, Quimidroga, technical grade) and Styrene (S, Quimidroga, technical grade) were used as received. Potassium persulfate (KPS, >99%, Sigma-Aldrich) was used as thermal initiator. Sodium lauryl sulphate (SDS, >99% Sigma-Aldrich) was used as conventional surfactant. GPC grade tetrahydrofuran (THF, Scharlau) was also used as received. Deionised water was used throughout the work.

3.2.2 Synthesis of hybrid particles latexes

High solids content latexes were prepared by seeded emulsion polymerization. Polymerizations were carried in a 1-L glass reactor equipped with a reflux condenser, a stainless steel anchor stirrer, sampling device, a feeding inlet, a Pt-100 probe and nitrogen inlet. The reaction temperature was kept constant at 70 ºC and the agitation at 150 rpm. First, a 50 wt% solids content polystyrene-co-butyl acrylate (S/BA = 50/50wt/wt) seed latex was synthesized by semi-continuous emulsion polymerization. The formulation used to prepare the seed latex is given in Table 3-1. A solution composed of 1% of the total surfactant and 50% of the total water was used as initial charge. The initial charge was heated and purged with nitrogen for 30 minutes. After reaching the desired temperature (70ºC) the rest of the formulation was fed during 3 hours. At the end of the feeding, the latex was left to react

batchwise during 1 hour. The formulations used to prepare the composite latexes are given in Table 3-2. The pre-emulsion (comonomer compositions from MMA/BA: 70/30 to MMA/BA: 100/0) was fed over 90 min and after that the latex was left to react batchwise for 30 min. The ratio between the seed polymer and second-stage polymer was varied from 40/60 to 90/10. The code describing these polymerizations is the following: the first number corresponds to the quantity of MMA in the ratio: MMA/BA and the second number corresponds to the quantity of the second stage polymer in the ratio soft first phase/hard second phase. Thus 70MMA/10 is a latex with 70 wt% of MMA in the second stage polymer with a second stage polymer corresponding to 10 wt% of the total particle. Latex films were produced by casting 0.5 g of latex (solids content 50%) in rectangular silicone molds (10 mm x 40 mm x 0.6 mm) and allowed to dry at 23 ºC and 55% of relative humidity for 24 hours. One sample of each film was annealed at a different temperature: 35, 60 and 100 ºC and 55% of relative humidity for 12 additional hours.

Table 3-1: Formulations of the seed

	Initial charge (g)	**Stream (g)**
Water	200	200
SDS	0.08	7.92
KPS	0	4
S	0	200
BA	0	200

Table 3-2: Formulations used to synthesize the core-shell latexes ($T_{polymerization}$ = 70 ºC)

	Initial charge	Feed									
		Soft first stage polymer/hard second stage polymer ratio									
		90/10			80/20			60/40			40/60
Seed (g)	240	0			0			0			0
Water (g)	0	13.2			29.72			79.27			178.4
SDS (g)	0	0.2			0.45			1.20			2.7
KPS (g)	0	0.045			0.10			0.27			0.6
		70MMA	80MMA	100MMA	70MMA	80MMA	100MMA	70MMA	80MMA	100MMA	80MMA
MMA (g)	0	9.24	10.6	13.2	20.8	23.8	29.73	55.5	63.4	79.26	142.7
BA (g)	0	4	2.6	0	8.9	5.9	0	23.8	15.9	0	35.7

3.2.3 Characterization

The particle size of the final latexes were measured by capillary hydrodynamic fractionation (CHDF). Residual monomers were measured by gas chromatography. Solids content of the latexes was measured by gravimetry. Glass transition temperature, T_g, of the acrylic polymer was measured by differential scanning calorimetry (DSC). The gel content of the polymers was determined by Soxhlet extraction. The molecular weight distributions were determined by gel permeation chromatography (GPC). Particles and film morphologies were determined by transmission electron microscopy (TEM). Particles were stained with RuO_4 for 20 min before analysis. The mechanical properties of the films cast from the synthesized latexes were determined by tensile test measurements. A detailed description of the characterization methods is provided in Appendix I.

3.3 Results and discussion

3.3.1 Latex characterization and particle morphology

With the aim of understanding how the dispersion of a hard phase within soft matrix allows affects the mechanical properties of latex films, latexes with the same soft core (S/BA: 50/50) and with a second stage polymer of different composition and thickness were synthesized by seeded semi-continuous emulsion polymerization. Table 3-3 summarizes the results for the polymerizations, the T_{gs} of the two phases and MFFT of the films. Conversion was high in all cases, with most reactions being in excess of 99% as measured by headspace

gas chromatography. Different batches of seed were used for the second-stage polymerizations which led to differences in particle sizes (from 166 to 233 nm). 70MMA/10 and 100MMA/10 present a bimodal distribution with a small population of ≈ 100 nm particles as the seed used for these hybrids was bimodal (seed B, see Figure 3-1). All latexes were free from gel, in agreement with previous works using similar monomer compositions.[5,6] In addition, molecular weights and dispersities were similar for all systems. Thus, given the similarity in the polymer properties, the differences in MFFT and film morphologies can be exclusively ascribed to the initial particle morphology and the glass transition temperature of the second stage polymer.

DSC was carried out to determine the T_{gs} of the two phases (Figure 3-2). The core of the particles presented a T_g of 19 ºC. The T_{gs} of the second stage polymer varied between 30 and 108 ºC depending on the copolymer composition. For similar MMA/BA ratio in the second stage polymer, those latexes that had lower volume fraction of shell to core had lower value of T_g of the second stage polymer. This observation is an effect of residual monomer present in the seed at the beginning of the second stage process. As the reactivity ratios of the monomer used favor the polymerization of styrene over butyl acrylate, residual monomer in the seed is predominantly composed of BA.[7] As such, at the start of the second stage process the monomer in the system is richer in BA. This results in a lower T_g of the polymer formed during the subsequent shell synthesis, particularly in those cases where the amount of monomer in the second stage is lower. TEM images (Figures 3-3 to 3-5) showed that the particles did not present a well-defined core-shell morphology, instead multi-lobed particles were obtained.

Table 3-3: Characteristics of the synthesized latexes

System	Residual monomers (ppm) (Conversion (%))	Seed	Particle size (nm)	Gel content (%)	Mn (kg/mol)	Mw (kg/mol)	Đ	T_gs (°C)	MFFT (°C)
Seed A	50000 (95)	/	134	< 2	113.9	347.1	3	22	18
Seed B	16000 (97.1)	/	210	< 2	115.5	310.8	2.7	21	18
Seed C	17000 (96.8)	/	131	< 2	132	351.1	2.7	22	18
70MMA/10	3000 (99.6)	B	233	< 2	158.8	365.8	2.3	22 / 30	17
70MMA/20	1800 (99.8)	C	166	< 2	169.5	344.6	2.03	21 / 37	17
70MMA/40	3600 (99.5)	C	213	< 2	183.2	418.2	2.28	22 / 45	22
80MMA/10	1800 (99.8)	A	193	< 2	167.2	372.8	2.23	21 / 63	18
80MMA/20	1700 (99.9)	A	174	< 2	189.9	333.3	1.76	22 / 62	19
80MMA/40	4900 (98.4)	A	198	< 2	181	362.4	2	23 / 64	26
80MMA/60	990 (99.9)	C	183	< 2	235.5	387.7	1.6	19 / 64	51
100MMA/10	1250 (99.9)	B	233	< 2	167.4	344.8	2.06	22 / 98	20
100MMA/20	2900 (98.8)	A	177	< 2	122.3	323.4	2.64	21 / 107	28
100MMA/40	5000 (97.5)	A	199	< 2	163.5	353.7	2.16	22 /110	90

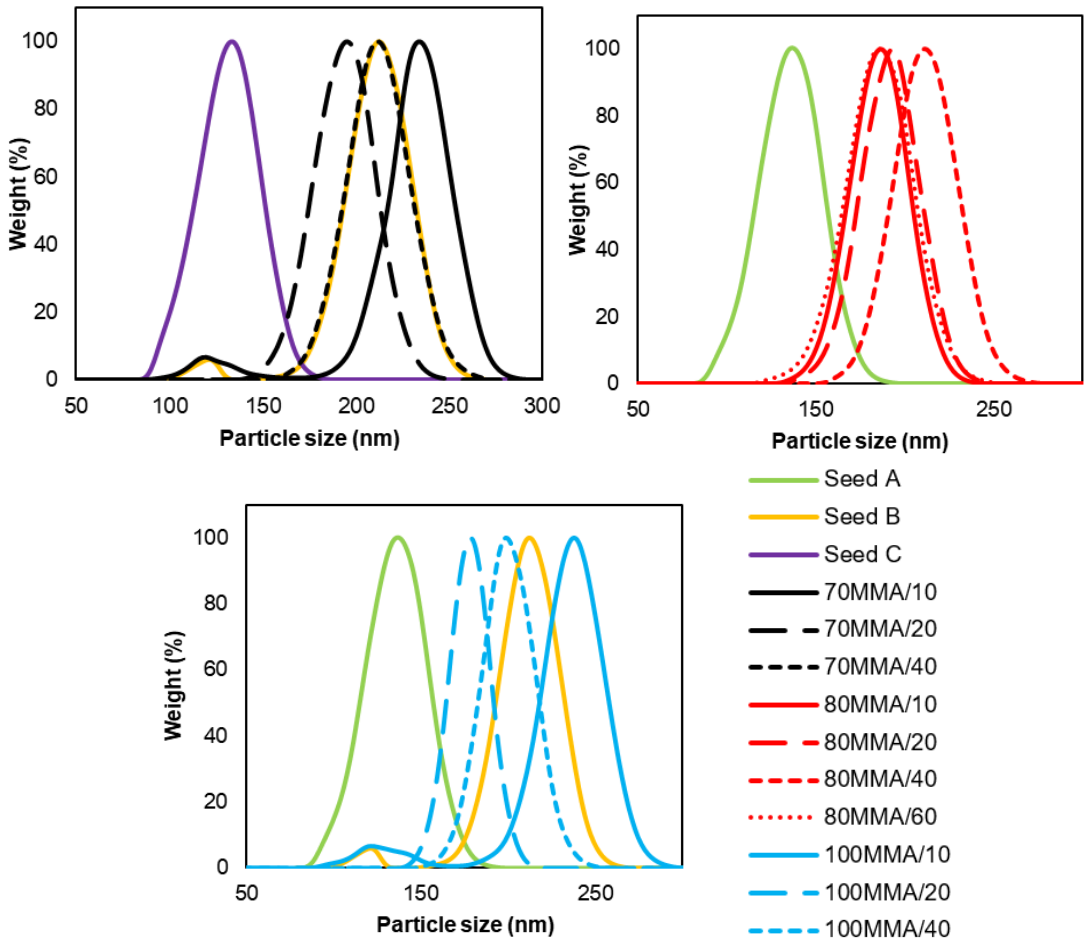

Figure 3-1: Particle size distributions

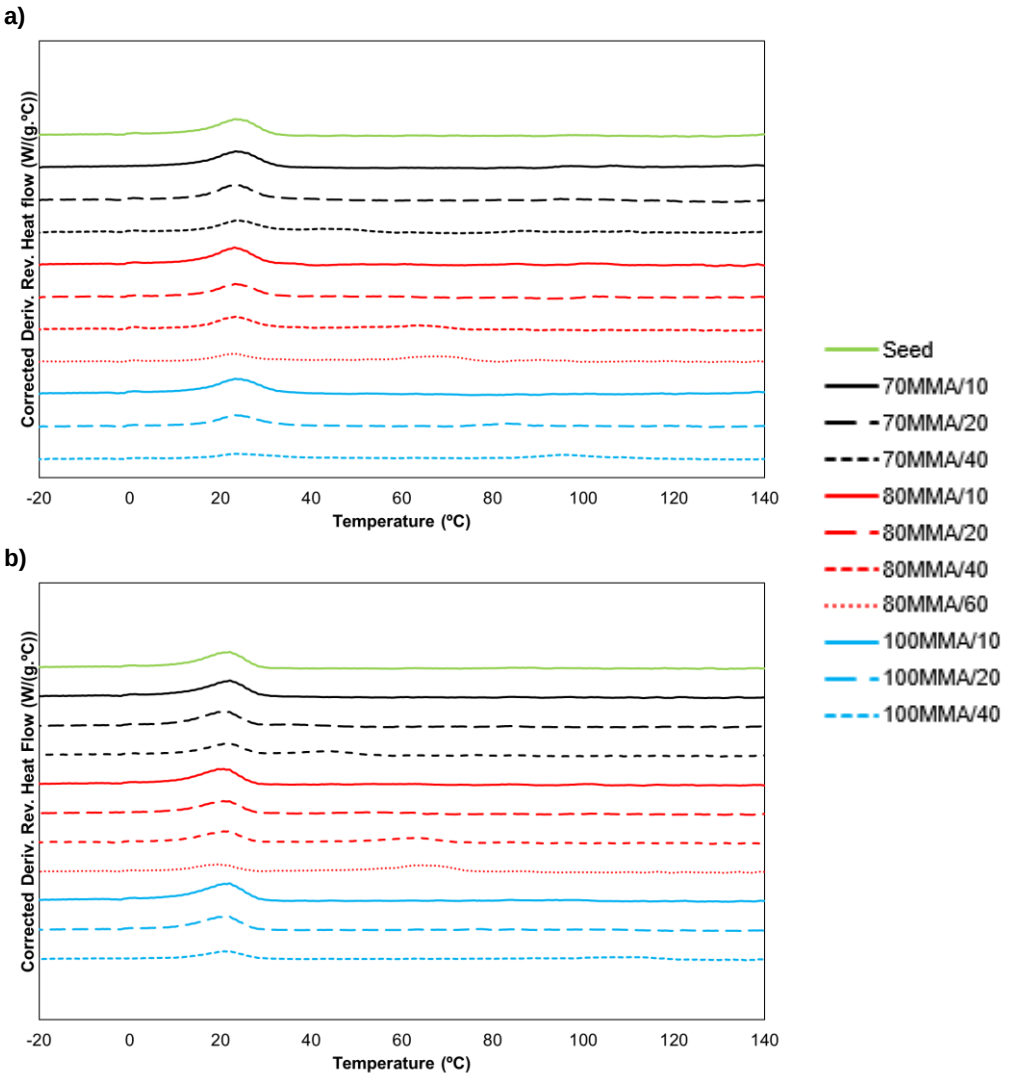

Figure 3-2: DSC curves for the different hybrid particles latexes during a) the first heatung cycle and b) the second heating cycle

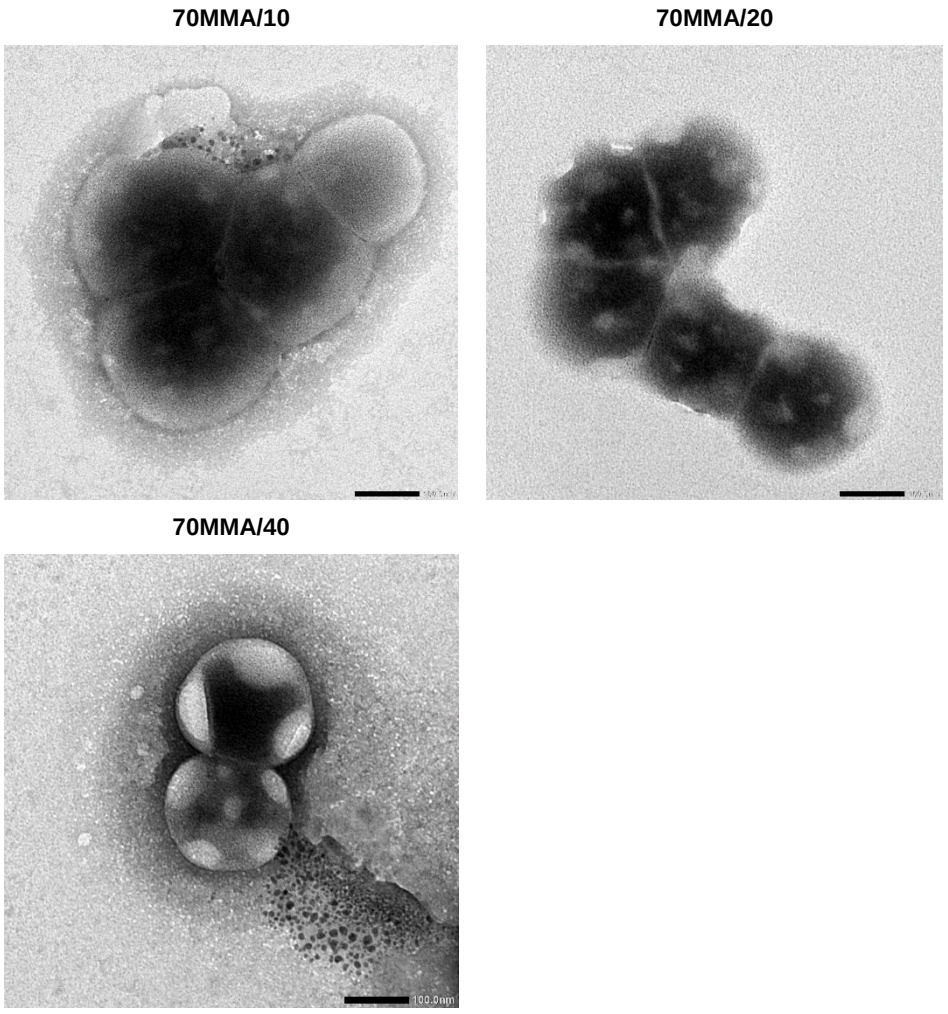

Figure 3-3: TEM images of the particle morphologies of series **70MMA**. Dark regions correspond to the styrene-rich (soft) phase (scale bar: 100 nm). Samples were stained with a vapor of RuO_4 for 20 min before analysis

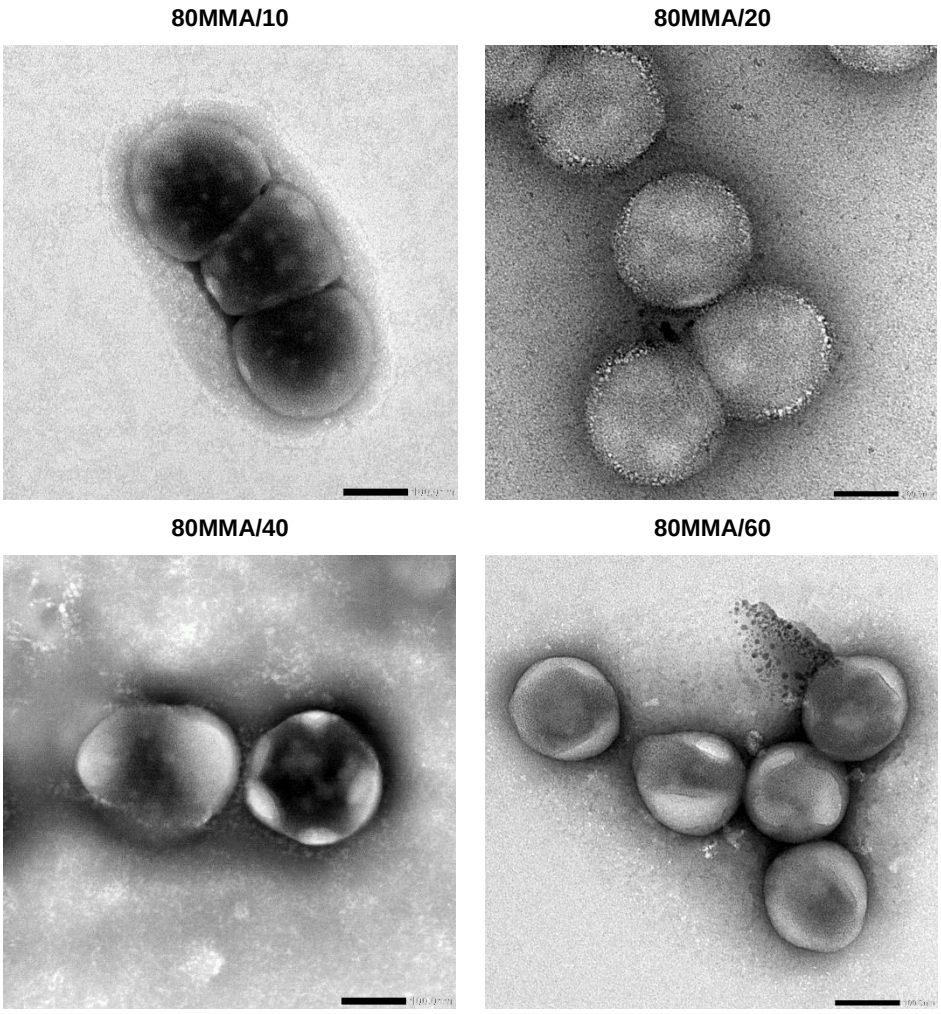

Figure 3-4: TEM images of the particle morphologies of series **80MMA**. Dark regions correspond to the styrene-rich (soft) phase (scale bar: 100 nm). Samples were stained with a vapor of RuO_4 for 20 min before analysis

100MMA/10

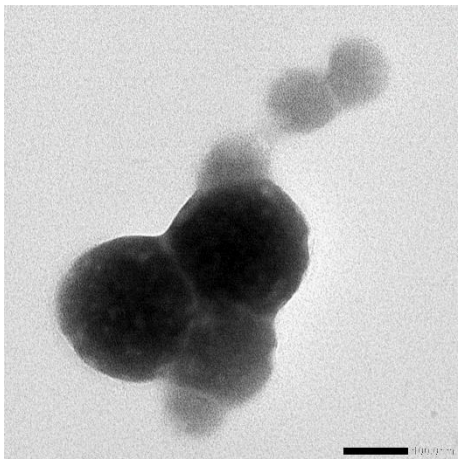

100MMA/20

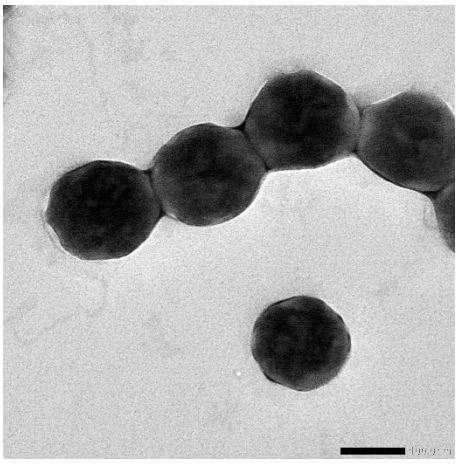

100MMA/40

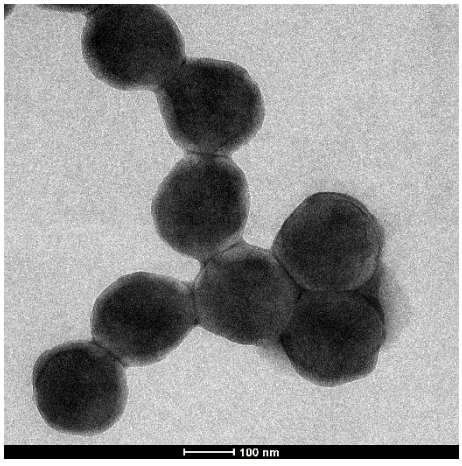

Figure 3-5: TEM images of the particle morphologies of series **100MMA**. Dark regions correspond to the styrene-rich (soft) phase (scale bar: 100 nm). Samples were stained with a vapor of RuO_4 for 20 min before analysis

Given the structure of the latex particles, having a hard polymer shell with T_g substantially above room temperature, it may be thought that film formation at ambient temperature would be difficult because the hard phase in the outer layer of the particle would hinder particle deformation. However, as can be seen in Table 3-3 and Figure 3-6, all hybrids with 10 wbp% of hard phase in the second stage polymer presented a MFFT close to the one of the seed polymer alone (18 ºC). Increasing the amount of the second stage polymer to 20 and 40 wbp%, the hybrids containing 70 % and 80 wbp% of MMA in the hard phase presented the same behavior for the MFFT, with the MFFT only slightly increasing until 40 wbp% of hard phase. An additional reaction was conducted to obtain a higher amount of second stage polymer comprising of 60 % of the total particle with a ratio of 80:20 MMA:BA for the second stage polymer (80MMA/60). Only in this case a significant increase in the MFFT was observed. In this case, as can be observed by the TEM image in Figure 3-4, a near complete shell later forms that limits polymer deformation during the film formation process. The series containing 100% of MMA in the hard phase presented different behavior. In this case, the MFFT increased substantially with the increase of the hard phase proportion in the polymer with the system 100MMA/40 presenting an MFFT of 90 ºC. The cause of this is likely due to the limited deformation possible of the soft core due to the near complete coverage with the hard second stage polymer. It should be noted that despite this, some limited coalescence and deformation may occur as the result of “gaps” in the shell as appears to be the case in the TEM image shown in Figure 3-5**.**

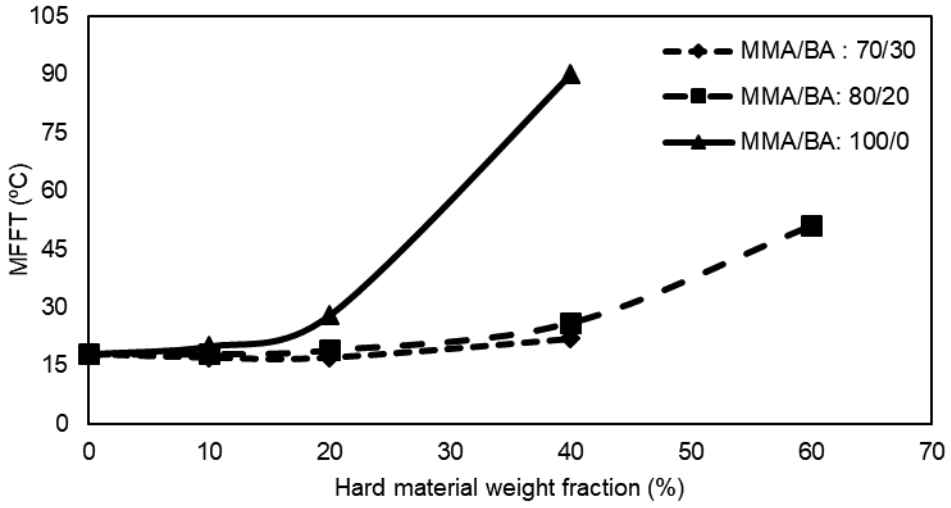

Figure 3-6: Latex MFFT as function of the percentage of high T_g polymer into the hybrids

3.3.2 Film morphology and properties at room temperature

All latexes except 100MMA/40 formed a macroscopically homogeneous film at room temperature (Figure 3-7). The morphology of the films was studied by electron microscopy. Figure 3-8 to 3-10 show the TEM images of cross-section of films cast from the different latexes and dried at 23 ºC and 55% relative humidity for 24 hours. Dark regions correspond to the styrene-rich soft phase and bright regions to the MMA-rich hard phase. Black dots are present on all the films as a result of surfactant pockets trapped in the film.[8,9] It can be seen that for second stage polymer contents up to 20 wt%, the film had a continuous soft phase. This continuous phase is reinforced by segments of hard phase polymer dispersed in the film,

such that no honeycomb structure was formed is these systems. This lack of a honeycomb structure is likely due to the hard phase not completely covering the soft seed particle and being instead primarily present in discrete lobes. As a result the soft phase could easily deform and coalesce around the hard segments. As the film formation temperature was lower than the T_g of the hard phase, the hard segments could not deform and they therefore kept the morphology that they had in the particles. This is in contrast to the results of Price *et al.* who showed that similar hard shell type latexes maintained their shape during film formation and led to films with poor cohesion which often cracked extensively during drying. Although the particle morphology was not extensively characterized in their work the differences with what is observed here is likely as a result of having a complete shell of the hard phase in their system.[4] This highlights the importance of the structure of the latex itself in the final properties of the film. For the series with 40% of second stage polymer, the particle morphology was different as the hard lobes covered a large area of the surface of the seed particles. Nevertheless, the MFFT of 70MMA/40 and 80MMA/40 was about room temperature and good films were formed, showing that capillary forces were able to deform shells with T_{gs} of 46 and 63 ºC. For 100MMA/40, no film could be formed at room temperature, which demonstrates that the capillary forces were not sufficient to deform the hard PMMA (T_g = 108 ºC) phase. It is interesting that no hard phase honeycomb structure was observed for 70MMA/40 and 80MMA/40, but instead they presented a soft continuous phase reinforced by non-spherical hard segments with higher aspect ratio with limited interconnectivity.

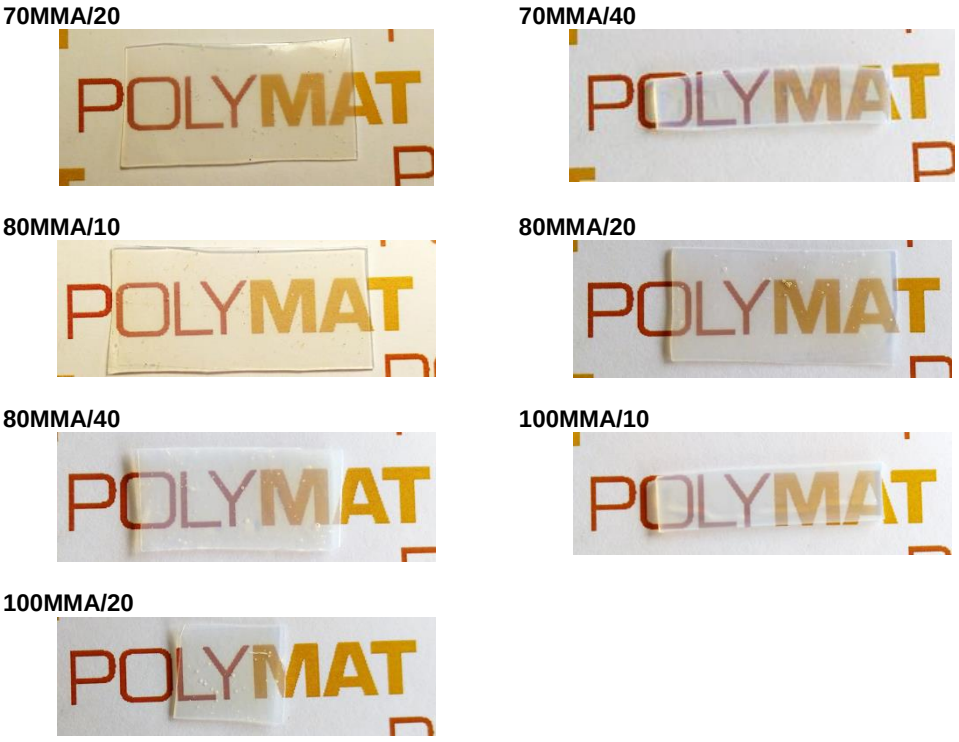

Figure 3-7: Photos of the films dried from the different latexes at 23 ºC and 55% relative humidity for 24h

70MMA/10

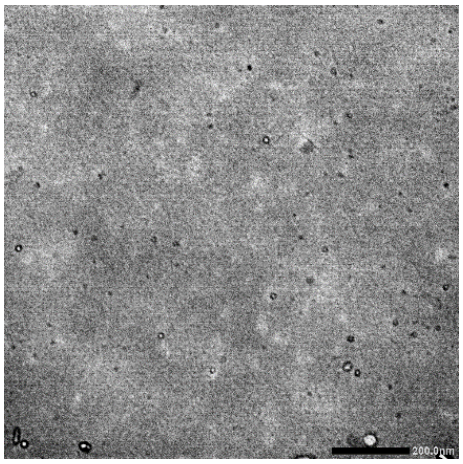

70MMA/20

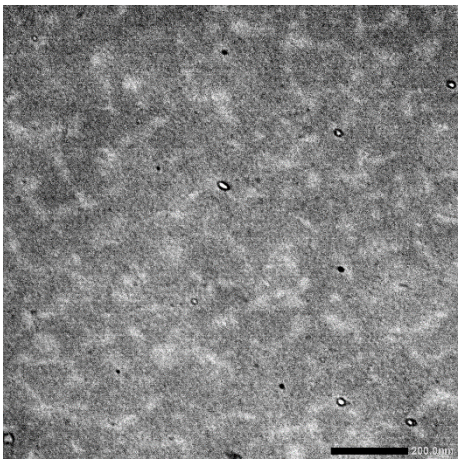

70MMA/40

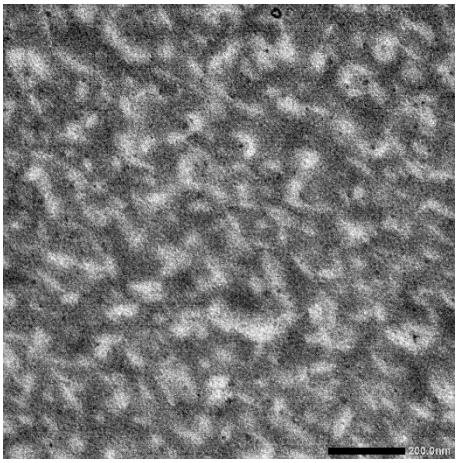

Figure 3-8: TEM images of the cross-cut film morphology of films from series **70MMA** dried at 23 ºC and 55% relative humidity (scale bar: 200 nm)

80MMA/10

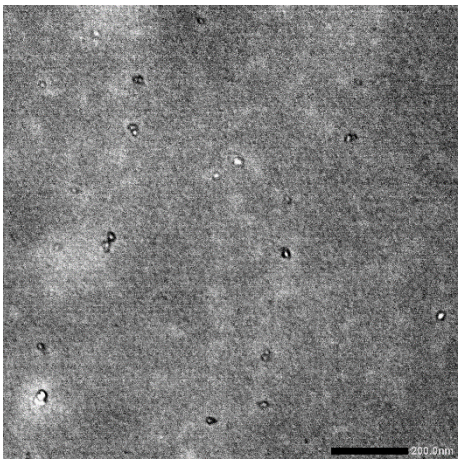

80MMA/20

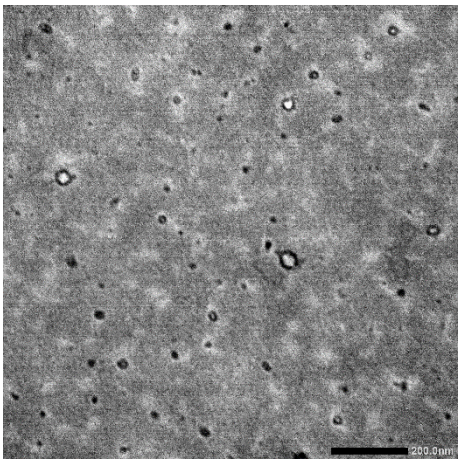

80MMA/40

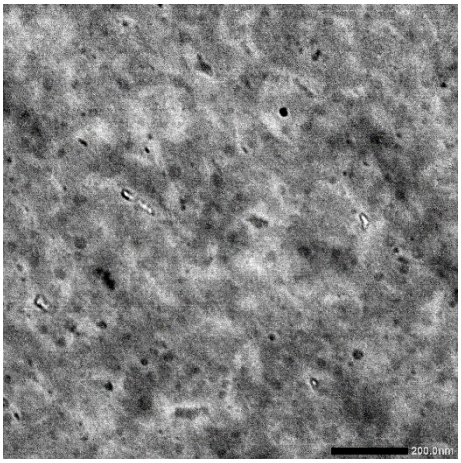

Figure 3-9: TEM images of the cross-cut film morphology of films from series **80MMA** dried at 23 ºC and 55% relative humidity (scale bar: 200 nm)

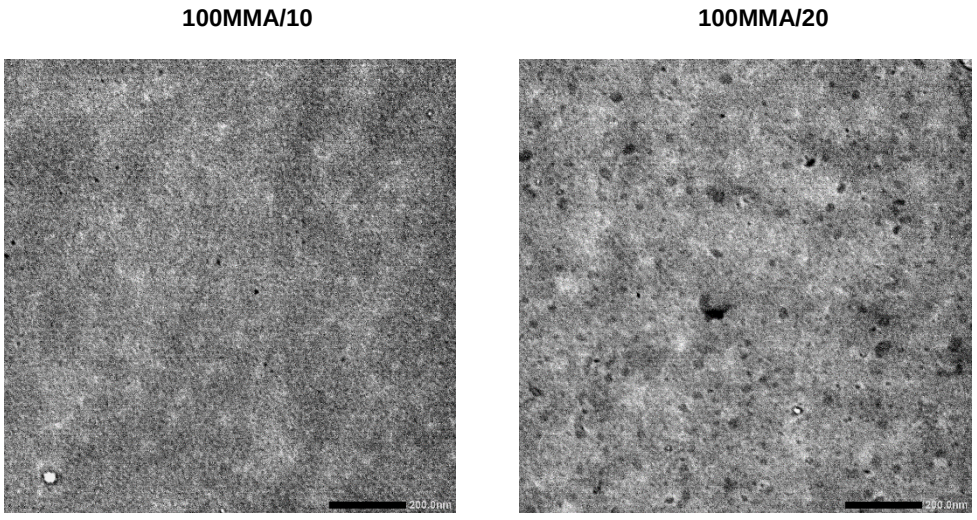

Figure 3-10: TEM images of the cross-cut film morphology of films from series **100MMA** dried at 23 ºC and 55% relative humidity (scale bar: 200 nm)

Figure 3-11 and Table 3-4 give the results of tensile tests of the different films dried at 23 ºC and 55% of relative humidity for 24h. No results are presented for 80MMA/60 and 100MMA/40 as their MFFT were above the temperature at which the films were cast. For all second stage polymer compositions, the increase of the amount of hard phase polymer induced an increase of Young's modulus and stress at break with a concomitant decrease in elongation at break. The increase in Young's modulus was particularly notable in those samples containing 40% of the hard second stage polymer as a result of the highly non-spherical hard segments present in the latex films. It should be noted that the yield at break (up

to 10 MPa) was substantially higher than what has been obtained previously (2-3 MPa)[1,4,10] while having quite ductile films that resisted deformations of at least 300 %.

Even though some of the latexes synthesized in this work outperform the previously reported VOC-free coatings, further improvement of the mechanical properties is expected if better connectivity between hard domains is achieved. A characteristic of the present films is that only limited migration of the hard phase occurred (Figures 3-8 to 3-10). Phase migration can however be encouraged by thermal treatment of the film.[11,12] This process is driven by the minimization of the surface energy and the thermodynamic equilibrium morphology is a system in which the two phases are completely separated. This morphology has no interest in the context of this work, but some intermediate morphologies between those in Figures 3-8 to 3-10 and the equilibrium completely phase-separated morphology may provide improved properties. Therefore, we decided to explore this possibility.

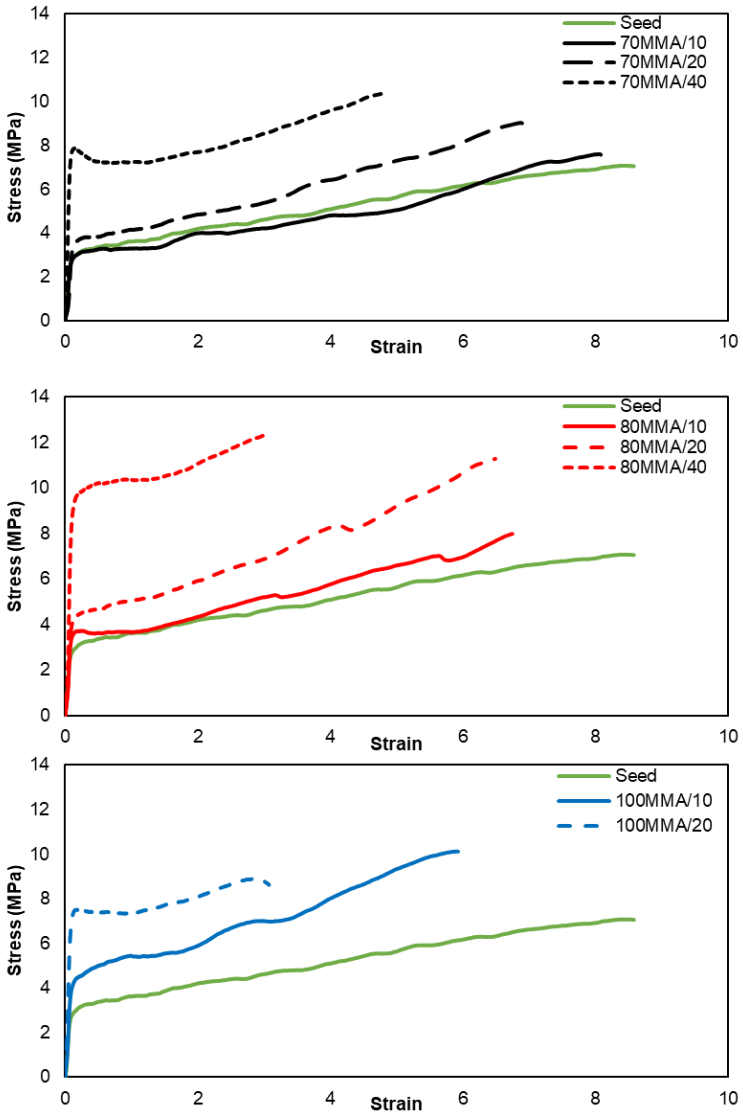

Figure 3-11: Stress-strain curves for films dried at 23 ºC and 55% relative humidity for 24h

Table 3-4: Tensile tests results for films dried at 23 ºC and 55% relative humidity for 24h

	Young modulus (MPa)	Elongation at break	Stress at break (MPa)	Toughness (MPa)
Seed	30 ± 8	8.5 ± 0.9	7.1 ± 0.8	44.4 ± 8.5
70MMA/10	39 ± 4	8.1 ± 0.4	7.6 ± 0.9	39.8 ± 4.5
70MMA/20	55 ± 1	6.9 ± 0.2	9.0 ± 0.7	41.2 ± 2.8
70MMA/40	114 ± 16	4.8 ± 0.2	10.4 ± 0.8	39.7 ± 3.6
80MMA/10	48 ± 6	6.8 ± 0.6	8.0 ± 1.6	36.4 ± 11
80MMA/20	53 ± 6	6.6 ± 0.3	11.0 ± 0.3	47.0 ± 2.3
80MMA/40	142 ± 7	3.1 ± 0.4	12.3 ± 0.6	33.0 ± 5.8
100MMA/10	72 ± 9	5.9 ± 0.6	10.1 ± 0.6	41.9 ± 4.9
100MMA/20	103 ± 15	3.3 ± 0.5	9.7 ± 1.8	29.0± 7.8

3.3.3 Thermal processing of the films

The films cast at room temperature were thermally treated at different temperatures for 12 hours in order to induce the migration of the hard phase in the soft matrix and the resulting morphologies were observed by TEM. The temperatures chosen were 35, 60 and 100 ºC which are in the range or slightly below the T_g of the hard phases in order to facilitate the diffusion of the hard phase in the soft matrix.

First, the effect of varying the composition of the hard phase was explored for the systems with a 20 wt% second stage polymer (Figure 3-12). For 70MMA/20 (T_{ghard} =30 ºC), some aggregations of clusters of hard phase can be observed at 35 ºC as the film converts from one with high aspect ratio clusters of hard phase to a film with a soft matrix with hard round inclusions (see cartoon in Figure 3-13). Phase migration is clearer at 60 ºC and occurs to a significant extent at 100ºC. As the T_g of the hard phase increased, the onset at which phase migration was observed changed accordingly. For 80MMA/20 (T_{ghard} = 60 ºC) modification of the initial morphology is only observed at 60 ºC and is more obvious at 100 ºC. For the hardest second stage polymer (100MMA/20, T_{ghard} = 104 ºC) only at 100 ºC some phase migration can be observed as the annealing temperature was approached the T_g of the hard phase.

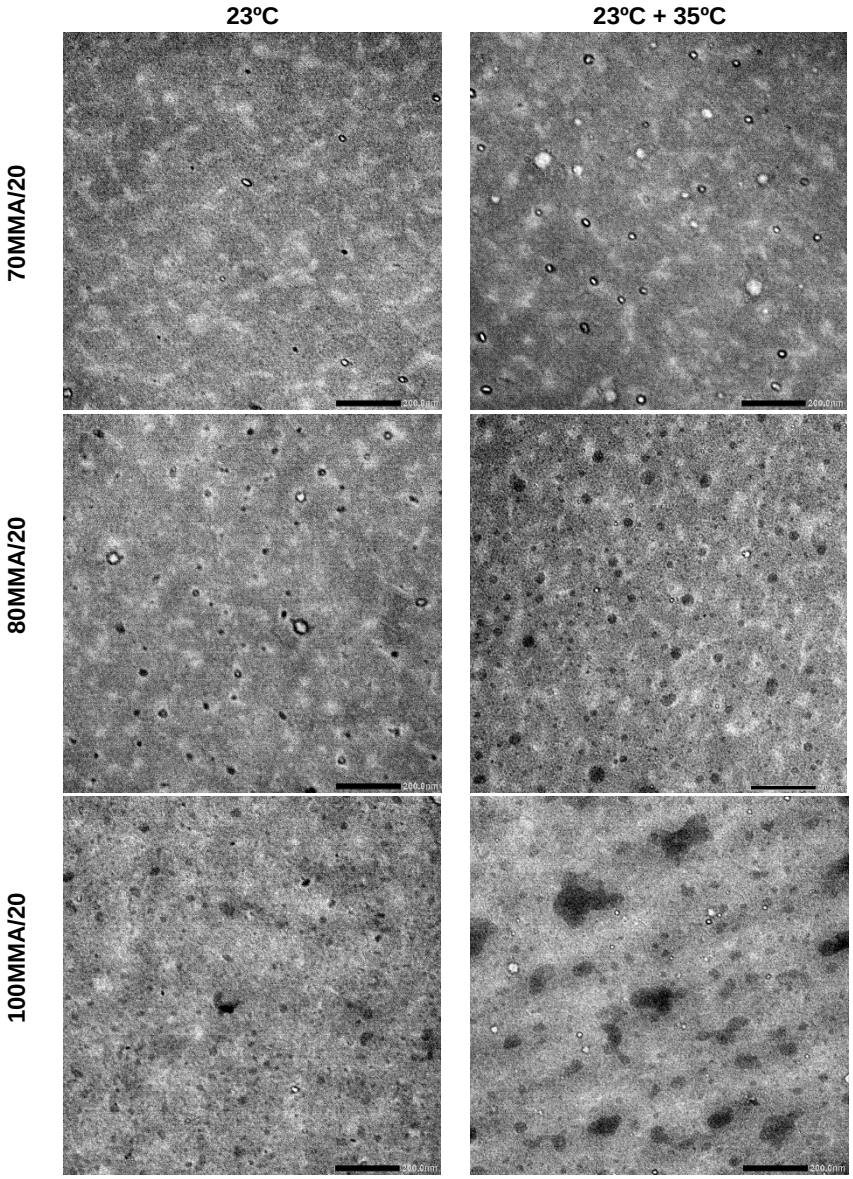

Figure 3-12 (left): TEM images of the film morphology of films cast from the xMMA/20 latexes series dried at 23 ºC for 12 hours and annealed for 12 hours at different temperatures (scale bar: 200nm)

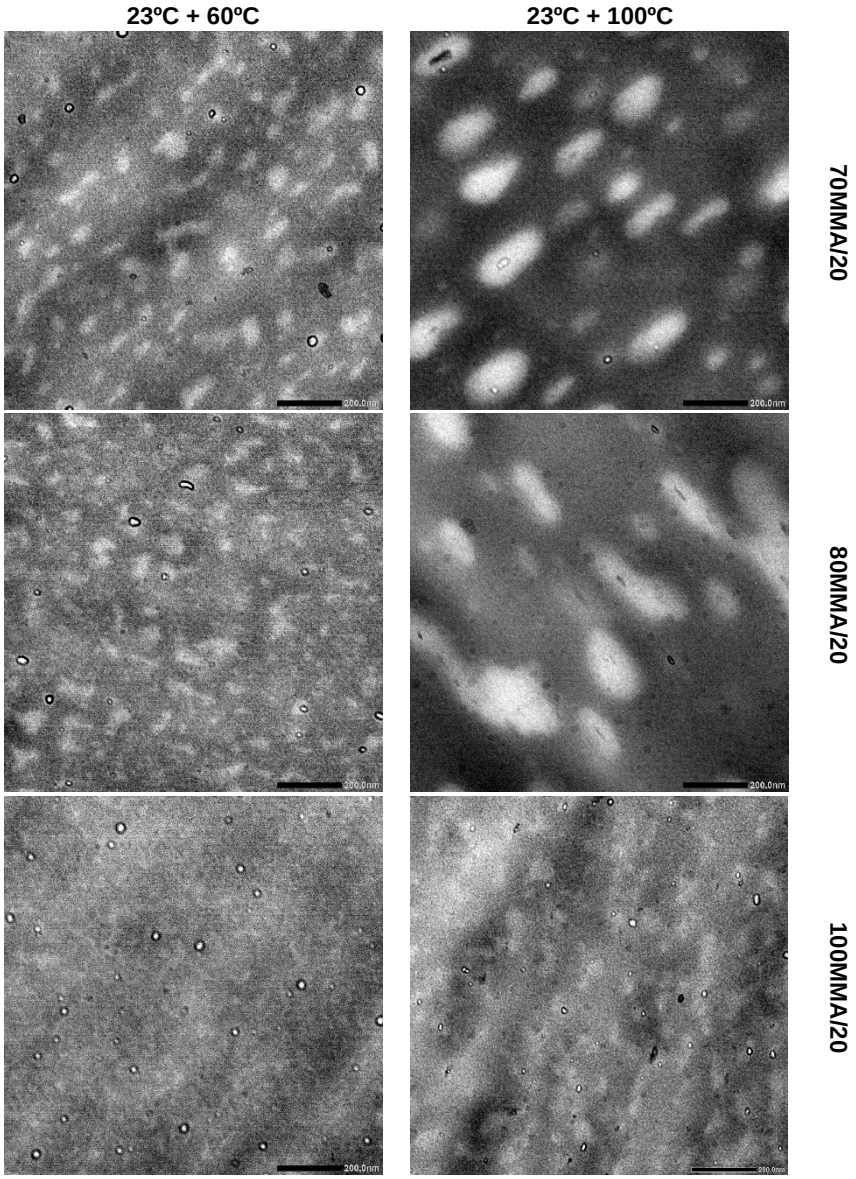

Figure 3-12 (right)

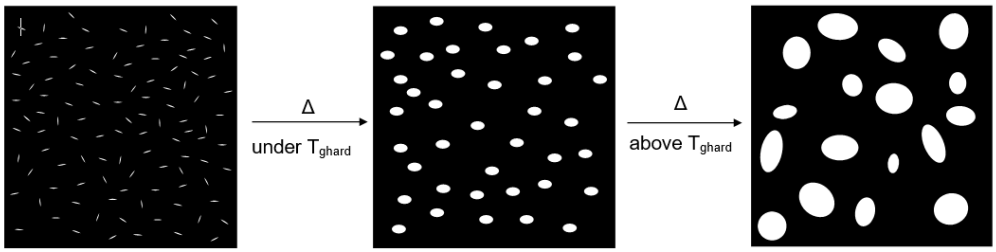

Figure 3-13: Sketches of the film structure from xMMA/20 latexes with thermal treatment

Mechanical properties of the thermally processed films were measured and are reported in Figure 3-14 and Table 3-5. When heating at 35 ºC, for all systems, Young's modulus, stress at break and toughness increased while the elongation at break was not significantly affected. The effect was stronger for 70MMA/20 because the processing temperature was above the T_g of the hard phase. After heating at 60 ºC, phase rearrangement was observed on the TEM images for 70MMA/20 and 80MMA/20, but the mechanical properties were similar to those obtained at 35 ºC, heating at 100 ºC did not affect significantly the Young's modulus of the films despite the strong phase rearrangement noticeable on the TEM images, indicating that when the hard phase forms isolated domains in the soft matrix, the Young's modulus is not significantly affected by the size of the hard phase domains. For 100MMA/20, thermal treatment at 100 ºC led to aggregation between hard domains with some connectivity between them (Figure 3-12). This resulted in an increase in the stress at break and interestingly the elongation at break also increased leading to an increase to the film toughness. The phase rearrangement led to a film more resistant to fracture.

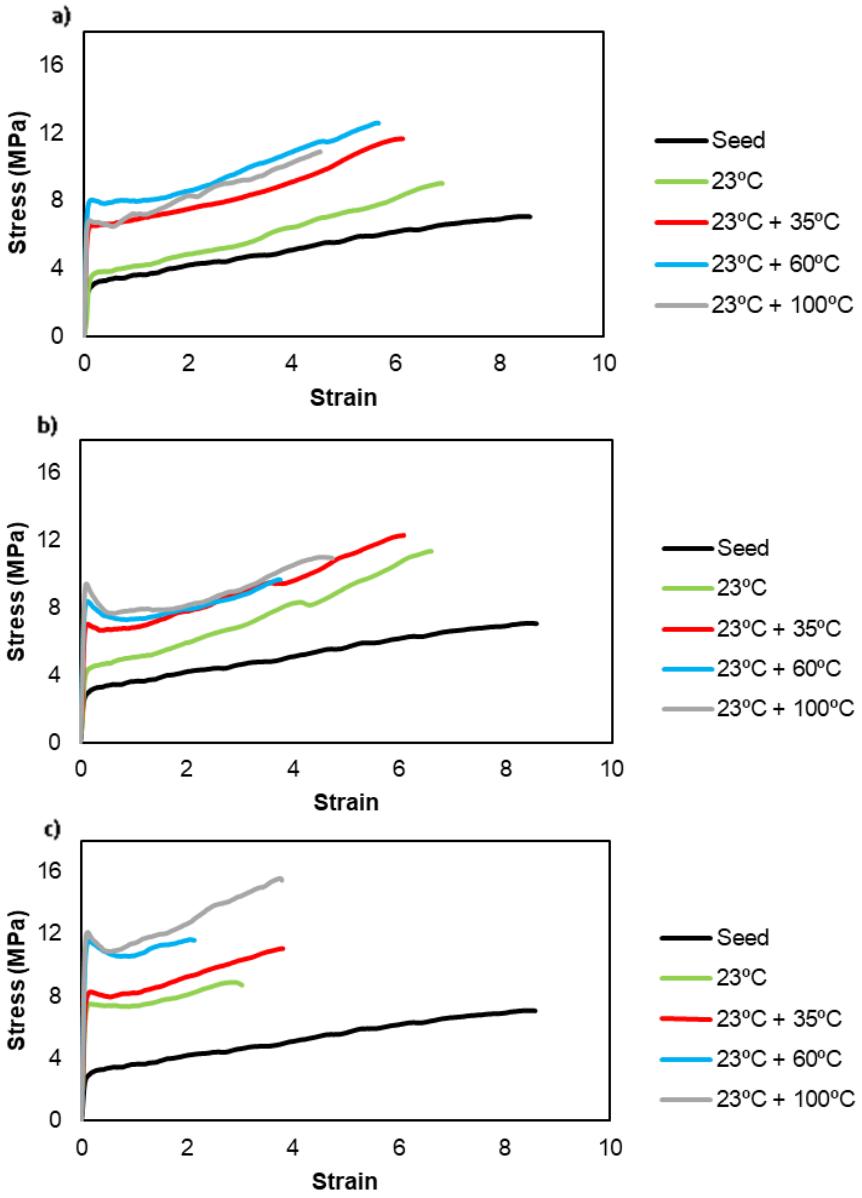

Figure 3-14: Stress-strain curves for films dried at 23 ºC and annealed at different temperatures from the latexes a) 70MMA/20, b) 80MMA/20 and c) 100MMA/20

Table 3-5: Tensile tests results for films dried from the latexes xMMA/20 at 23 ºC and annealed at different temperatures

	Young's modulus (MPa)	Elongation at break	Stress at break (MPa)	Toughness (MPa)
Seed	30 ± 8	8.5 ± 0.9	7.1 ± 0.8	44.4 ± 8.5
70MMA/20				
23 ºC	55 ± 1	6.9 ± 0.2	9.0 ± 0.7	41.2 ± 2.8
23 ºC + 35 ºC	95 ± 20	6.1 ± 0.3	11.7 ± 0.7	47.9 ± 3
23 ºC + 60 ºC	137 ± 25	5.7 ± 0.02	12.6 ± 1.4	54.7 ± 6.7
23 ºC + 100 ºC	135 ± 14	4.5 ± 0.7	10.9 ± 1.1	38.1 ± 8.5
80MMA/20				
23 ºC	53 ± 6	6.6 ± 0.3	11.0 ± 0.3	47.0 ± 2.3
23 ºC + 35 ºC	99 ± 19	6.1 ± 0.4	12.3 ± 0.8	48.8 ± 5.5
23 ºC + 60 ºC	151 ± 18	4.3 ± 0.5	11.5 ± 1.8	40.5 ± 5
23 ºC + 100 ºC	135 ± 6	4.7 ± 0.8	11.0 ± 0.6	41.8 ± 6
100MMA/20				
23ºC	103 ± 15	3.3 ± 0.5	9.7 ± 1.8	29.0 ± 7.8
23ºC + 35ºC	136 ± 12	3.8 ± 0,5	11.0 ± 1	35.0 ± 5,7
23ºC + 60ºC	183 ± 11	2.1 ± 0.6	11.6 ± 0.6	23.0 ± 7
23ºC + 100ºC	203 ± 9	3.8 ± 0.4	15.5 ± 1.5	48.3 ± 7

A possible reason why in Figure 3-12 the thermal treatment led to isolated domains of the hard polymer dispersed in the matrix of the soft polymer is the fraction of hard polymer was too small (20%). Therefore, the effect of varying the amount of hard phase was explored for the 80MMA series (see Figure 3-16). The mechanical properties of the films are reported in Figure 3-17 and Table 3-6. It can be seen that for 10 and 20 wt% of second stage polymer, the effect of the thermal treatment on the mechanical properties was very modest even though the film morphology varied substantially (mainly when the films were heated at 100 ºC). In contrast, the films cast with core-shell particles containing 40 wt% of second stage polymer, showed a substantial improvement in the mechanical strength when heated at and above the T_g of the hard phase. Figure 3-17 shows that a yield stress of about 20 MPa was obtained with a relatively ductile film that resisted deformations of up to 200 %. These properties were due to the formation of an almost percolating structure of hard polymer (see Figure 3-15 for representation of film structue). and reinforce the idea that by generating an interconnected hard phase mechanical strength can be substantially improved.

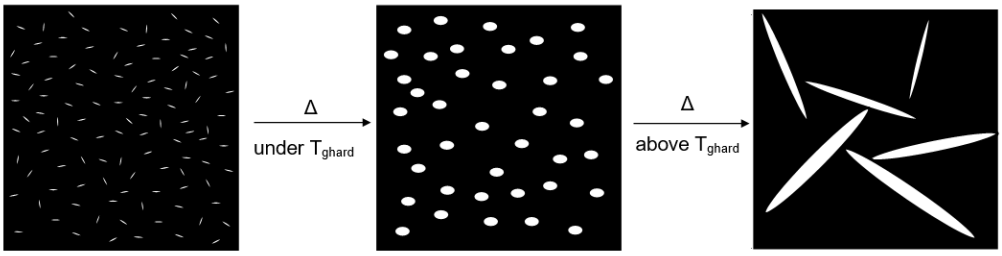

Figure 3-15: Sketches of the film structure of 80MMA/40 with thermal treatment

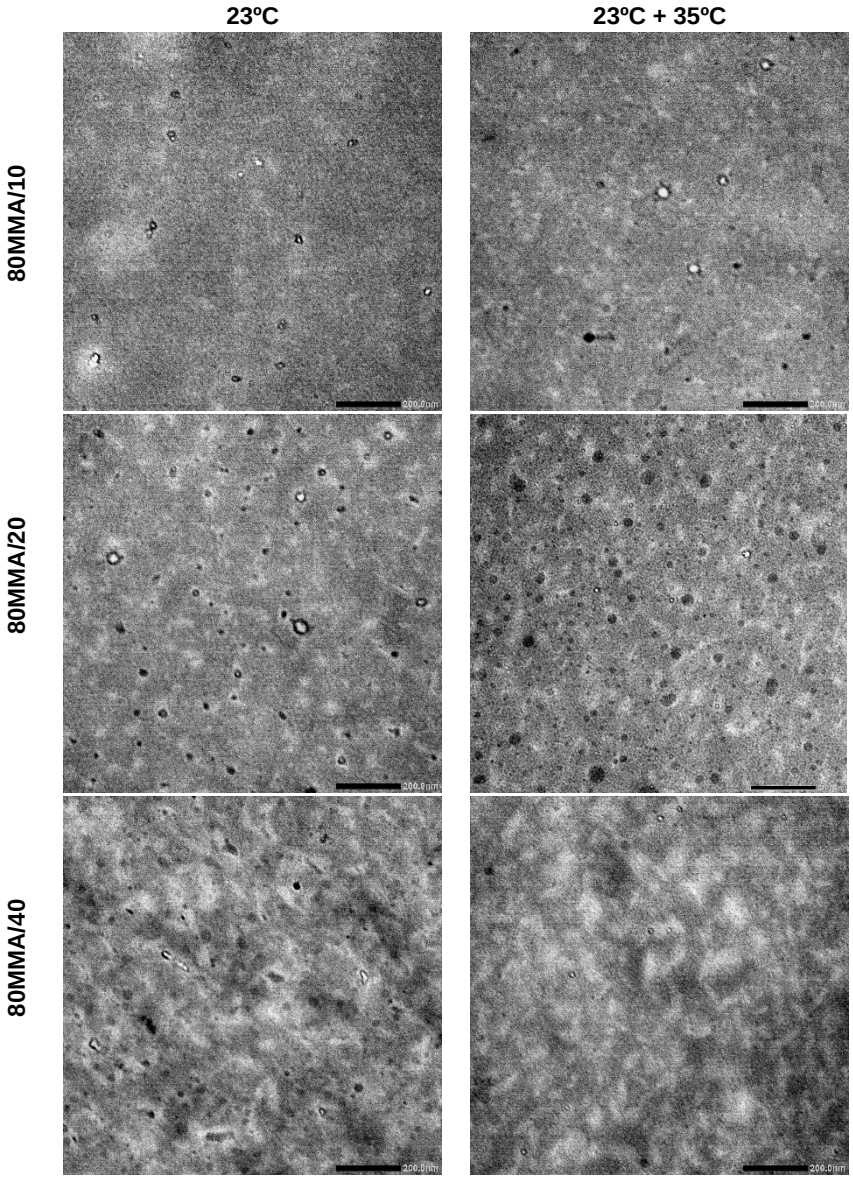

Figure 3-16 (left): TEM images of the film morphology of films cast from the 80MMA latexes series dried at 23ºC for 12 hours and annealed for 12 hours at different temperatures (scale bar: 200 nm)

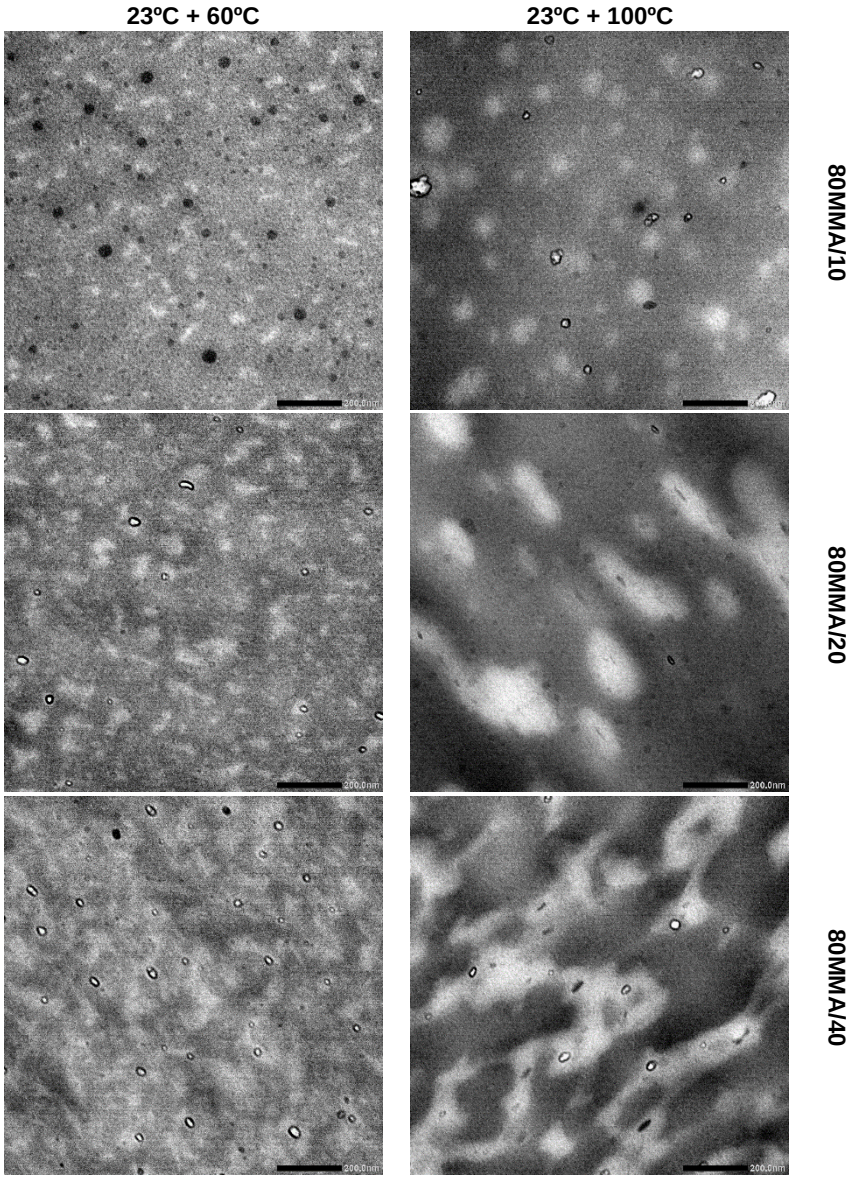

Figure 3-16 (right)

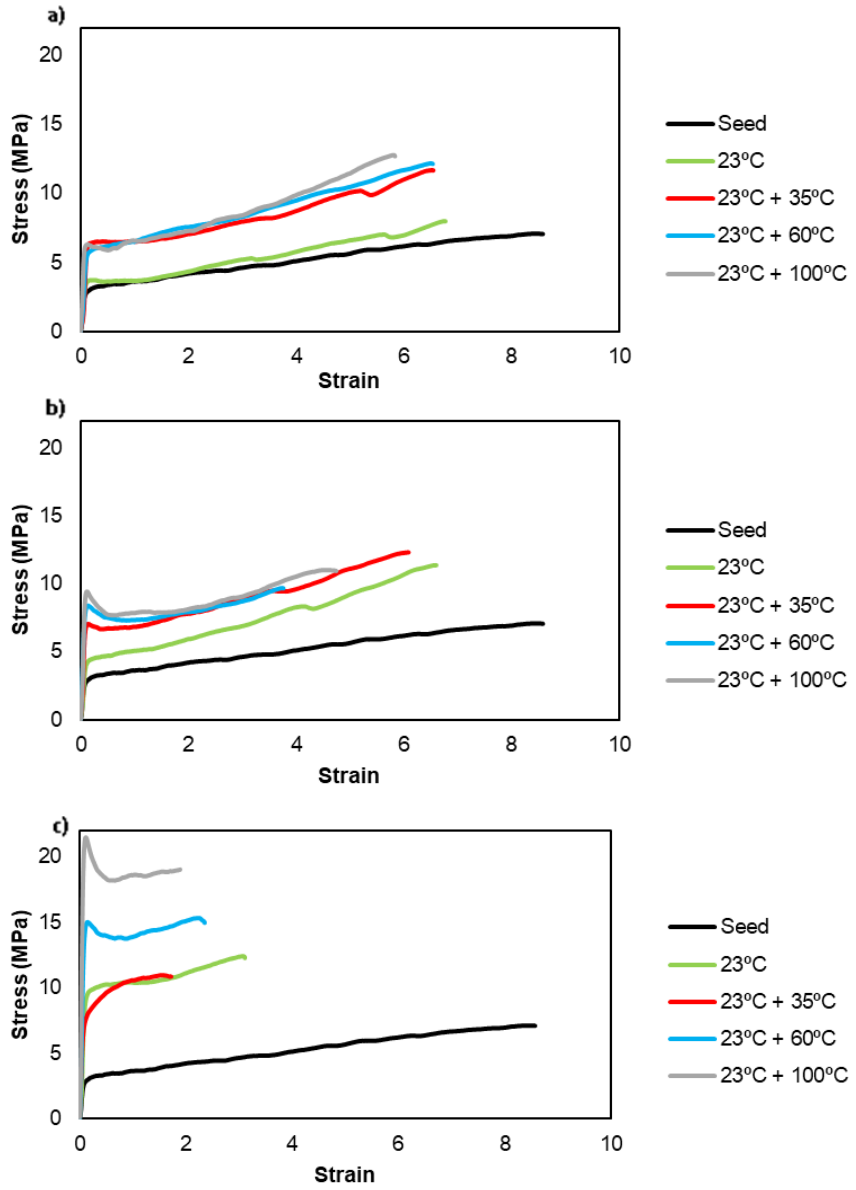

Figure 3-17: Stress-strain curves for films dried from the latexes a) 80MMA/10, b) 80MMA/20 and c) 80MMA/40 at 23 ºC and annealed at different temperatures

Table 3-6: Tensile tests results for films dried from the latexes 80MMA/10, 80MMA/20 and 80MMA/40 at 23 ºC and annealed at different temperatures

	Young's modulus (MPa)	Elongation at break	Stress at break (MPa)	Toughness (MPa)
Seed	30 ± 8	8.5 ± 0.9	7.1 ± 0.8	44.4 ± 8.5
80MMA/10				
23 ºC	48 ± 6	6.8 ± 0.6	8.0 ± 1.6	36.4 ± 11
23 ºC + 35 ºC	83 ± 10	6.6 ± 0.3	11.6 ± 0.5	54.6 ± 2.1
23 ºC + 60 ºC	69 ± 1.5	6.5 ± 0.2	12.2 ± 0.3	57.1 ± 3.5
23 ºC + 100 ºC	98 ± 5	5.8 ± 0.2	12.8 ± 1.2	50.5 ± 4
80MMA/20				
23 ºC	53 ± 6	6.6 ± 0.3	11.0 ± 0.3	47.0 ± 2.3
23 ºC + 35 ºC	99 ± 19	6.1 ± 0.4	12.3 ± 0.8	48.8 ± 5.5
23 ºC + 60 ºC	151 ± 18	4.3 ± 0.5	11.5 ± 1.8	40.5 ± 5
23 ºC + 100 ºC	135 ± 6	4.7 ± 0.8	11.0 ± 0.6	41.8 ± 6
80MMA/40				
23 ºC	142 ± 7	3.1 ± 0.4	12.3 ± 0.6	33.0 ± 5.8
23 ºC + 35 ºC	134 ± 16	1.7 ± 0.01	10.8 ± 1.8	15.6 ± 0.2
23 ºC + 60 ºC	248 ± 20	2.3 ± 0.2	15.2 ± 1.5	32.5 ± 6
23 ºC + 100 ºC	402 ± 17	4.4 ± 0.3	21.7 ± 1.6	67 ± 11

These results indicate that the thermal processing of the films for these systems led to the formation of clusters of the hard phase dispersed in the soft continuous phase. Only in certain cases, utilizing high volume fractions of the hard phase, it was possible to generate cocontinuous structures following thermal processing. In such cases where both phases form a percolating network the film hardness increases substantially. In other cases, changes in mechanical properties were limited regardless of the size of the clusters. However, thermal processing led to a loss of transparency of the films due to increased scattering of larger domains (Figure 3-18) which would be undesirable in a commercial setting. For practical applications, where phase migration is undesirable due to loss of transparency, the use of higher Tg polymers in the hard phase allows a significantly large temperature window such that under typical ambient conditions the film structure is stable.

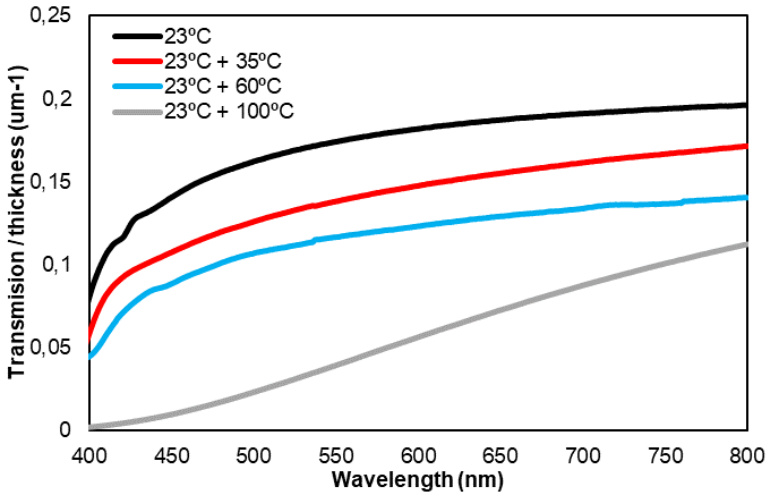

Figure 3-18: Light transmission of films dried from 70MMA/20 at 23ºC and annealed at different temperatures

3.4 Conclusions

Latex particles containing a soft core and a multi-lobed hard shell were synthesized in order to obtain homogeneous transparent films with good mechanical properties (high toughness and elasticity) as well as a low MFFT. Different latexes were synthesized with the same soft core (S/BA: 50/50) and a second stage polymer (MMA/BA) of different composition and amount (10 to 60% of the particle). It was possible to cast films from the latexes up to a hard phase content of 40 wt%, above which the MFFT was significantly higher than room temperature. The surface tension induced deformation of the soft during drying led to transparent films with a morphology composed of a continuous soft phase reinforced by aspherical hard segments. These morphologies led to an increase of film stiffness proportional to the amount and T_g of the hard phase. Thermal treatment was performed at different temperatures in order to study the diffusion of the hard phase in the soft matrix. When annealing temperature was above the T_g of the hard phase, phase migration was seen to occur. For low amounts of dispersed phase spherical inclusions were formed and limited improvement of mechanical properties was observed. However, for high amount of hard dispersed phase (40 wt%) annealing led to the formation of an interconnected network which led to a film with high tensile strength.

3.5 References

(1) Domingues Dos Santos, F.; Fabre, P.; Drujon, X.; Meunier, G.; Leibler, L. Films from soft-core/hard-shell hydrophobic latexes: Structure and thermomechanical properties *J. Polym. Sci. Part B Polym. Phys.* **2000**, *38*, 2989–3000.

(2) Geurts, J.; Bouman, J.; Overbeek, A. New waterborne acrylic binders for zero VOC paints *J. Coatings Technol. Res.* **2008**, *5*, 57–63.

(3) Heuts, M. P. J.; le Febre, R. A.; van Hilst, J. L. M.; Overbeek, G. C. Influence of Morphology on Film Formation of Acrylic Dispersions *Film Form. Waterborne Coatings* **1996**, 271–285.

(4) Price, K.; Wu, W.; Wood, K.; Kong, S.; McCormick, A.; Francis, L. Stress development and film formation in multiphase composite latexes *J. Coatings Technol. Res.* **2014**, *11*, 827–839.

(5) Plessis, C.; Arzamendi, G.; Leiza, J. R.; Schoonbrood, H. A. S.; Charmot, D.; Asua, J. M. Kinetics and polymer microstructure of the seeded semibatch emulsion copolymerization of n-butyl acrylate and styrene *Macromolecules* **2001**, *34*, 5147–5157.

(6) Elizalde, O.; Arzamendi, G.; Leiza, J. R.; Asua, J. M. Seeded Semibatch Emulsion Copolymerization of n -Butyl Acrylate and Methyl Methacrylate *Ind. Eng. Chem. Res.* **2004**, *43*, 7401–7409.

(7) Hamzehlou, S.; Reyes, Y.; Hutchinson, R.; Leiza, J. R. Copolymerization of n-butyl acrylate and styrene: Terminal Vs penultimate model *Macromol. Chem. Phys.* **2014**, *215*, 1668–1678.

(8) Aguirreurreta, Z.; Dimmer, J. A.; Willerich, I.; De La Cal, J. C.; Leiza, J. R. Water Whitening Reduction in Waterborne Pressure-Sensitive Adhesives Produced with Polymerizable Surfactants *Macromol. Mater. Eng.* **2015**, *300*, 925–936.

(9) Chesne, A. Du; Gerharz, B.; Lieser, G. The Segregation of Surfactant upon Film Formation of Latex Dispersions: an Investigation by Energy Filtering Transmission Electron Microscopy *Polym. Int.* **1997**, *43*, 187–196.

(10) Domingues Dos Santos, F.; Leibler, L. Large deformation of films from soft-core/hard-shell hydrophobic lattices *J. Polym. Sci. Part B Polym. Phys.* **2003**, *41*, 224–234.

(11) Yuan, X.; Huo, D.; Qian, Q. Effect of annealing on the phase structure and the properties of the film formed from P(St-co-BA)/P(MMA-co-BA) composite latex *J. Colloid Interface Sci.* **2010**, *346*, 72–78.

(12) Lee, C. F. The properties of core-shell composite polymer latex. Effect of heating on the morphology and physical properties of PMMA/PS core-shell composite latex and the polymer blends *Polymer* **2000**, *41*, 1337–1344.

Chapter 4. Understanding the curing process of films cast from acrylic/alkyd hybrid latexes via nanomechanical mapping

4.1 Introduction

The first known paints date back to the Stone Age some 25,000 years ago. These paints represented the animal's hunters and cave dwellers hunting (Lascaux Cave, France). These paints were composed of a binder and pigment based on iron and manganese oxides providing different colors: black, red and yellow. The binder, animal fat, was used to make the pigments stick to the cave wall.[1] In the period 600BC – 400AD, the Greeks and Romans developed coatings that besides being decorative also served to preserve the objects. These coatings were the first paints containing oxidatively-drying oils extracted from linseeds, soybeans and sunflower seeds. The protective value of drying oils was recognized in Europe in the thirteen century. During the Middle Ages, wood objects were protected by varnishes made by dissolving resins in oils. Over the centuries, demands for paints of all types increased and the business of paint became worldwide. At the beginning of the 20th century, the development of synthetic polymers, polyesters modified with unsaturated fatty acids, named alkyds, were introduced.[1–3]

Alkyd resins are an alternative to the use of low T_g acrylic polymers in multiphase polymer particles for architectural coatings. The term “alkyd” comes from the chemical used to synthesize it, namely alcohols and acids. The alkyd resin is in a liquid like state before film formation and thus reduces the minimum film formation temperature (MFFT) but double bonds present in the resin are cured by an autoxidative process after film formation, leading to hardening after film formation.[4]

The synthesis of acrylic / alkyd hybrid particles,[5–12] as well as the morphologies of films cast from these hybrid particles latexes,[5,13,14] has been widely studied. For example, Goikoetxea *et al.*[5] synthesized acrylic / alkyd hybrid particles with a core-shell morphology with a core of hydrophobic alkyd resin and a shell of acrylic polymer. In the film cast from the hybrid latex particles they observed a significant degree of migration of the discrete polymer domains, resulting in a polymer film containing domain sizes significantly larger than the original latex particles,. It was shown by a simulation model for film formation that phase migration was heavily influenced by the compatibility between the acrylic polymer and the free alkyd resin that was determined by the presence of alkyd-acrylic graft copolymer.[5] The graft copolymer can form as a result of the presence of radicals, either by radical addition to the double bonds of the resin or alternatively by abstraction of allylic hydrogen in a chain transfer reaction,[5,15] and subsequent propagation or termination on the alkyd during the radical polymerization process. Another critical feature that influences the film structure of acrylic/alkyd hybrids is the hardening of the alkyd resin itself. When the rate of hardening of the alkyd resin is much faster than that of phase migration and coalescence it would be expected that small domains sizes would be obtained and the film morphology would be determined by the initial particle morphology.

Alternatively, if the rate of hardening is slow then significant phase migration will occur, leading to large domain sizes. Given that the film structure is of paramount importance in determining the physical properties of the film,[16–20] understanding the curing process of the alkyd resin in such hybrids is essential for enhancing product performance.

The curing of the alkyds is a complex autoxidative process, in which oxygen reacts with unsaturated fatty acid side chains of the alkyd resin (Figure 4-1). The process is divided in several stages: (1) initiation, (2) hydroperoxide formation, (3) hydroperoxide decomposition and (4) cross-linking.[21] In the first step, abstraction of the double allylic hydrogen of the unsaturated fatty acid occurs. The resulting radical reacts instantaneously with oxygen to form a hydroperoxide radical. Abstraction of another H-atom from an unsaturated fatty acid leads to a hydroperoxide. Next, the hydroperoxides decompose into radical species. This step is slow and is aided by the addition of catalyst. The last step is the cross-linking which occurs through termination of the radical species by recombination resulting in a range of crosslinking points including ether (COC), peroxide (COOC) and carbon-carbon (CC) bonds.[22,23]

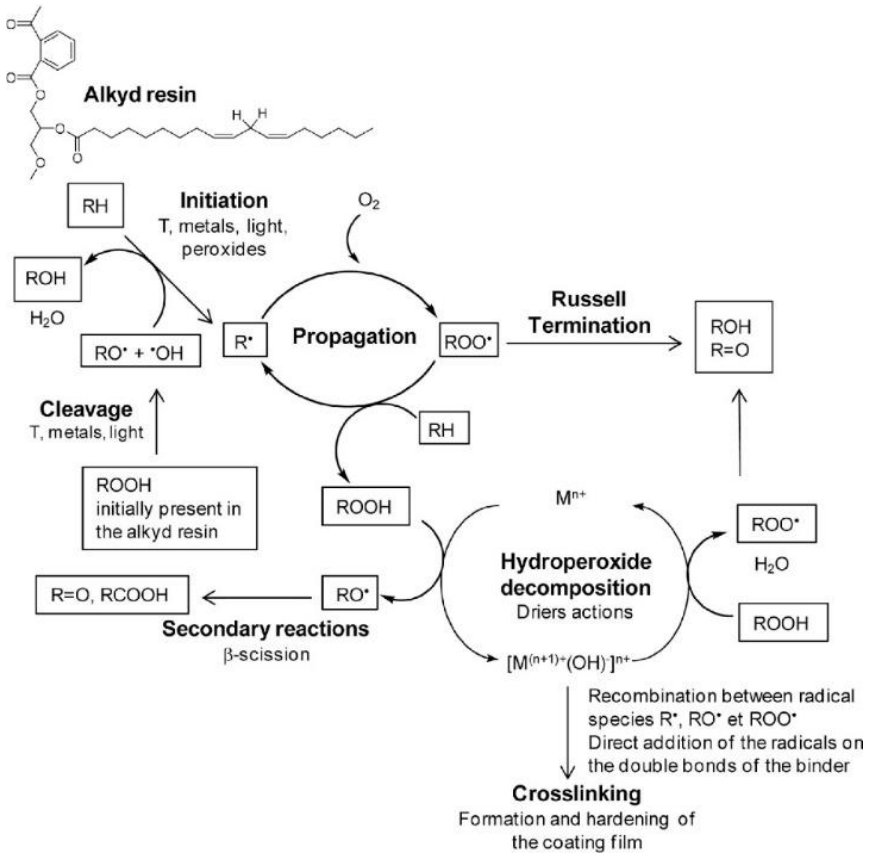

Figure 4-1: Radical reactions involved during the autoxidation of alkyd resin[23] Reproduced with permission from Elsevier

Two kinds of catalysts are used to accelerate the curing process: primary and secondary catalysts. The primary catalysts (also called surface catalysts) accelerate the decomposition of peroxides[22] and additionally have been reported to increase the initial rate of peroxide formation.[23] Although, for many years, the most commonly used commercial catalysts

have been cobalt based,[24] because of its potential carcinogenic properties,[25,26] cobalt catalysts are now often replaced by iron or manganese based catalysts.[27–29] When used alone in pure alkyd resins, primary catalysts tend to inhomogeneously cure the film.[22,30] A highly cross-linked region is soon formed near the film-air interface whereas the interior remains fluid. This cross-linked region advances very slowly towards the interior of the film such that even after several days the interior may remain uncured.[31,32] This has been attributed to the low rate of diffusion of oxygen across the highly cross-linked region which, as oxygen is required for the propagation step (see Figure 4-1), retards curing.

The secondary catalysts (zirconium, strontium, aluminum, calcium, potassium, lithium) are claimed to enhance homogeneous curing.[32,33] Although they are universally applied in alkyd coatings formulations the mechanism by which improvements in the curing process is achieved remains unclear.[32] Mallegol *et al.*[4] reported that using Co as primary catalyst, the secondary catalyst accelerated the initial phases of curing and in addition they led to a more homogeneous curing. These are conflicting findings because if diffusion limitations are the reason for the heterogeneous curing, faster curing should lead to a more heterogeneous curing. Mechanisms were suggested to explain these findings without determining exactly how they work.[32]

All the work on curing discussed above deal with pure alkyds resins. However, there are no studies on curing of acrylic/alkyd hybrids, where curing is complicated due to the additional effects of phase migration. In this work, we study the curing process of an alkyd resin in films cast from hybrid acrylic/alkyd particles latex and explore how it affects the development of film morphology and mechanical strength. First, the effect of concentration of the Mn-based primary

catalyst on the curing of the alkyd and the morphology of the polymeric film is explored using an AFM based nanomechanical mapping technique. In the second part, two secondary catalysts are studied in order to understand their influence on the curing process and the film morphology of the hybrid material.

4.2 Experimental part

4.2.1 Materials

Methyl methacrylate (MMA, Quimidroga, technical grade), butyl acrylate (BA, Quimidroga, technical grade), stearyl acrylate (SA, Aldrich, technical grade), tert-butyl hydroperoxide (TBHP, Panreac, >98%), $NaHCO_3$ (Aldrich, >99,5%) and FF7 (Bruggolite) were used as received. 2,2´-Azobis (2-methylpropionitrile) (AIBN, Sigma-Aldrich, 98%) was used as thermal initiator. Dowfax 2A1 (alkyldiphenyloxide disulfonate, Dow Chemical Co.) was used as surfactant. The alkyd resin (SETAL 293, hydrophobic) was kindly provided by Allnex. GPC grade tetrahydrofuran (THF, Scharlau) was used as received. Nuodex DRYCOAT (Huntsman, Mn primary catalyst), Durham Nuodex Zirconium 12 (Huntsman) and Octa-Soligen Calcium 10 (Borchers) were used as catalysts. Deionized water was used throughout the work.

4.2.2 Miniemulsion polymerizations

A 50 wt % solids content miniemulsion was prepared as follows. First, the organic phase was prepared by dissolution of the alkyd resin SETAL 293 (50 wt % based on monomers, wbm), SA (4 wbm%) and azobisisobutyronitrile (AIBN) (1.6 wbm %) into the monomer mixture methyl methacrylate(MMA)/butyl acrylate(BA)/ acrylic acid(AA) (MMA/BA/AA, 49.5/49.5/1 wt %). Then, the organic phase was poured into an aqueous solution of Dowfax 2A-1 (2.7 % weight based on organic phase,wbop, of active surfactant) and sodium bicarbonate ($NaHCO_3$,0.015M) under magnetic stirring at 700 rpm to create an emulsion. The resulting emulsion was sonicated with a Branson 450W sonificator for 10 minutes at an amplitude of 70% and a duty cycle of 80%. During sonication, the flask was immersed in an ice bath to avoid overheating. Polymerization was carried out in batch in a 500-mL glass reactor equipped with a reflux condenser, stirrer, sampling device, and nitrogen inlet. The reaction temperature was 70°C for 7 hours. The latex obtained was post-polymerized with a redox initiator tert-butyl hydroperoxide/disodium hydroxysulfinoacetate (TBHP/FF7). The feeding time was 90 min and a molar ratio of 100/25/12.5 (residual monomer/oxidant/reductor) was used. Finally, the reaction was maintained in batch for an hour. The recipe for the reaction is given in Table 4-1.

A 25 wt % solids content miniemulsion was prepared as follows. First, the organic phase was prepared by dissolution of the SA (4 wbm%) into the monomer mixture (MMA/BA/AA, 49.5/49.5/1 wt %). Then, the organic phase was poured into an aqueous solution of Dowfax (2.7 % weight based on organic phase,wbop, of active surfactant) and $NaHCO_3$ (0.015M) under magnetic stirring at 700 rpm to create an emulsion. The resulting emulsion was sonicated with a Branson 450W sonificator for 10 minutes at an amplitude of 70% and a duty cycle of 80%.

During sonication, the flask was immersed in an ice bath to avoid overheating. Polymerization was carried out in batch in a 500-mL glass reactor equipped with a reflux condenser, stirrer, sampling device, and nitrogen inlet. When the reaction mixture reached 70ºC a shot of initiator (KPS, 1.3 wbm% in 7 wt% of the total amount of water) was added and the reaction was let to react for 7 hours. The formulation for the reaction is given in Table 4-2.

Table 4-1: Formulation for the synthesis of the acrylic / alkyd hybrid particles latex

Compounds	Weight (g)
Water	449.56
Dowfax 2A-1*	11.75
BA	103.58
MMA	103.58
AA	2.07
Alkyd 293	217.6
SA	8.38
AIBN	3.48
$NaHCO_3$	0.57
TBHP**	5.2
FF7**	2.75
Water**	39.2

*active matter
**during post-polymerization

Table 4-2: Formulation for the synthesis of the acrylic particles latex

Compounds	Weight (g)
Water	268.5
Dowfax 2A-1*	1.1
BA	37.1
MMA	37.1
AA	0.75
$NaHCO_3$	0.32
SA	4.5
KPS	1

4.2.3 Film preparation

Before film formation, the catalyst was added to the latex under stirring in a vortex mixer (VELP scientifica ZX3) for 30s at 2500 rpm and then 1h under magnetic stirring using 0.25, 1 and 2 wt% (based on alkyd resin content) of Nuodex DRYCOAT, an oil-based manganese primary catalyst. Secondary catalysts (Nuodex Zirconium 10 – 3.5 wt%, and Octa-Soligen Calcium 10 – 0.79 wt%) were added under the same conditions. Table 4-3 summarizes the different systems studied. Films were produced by casting 0.3 g of latex in rectangular silicone molds (10 x 40 mm x 1 mm) and allowed to dry at 23 ºC and 55% relative humidity (RH) for 1, 3 and 8 days. After evaporation, the thickness of the films was about 0.24 mm. Moreover, a film

of pure alkyd resin was also prepared for comparison. A cobalt based catalyst was added at 1 wt% to pure alkyd resin. The mixture was stirred in a vortex mixer for 30 seconds and then 1 hour under magnetic agitation. The film was cast on a polyethylene terephthalate (PET) sheet and let to dry in an oven at 65ºC for two weeks.

Table 4-3: Compositions of the different systems studied

Name code	DRYCOAT (%, based on alkyd resin)	Durham Nuodex Zirconium 10(%, based on alkyd resin)	Durham Nuodex Calcium 10 (%, based on alkyd resin)
0.25%-Mn	0.25	/	/
1%-Mn	1	/	/
2%-Mn	2	/	/
1%-Mn + Zr	1	3.5	/
1% Mn + Ca	1	/	0.79

4.2.4 Characterizations

The particle size of the final latexes were measured by both dynamic light scattering using a Malvern Zetaziser. Residual monomers were measured by gas chromatography. The gel content of the polymers was determined by Soxhlet extraction. The molecular weight distribution and the mass fraction of alkyd grafted to the acrylic polymer (resin degree of grafting: RDG) in the sol fraction were determined by gel permeation chromatography (GPC). The double bond content of the resin in the particles was measured by iodine value titration. Particles morphology were determined by transmission electron microscopy (TEM).The sample was stained with OsO_4 before analysis. The mechanical properties of the films cast from the synthesized latexes were determined by tensile tests. A detailed description of these characterization methods is provided in Appendix I.

Atomic Force Microscopy measurements were carried out using a Bruker Multimode 8 equipped with a Nanoscope V controller. The Peak Force Quantitative Nanomechanical Mapping (PF-QNM) method was used as imaging and characterization technique. Measurements were carried out at room conditions of 25 ºC and 40 %RH. All images were processed offline, using the Nanoscope Analysis 1.9 software (Bruker). For AFM measurements, films were cut with a microtome equipped with a diamond knife at 6ºC. A sample holder designed for cross-section analysis was used. This fixed the sample in the same position throughout the whole process (cutting + imaging). Considering that once the sample cross-section is exposed to the air conditions cross-linking will start taking place, PF-QNM analysis was carried out immediately after microtoming. Also, following these considerations, it is impossible to use the same sample for a continuous analysis as a function of time. In order

to perform measurements with time, each AFM measurement was carried out on a nominally equivalent, but separate film. Finally, we note that all samples were thick enough to allow disregarding the possible impact of the supporting substrate on the nanomechanical properties.

Briefly, PF-QNM allows capturing force-distance curves at each pixel, at a high speed and with a high resolution. Every force curve records the force on the tip as it approaches and retracts from a point on the sample surface. When the force reaches a user specified trigger value, or Peak Force, the system records the height for that pixel and the tip retracts. This allows having both topography information and mechanical properties, simultaneously. In our work, we used a fixed peak force setpoint value of 15 nN for all the probed samples. We calculated the mechanical modulus from the force curves using the Derjaguin-Müller-Toporov (DMT) model[34]:

$$F - F_{\text{adh}} = \frac{4}{3}\frac{E}{(1-\nu^2)}R^{1/2}\delta^{3/2} \qquad \textbf{(4-2)}$$

where F is the force, F_{adh} the adhesion force taking place during tip retraction from the surface, E the mechanical modulus, R the tip radius, δ the indentation, and υ the Poisson ratio of the sample. The mechanical modulus fit, following eq. 1, was performed taken 90% and 20% of the peak force setpoint as maximum and minimum boundaries, respectively. In this region of the force curve, the trace and retrace superimposed, indicating an elastic response. This approach has been used extensively in recent literature to study the nanomechanical properties of polymers.[35–37]

All samples were probed using Multi75-G probes, by BudgetSensors (tip radius ~15 nm). The spring constant was determined by the Sader method,[38] giving a usual value around 3.5 N/m. PF-QNM quantitative images were acquired following the relative calibration method proposed by Bruker, and recently used in the literature.[39,40] The relative method of calibration uses a sample of known modulus to obtain the ratio of spring constant to the square root of the tip end radius. In our work, we used as a reference an acrylic sample prepared by us (MMA/BA: 50/50 wt/wt), with a known modulus of 70 MPa (υ = 0.4),[41] for imaging the mechanical maps of the hybrid latex films (Figures 4-6, 4-7, 4-8, 4-11 and 4-12). Using this reference, we obtained maps with good mechanical contrast between soft/hard areas. However, we observed that mechanical modulus values lower than 30 MPa were not properly resolved. We based tis reasoning on the severely distinct force-curves of these areas. This is an indication that the test conditions in these zones were not similar to those used during calibration. Exploring our hybrid particles latex film mechanical maps we noticed that the MMA/BA reference sample only allowed measuring reliable modulus values in the 30 ≤ E (MPa) ≤ 150 range. The problem of modulus resolving capabilities in AFM-based mechanical measurements has been discussed in the literature,[42] and it is out of the scope of this work. Then, to guarantee similar reference/sample test conditions in the soft areas, we changed our reference material to a polydimethylsiloxane (PDMS) sample of known modulus 3.5 MPa (provided by Bruker, υ = 0.5)[41]. We observed good agreement in the mechanical response of soft areas in the hybrid latex films and that of the PDMS sample. In this case, we obtained a confidence modulus range of 2 ≤ E (MPa) ≤ 30. Taking this into consideration, the quantitative mechanical modulus values of the soft areas in our films were calculated (offline) using the PDMS reference (Figures 4-5 and 4-10).

4.3 Results and discussion

4.3.1 General overview of the latex characteristics

Table 4-4 summarizes the results for the polymerization of the waterborne acrylic/alkyd hybrid latex by miniemulsion polymerization. A relatively low conversion was obtained after the initial polymerization process, likely as a result of the rate retarding effect of the double bonds present in the alkyd resin.[9,15,43] In addition, a broad distribution of molecular weights was observed because the sample includes the high molecular weight acrylic polymer and the low molecular weight alkyd resin.[9] In order to reduce the residual monomer concentration, a post-polymerization process was performed. As shown in Table 4-4, a final residual monomer concentration of 2700 ppm was obtained. After post-polymerization, an increase of the molecular weight was observed, again with a broad distribution. This increase is related to the increase of the alkyd grafting on the acrylic chains from 8% to 15%. Indeed, the high number of oxygen centered radicals that are generated from the TBHP/FF7 redox system leads to significant hydrogen abstraction, which produces grafting. However, a final grafting of 15% is still low, meaning that most of the alkyd resin is ungrafted. In addition, a small gel fraction was formed during post-polymerization, again due to the increase of grafting through the double bonds of the alkyd resin. Considering that cross-linking requires “free” double bonds, in Table 4-4 we present the percentage of reacted resin double bonds (RDB). We observed that the relative amount of RDB was low, even after postpolymerization, leaving most of the double bonds available for cross-linking. By comparing the values of grafting and RDB after post-polymerization we can determine that the principal site for grafting is the allylic hydrogen to the double bond in the alkyd resin as this mechanism does not affect the number of conjugated

double bonds.[15] Figure 4-2 shows a TEM image of the synthesized latex after postpolymerization demonstrating a core-shell morphology with an alkyd-rich core and acrylic-rich shell. Sizes of the particles from the TEM image agree well with those found by DLS (Table 4-4).

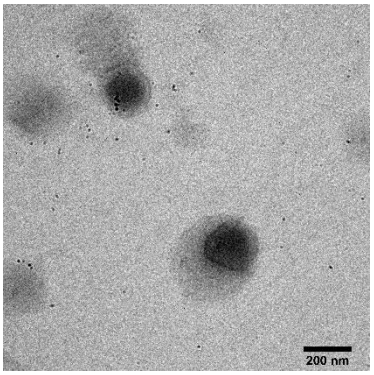

Figure 4-2: TEM image of the acrylic / alkyd hybrid particles. Dark regions correspond to the alkyd rich phase (scale bar: 200 nm)

Table 4-4: Characteristics of the synthesized latex

	Residual monomers (ppm)	Particle size (nm)	Gel content (%)	M_n (kg/mol) (a)/(b)*	M_w (kg/mol) (a)/(b)*	*Đ* (a)/(b)*	Degree of grafting (%)	RDB (%)
Polym.	25500	155	0	4.8/34.4	48,4/55.8	10.1/1.2	8	0.8
Post-polym.	2700	163	3.8	5.2/75.9	55.9/93.4	10.8/1.11	15	3.2

*(a) Whole polymer and (b) acrylic polymer

In order to get an idea of the expected distribution of the moduli of the two polymer phases, before analysis of the hybrids we performed PF-QNM measurements on films cast from acrylic and alkyd phases separately. Figure 4-3abc shows the PF-QNM mechanical modulus maps of a bare MMA/BA film cast on a PET sheet dried for 8 days at 23 ºC and 55% relative humidity. It should be noted that these images correspond to the "top" of a film, i.e., without cross sectioning. We present three different probed areas of the film, measured on different days. All the images showed a mean mechanical modulus of 70 MPa, with a broad distribution (see histograms). The modulus distribution broadness could be probably related to the batch process used to synthesis the polymer that, because of the different reactivity ratios of the monomers,[44] led to a broad polymer composition distribution. From the results in Figure 4-3abc, we can expect that the MMA/BA areas in the PF-QNM modulus maps of hybrid samples would appear in colors ranging from green to black, indicating a modulus distribution in the range $40 \leq E\ (MPa) \leq 100$.

Figure 4-3d shows the elastic modulus map of a pure alkyd resin film, with a Co-based catalyst, dried at 65 ºC for two weeks. We found a mean elastic modulus of 35 MPa, with a narrow distribution (light green monocolor image). We consider this to be the *best possible scenario* of a fully dried alkyd sample. In other words, uncured alkyd areas in the PF-QNM modulus maps are expected to have a modulus below 35 MPa. Thus, we expect that the hybrid film will contain regions with widely different moduli. As discussed in the Experimental Part, this is a long-standing challenge in AFM-based mechanical measurements.[42] Here, the challenge was overcome by using different conditions for the two objectives of this work. To study the curing process attention should be paid to the increase of the modulus of the soft areas of the

hybrid films (alkyd regions). In this case, the reference was a PDMS sample of known modulus (E= 3.5 MPa) and this allowed to get accurate measurements in the range $2 \leq E\ (MPa) \leq 30$. On the other hand, when the evolution of the morphology was studied an acrylic sample with a modulus of 70 MPa was used as a reference and this allowed us to have accurate measurements in a range of $30 \leq E\ (MPa) \leq 150$. In this case, the modulus of the alkyd regions cannot be accurately detected and therefore in the PF-QNM mechanical maps used to investigate the evolution of the film morphology the (not completely cured) alkyd regions (≤ 30 MPa) will appear red and the acrylic areas (40-100 MPa) in green to black.

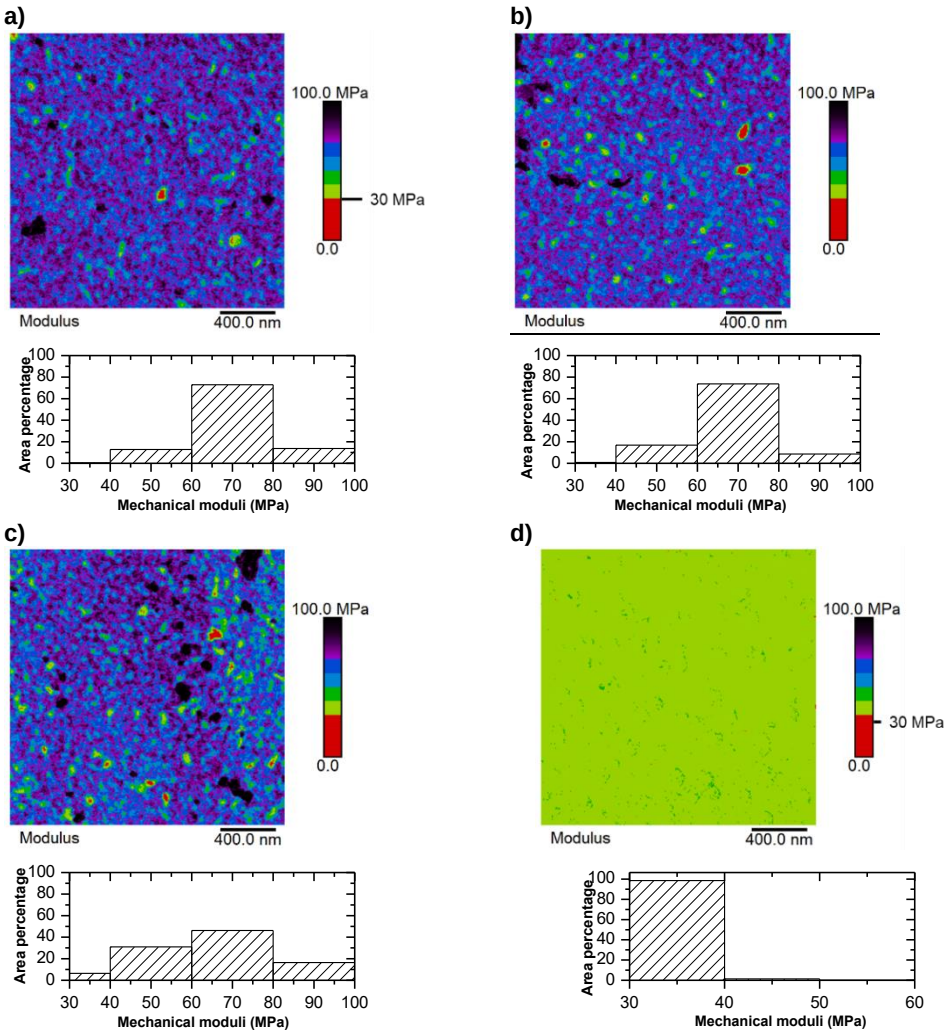

Figure 4-3: Mechanical maps and histograms of the modulus distribution of the surface of a,b,c) pure acrylic polymer films dried at 23 ºC for 8 days and d) pure alkyd film with Co-based catalyst dried at 65 ºC for 8 days

4.3.2 Effect of catalyst on the curing process of hybrid latex films

4.3.2.1 Effect of catalyst on mechanical properties of the films

A film was formed from the hybrid latex described above at various concentrations of Mn catalyst in order to investigate how the curing process of the alkyd influences the mechanical strength of the final film. Figure 4-4 and Table 4-5 show the tensile test results for films prepared with the Mn-based catalyst at 0%, 0.25 wt%, 1 wt%, and 2 wt% concentrations cured at 23 ºC and 55% relative humidity for 1, 3 and 8 days. For the sake of comparison, the results obtained with a pure (meth)acrylic latex are also included in Table 4-5. The catalyst-free film (0% Mn) showed limited mechanical resistance even after 8 days of curing (Figure 4-4c) and a Young's modulus of about 0.5 MPa was measured. This is almost two orders of magnitude lower than that of the pure acrylic polymer film (Table 4-5) which indicates that the alkyd did not undergo any curing. The addition of the Mn catalyst significantly affected the mechanical properties of all films. After 1 day of curing, the three systems showed a Young's modulus value around 2.5 MPa, i.e., an increase in a factor ~5 compared to the catalyst-free film. The rest of the mechanical properties (stress at break, and toughness) also showed improvement (Table 4-5). After 3 days of curing, all films presented similar mechanical properties, showing an overall enhanced mechanical response. The Young's modulus kept on increasing reaching about 6.5 MPa after curing for 8 days. No effect of the concentration of the Mn on the Young's modulus was observed although the elongation and therefore the toughness of the films showed an increase with catalyst concentration.

Tensile tests give the mechanical properties of the film as a whole without differentiating the different phases. However, this method does not give quantitative values of curing of the alkyd resin in the hybrid particles. In order to explore with detail the role of the acrylic/alkyd phases, an AFM-based nanomechanical mapping technique was used to quantify the extent of curing in the films.

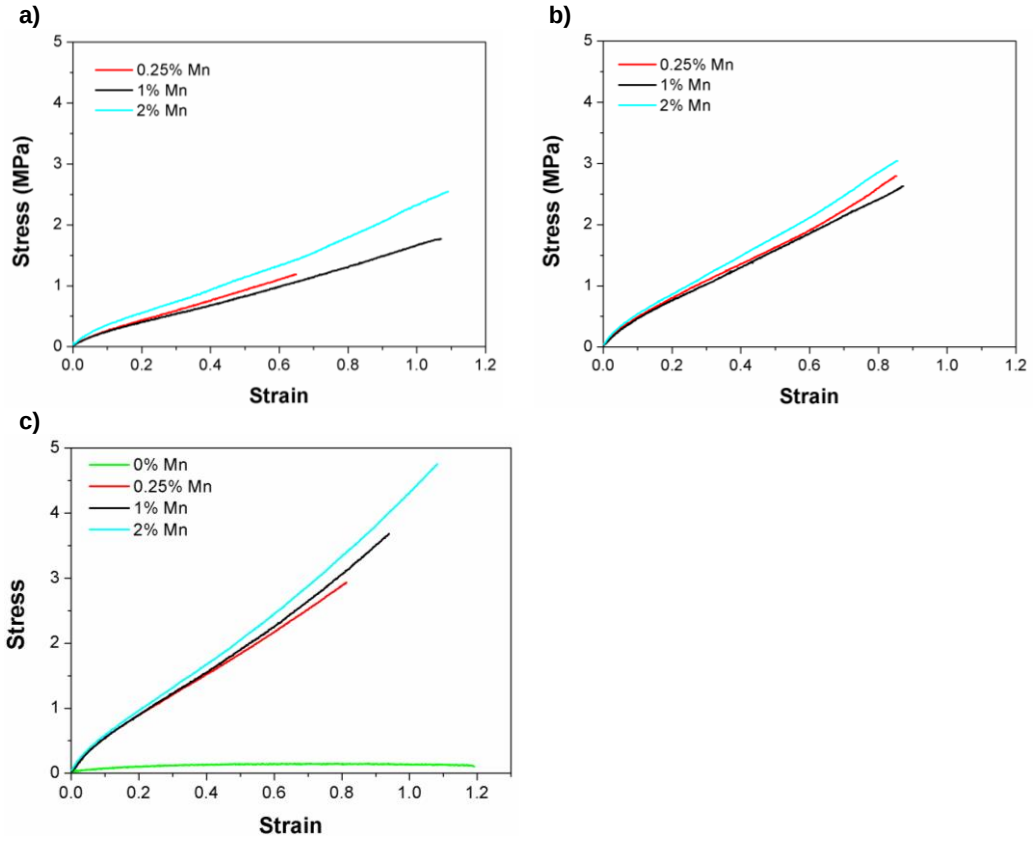

Figure 4-4: Stress- strain curves of dried films from acrylic / alkyd resin hybrid particles latex with different concentration of Mn-based catalyst after a) 1 day, b) 3 days and c) 8 days

Table 4-5: Tensile test results of dried films from acrylic / alkyd resin hybrid particles latex with different concentration of Mn-based catalyst after 1,3 and 8 days

	Young's modulus (MPa)	**Elongation at break**	**Stress at break (MPa)**	**Toughness x 10^6 (J/m^3)**
0% Mn – 8 days	0.512 ± 0.2	1.16 ± 0.19	0.123 ± 0.004	0.127 ± 0.036
0.25% Mn - 1 day	2.3 ± 0.2	0.65 ± 0.04	1.19 ± 0.14	0.41 ± 0.08
1% Mn - 1 day	2.7 ± 0.3	1.06 ± 0.05	1.77 ± 0.37	0.95 ± 0.17
2% Mn - 1 day	3.0 ± 0.9	1.01 ± 0.14	2.1 ± 0.43	1.08 ± 0.3
0.25% Mn - 3 days	4.9 ± 0.8	0.85 ± 0.05	2.80 ± 0.28	1.22 ± 0.17
1% Mn - 3 days	4.9 ± 0.3	0.87 ± 0.09	2.65 ± 0.45	1.22 ± 0.48
2% Mn- 3 days	5.6 ± 0.7	0.85 ± 0.09	3.04 ± 0.27	1.34 ± 0.23
0.25% Mn - 8 days	6.5 ± 0.8	0.81 ± 0.03	2.93 ± 0.56	1.25 ± 0.26
1% Mn - 8 days	6.4 ± 0.5	0.94 ± 0.1	3.68 ± 0.44	1.72 ± 0.34
2% Mn- 8 days	6.7 ± 1.5	1.08 ± 0.11	4.74 ± 0.51	2.48 ± 0.42
Pure acrylic	54 ± 9.8	3.4 ± 0.17	7.3 ± 0.65	17 ± 2.11

4.3.2.2 Evolution of curing of the alkyd resin with the primary catalyst

PF-QNM measurements were performed on cross-sections of films after 1, 3 and 8 days of curing with 0.25%, 1%, and 2% wt of the Mn based catalyst. The measurements were performed at three different areas of the cross-sections: (1) close to the air-film interface, (2) in the center of the films, and (3) close to the film-substrate interface. The goal of these measurements was two-fold. First, to measure the degree of curing of the alkyd rich zones and second to study the effect of curing on the development of the film morphology (height images are available in Appendix II). In this section, the development of the curing process of the alkyd resin was monitored by measuring the time evolution of the mechanical modulus of the soft areas in the different parts of the film. We defined an area as "soft" if the mechanical modulus was below 30 MPa. We identified those zones using the PF-QNM mechanical maps, and, to have a proper quantification of the mechanical modulus in these soft areas, we used a PDMS standard as reference, a detailed in the experimental section.

In the absence of catalyst, even after 8 days of curing, the AFM probe stuck to the film surface preventing the measurement, which agrees with the liquid-like behavior observed in the tensile tests (Figure 4-4c). For the system with 0.25 wt% Mn based catalyst, the curing after 1 day was not sufficient to perform the measurement as the sample also exhibited liquid-like behavior. This may be due to a slow curing rate because of the low catalyst concentration or alternatively due to an inhibition period that initially prevents curing, as previously reported for Mn-based catalysts.[32,45]

In order to gauge the effect of catalyst concentration of the through-curing of the films, Figure 4-5 presents the time evolution of the mechanical modulus of the soft areas in the different regions (near the surface, in the center and close to the substrate) with varying Mn concentration. The mechanical modulus reported in this graph by PF-QNM was calculated as the mean value of 50 points randomly located in the soft phase material (E < 30 MPa). The error bars correspond to the standard deviation. It can be seen that after 1 day curing with 1 and 2 wt% of Mn curing (hardening) increased with the primary catalyst concentration and that curing was highest near the air-film interface and minimum in the center of the film. This indicates that curing did not occur homogeneously, but with a stronger impact on the borders of the film. It has to be pointed out that the substrate used was a silicone mold, a material permeable to oxygen (oxygen permeability of silicone rubber: 600 Barrer).[46] Thus, the oxygen diffusion through the substrate and the differences in oxygen availability resulted in an initial non-homogeneous curing of the alkyd resin.

After 3 days, curing increased in all positions in the film and the edges of the film were still harder, although the differences with the center were smaller than for 1 day. For a curing time of 8 days, there was no further evolution of the mechanical modulus of the soft areas for 0.25 wt% of Mn (Figure 4-5). This could result from the deactivation of the catalyst with the acid groups of the acrylic polymer, as previously reported.[47] For higher catalyst concentrations, the mechanical modulus of the soft areas increased further, the increase being more substantial in the center of the film. At catalyst concentrations above 1 wt% Mn, the long term effect of the concentration of the primary catalyst was small, because almost the same modulus was achieved. In addition, a rather homogeneous degree of curing was achieved through the film.

In comparison, in a ~200 µm film cast from the pure alkyd resin with 1% Mn catalyst we observed the incipient development of a curing front. Later, after curing for 8 days, a clear curing front appeared on the top of the film, leaving a completely liquid core (Figure II-6, in Appendix II). This suggests that the front was strictly oxygen impermeable, hindering the curing deeper in this film. Thus, comparing the pure alkyd with the results obtained with the hybrid film indicates that the acrylic phase in the hybrid films appears to aid oxygen diffusion. However, this does not mean that there were no diffusional limitations for the oxygen in the hybrid, as a demonstrated by the differences in the curing at different points in the film.

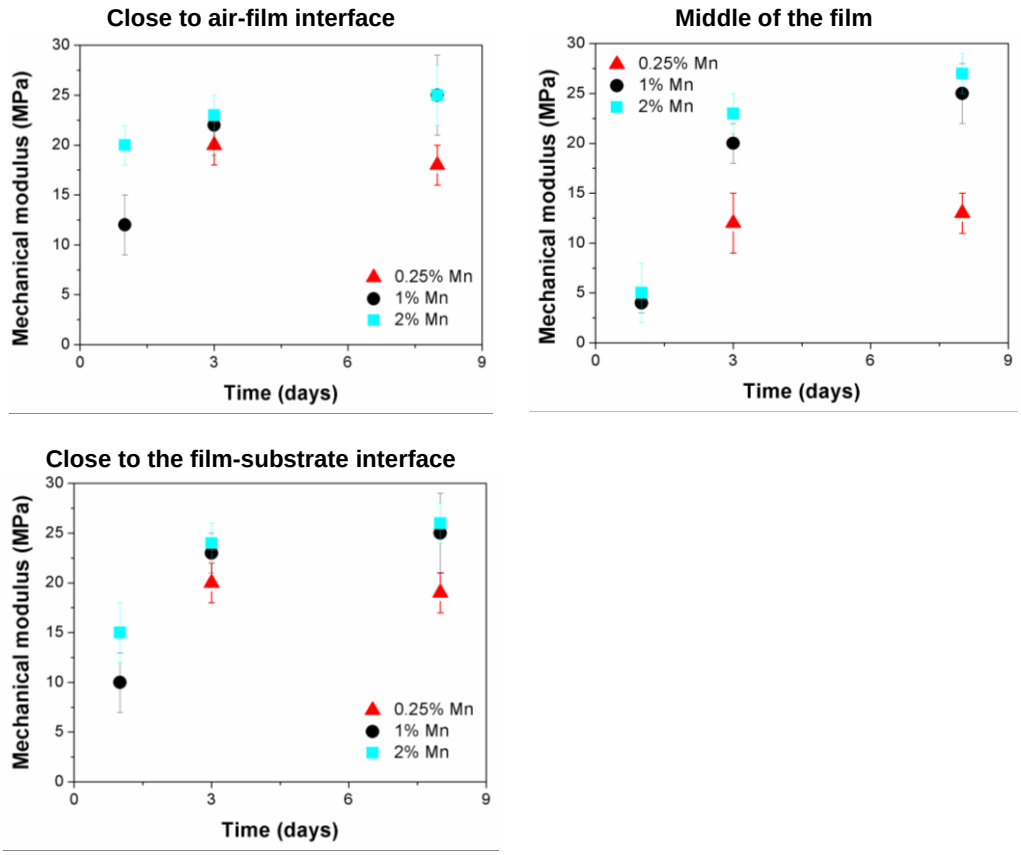

Figure 4-5: Evolution of the mechanical modulus of the soft areas of the films cured at 23 ºC and 55% relative humidity with time close to air-film interface, in the center and close to the film-substrate

4.3.2.3 Morphology evolution with the curing of alkyd resin

Figures 4-6, 4-7 and 4-8 display the AFM mechanical maps of the systems measured after 1, 3 and 8 days of curing with 0.25%, 1%, and 2% wt of the Mn based catalyst. In these figures the reference material was a (meth)acrylic polymer of E=70 MPa, and hence the accurate modulus range was between 30 and 150 MPa. All areas in which E < 30 MPa that correspond to the alkyd were depicted in red. Figure 4-6a-c shows the results for the 1% Mn sample after 1 day. It can be seen that most of the film section is covered by a rather soft material (red colored zones in the maps) than can be attributed to the alkyd. However, the fraction covered exceeds by far the proportion of alkyd in the formulation. The most likely reason for this is that the alkyd phase, which was basically uncured (Figure 4-5), spread during microtoming, forming a layer that covered the sample surface. Quite likely, in Figure 4-6c, the liquid alkyd was removed leaving the hard acrylic polymer. Figure 4-6d-f show the results for the 2%-Mn sample. For this sample, the area in the middle of the film was more covered by the alkyd resin than at the air-film and film-substrate interfaces. The reason for this observation was the low degree of curing of the alkyd in the center of the film (Figure 4-5). On the other hand, in the regions where curing was significant (regions close to the air and substrate) aggregates of alkyd of sizes with average diameter about 300 nm, namely larger than the latex particles, are observed showing that substantial migration occurred.

Figure 4-7 shows the results after 3 days of curing for samples containing 0.25%, 1% and 2% Mn catalyst. All samples were sufficiently cured to perform the nanomechanical mapping and no covering of the microtomized surface was observed. After 3 days for all Mn concentrations, the alkyd-rich domains measured a mean diameter of 550 $\pm$ 100 nm (measured

on the length of the domains). This implied an increase in almost 70 % in comparison to the sizes measured after curing for 1 day in the film with 2% Mn. In other words, in the time period from 1 to 3 days, the alkyd phase still had enough mobility to allow phase migration to occur. However, due to the complex geometrical shapes of the domains exact quantification of this effect was not attempted.

Figure 4-8 shows the nanomechanical maps after curing for 8 days. Considering first the effect of the Mn concentration at each position, it can be seen that the area covered by “pure” acrylic domains (zones with a high value of modulus) increased with the Mn concentration. This suggests that the curing of the alkyd is a driving force for phase separation, *i.e.* the alkyd, which has initially some partial miscibility in the acrylic phase, is driven out by curing. On the other hand, comparison of the maps obtained at different positions for each Mn concentration shows that the strongest separation occurred at the center of the film followed by the region close to the substrate, with the region near the air-film interface showing less separation. A possible explanation is that curing of the alkyd reduced its mobility and therefore the slower the curing (center) the longer the alkyd had to migrate. This is supported by the size of the alkyd domains, which in general decreased with the concentration of Mn.

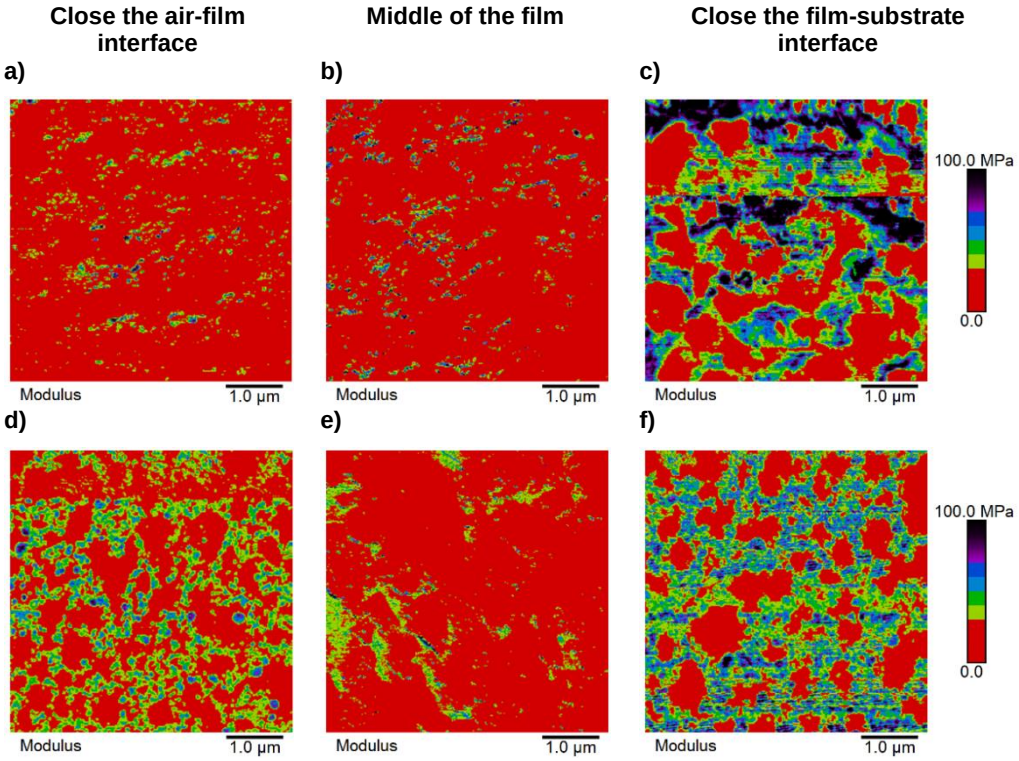

Figure 4-6: Mechanical maps for the films with 1% of Mn-based catalyst abc) and 2% Mn-based catalyst def) after 1 day of curing at 23ºC and 55% relative humidity. For each system, the left image was performed close to air-film interface, the second in the center of the film and the right image close to the film-substrate interface

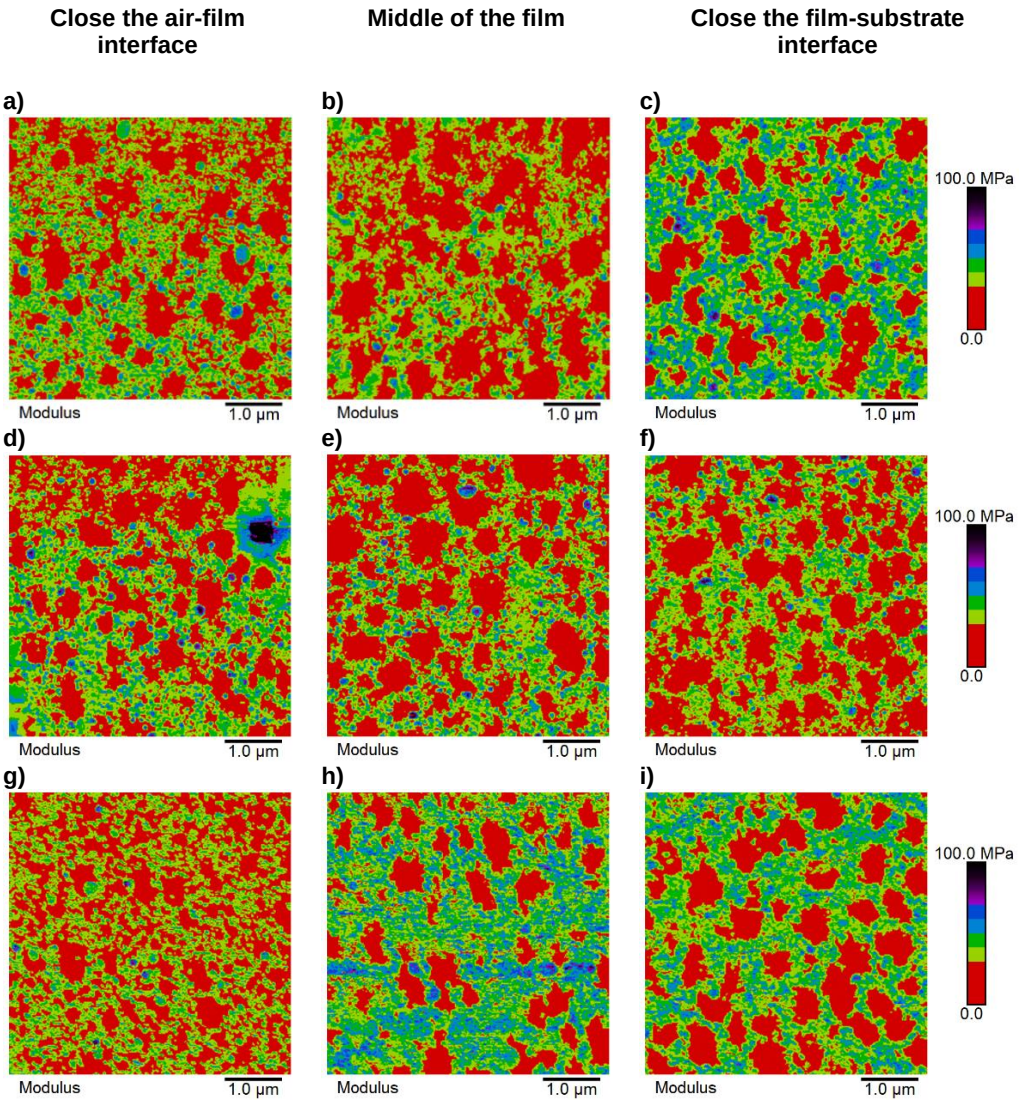

Figure 4-7: Mechanical maps for the films with 0.25% of Mn-based catalyst abc),1% of Mn-based catalyst def) and 2% of Mn-based catalyst ghi) after 3 days of curing at 23ºC and 55% relative humidity. For each system, the left image was performed close to air-film interface, the second in the center of the film and the right image close to the film-substrate interface

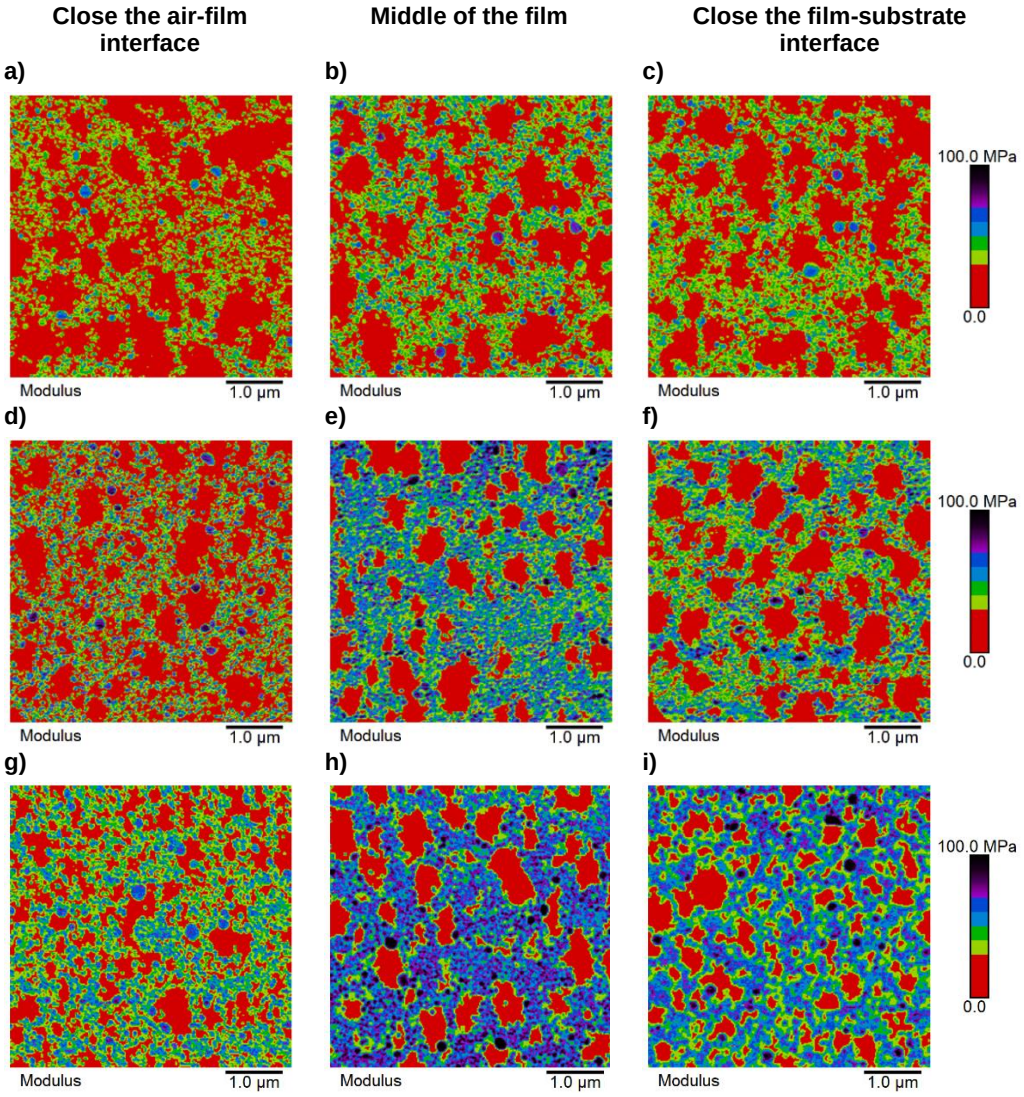

Figure 4-8: Mechanical maps for the films with 0.25% of Mn-based catalyst abc),1% of Mn-based catalyst def) and 2% of Mn-based catalyst ghi) after 8 days of curing at 23ºC and 55% relative humidity. For each system, the left image was performed close to air-film interface, the second in the center of the film and the right image close to the film-substrate interface

4.3.3 Effect of secondary catalyst on film morphology and properties

4.3.3.1 Effect of secondary catalysts on mechanical properties of the films

As described in the introduction, secondary catalysts have been used to enhance the effectiveness of the primary catalyst. They are variously described to increase the cross-linking rate, improve oxygen diffusion, decrease inhibition time, or be used as "sacrificial catalysts".[32] In the latter case, the secondary catalysts would deactivate instead of the primary.[4] In order to try to understand the role of the secondary catalyst, we evaluated the influence of Zr and Ca-based secondary catalysts on the curing of hybrid latexes films.

Figure 4-9 and Table 4-6 present the results of the tensile test for hybrid films with 1 wt % of the Mn based primary catalyst plus Zr or Ca-based secondary catalysts. Measurements were performed after 1 and 8 days of curing at 23 ºC and 55 % relative humidity. After 1 day of curing, we found a slightly lower Young's modulus for the films prepared using secondary catalysts. The E values were the same when using either Zr or Ca catalysts, and represented a decrease of about 55 %, compared with the sole Mn film. The rest of the mechanical properties were also worsened with the addition of the secondary catalysts at short times. After curing for 8 days, the mechanical properties of the films improved, showing the effect of curing, and the film containing Zr showed slightly higher Young's modulus and tensile strength. All three presented similar toughness (Table 4-6). As these results were not conclusive in terms of the effect of the secondary catalyst on the curing of the alkyd resin throughout the film, we subsequently used the nanomechanical mapping technique.

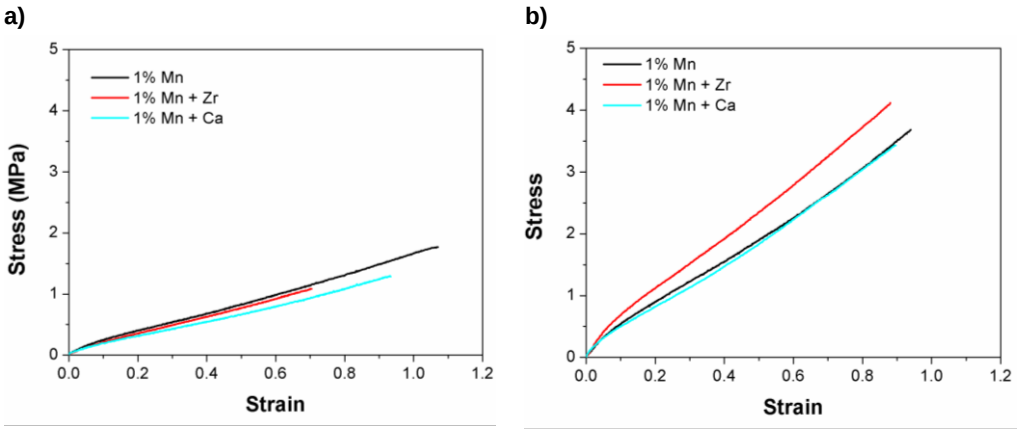

Figure 4-9: Stress- strain curves of dried films from acrylic / alkyd resin hybrid particles latex with 1 wt% of Mn-based catalyst and different secondary catalysts after a) 1 day and b) 8 days

Table 4-6: Tensile test results of dried films from acrylic / alkyd resin hybrid particles latex with 1 wt% of Mn-based catalyst and different secondary catalysts after a) 1 day and b) 8 days

	Young's modulus (MPa)	**Elongation at break**	**Stress at break (MPa)**	**Toughness x 10^6 (J/m^3)**
1% Mn - 1 day	2.7 ± 0.3	1.06 ± 0.05	1.77 ± 0.37	0.95 ± 0.17
1% Mn + Zr - 1 day	1.5 ± 0.2	0.71 ± 0.08	1.09 ± 0.12	0.39 ± 0.06
1% Mn + Ca - 1 day	1.5 ± 0.2	0.87 ± 0.03	1.17 ± 0.18	0.51 ± 0.09
1% Mn - 8 days	6.4 ± 0.5	0.94 ± 0.1	3.68 ± 0.44	1.72 ± 0.34
1% Mn + Zr - 8 days	9.0 ± 1.6	0.88 ± 0.01	4.10 ± 0.11	1.86 ± 0.06
1% Mn + Ca - 8 days	5.3 ± 0.2	0.9 ± 0.14	3.44 ± 0.62	1.6 ± 0.5

4.3.3.2 Evolution of curing of the alkyd resin with the secondary catalysts

Figure 4-10 presents the effect of the presence of secondary catalyst on the hardness of the soft areas (considered to be proportional to the extent of alkyd curing) at different positions in the film. It can be seen that near the air-film interface the presence of secondary catalyst accelerates curing. Due to the presence of acrylic polymer that facilitates oxygen diffusion and the proximity to the air-film interface, it is unlikely that there was a lack of oxygen in this region, meaning that the observed effect of the secondary catalyst was not due to the enhancement of the oxygen diffusion. This is supported by the fact that the effect of secondary catalysts in the center of the film and near the substrate was relatively modest, although clearly visible. One of the roles attributed to secondary catalysts is to be a sacrificial compound that reacts with carboxylic groups in the film, which are considered as poisons for the primary catalyst.[47] The data available does not allow us to reach a conclusion, although the fact that the ultimate curing level did not increase (in fact it decreased for Ca) in the presence of the secondary catalyst does not agree with this hypothesis.

A surprising result in Figure 4-10 is that Ca, which initially gave the fastest curing, led to lower curing after 8 days and gave the most heterogeneous film in terms of degree of curing at different points in the film. A possible explanation is that the secondary catalysts accelerate the process of curing as has been observed in the curing of pure alkyd films[4] and the fast initial curing reduced oxygen diffusion towards the interior of the film.

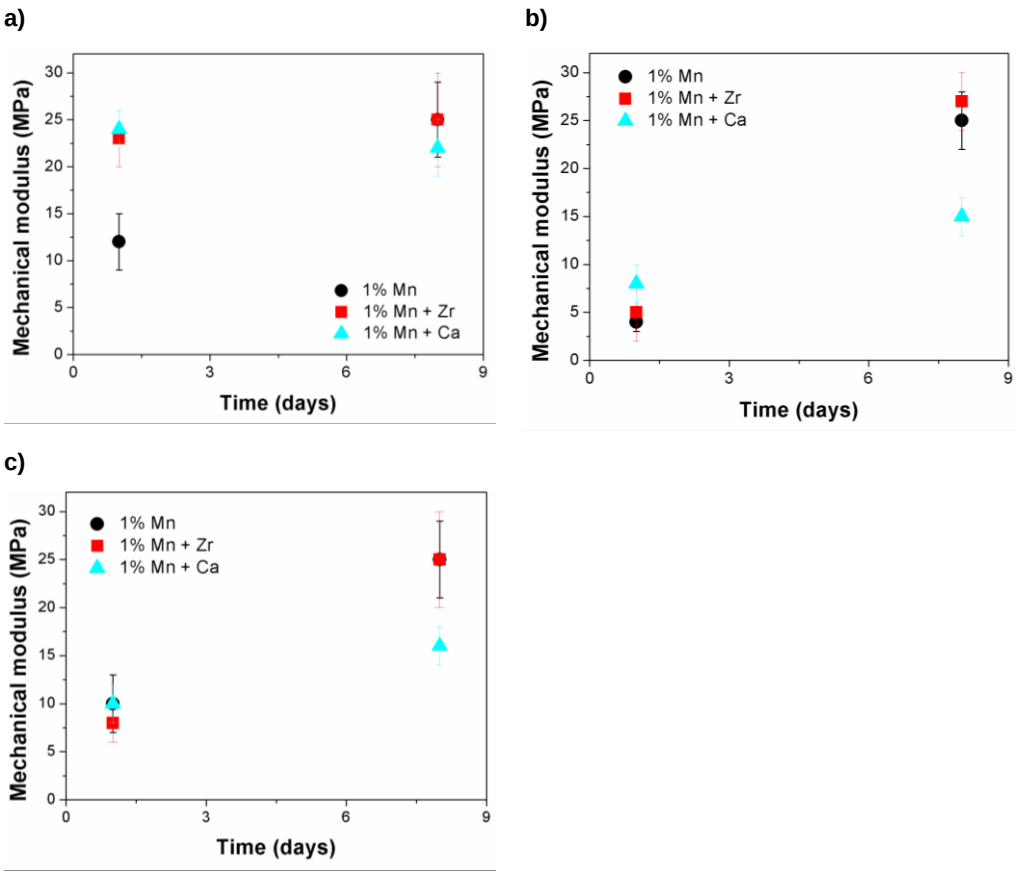

Figure 4-10: Evolution of the mechanical modulus of the soft areas of the films cured at 23ºC and 55% relative humidity with time a) close to air-film interface, b) in the center and c) close to the film-substrate

4.3.3.3 Film morphology evolution with the secondary catalysts

Figures 4-11 and 4-12 present the nanomechanical maps for the films containing 1 wt% Mn, 1 wt% Mn + Zr and 1 wt% Mn + Ca after 1 and 8 days of curing, respectively. As previously explained, after 1 day, the alkyd in the samples prepared with only Mn was not cured and therefore the alkyd was either spread over the sample (Figures 4-11 a and b) or removed (Figure 4-11c). Figure 4-11 shows that the differences in curing rate affected the film morphology. Near the surface where the rate of curing was fast, the segregation was moderate because the cured alkyd was too hard to migrate. Phase separation was stronger near the substrate, in agreement with a slower curing. The strongest segregation was observed in the center of the film where the curing was slowest.

Figure 4-12 presents the nanomechanical maps after 8 days of curing. Comparison with Figure 4-11 (1 day of curing) shows that segregation was stronger, namely, the alkyd resin and the acrylic polymer separated further during this period of time. This occurred also near the surface of the film, where for Mn + Zr and Mn + Ca a high degree of curing was achieved in 1 day and only a slight increase occurred thereafter (Figure 4-10). The stronger time effect was observed in the center and near the substrate for Mn + Zr, which likely is the combination of a low initial curing that facilitates the coalescence of the domains of alkyd resin, and a high final curing that provoked a strong segregation of the cured alkyd and the acrylic polymer. The segregation was lower for Ca because on the one hand the initial rate of curing was high, limiting the segregation of the uncured alkyd, and on the other the final degree of curing was low allowing some compatibility of the alkyd and the acrylic polymer.

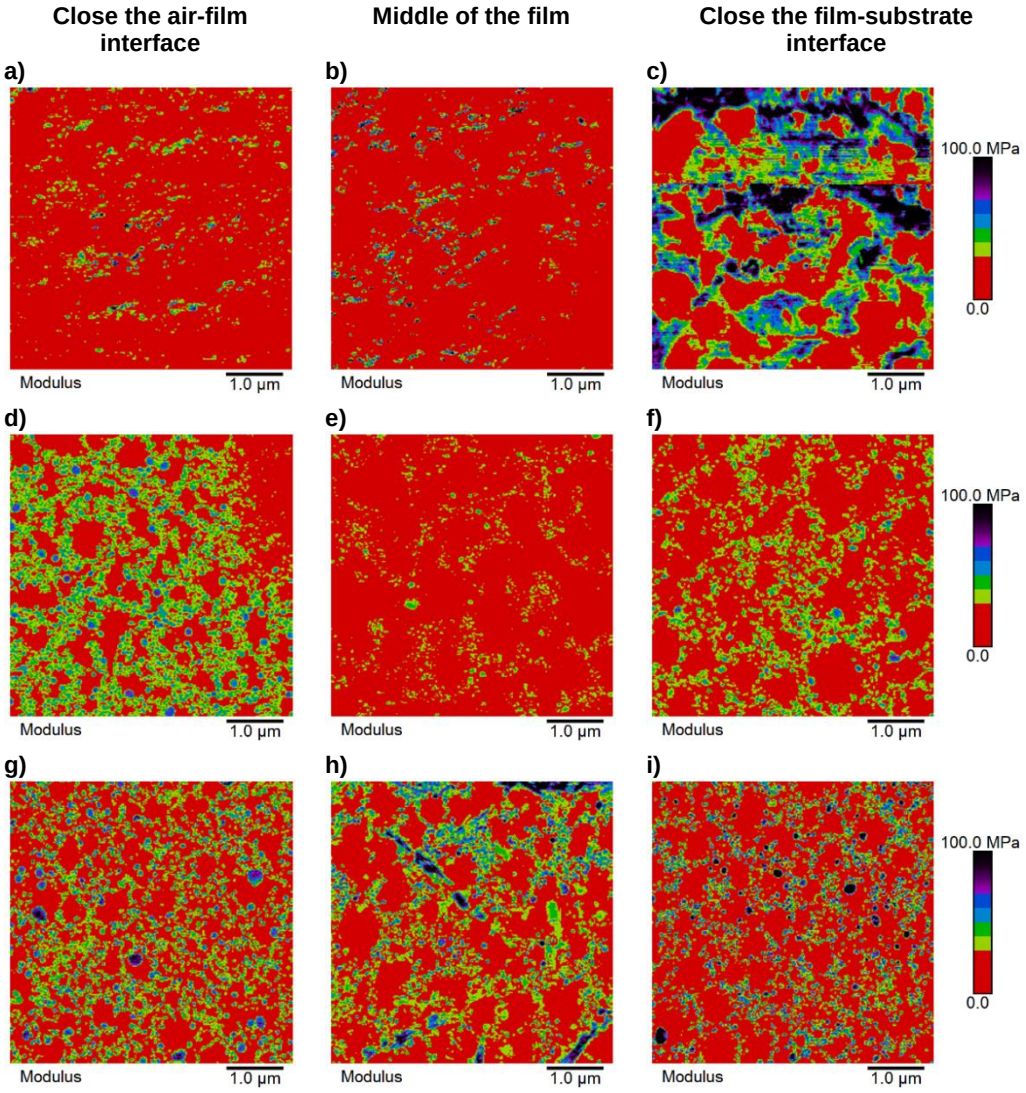

Figure 4-11: Mechanical maps for the films with 1% Mn-based catalyst solely abc),and Zr-based catalyst def) and Ca-based catalyst ghi) after 1 day of curing at 23ºC and 55% relative humidity. For each system, the left image was performed close to air-film interface, the second in the center of the film and the right image close to the film-substrate interface

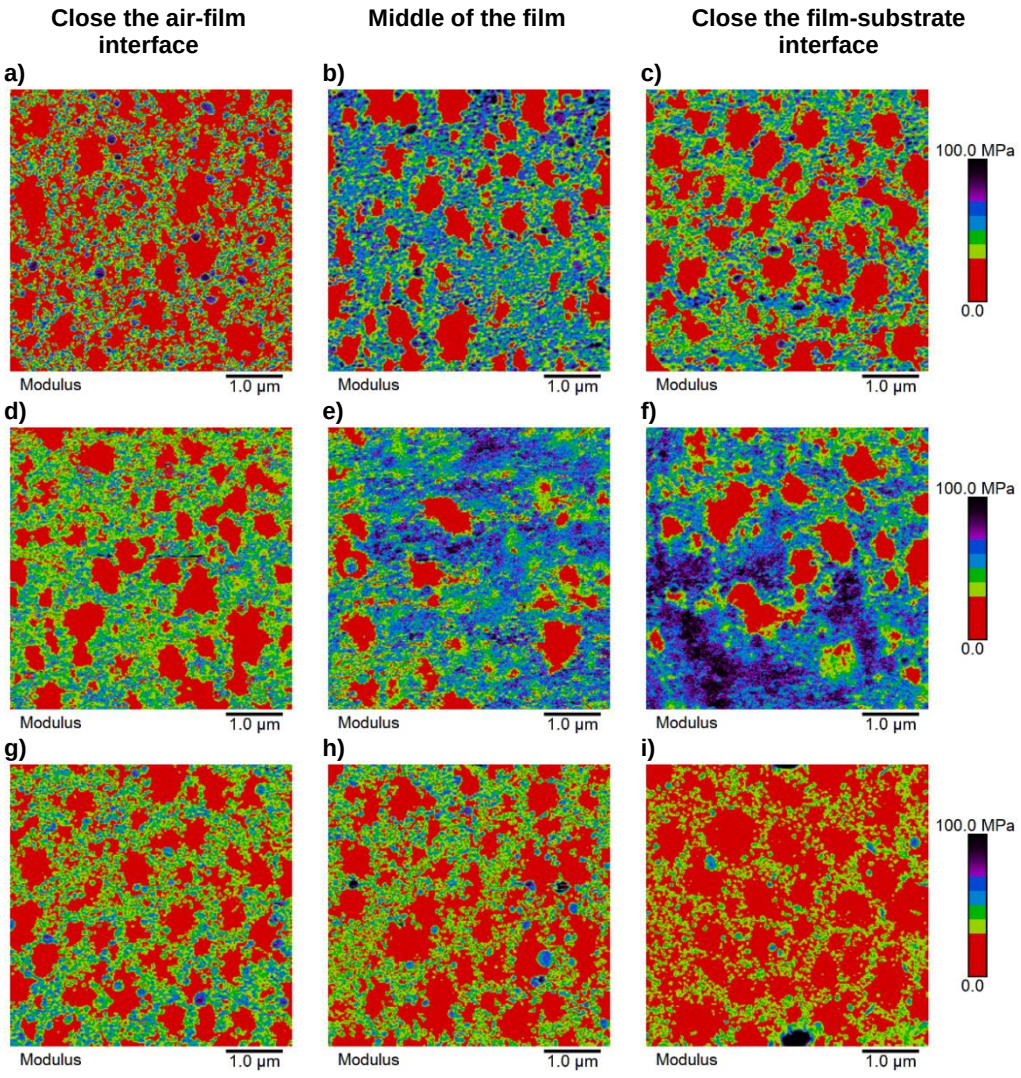

Figure 4-12: Mechanical maps for the films with 1% Mn-based catalyst solely abc),and Zr-based catalyst def) and Ca-based catalyst ghi) after 8 days of curing at 23ºC and 55% relative humidity. For each system, the left image was performed close to air-film interface, the second in the center of the film and the right image close to the film-substrate interface

4.3.4 Discussion

The results presented above show that the formation of acrylic-alkyd hybrid films differs from that of the widely studied pure alkyd films. After water evaporation, which occurs in a short period of time, the evolution of the film is determined by the interplay between the curing of the alkyd resin and phase separation/migration, two processes that occur in parallel.

Curing of the alkyd follows the classical oxidative crosslinking scheme (see Figure 4-1) and is limited by oxygen availability. In the alkyd phase, oxygen diffusion decreased with curing. Therefore, the surface cures faster than the interior of the film. However, the effect of curing on the overall oxygen diffusion is less than in the pure alkyd films as oxygen also diffuses through the acrylic polymer and this contribution is roughly constant over time. Consequently, although the differences in crosslinking through the film are significant at short times (1 day), over longer times (3-8 days) a rather homogeneous degree of crosslinking is achieved. Secondary catalysts accelerate curing and the initial effect seems to be stronger for Ca than for Zr. A fast initial rate of curing reduces the extent of curing of the interior of the film at long times.

Acrylic polymer and alkyd resin separate over time. The results available show that the alkyd migrates, forming aggregates. The reason is the low viscosity of the alkyd (and the fact that it has the lowest volume ratio as a fraction of the alkyd was grafted on the acrylic polymer). Curing has several effects on the development of the film morphology. On one hand, the compatibility between the alkyd and the acrylic polymer decreases with curing, namely, curing enhances phase separation. On the other, curing reduces the movement of the alkyd making it

more difficult to form aggregates. The combination of these two effects leads to a situation where the maximum segregation is achieved by delayed but strong curing, which allows a substantial movement of the uncured alkyd in short times, and a final segregation upon curing.

4.4 Conclusions

In this work, the curing process of alkyd resin and its effect on the morphology of films cast from acrylic/alkyd hybrid particles latex has been studied using an AFM based nanomechanical mapping technique. This allowed us to probe both the development of the curing of the alkyd phase as well as the phase separation between the two polymer phases with time. It was shown that as for conventional alkyd based coatings, curing of the alkyd was stronger at the oxygen rich air-film interface at the early stages of curing. However, unlike conventional alkyd resins, which were shown to develop a curing front that inhibited curing of the resin on the interior of the film, films from hybrid particles displayed homogeneous curing at long times. This was due to the presence of acrylic domains, which aided oxygen diffusion and facilitated the curing process. It was shown that the rate and extent of curing, which is primarily controlled by the concentration and type of catalyst used, has a substantial effect on the film morphology. Slow curing leads to extensive phase migration of the alkyd in the uncured state, leading to the development of large, aggregated domains of the two polymer phases. Due to the partial miscibility of the uncured alkyd resin with the acrylic phase, as curing progresses phase separation is increasingly favored, leading to formation of larger alkyd domains at long

times. These results highlight the importance of the curing process on the development of morphology of the film and consequently on the mechanical strength.

4.5 References

(1) Lambourne, R.; Strivens, T. A. *Paint and Surface Coatings - Theory and Practice (2nd Edition)*; Woodhead Pub, 1999.

(2) Paul; S. Surface coatings. Science and technology, 1985.

(3) Z.W. Wicks, F.N. Jones, S.P. Pappas, D. A. W. *Organic Coatings: Science and Technology*; 2007.

(4) Mallégol, J.; Barry, A. M.; Ciampi, E.; Glover, P. M.; McDonald, P. J.; Keddie, J. L.; Wallin, M.; Motiejauskaite, A.; Weissenborn, P. K. Influence of drier combination on through-drying in waterborne alkyd emulsion coatings observed with magnetic resonance profiling *J. Coatings Technol.* **2002**, *74*, 113–124.

(5) Goikoetxea, M.; Reyes, Y.; De Las Heras Alarcón, C. M.; Minari, R. J.; Beristain, I.; Paulis, M.; Barandiaran, M. J.; Keddie, J. L.; Asua, J. M. Transformation of waterborne hybrid polymer particles into films: Morphology development and modeling *Polymer* **2012**, *53*, 1098–1108.

(6) Wu, X. Q.; Schork, F. J.; Gooch, J. W. Hybrid miniemulsion polymerization of acrylic/alkyd systems and characterization of the resulting polymers *J. Polym. Sci. Part A Polym. Chem.* **1999**, *37*, 4159–4168.

(7) Nabuurs, T.; Baijards, R. A.; German, A. L. Alkyd-acrylic hybrid systems for use as binders in waterborne paints *Prog. Org. Coatings* **1996**, *27*, 163–172.

(8) Van Hamersveld, E. M. .; Van Es, J. J. G. .; German, A. .; Cuperus, F. .; Weissenborn, P.; Hellgren, A.-C. Oil-acrylic hybrid latexes as binders for waterborne coatings *Prog. Org. Coatings* **1999**, *35*, 235–246.

(9) Goikoetxea, M.; Minari, R. J.; Beristain, I.; Paulis, M.; Barandiaran, M. J.; Asua, J. M.

Polymerization kinetics and microstructure of waterborne acrylic/alkyd nanocomposites synthesized by miniemulsion *J. Polym. Sci. Part A Polym. Chem.* **2009**, *47*, 4871–4885.

(10) Heiskanen, N.; Jämsä, S.; Paajanen, L.; Koskimies, S. Synthesis and performance of alkyd-acrylic hybrid binders *Prog. Org. Coatings* **2010**, *67*, 329–338.

(11) Moreno, M.; Miranda, J. I.; Goikoetxea, M.; Barandiaran, M. J. Sustainable polymer latexes based on linoleic acid for coatings applications *Prog. Org. Coatings* **2014**, *77*, 1709–1714.

(12) Elrebii, M.; Kamoun, A.; Boufi, S. Waterborne hybrid alkyd–acrylic dispersion: Optimization of the composition using mixture experimental designs *Prog. Org. Coatings* **2015**, *87*, 222–231.

(13) Udagama, R.; de las Heras Alarcón, C.; Keddie, J. L.; Tsavalas, J. G.; Bourgeat-Lami, E.; McKenna, T. F. L. Acrylic-Alkyd Hybrids: Secondary Nucleation, Particle Morphology, and Limiting Conversions *Macromol. React. Eng.* **2014**, *8*, 622–638.

(14) Colombini, D.; Jowkar-Deriss, M.; Karlsson, O. J.; Maurer, F. H. J. Direct and Reverse Mechanical Modeling of an Alkyd Acrylic Hybrid System: A Morphological Study *Macromolecules* **2004**, *37*, 2596–2602.

(15) Tsavalas, J. G.; Luo, Y.; Schork, F. J. Grafting mechanisms in hybrid miniemulsion polymerization *J. Appl. Polym. Sci.* **2003**, *87*, 1825–1836.

(16) Schuler, B.; Baumstark, R.; Kirsch, S.; Pfau, A.; Sandor, M.; Zosel, A. Structure and properties of multiphase particles and their impact on the performance of architectural coatings *Prog. Org. Coatings* **2000**, *40*, 139–150.

(17) Hagen, R.; Salmén, L.; Karlsson, O.; Wesslén, B. Viscoelastic properties and film morphology of heterogeneous styrene-butadiene latexes *J. Appl. Polym. Sci.* **1996**, *62*, 1067–1078.

(18) Domingues Dos Santos, F.; Fabre, P.; Drujon, X.; Meunier, G.; Leibler, L. Films from soft-core/hard-shell hydrophobic latexes: Structure and thermomechanical properties *J. Polym. Sci. Part B Polym. Phys.* **2000**, *38*, 2989–3000.

(19) Heuts, M. P. J.; le Febre, R. A.; van Hilst, J. L. M.; Overbeek, G. C. Influence of Morphology on Film Formation of Acrylic Dispersions *Film Form. Waterborne Coatings* **1996**, 271–285.

(20) Limousin, E.; Ballard, N.; Asua, J. M. The influence of particle morphology on the structure and mechanical properties of films cast from hybrid latexes *Prog. Org. Coatings* **2019**, *129*, 69–76.

(21) Erich, S. J. F.; van der Ven, L. G. J.; Huinink, H. P.; Pel, L.; Kopinga, K. Curing Processes in Solvent-Borne Alkyd Coatings with Different Drier Combinations *J. Phys. Chem. B* **2006**, *110*, 8166–8170.

(22) Soucek, M. D.; Khattab, T.; Wu, J. Review of autoxidation and driers *Prog. Org. Coatings* **2012**, *73*, 435–454.

(23) Dubrulle, L.; Lebeuf, R.; Thomas, L.; Fressancourt-Collinet, M.; Nardello-Rataj, V. Catalytic activity of primary and secondary driers towards the oxidation and hydroperoxide decomposition steps for the chemical drying of alkyd resin *Prog. Org. Coatings* **2017**, *104*, 141–151.

(24) Okan Oyman, Z.; Ming, W.; Van der Linde, R.; Oyman, Z. O.; Ming, W.; Van der Linde, R. Oxidation of model compound emulsions for alkyd paints under the influence of cobalt drier *Prog. Org. Coatings* **2003**, *48*, 80–91.

(25) Lison, D.; De Boeck, M.; Verougstraete, V.; Kirsch-Volders, M. Update on the genotoxicity and carcinogenicity of cobalt compounds. *Occup. Environ. Med.* **2001**, *58*, 619–625.

(26) Bucher, J. R.; Hailey, J. R.; Roycroft, J. R.; Haseman, J. K.; Sills, R. C.; Grumbein, S. L.; Mellick, P. W.; Chou, B. J. Inhalation toxicity and carcinogenicity studies of cobalt sulfate *Toxicol. Sci.* **1999**, *49*, 56–67.

(27) Liu, Z.; Kooijman, H.; Spek, A. L.; Bouwman, E. New manganese-based catalyst systems for alkyd paint drying *Prog. Org. Coatings* **2007**, *60*, 343–349.

(28) Bouwman, E.; Van Gorkum, R. A study of new manganese complexes as potential driers for alkyd paints *J. Coatings Technol. Res.* **2007**, *4*, 491–503.

(29) Pirš, B.; Znoj, B.; Skale, S.; Zabret, J.; Godnjavec, J.; Venturini, P. Iron as an alternative drier for curing of high-solid alkyd coatings *J. Coatings Technol. Res.* **2015**, *12*, 965–974.

(30) van Gorkum, R.; Bouwman, E. The oxidative drying of alkyd paint catalysed by metal complexes *Coord. Chem. Rev.* **2005**, *249*, 1709–1728.

(31) Erich, S. J. F.; Laven, J.; Pel, L.; Huinink, H. P.; Kopinga, K. Dynamics of cross linking

fronts in alkyd coatings *Appl. Phys. Lett.* **2005**, *86*, 1–3.

(32) Erich, S. J. F.; Gezici-Koç, Ö.; Michel, M. E. B.; Thomas, C. A. A. M.; van der Ven, L. G. J.; Huinink, H. P.; Flapper, J.; Duivenvoorde, F. L.; Adan, O. C. G. The influence of calcium and zirconium based secondary driers on drying solvent borne alkyd coatings *Polymer* **2017**, *121*, 262–273.

(33) Mallégol, J.; Lemaire, J.; Gardette, J.-L. Drier influence on the curing of linseed oil *Prog. Org. Coatings* **2000**, *39*, 107–113.

(34) Derjaguin, B. V; Muller, V. M.; Toporov, Y. . Effect of contact deformations on the adhesion of particles *J. Colloid Interface Sci.* **1975**, *53*, 314–326.

(35) Martínez-Tong, D. E.; Najar, A. S.; Soccio, M.; Nogales, A.; Bitinis, N.; López-Manchado, M. A.; Ezquerra, T. A. Quantitative mapping of mechanical properties in polylactic acid/natural rubber/organoclay bionanocomposites as revealed by nanoindentation with atomic force microscopy *Compos. Sci. Technol.* **2014**, *104*, 34–39.

(36) Lorenzoni, M.; Evangelio, L.; Verhaeghe, S.; Nicolet, C.; Navarro, C.; Pérez-Murano, F. Assessing the Local Nanomechanical Properties of Self-Assembled Block Copolymer Thin Films by Peak Force Tapping *Langmuir* **2015**, *31*, 11630–11638.

(37) Wu, X.; Shi, S.; Yu, Z.; Russell, T. P.; Wang, D. AFM nanomechanical mapping and nanothermal analysis reveal enhanced crystallization at the surface of a semicrystalline polymer *Polymer* **2018**, *146*, 188–195.

(38) Sader, J. E.; Chon, J. W. M.; Mulvaney, P. Calibration of rectangular atomic force microscope cantilevers *Rev. Sci. Instrum.* **1999**, *70*, 3967.

(39) Imre, B.; Check, C.; Chartoff, R.; Vancso, J.; Gojzewski, H. Mechanical mapping and morphology across the length scales unveil structure-property relationships in polycaprolactone based polyurethanes *J. Polym. Sci. Part B Polym. Phys.* **2016**, *54*, 2298–2310.

(40) Gojzewski, H.; Obszarska, J.; Harlay, A.; Hempenius, M. A.; Vancso, G. J. Designer poly(urea-siloxane) microspheres with controlled modulus and size: Synthesis, morphology, and nanoscale stiffness by AFM *Polymer* **2018**, *150*, 289–300.

(41) Mark, J. *Polymer Data Handbook*; Oxford University Press, 1999.

(42) Bahrami, A.; Bailly, C.; Nysten, B. Spatial resolution and property contrast in local

mechanical mapping of polymer blends using AFM dynamic force spectroscopy *Polymer* **2019**, *165*, 180–190.

(43) Hudda, L.; Tsavalas, J. G.; Schork, F. J. Simulation studies on the origin of the limiting conversion phenomenon in hybrid miniemulsion polymerization *Polymer* **2005**, *46*, 993–1001.

(44) Paquet, D. A.; Jackson, C.; McMinn, J. H.; Hutchinson, R. A.; Beuermann, S. A Pulsed-Laser Study of Penultimate Copolymerization Propagation Kinetics for Methyl Methacrylate/ n -Butyl Acrylate *Ind. Eng. Chem. Res.* **2002**, *36*, 1103–1113.

(45) Gezici-Koç, Ö.; Thomas, C. A. A. M.; Michel, M. E. B.; Erich, S. J. F.; Huinink, H. P.; Flapper, J.; Duivenvoorde, F. L.; van der Ven, L. G. J.; Adan, O. C. G. In-depth study of drying solvent-borne alkyd coatings in presence of Mn- and Fe- based catalysts as cobalt alternatives *Mater. Today Commun.* **2016**, *7*, 22–31.

(46) Robb, W. L. Thin silicone membranes - Their permeation properties and some applications *Ann. N. Y. Acad. Sci.* **1968**, *146*, 119–137.

(47) Bieleman, J. *Additives for coatings*; Wiley-VCH, 2000.

Chapter 5. Evaluation of acrylic / alkyd resin particles latex as binders in paint applications

5.1 Introduction

Alkyd resin and acrylic polymers particle latexes are usually used as binders in architectural paints.[1,2] The addition of pigments and different additives affects film morphology compared to the corresponding latex films and thus the final properties of the paints.[3–5] The goal of this work was to study the effect of particle morphology of latexes used as binders in waterborne paints. For this, different acrylic / alkyd hybrid particles latexes were synthesized. The composition of the acrylic polymer and the hydrophobicity of the alkyd resin were varied in order to obtain different morphologies. Moreover, a blend of alkyd resin particles and acrylic polymer particles and a pure alkyd resin dispersion were used as binders in order to make comparisons. All the work was performed without the addition of catalyst in order to focus on the effect of the particle morphology. This work of this chapter was carried out at BASF SE in Ludwigshafen, Germany.

5.2 Experimental part

5.2.1 Materials

Technical grade monomers, methyl methacrylate (MMA, BASF), n-butyl acrylate (BA, BASF), n-butyl methacrylate (BMA, BASF), stearyl acrylate (SA, Sigma-Aldrich), acrylic acid (AA, BASF), were used without purification. 2,2'-Azobis(2-methylbutyronitrile) (V-59, Wako chemicals) and potassium persulfate (KPS, Fluka) were used as thermal initiators. Tert-butyl hydroperoxide (TBHP, BASF) and ascorbic acid (AsAc, BASF) were used as redox initiators. Dowfax 2A1 (alkyldiphenyloxide disulfonate, Dow Chemical Co.) was used as surfactant. $NaHCO_3$ (BASF, >99,5%) was used to reduce the miniemulsion viscosity. The alkyd resin SETAL 293 (hydrophobic) was supplied by Allnex and the alkyd emulsion WorléeSol E 150W (hydrophilic) was supplied by Worlée. Brochers®. Dysperbik 190 (BYK Chemie), titatium dioxide Tiona 595 (TiO_2, Cristal), Natrosol 250 HR (Brenntag) Rheovis Pu 1340 and Rhevois Pu 1191 (BASF) were used as received. Demineralized water was used throughout the work.

5.2.2 Polymerizations

Two series of hybrids were synthesized: Series S using a hydrophobic alkyd resin (Setal 293 supplied by Allnex) and Series W using a hydrophilic alkyd emulsion (WorléeSol E 150W supplied by Worlée). Table 5-1 gives the characteristics of the two alkyd resins. In each series, two (meth)acrylic systems (butyl acrylate/methyl methacrylate (BA/MMA: 50/50) and butyl methacrylate(BMA)/butyl acrylate (BMA/BA: 85/15)) were used. The alkyd resins Setal 293 and

WorléeSol E 150W presented different acid values (11 and 30 mg_{KOH}/g respectively). The acid value of the rest of the formulation was adjusted in order to work under the same conditions. In Series W, no acrylic acid (AA) was used and the surfactant concentration was decreased. For the sake of comparison of film morphologies, a blend was made from an all-acrylic latex and the alkyd emulsion WorléeSol E 150W in a 50/50 weight ratio. The acrylic latex (R1) was made from MMA/BA (50/50 wt/wt). The different systems studied are listed in Table 5-2. The polymerization strategies present differences from the one presented in Chapter 4 so they are described in the following paragraph.

Table 5-1: Characteristics of the alkyd resins

	Setal 293	**WorléeSol E 150W**
Solids content (%)	100	40
Particle size (nm)	/	40
Iodine value (g/100g)	106	40
Acid value (mg_{KOH}/g)	11	30
Mn (kg/mol)	2.5	3
Mw (kg/mol)	11.7	111

Table 5-2: Compositions of the latexes

Series	Samples	Alkyd resin	Monomer system	Dowfax (% of active matter, wbop)
S	**S1**	Setal 293	MMA/BA/AA:49.5/49.5/1	2.7
S	**S2**	Setal 293	BMA/BA/AA:84.5/14.5/1	2.7
W	**W1**	WorléeSol E 150W	MMA/BA:50/50	1
W	**W2**	WorléeSol E 150W	BMA/BA/:85/15	1
/	**R1**	/	MMA/BA:50/50	1

38 wt % solids content miniemulsions were prepared as follows. First, the organic phase was prepared by dissolution of SA (4 wbm%) and Setal 293 (when used) into the monomer mixture. Then, the organic phase was poured into an aqueous solution of Dowfax 2A-1 (2.7 wbop%, of active surfactant) and NaHCO3 (0.020M) under magnetic stirring at 700 rpm to create an emulsion. When WoorléeSol E 150W was used, it was dispersed in the water phase. The resulting emulsion was sonicated with a Hielscher UP400S sonicator for 10 minutes at an amplitude of 70% and a duty cycle of 80%. During sonication, the flask was immersed in an ice bath to avoid overheating. Polymerization was carried out in batch in a 2-L glass reactor equipped with a reflux condenser, a stainless-steel anchor type stirrer, a feeding inlet, a Pt-100 probe and nitrogen inlet. A solution of KPS (1.6 wbm%) in 15% of the total amount of water was fed to the reactor for 1h and then the system was left to react for 3 hours in batch at 70 °C. The latexes obtained were post-polymerized with TBHP and Ascorbic acid (AsAc) that were fed separately for 90 min with a molar ratio of 100/25/12.5 (residual monomer/oxidant/reductor).

Finally, the reaction was maintained in batch for one hour. The recipes for the reactions are given in Table 5-3.

A 41% solids content MMA/BA (50/50 wt/wt) latex, R1, was synthesized by emulsion polymerization as follows. An anionically stabilized polystyrene seed (with a particle size of 30 nm) was charged with 25% of the total amount of water into a 2-L glass reactor equipped with a reflux condenser, a stainless-steel anchor type stirrer, a feeding inlet and a Pt-100. The pre-emulsion and a solution of KPS (7 wt%) were fed separately into the reactor for 3 hours. After half an hour of batch reaction, TBHP and AsAc were fed separately for an hour. The reaction temperature was 70 °C. The recipe of the reaction is given in Table 5-3. For the sake of comparison, the acrylic latex was blended with the alkyd emulsion WorléeSol E 150W in a polymer ratio 1:1. In order to make the composition of the blend equal to the latex W1, 0.5 wbop% of Dowfax 2A-1 was added to the blend. The formulation of the blend is given in Table 5-4.

Table 5-3: Formulations of the polymerizations

Reaction	S1	S2	W1	W2	R1
Water (g)	495.5	495.5	184.9	184.9	546
Seed (g)	-	-	-	-	17.34
MMA (g)	99.5	-	101.8	-	220
BA (g)	99.5	29.9	102	30.5	220
BMA (g)	-	169	-	173	-
SA (g)	7.96	7.96	8.14	8.14	-
AA (g)	2	2	-	-	-
Setal 293 (g)	209	209	-	-	-
WorléeSol E 150W[a] (g)	-	-	529.07	529.07	-
$NaHCO_3$ (g)	1.29	1.29	1.41	1.41	-
Dowfax 2A-1[b] (g)	25.08	25.08	9.41	9.41	9.78
KPS (g)	3.34	3.34	3.42	3.42	0.88
TBHP[c]* (g)	12.11	2.2	14	5.6	6.6
AsAc* (g)	1.19	0.2	1.3	0.54	1.10
Water (g)*	166.7	117.6	164.7	173.9	7.3

*during post-polymerization
[a] 40 wt% in water
[b] 45 wt% in water
[c] 10 wt% in water

Table 5-4: Formulation of the blend

Blend	R1 (g)	WorléeSol E 150W[a] (g)	Dowfax 2A-1[b] (g)
B1	50	50	0.44

[a] 40 wt% in water
[b] 45 wt% in water

5.2.3 Characterizations

Droplet size was measured by dynamic light scattering using a Microtrac Nanotrac devise. The particle size of the final latexes were measured by both dynamic light scattering using a Malvern Zetaziser and hydrodynamic chromatography (HDC). Residual monomers were measured by gas chromatography. Solids content of the latexes was measured using a thermobalance. Glass transition temperature, T_g, of the acrylic polymer was measured by differential scanning calorimetry (DSC). The gel content of the polymers was determined by Soxhlet extraction. The molecular weight distribution and the mass fraction of alkyd grafted to the acrylic polymer (resin degree of grafting: RDG) in the sol fraction were determined by gel permeation chromatography (GPC). The double bond content of the resin in the particles was measured by iodine value titration. Particles morphology were determined by transmission electron microscopy (TEM).The samples were stained with OsO_4 before analysis. The cross-section topography was measured by atomic force microscopy. The mechanical properties of the films cast from the synthesized latexes were determined by tensile tests. A detailed description of the characterization methods is provided in Appendix I.

5.3 Results and discussion

5.3.1 Characterization and performance of acrylic / alkyd resin hybrid particles latexes

Hybrid particles containing acrylic and alkyd phases were synthesized by miniemulsion polymerization. The characteristics of the synthesized latexes are summarized in Table 5-5. Post-polymerization was needed for all latexes due to the low conversion obtained. Indeed, low conversion is common for acrylic / alkyd hybrid latexes due to the fact that the alkyd acts as a radical sink.[6–9] Residual monomers were higher for the acrylic formulation MMA/BA (50/50 wt/wt) than BMA/BA (85/15 wt/wt). It has to be noted that a large fraction of residual monomers corresponded to BA in all cases, because of the lower reactivity ratio of BA. The higher concentration of BA in S1 and W1 with respect to S2 and W2 had also an effect on the conversion at the end of the regular polymerization. The higher the concentration of BA the lower the conversion likely due to the higher reactivity of the acrylate radicals to react with the double bonds of the alkyd that act as a radical sink. After post-polymerization, the residual monomers were still above industrial requirements (< 100 ppm) but were at sufficient low levels to continue the study. Larger particle sizes are obtained by DLS than HDC. HDC chromatograms showed the presence of a small fraction of particle with a diameter around 500 nm. This second population resulted in higher value given by DLS as this method gives the z-average diameter which is weighted towards larger particle sizes In Series W, the preformed alkyd particles were used as seed for the (meth)acrylic monomers. This led to higher number of final particles with lower particle size.

Table 5-6 presents the molecular weights and degree of grafting of the alkyd resin on acrylic chains (DG) before and after post-polymerization; the gel content and fraction of reacted resin doubled bonds on the final polymer; and the T_g of the acrylic polymer. An important characteristic is the number of reacted resin double bonds of the resin (RDB), because double bonds are needed for cross-linking. Table 5-6 shows that the fraction of reacted double bonds was relatively low in all cases (< 16%) leaving most of the double bonds for cross-linking. The molecular weight distributions were broad because they include the relatively high molecular weight of the acrylic polymer and the low molecular weight of the alkyd resin. Molecular weights of the soluble polymer of Series W were higher than in Series S. This was linked to the difference in particle size: smaller particles have higher molecular weights. Moreover, for the same number of grafting events, a higher molecular weight polymer will enhance gel formation. The increase of gel led to a decrease of molecular weight of the soluble polymer after post-polymerization in Series W due to more likely incorporation of long chains into the gel. The grafted acrylic/alkyd hybrid that was contained in the gel hindered the calculation of the degree of grafting (DG). When low grafting was measured, the T_g of the acrylic phase was around 10-15°C as expected. However, the T_g of W2 was lower due to the incorporation of the low T_g alkyd polymer to the acrylic chains.

Table 5-5: Characteristics of the synthesized latexes

Latex	d_d* (nm)	d_p* (nm)	d_p** (nm)	Residual monomers before post-polymerization (ppm) (conversion (%))	Residual monomers after post-polymerization (ppm)	Solids content (%)
S1	185	215	139.9	7600 (93.2)	2400	38.09
S2	229	234	133	1360 (99.1)	630	40.9
W1	115	170	88.3	8000 (91.3)	1600	36.55
W2	103	187	88.5	3400 (97.5)	680	36.49
R1	/	114	113.5	Not measured	1800	43.65

* measured by DLS
** measured by HDC

Table 5-6: Effect of particle morphology on the polymer architecture

	Before post-polymerization			After post-polymerization					
Latex	M_n (kg/mol)	M_w (kg/mol)	DG (%)	Gel (%)	M_n (kg/mol)	M_w (kg/mol)	DG (%)	RDB (%)	T_g (°C)
S1	2.6	120	7.9	0	2.6	130	8.4	1.9	12
S2	2.6	165	5.4	0	2.7	165	6	0.5	15
W1	4.5	320	*	39	3.6	190	*	11.1	15
W2	5.3	410	*	32	4.4	290	*	16.4	-4
R1	not measured	not measured	/	0	850.5	1710	/	/	22.7

* not measurable due to the high amount of gel

5.3.2 Particle morphology

Figure 5-1 shows the TEM images of the particle morphologies after post-polymerization. Samples were stained with vapors of OsO_4. With this staining, the alkyd resin will appear darker through reactions of the double bonds of the alkyd resin with the OsO_4.[10] Two hours of staining were sufficient to see a contrast between the two polymers for series S whereas four hours were necessary for Series W. The particle morphology of S1, using a hydrophobic alkyd, resulted in a core-shell morphology with a core of alkyd resin and a shell of acrylic polymer. For system S2, with a more hydrophobic acrylic polymer, a half-moon morphology was obtained. This result is in agreement with what may be expected for the equilibrium morphology when the shell component of a core-shell morphology is rendered more hydrophobic.[11] For Series W, the particle morphology of W1 was half-moon (shown by arrows) whereas W2 had a core-shell morphology with an alkyd-rich core and an acrylic rich shell. It has to be pointed out that the big particles looked darker due to their size and their morphology was not well-defined.

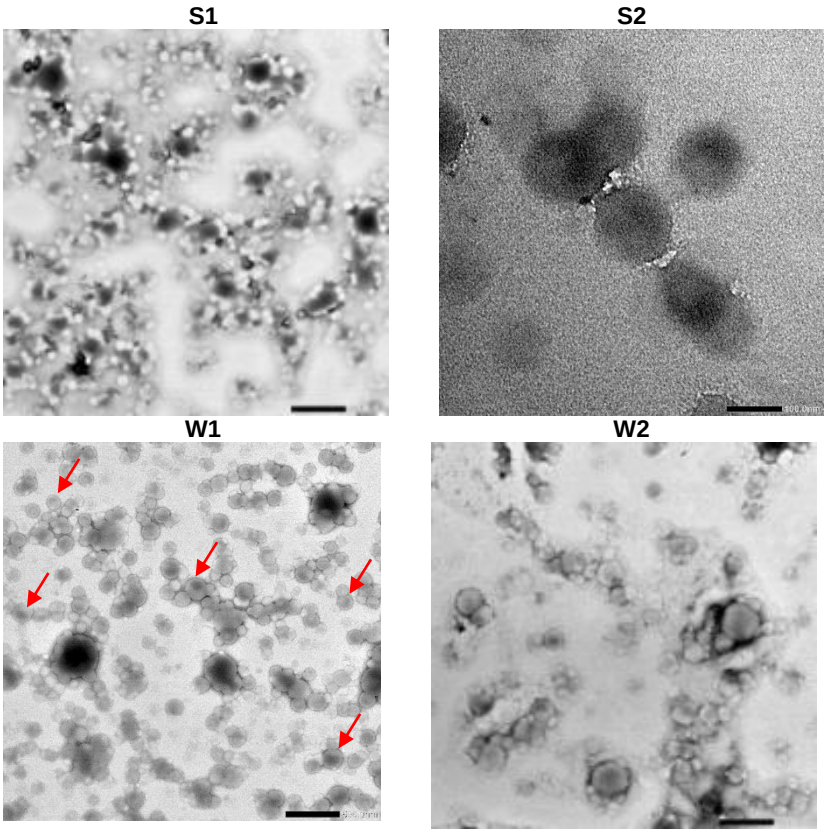

Figure 5-1: Particle morphology for the hybrid latexes, using the hydrophobic Setal 293 resin after post-polymerization (scale bar: 500 nm and 100 nm for S2)

5.3.3 Film morphology and properties

Figure 5-2 presents the AFM of cross-sections of the latex films cast a room temperature. Films were allowed to cure one week before the measurement. S1 and S2 presented a severe phase separation with alkyd domains with a diameter close to 1 µm due to the incompatibility between the alkyd resin and the acrylic polymer and the low grafting between them. The size of the alkyd aggregates seems to be bigger for S1 than for S2, which might be due to the lower interfacial tension between the acrylic polymer and the alkyd in S2. However, this conclusion should be taken with caution. For Series W, no major migration of the alkyd or acrylic rich domains was visible thanks to the higher compatibility between the phases through grafting. In W1, some aggregation of alkyd domains occurred due to the half-moon morphology of the particles. The structure of W2 was composed of a continuous phase of pure acrylic polymer and spherical domains composed of the pure alkyd and the grafted polymer in agreement with the initial core shell morphology. Figure 5-3 displays the AFM images of the cross section of the blend of acrylic particles with alkyd resin particles, B1. In this case a continuous acrylic phase can be seen with alkyd emulsion particles dispersed in it. The morphology was similar through all the film. Despite the difference of particles sizes between the two components of the blend, the alkyd particles presenting a particle size of 40 nm and the acrylic polymer of 113 nm, stratification of particles in layers did not occur.

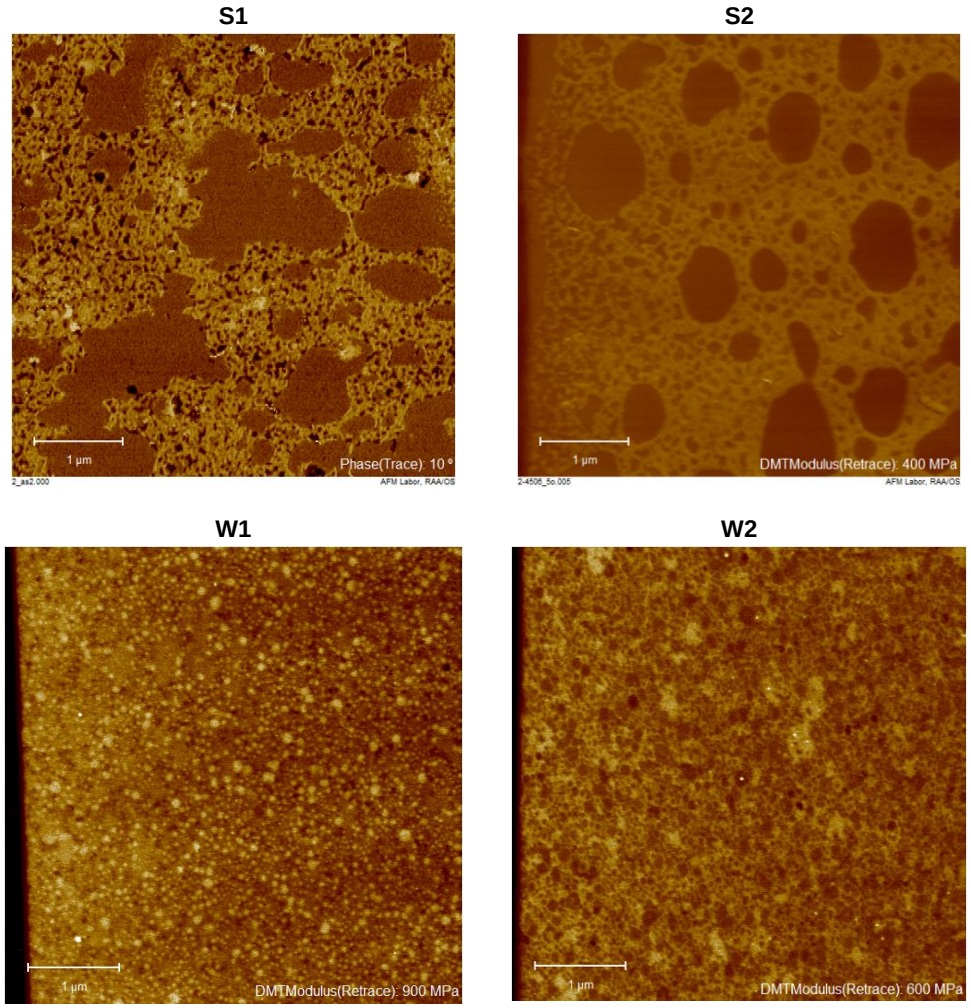

Figure 5-2: AFM DMT modulus images of the cross-sections latex films from the hybrid particles latexes. Dark regions correspond to the soft phase and bright region to the harder phase (scale bar: 1 µm, all images were done close to the air-film interface)

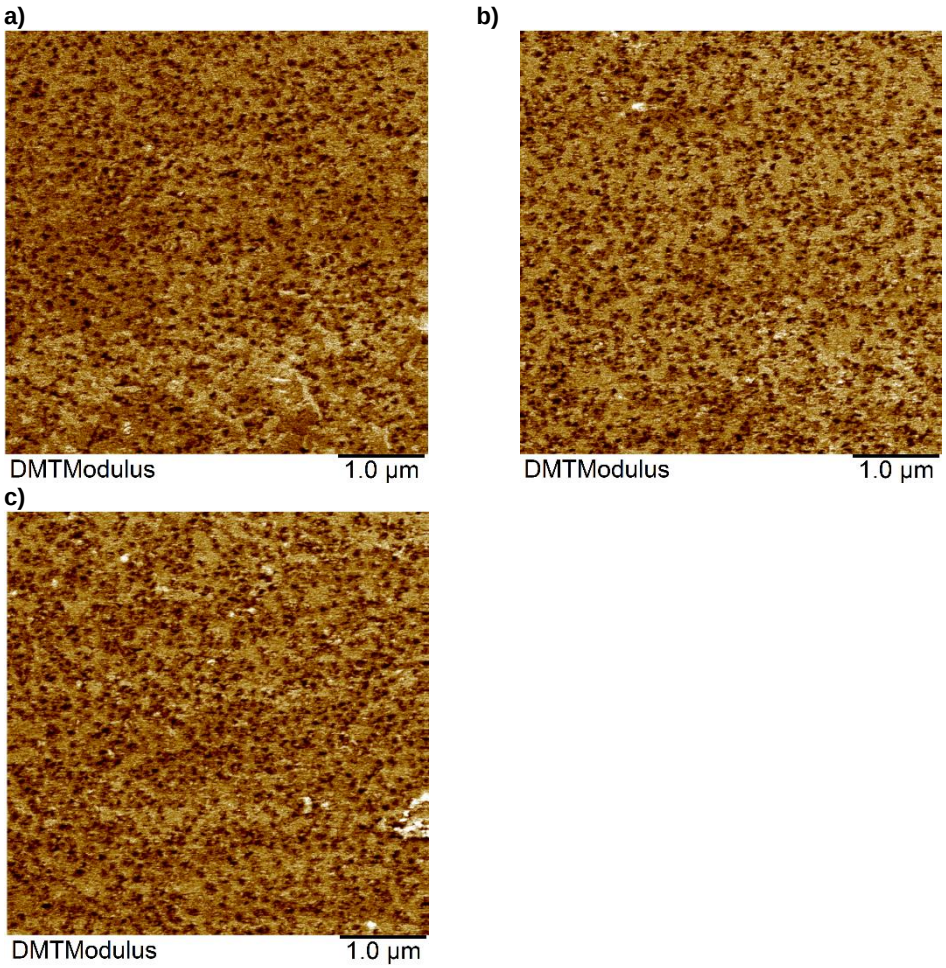

Figure 5-3: AFM DMT modulus images of the cross-section of the blend B1 a) close to air-film interface, b) close to the film-substrate and c) in the middle of the film (Dark regions correspond to the soft phase and bright region to the harder phase)

Figure 5-4 and Table 5-7 present the results of the tensile tests measurements of the latex films, performed after two weeks of curing at 23 ºC and 55% relative humidity. No measurements were performed for R1 because the casting temperature was close to the MFFT of the latex, the film was brittle and presented large cracks. It has to be pointed out that, in addition to their difference in hydrophobicity, the alkyd resins have different compositions, which would lead to different final properties. Indeed, films from Series S presented low Young's modulus compared to Series W. Moreover, S1 and S2 presented large difference in mechanical properties as S2 was tougher than S1. S1 presented larger domains of pure alkyd resins (Figure 5-2) which decreased the elongation at break. W1 and W2 presented similar toughness, but W2 had a lower stress at break and higher Young's modulus. Two features have to be taken in account to explain these results. First, W2 had a lower T_g than W1 (T_{gW1} = 15 ºC. T_{gW2} = -4 ºC, Table 5-6) which softened the film. Secondly, the acrylic polymer composed of MMA/BA in W1 gives a harder polymer than the one composed of BMA/BA in W2 due to the difference the difference of reactivity ratio between methacrylates and acrylates. As the methacrylates are consumed faster than the acrylates, a gradient of polymers is formed in the polymer chains and the rich-MMA part harden the system due to its high T_g (T_{gMMA} = 105 ºC) compared to BMA (T_{gBMA} = 32 ºC). The blend, B1, was more brittle (higher Young's modulus and lower elongation at break) than the hybrids and the alkyd resin alone as the film was composed of an acrylic continuous phase with alkyd resin particles. Also, this system was free of gel compared to the hybrid of Series W which led to higher stiffness of the film.

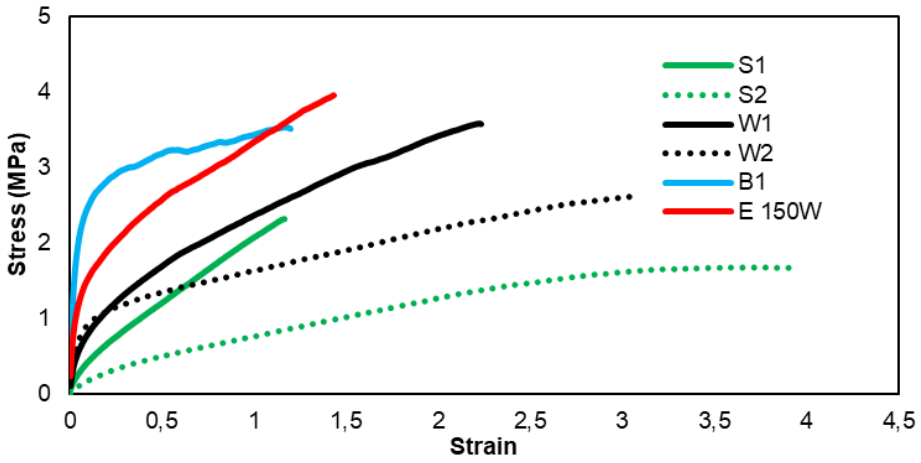

Figure 5-4: Stress-strain curves the films cast from the latexes at room temperature

Table 5-7: Tensile tests results of the films cast from the latexes at room temperature

	Young's modulus (MPa)	Elongation at break	Stress at break (MPa)	Toughness (MPa)
S1	4.9 ± 1.6	1.17 ± 0.17	2.32 ± 0.18	1.55 ± 0.32
S2	1.4 ± 0.3	3.92 ± 0.62	1.68 ± 0.27	4.49 ± 1.36
W1	12.2 ± 3.2	2.23 ± 0.25	3.59 ± 0.18	5.34 ± 1.1
W2	20.8 ± 2.8	3.06 ± 0.17	2.61 ± 0.15	5.76 ± 0.4
B1	64.92 ± 8.2	1.19 ± 0.32	3.52 ± 0.15	3.69 ± 0.72
E 150W	41.48 ± 4.1	1.43 ± 0.1	3.96 ± 0.23	4.03 ± 0.42

5.4 Incorporation of acrylic / alkyd resin hybrid as binders in paint formulations

The addition of pigments to the formulation of paints strongly affects the film morphology and properties.[3–5] Indeed, the pigments are dispersed into the polymer matrix and film formation is affected. Previous works showed that the binder composition (monomer system, presence of functional groups) has an effect on the dispersion of the pigment into the paints and consequently on the final morphology of the paints.[3,12] Also, the additives used (dispersing agent, defoamer and thickener) can affect the film morphology and properties.[13,14] Therefore, paint films can present a different behavior compared to the latex films and in the case of hybrid system the effect of the particle morphology can be hindered. In this part of the work, the effects of the use of hybrid particles as binders in paint formulation on paints properties were investigated.

5.4.1 Preparation of waterborne paints

Acrylic / alkyd resin hybrid latexes, the blend and the pure alkyd emulsion E 150W were used as binders in the preparation of glossy paints in a two steps process using the formulation in Table 5-9. First, the mill base (formulation in Table 5-8) was prepared by mixing the dispersant (Dispex CX 4231, BASF), rheology modifiers (Rheovis PU1 340 and Rheovis PU 1191, BASF), defoamer (Tego Foamex 810, Evonik) and water while stirring at about 400 rpm using a speed disperser blade (Disperlux). The pigment (Tiona 595) was added slowly at 200

rpm. Then the mixture was stirred for 20 min. Finally, the polymer latex, a rheology modifier and water were incorporated to the mill base and mixed in a speed mixer for 1 min 50 at 2350 rpm. Solids content of the latexes were previously increased to obtain final paints with a final solids content of 50% and the pH of the paints was increased to 8 to avoid coagulation during blending with the mill base. No paint was prepared with the pure acrylic latex (R1) due to coagulation during blending with the mill base. Paints were left for 24h before using. For the denomination of the paints, the letter P was added at the name of the corresponding latex used as binder in the paint.

Table 5-8: Mill base formulation

Compound	Product	Weight (g)
Water		40
Defoamer	Tego Foamex 810	6
Pigment dispersion	Dispex CX 4231 (30 wt%)	7,5
Ammonia	25 wt%	2
High sheer thickener	Rheovis PU 1340 (20 wt%)	14
Low sheer thickener	Rheovis PU 1191 (30 wt%)	2
TiO_2	Tiona 595 (dp= 0.25 µm)	230

Table 5-9: Paint formulations

	Solids content latex (%)	Weight binder (g)	Weight mill base (g)	Additional water (g)	Additional Rheovis PU 1191 (g)	Solids content paint (%)
PS1	40.8	120	54.3	4	1	50.2
PS2	40.9	119.6	54.3	4	0.6	50.2
PW1	40.9	119.6	54.3	4	0	50.2
PW2	40.15	121.7	54.3	4	0	50.1
PB1	40	121.5	54.3	4	0	50
PR1	/	/	54.3	/	/	/
PE150W	40	121.5	54.3	4	0	50

The pigment volume content (PVC) of paints is essentially the volume fraction of pigment in the total volume of solids in the paint calculated as

$$\boldsymbol{PVC}\ \% = \frac{\boldsymbol{volume\ of\ pigment}}{\boldsymbol{volume\ of\ binder + volume\ of\ pigment}} \times \mathbf{100} \qquad \textbf{(5-1)}$$

In paint technology, the terms gloss and matte refer to visual appearance of a finish with respect to its gloss level. Glossy paints reflect most light in the specular (mirror-like) direction and they provide a bright sheen when they are dried. Alkyd resins are used in glossy paints.[15,16] For gloss paints, low PVC has to be applied to prevent particles disrupting the

surface and so reducing the gloss of the film.[17] PVC below 20% is so typically used for gloss paints. In this study, the PVC of the formulated paints was 18%.

5.4.2 Characterizations of the paints

The morphology of the paints was analyzed by scanning electron microscopy using a Hitachi TM3030 scanning electron microscope. The mechanical properties of the polymer films were determined by tensile tests.

In term of visual appearance, gloss is one of the key features of paints. Gloss was measured using a glossmeter BYK micro-TRI-gloss meter. A glossmeter measures the specular reflection. The light intensity is registered over a small range of the reflection angle. The intensity is dependent on the material and the angle of illumination. In case of coatings, the amount of reflected light increases with the increase of the illumination angle. The remaining illuminated light penetrates the material and is absorbed or diffusely scattered dependent on the color. In order to obtain a clear differentiation over the complete measurement range from high gloss to matte, 3 different geometries, i.e. 3 different ranges, were defined: high gloss, semi-gloss, and low gloss which are respectively measured with the 20°, 60° and 85° geometry. Here, the gloss measurements of the paints were measured at 20º.

Water uptake of the paint films were measured, films from the paints were cast on PET film with a wet thickness of 500 µm. After drying for 4 days films were removed from the substrate and cut in a disk of 3 cm diameter. Cut films were let to dry at 23 °C and 55% of relative humidity for 10 additional days. Water uptake measurements were performed as for the latexes films for an immersion time of 24h.

Chemical resistance of the paints was measured: red beet, coffee, mustard, lipstick and FeO_2 were applied on the paint panels previously dried for two weeks for 30 minutes. Then the chemical were carefully removed with water and a clean paper cloth. The damages that the chemicals produced to the paint were measured by Lab color space. Five hours after removing the chemicals, the difference in color between the damaged paint and the clear paint was calculated with the formula:

$$\Delta E = \sqrt{(L_2^* - L_1^*)^2 + (a_2^* - a_1^*)^2 + (b_2^* - b_1^*)^2} \quad \textbf{(5-2)}$$

where ΔE is the measure of change in visual perception of two given colors, Lab^*_2 are the colors space of the damaged film and lab^*_1 the color space of the film before contact with the chemical. Then, the changes of colors can be evaluated following the Table I-2. For the hand cream resistance test, the damages were measured in terms of differences of gloss and pendulum hardness of the films.

Table 5-103: Guide table for the determination of changes in colors

ΔE	Perception
< 1	Not perceptible by human eyes
1 – 2	Perceptible through close observation
2 – 10	Perceptible at a glance
11 – 49	Colors are more similar than opposite
100	Colors are exact opposite

5.4.3 Film morphologies and properties of the paints

Figures 5-5 to 5-8 give the SEM images of the surfaces and fractures of paints films dried at 23 ºC and 55% of relative humidity for two weeks. PS1 was not homogeneous and the pigments appeared to segregate at the bottom of the film. However, pigments were homogenously present on the surface of the paint film. Paints from Series W presented a good pigment distribution into the film, which was in agreement with the latexes films morphologies. PB1 presented domains deprived of pigments through the entire film (Figure 5-8). PE 150W had a homogeneous film morphology due to homogeneous alkyd particles used as binder. Film morphology is not provided for PR1, the paint from the pure acrylic polymer, as it coagulated during paint preparation. This coagulation was due to an incompatibility between the acrylic polymer and the TiO_2. Therefore, latex S1 which has the acrylic polymer in its shell presented incompatibility also, compared to S2 that showed a hemispherical shape was homogeneous. For Series W, the hydrophilic resin was more accessible than the hydrophobic resin used in

Series S and the corresponding paints were more compatible with TiO_2. The incompatibility between the acrylic polymer and TiO_2 also explained the inhomogeneity of PB1.

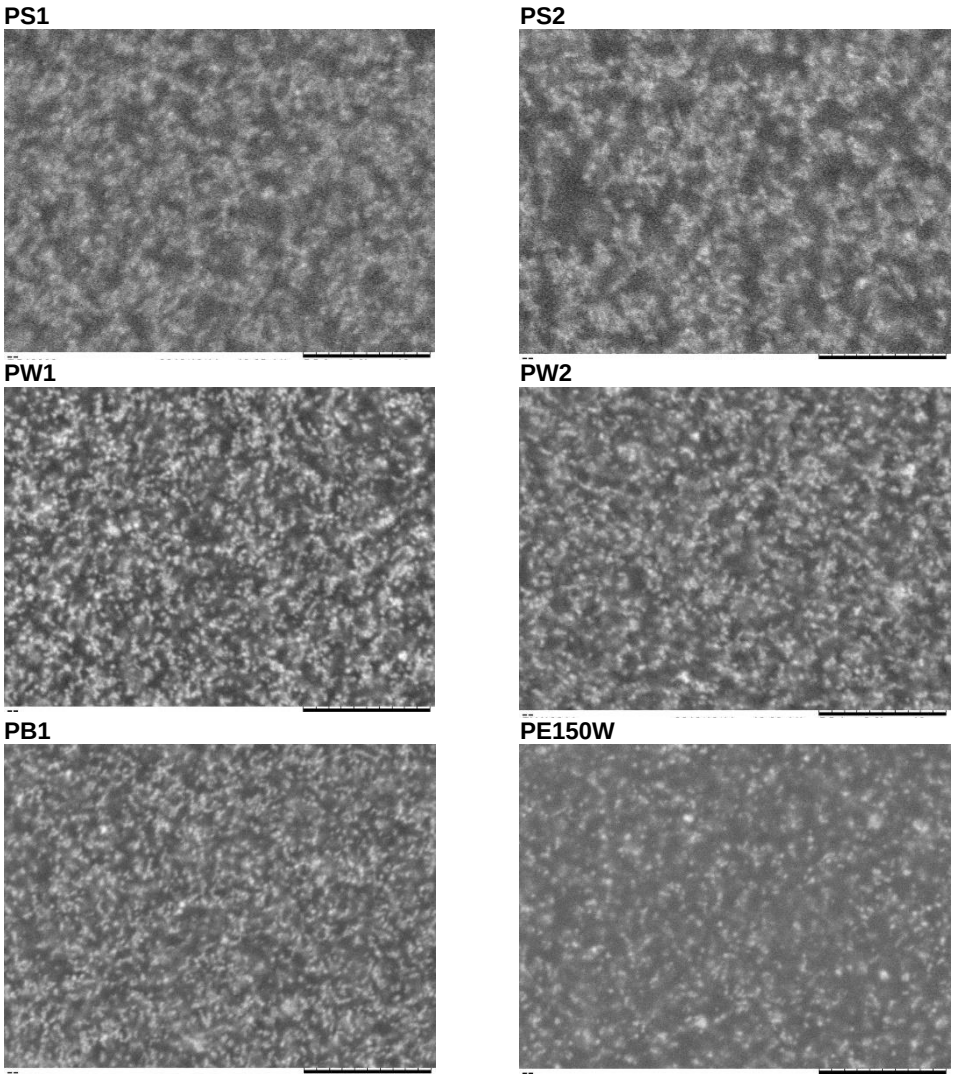

Figure 5-5: SEM images of the surface of the paints (scale bar: 10 µm)

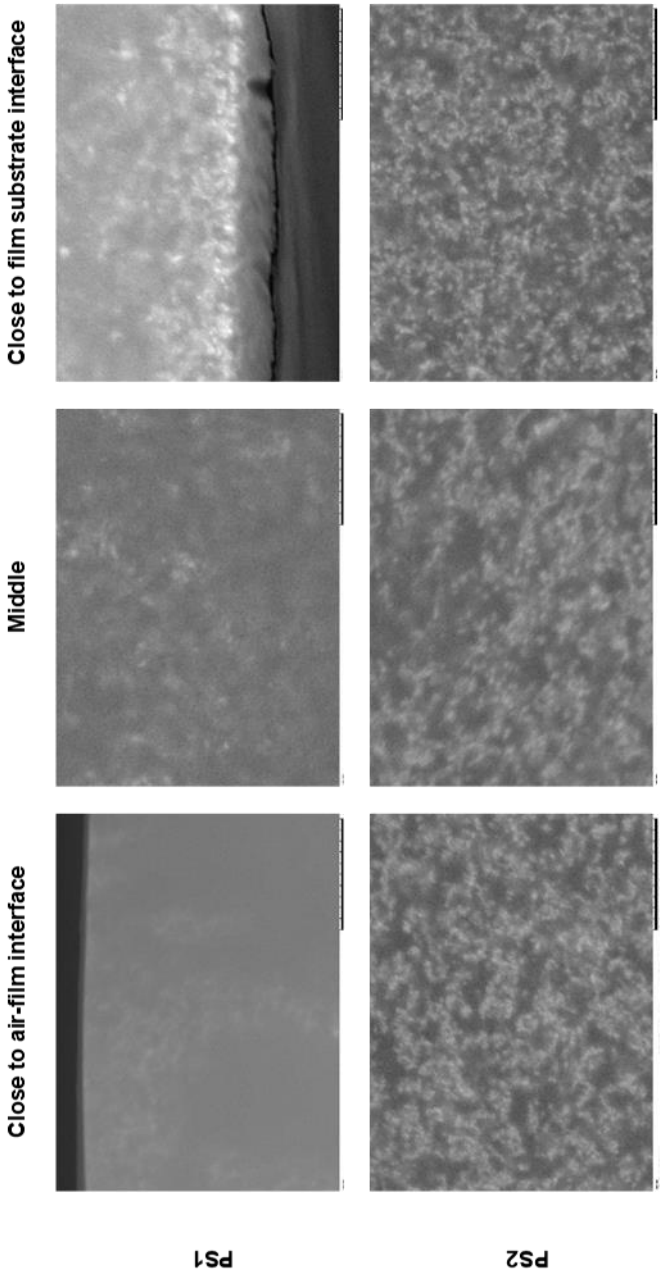

Figure 5-6: SEM images of the fracture of the paint PS1 and PS2 (scale bar: 10 µm)

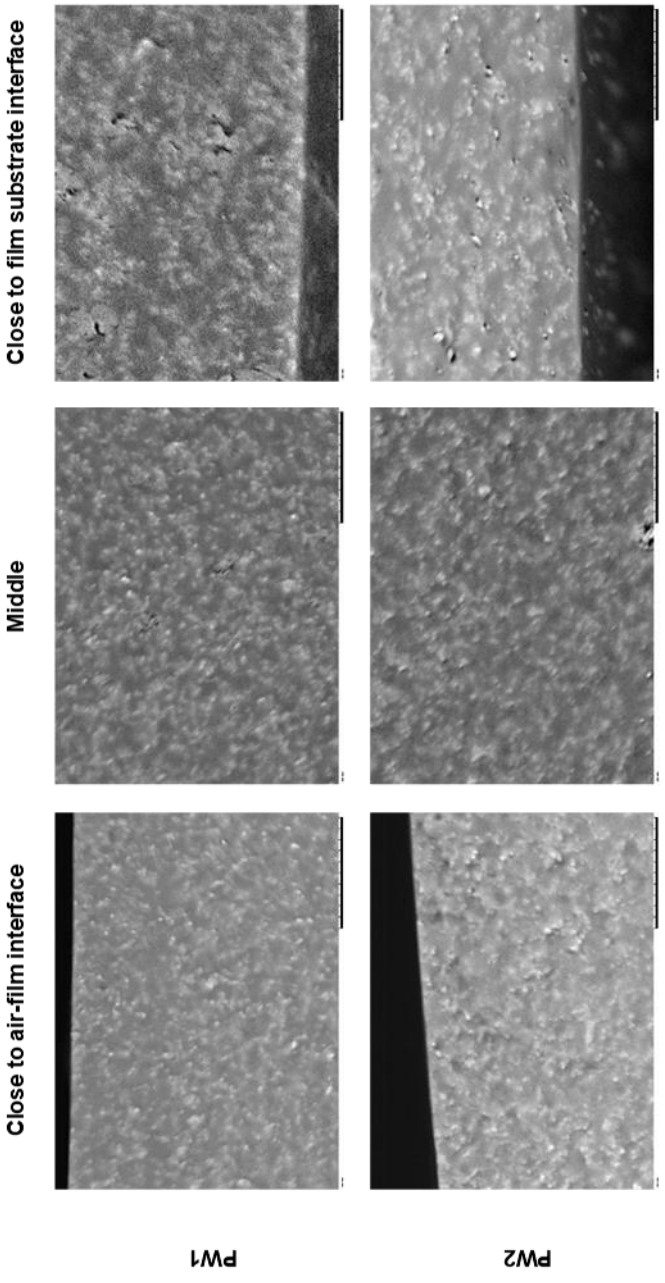

Figure 5-7: SEM images of the fracture of the paint PW1 and PW2 (scale bar: 10 µm)

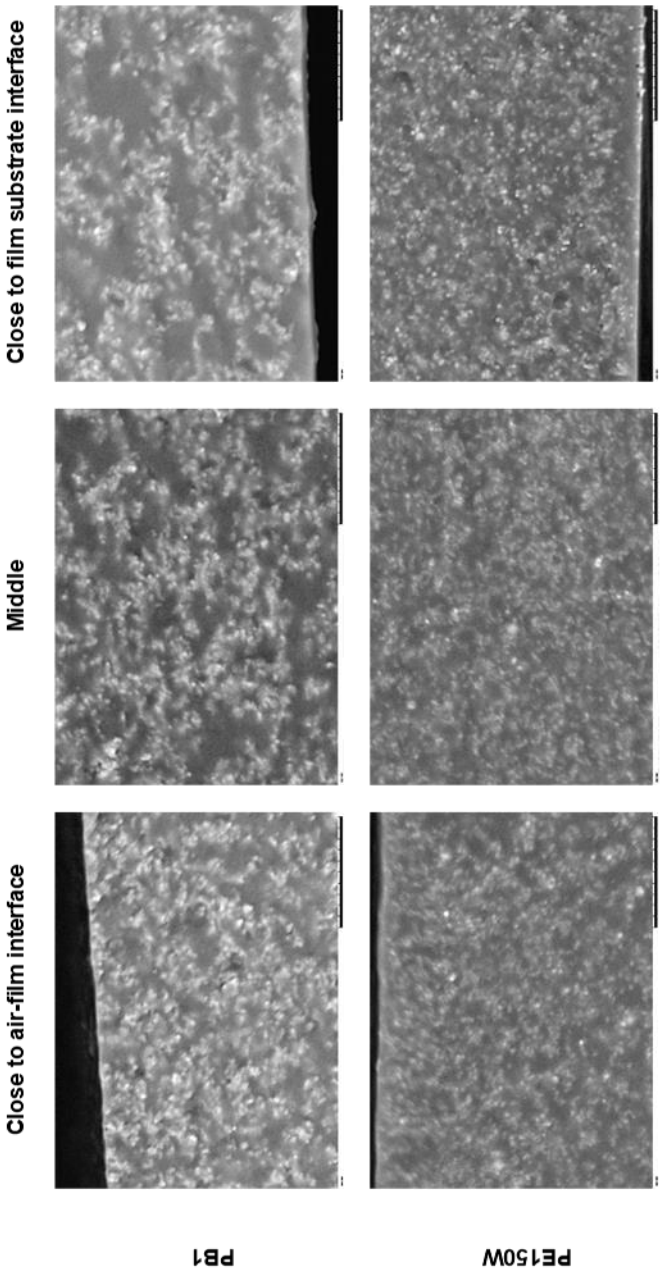

Figure 5-8: SEM images of the fracture of the paint PB1 and PE150W (scale bar: 10 µm)

Figure 5-9 presents the values of gloss. For Series S, PS1 presented a low gloss compared to S2 despite their similar surface morphology. (Figure 5-5). Series W presented a high gloss resulting from a good pigment distribution on the surface of the film (Figure 5-5). The blend, PB1 presented a lower gloss than the hybrid PW1 and PE150W. These differences in gloss could be related to surface roughness. However, no AFM measurements were performed on the paints to confirm this statement.

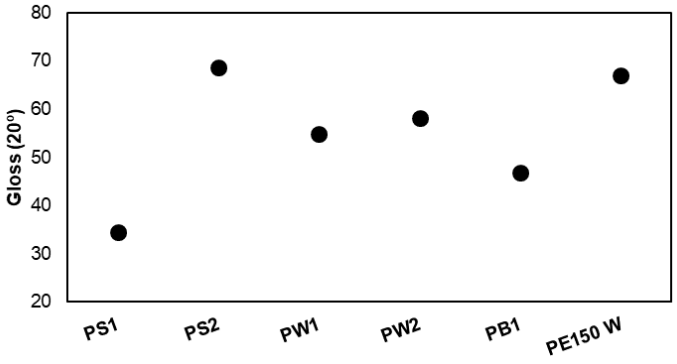

Figure 5-9: Gloss of the paints

Figure 5-10 and Table 5-11 give the mechanical properties of the paints. Paints from Series S were liquid like. As the same mill base was used for all paints there is nothing indicating that an inhibition of curing could have occurred with a component of the mill base for Series S. The results suggest that plasticization of the acrylic polymer by the alkyd resin

occurred for the paints from Series S. As these paints films were excessively soft, additional properties were not measured for this series. The other paints showed similar trends to the films cast from the latexes alone as described in Section 5.3.3. This indicates that although the inclusion of pigment may influence slightly film morphology, the general structure of the film is not significantly altered and therefore the trends observed in the latex films can be directly translated into the formulated product. Paints films were more brittle (higher Young's modulus and stress at break and lower toughness) than the corresponding latex films (see Tables 5-7 and 5-10) due to the incorporation of the hard pigment.

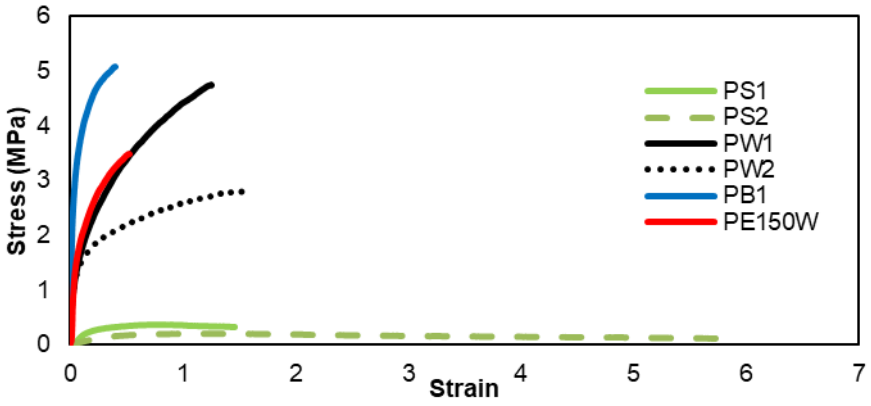

Figure 5-10: Stress-strain curves for the different paints

Table 5-11: Tensile tests results for the different paints

	Young's modulus (MPa)	Elongation at break	Stress at break (MPa)	Toughness (MPa)
PS1	2.7 ± 0.6	1.69 ± 0.13	0.31 ± 0.01	0.52 ± 0.03
PS2	0.39 ± 0.05	5.9 ± 1.6	0.11 ± 0.06	0.9 ± 0.14
PW1	44.6 ± 11.3	1.25 ± 0.09	4.74 ± 0.17	4.31 ± 0.4
PW2	52.1 ± 9.9	1.53 ± 0.37	2.78 ± 0.12	3.53 ± 0.85
PB1	142.5 ± 20.2	0.40 ± 0.07	5.08 ± 0.15	1.69 ± 0.26
PE 150W	65.6 ± 7.4	0.53 ± 0.08	3.49 ± 0.26	1.38 ± 0.14

Figure 5-11 gives the results of water uptake after 24h of immersion of the paints. The hybrids form Series W presented a high water uptake even though the same amount of surfactant was added to Series W and to the blend. The higher water of Series W is related to the presence of hydrophilic material. Actually, in Series W, the alkyd resin was predispersed into water without any surfactant.

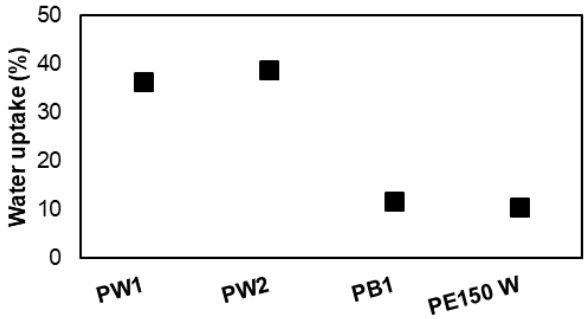

Figure 5-11: Water uptake of paint films (film thickness: 150 µm). Paint films were dried at 23 ºC and 55% relative humidity for two weeks

Figure 5-12 gives the results of the chemical resistance of the paints to red beet, coffee, mustard, lipstick and Fe_2O_3 dispersion measured after two weeks of curing at 23 ºC and 55% relative humidity. High value of ΔE corresponds to low resistance of the paint. PE150W, which contained homogeneous particles of alkyd resin, presented the best resistance to all chemicals. Paints from Series W and from the blend, PB1, had relatively low chemical resistance seemingly due to the presence of non-crosslinked alkyd which limit the performance of the final paints. However, this assumption has to be taken with precaution as more characterization of the paints would be needed to support it.

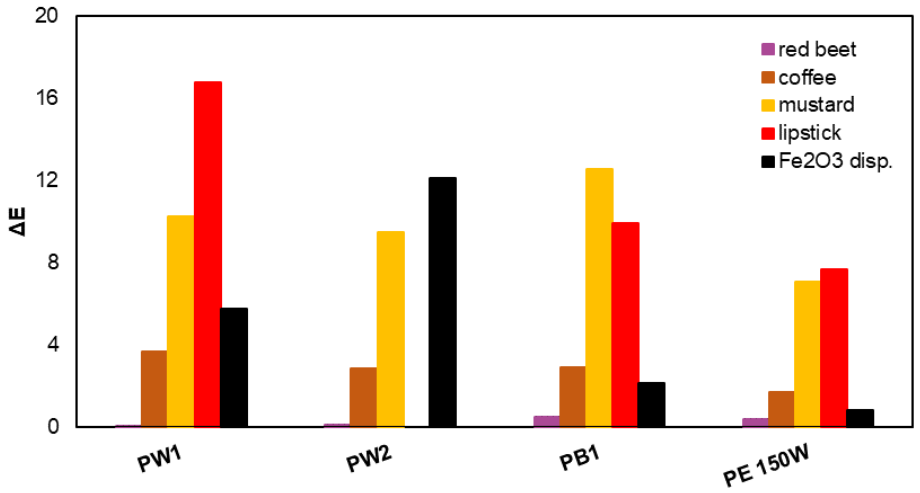

Figure 5-12: Chemical resistance of the paints (film thickness: 150 µm) *no measurement available

5.5 Conclusions

Latexes with different particle morphologies were synthesized by miniemulsion polymerization using two acrylic polymers (MMA/BA: 50/50 and (BMA/BA: 85/15) and two alkyd resins. Through variation of the hydrophobicity of the two components, core-shell and half-moon particle morphologies were obtained. The films obtained with the hydrophobic alkyd resin, Series S, presented large phase separation due to the incompatibility of the two polymers, which led to film with low toughness. Latexes formed with the hydrophilic resin, Series W, presented high grafting of the alkyd resin on the acrylic polymer ensuring a

homogeneous film morphology. Moreover, the films morphologies were in agreement with the particle morphologies and the film properties were dependent of the acrylic composition. A comparison was made with a blend of acrylic particles and alkyd resin ones. The film from the blend was composed of an acrylic continuous phase with alkyd resin dispersed in it leading to a stiffer film than from the corresponding latex film. Paints were prepared using the latexes as binders. The morphology of the paints films were in agreement with those of the latex films. Moreover, paints properties were in the same orders than the latexes films meaning that the addition of pigments and additives did not disrupt the effect of the particle morphology and latex characteristics. In the context of the work of this thesis this is a significant result as it suggests information about the structure property relation of latex films can be directly translated into the formulated product.

5.6 References

(1) Lee, Y.; Ling, C.; Fang, H.; Hu, J.; Zhang, P. Alkyd coating formulations. WO2011085520A1, 2010.

(2) Larson, G. R.; Wilhelm, J.; Cinoman, D. S. Acrylic resins and powder coating compositions and powder coated substrates including the same. WO2015128361A1, 2015.

(3) Tiarks, F.; Frechen, T.; Kirsch, S.; Leuninger, J.; Melan, M.; Pfau, A.; Richter, F.; Schuler, B.; Zhao, C. L. Formulation effects on the distribution of pigment particles in paints *Prog. Org. Coatings* **2003**, *48*, 140–152.

(4) Emmons, W. D.; Vogel, M.; C., K. E.; Thibeault, J. C.; Sperry, P. R. Process for preparing an aqueous dispersion including polymeric latex and titanium dioxide pigment. US20020096088A1, 1993.

(5) Steward, P. A.; Hearn, J.; Wilkinson, M. C. Overview of polymer latex film formation and properties *Adv. Colloid Interface Sci.* **2000**, *86*, 195–267.

(6) Tsavalas, J. G.; Luo, Y.; Schork, F. J. Grafting mechanisms in hybrid miniemulsion polymerization *J. Appl. Polym. Sci.* **2003**, *87*, 1825–1836.

(7) Hudda, L.; Tsavalas, J. G.; Schork, F. J. Simulation studies on the origin of the limiting conversion phenomenon in hybrid miniemulsion polymerization *Polymer* **2005**, *46*, 993–1001.

(8) Minari, R. J.; Goikoetxea, M.; Beristain, I.; Paulis, M.; Barandiaran, M. J.; Asua, J. M. Post-polymerization of waterborne alkyd/acrylics. Effect on polymer architecture and particle morphology *Polymer* **2009**, *50*, 5892–5900.

(9) Udagama, R.; de las Heras Alarcón, C.; Keddie, J. L.; Tsavalas, J. G.; Bourgeat-Lami, E.; McKenna, T. F. L. Acrylic-Alkyd Hybrids: Secondary Nucleation, Particle Morphology, and Limiting Conversions *Macromol. React. Eng.* **2014**, *8*, 622–638.

(10) Li, Z. R. *Industrial Applications of Electron Microscopy*; Marcel Dekker, 2003.

(11) Gonzalez-Ortiz, L. J.; Asua, J. M. Development of Particle Morphology in Emulsion Polymerization. 1. Cluster Dynamics *Macromolecules* **1995**, *28*, 3135–3145.

(12) Alvarez, V.; Paulis, M. Effect of acrylic binder type and calcium carbonate filler amount on the properties of paint-like blends *Prog. Org. Coatings* **2017**, *112*, 210–218.

(13) Funke, W. Additives for Coatings *Prog. Org. Coatings* **2001**, *41*, 191.

(14) Kästner, U. The impact of rheological modifiers on water-borne coatings *Colloids Surfaces A Physicochem. Eng. Asp.* **2001**, *183–185*, 805–821.

(15) Resins, D. S. M.; Box, P. O.; Zwolle, A. P. Making Paint from Alkyd Emulsions *ACS Symp. Ser.* **1997**, *663*, 183–195.

(16) Lehmann, K. Influence of TiO2 on alkyd emulsions *Eur. Coatings J.* **1999**, 6.

(17) Braun, J. .; Fields, D. . Gloss of paint films. II: Effects of pigment size *JCT, J. coatings Technol.* **1994**, *66*, 93–98.

Chapter 6. Synthesis of cellulose nanocrystal armored latex particles for mechanically strong nanocomposite films

6.1 Introduction

Cellulose constitutes one of the world's most abundant sources of renewable polymers and is well known for its use in the form of fibers or derivatives in a wide spectrum of products and materials.[1] Cellulose nanocrystals (CNCs) are rod-shaped, highly crystalline nanoparticles (Figure 6-1) with a typical width of 3-10 nm in width and lengths ranging from 100 to in excess of 1000 nm[2,3], which can be extracted from wood,[4] cotton,[5] bacteria,[6] agricultural waste[7] and other plant sources.[8–10] Cellulose nanocrystals are most commonly prepared by acid hydrolysis of microfibrils obtained by mechanical processing of wood fibers using sulfuric acid. This process hydrolyzes the amorphous part of the cellulose microfibrils to obtain nanocrystals with anionic sulfate half-ester groups on their surface (approximately 1 sulfate half-ester per 3 nm^2).[11] One of the unique features of CNCs is their incredible mechanical strength as shown in Table 6-1. CNCs not only have a high axial elastic modulus (higher than Kevlar) and a high tensile strength, but they are also low density materials, which makes them particularly attractive to use in hybrid materials. Moreover, as a relatively low cost biopolymer, CNCs are very attractive materials for industry.[12]

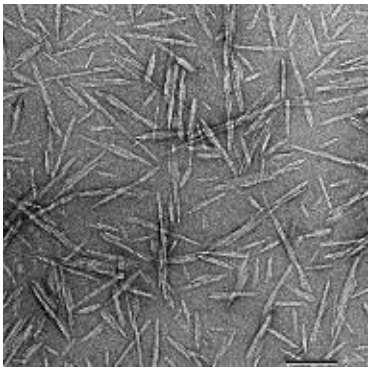

Figure 6-1: TEM picture of a dispersion of cellulose nanocrystals (scale bar: 100 nm) provided by Alberta Innovates Technology Futures

Table 6-1: Comparison of CNC properties with alternative reinforcing materials

Material	Density (g/cm^3)	Axial elastic modulus (GPa)	Tensile strength (GPa)
Kevlar KM2 fiber[13]	1.4	88	3.8
Glass fiber[14]	2.5	86	4.8
Carbon fiber[15]	1.8	210	4.1
Stainless steel wire[16]	7.8	210	1.28
Carbon nanotubes[15]	2.1	270-950	11-63
CNC[15]	1.6	110-220	7.5-7.7

The high strength of cellulose derivatives (such as microfibrils and nanocrystals) allows them to substantially improve properties of composite materials.[17–26] This is of particular interest in the development of mechanically strong polymer films cast from latex dispersions, where traditionally the strength of the film has been limited by the requirement of having relatively low T_g polymers in order to form a coherent film at room temperature.[27,28] For example, Favier *et al.*[18] used cellulose microfibrils (length of several µm, and width of 10-20 nm) as reinforced material in a polymer matrix composed of poly(S-*co*-BA) by blending of the two dispersions. A rigid network was formed resulting from the strong interactions between adjacent whiskers by hydrogen bonding, which led to an enhancement of the mechanical properties.[17] Indeed, the Young's modulus passed from 0.2 MPa when no microfibrils were added to 32.3 MPa with 6 wt% of microfibrils. Vatansever *et al.*[29] utilized blends of a poly(MMA-*co*-BA) latex with dispersions of CNCs of different concentration (1, 2 and 3 wbp%, weight based on polymer). They measured the mechanical properties of these films and compared them with a blend of the poly(MMA-*co*-BA) latex with sodium montmorillonite (Na-MMT, 3 wbp%). Mechanical properties were enhanced for both systems, with better results for the CNCs composite. They claimed that this enhancement was thanks to the improved dispersion of the CNCs in the polymer and their crystallinity.

An interesting approach to achieve intimate contact between CNCs and the latex, and to thus control the subsequent film structure, is through the use of CNCs as a stabilizer in the production of the latex itself. The use of solid particles to stabilize emulsions, known as Pickering stabilization, has been well documented since the beginning of the 20th century,[30,31] while solid stabilized suspension polymerization processes were reported as early as the

1930s.[32] Pickering miniemulsion polymerizations, which allow for the production of particles that can be used in the dispersed state (for example in coatings applications) have been developed over the last 15 years, predominantly using silica and nanoclay as the solid stabilizer.[33–35] Emulsion polymerization processes to generate solid stabilized latexes have also been reported,[36–41] marking a major step in the industrial viability of such processes.

The ability of CNC to act as Pickering stabilizers has become a subject of great interest over the past decade.[42–51] Adsorption of CNCs to liquid-liquid interfaces is strong and furthermore, due to the high interfacial area occupied by a single particle, low concentrations are required to obtain stable emulsions. While most demonstrations of the ability of CNC to act as emulsion stabilizer are for non-polymerizable oils, a few works have reported on formation of emulsions of vinyl monomers such as styrene or methyl methacrylate which is of interest here for the generation of hybrid latex particles.[42,44,45,47–50,52,53] However, in almost all these examples the monomers have been polymerized in suspension leading to large, micron sized particles, which have limited practical application.

Kalashnikova *et al.* reported the efficient Pickering stabilization of hexadecane with bacterial cellulose nanocrystals (BCN) with a length of 850 nm and a width of 20 nm (aspect ratio: 43). Due to the length of the nanocrystals the resulting emulsion droplets were large (approximately 4 µm).[42] By emulsifying styrene and subsequent suspension polymerization using a hydrophobic azo based initiator they obtained large polymer microparticles as well as a crop of nanosized particles that were formed during the polymerization. Moreover, SEM pictures given in Figure 6-2 show that despite their crystalline nature, the BCN could bent on

the surface of the particles. Fujisawa *et al.* presented the use of cellulose nanofibrils to form stable Pickering emulsions with styrene.[47] The initial emulsion droplet size was on the order of microns but, similar to other reports and common to many suspension polymerization processes,[54] upon polymerization an additional crop of significantly smaller particles were obtained. Similarly, Werner and coworkers reported the use of acetylated CNCs to produce stable Pickering emulsions of a wide range of monomers.[48,52] Hydrophobic initiators were used to induce the suspension polymerization leading to formation of micron sized particles with a second population of small nanosized particles.

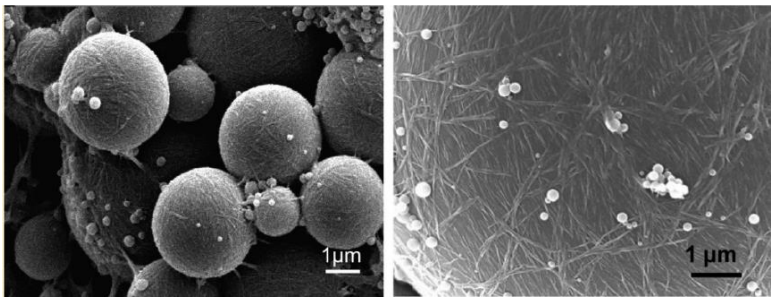

Figure 6-2: SEM images of polystyrene particles stabilized with bacterial cellulose nanocrystals.[42] Reproduced with permission from American Chemical Society

Kedzior *et al.* used CNCs blended with various surfactants to form stable emulsions with methyl methacrylate.[44] When CNCs and surfactants of the same charge were used, there was no interaction either between surfactant and CNC or CNC and polymer particles. Thus, a stable

miniemulsion was obtained in which the CNCs did not interact with the miniemulsion formation and subsequent polymerization yielded a blend of surfactant stabilized latex particles and CNCs. Conversely, when the CNCs and surfactants were of opposite charge, the charge neutralized CNC stabilized the latex and led to the formation of micron-sized CNC armored particles. Subsequently, the biopolymer methyl cellulose has been used in a similar way to coat the CNCs for the stabilization of methyl methacrylate in water emulsions.[50] Polymerization resulted in a dispersion that contained methyl cellulose coated CNC stabilized particles of several microns diameter and free methyl cellulose stabilized nano particles. Ben Mabrouk *et al* demonstrated the synthesis of CNC-polymer nanocomposites by miniemulsion polymerization of butyl methacrylate.[49] Negatively charged cellulose nanowhiskers were used in combination with a cationic surfactant to stabilize the miniemulsion. However, SEM images suggest that the cationic surfactant played the main role in stabilization and a large number of particles did not appear to have any nanocellulose at the surface.

To the best of our knowledge the only report in the literature of a true solid stabilized miniemulsion system that results in formation of a stable latex is that reported by Zhang and coworkers.[55] By using hydrophobically modified CNCs they showed that stable styrene in water miniemulsions with average droplet size as low as 250 nm could be formed. Subsequent polymerization led to stable latexes with nanocellulose clearly adsorbed to the surface. Thus, except for this one report on miniemulsion polymerization the majority reports to date that involve CNC stabilized polymer dispersions are based on suspension polymerization type systems that lead to micron sized particles. It should be noted that the use of miniemulsion polymerization also comes with its drawbacks due to the large amounts of energy required to

generate the initial nanosized emulsion droplets, which leads to issues with regards to scaling up.[56]

In this work, we report the synthesis of cellulose nanocrystal armored latex particles directly by emulsion polymerization. As the cellulose nanocrystals are highly hydrophilic with a strong anionic charge, a cationic initiator was employed in order to induce electrostatic interactions between the latex and the CNCs, resulting in their adsorption to the interface polymer water interface (Scheme 6-1). The parameters that control particle formation and emulsion stability were explored in order to obtain stable hybrid latexes. Films were cast from different hybrid latex dispersions and their mechanical properties were explored. It is shown that the use of CNCs is a potential route to generating polymer films with extremely high mechanical strength.

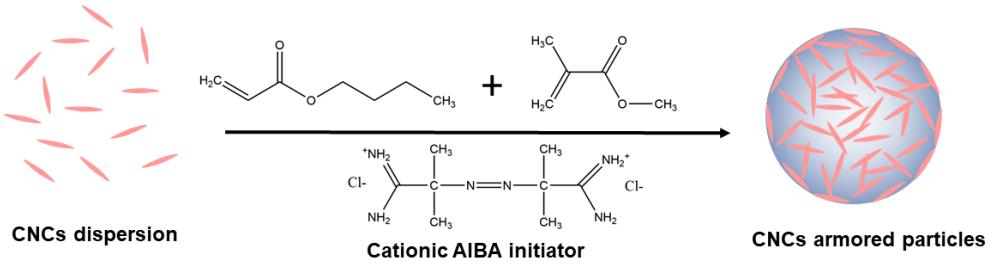

Scheme 6-1: Schematic representation of the formation of CNCs armored poly(methyl methacrylate-*co*-butyl acrylate) particles with a cationic 2,2′-azobis(2-methylpropionamidine) dihydrochloride (AIBA) initiator

6.2 Experimental part

6.2.1 Materials

Methyl methacrylate (MMA, technical grade, Quimidroga) and butyl acrylate (BA, technical grade, Quimidroga)) were used as received. 2,2′-Azobis(2-methylpropionamidine) dihydrochloride (AIBA, 97%, Sigma-Aldrich) was used as thermal initiator. Cellulose nanocrystals were provided by Alberta Innovates Technology Futures. Deionized water was used throughout the work.

6.2.2 Synthesis of CNC stabilized particles and blends preparation

A 10.9 wt % solids content emulsion was prepared using the formulation, L1, in Table 6-2. The cellulose nanocrystals, with the characteristics described elsewhere,[3] were dispersed in water and sonicated for 10 min with a Hiehscher sonicater at amplitude of 100 %. Then, the initiator, 2,2′-Azobis(2-methylpropionamidine) dihydrochloride (AIBA) was dissolved in 10 wt% of the total amount of water and added to the dispersion under agitation. The mixture was poured into a 500-mL glass reactor equipped with a reflux condenser, an Ekato Mig impeller and nitrogen inlet. The monomers (methyl methacrylate (MMA)/ butyl acrylate (BA): 50/50 wt/wt) were added under agitation at 250 rpm (for L10, agitation was 350 rpm due to the high viscosity of the medium). The system was purged with nitrogen for 20 min then heated to 70 °C. When the temperature was reached, the nitrogen outlet was moved on top of the reaction

mixture to form a nitrogen blanket. After formation of the emulsion (the reaction media turned white), the agitation was decreased to 150 rpm and the mixture was left to react for 7 hours. For latex L0, the initiator and the water were poured into the reactor equipped as before. The monomers were added under agitation at 150 rpm. The system was purged with nitrogen for 20 min and left to react at 70 °C for 7 hours. Table 6-2 summarizes the different reactions performed with variation of the initiator and CNC concentration and solids content.

Blends were prepared with latexes L5 and L0 (latex devoid of CNCs). The idea was to decrease the amount of CNCs in the final film while blending L5 with a conventional polymer latex. The different blends are summarized in Table 6-3.

Table 6-3: Compositions of the different blends of L5 and L0 (see Table 6-1)

Name	Ratio	L5 (g)	L0 (g)	CNCs (wbp %)
L5:L0 - 9:1	9:1	9	1	18
L5:L0 - 2:1	2:1	6.66	3.33	13.3
L5:L0 - 1:1	1:1	5	5	10
L5:L0 - 1:2	1:2	3.33	6.66	6.66

Table 6-2: Formulations used for the synthesis of the latexes by emulsion polymerization at 70 ºC

Compounds	L0 (g)	L1 (g)	L2 (g)	L3 (g)	L4 (g)	L5 (g)	L6 (g)	L7 (g)	L8 (g)	L9 (g)	L10 (g)
Water	302	298	293	299	298	298	298	293	299	293	265
CNC	0	6	9	3	6	6	6	9	3	9	11
MMA	15	15	15	15	15	15	15	15	15	22.5	27.6
BA	15	15	15	15	15	15	15	15	15	22.5	27.6
AIBA	0.3	0.3	0.3	0.3	0.6	0.15	0.075	0.15	0.15	0.225	0.276
[monomer]/ [AIBA]	241	241	241	241	121	482	965	482	482	482	482
CNCs :AIBA charge ratio[a]	-	0.56	0.84	0.28	0.28	1.12	2.23	1.68	0.56	1.12	1.11

[a] CNC/AIBA charge ratio is calculated based on previously published data on the charge density of the CNCs in ref [3].

6.2.3 Characterizations

Zeta potential was calculated from the measure of electrophoretic mobility of the latexes and the CNCs dispersion. The particle morphology and particle sizes of the latexes and blends were measured by transmission electron microscopy (TEM). The film morphologies were studied by means of Atomic force microscope (AFM). The mechanical properties of the films cast from the synthesized latexes and blends were determined by tensile test measurements. A detailed description of the characterization methods is provided in Appendix I.

6.3 Results and discussion

6.3.1 Interactions between CNCs and cationic initiator (AIBA)

The zeta potential and viscosity of the aqueous phase mixtures of CNCs and the cationic initiator AIBA were first measured in the absence of monomer to gain an insight into the nature of the interaction that may take place between CNCs and AIBA during the polymerization process. Figure 6-3 shows the effect of CNCs and AIBA concentrations on the zeta potential (which is proportional to the surface charge). A similar plot , showing the effect of the CNC/AIBA charge ratio, calculated using previously published values for the charge density of the CNCs, is shown in Figure III-1 in Appendix III.[3] In this plot it can be observed that when described as a charge ratio all the data in Figure 6-3 collapse onto a single line. It should be noted that the model for calculation of zeta potential from electrophoretic motion relies on the assumption of a spherical particle and therefore these measurements serve only to compare the samples qualitatively. When a low concentration of CNCs was used, 10 g/L, addition of

small amounts of AIBA resulted in a rapid increase in the zeta potential, signifying that high charge suppression of the anionic sulfate half ester groups from the CNCs with AIBA occurred. Similarly, although to a lesser extent, with 20 g/L of CNCs as the concentration of AIBA was increased the zeta potential increased and at 1 g/L of AIBA, high charge suppression occurred. With 30 g/L of CNCs even at higher concentrations of AIBA (1 g/L) only moderate charge compensation of the sulfate half esters groups occurred, meaning that free sulfate half ester groups were present. With the increase of AIBA concentration to 2 g/L, the zeta potential became less negative and resulted in increased aggregation.

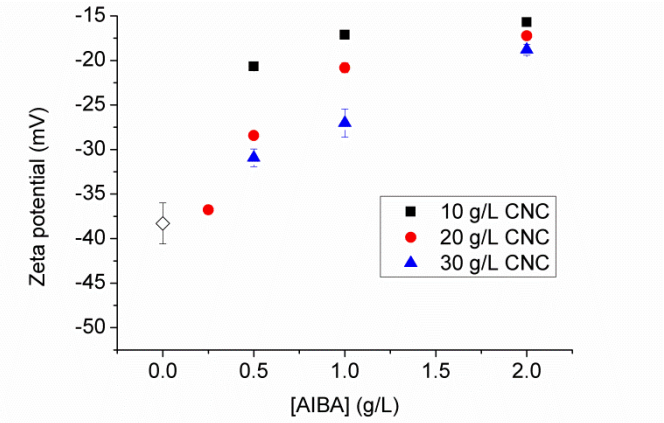

Figure 6-3: Zeta potential of different solutions of cellulose nanocrystals with variation of 2,2′-Azobis(2-methylpropionamidine) dihydrochloride

Figure 6-4 presents the viscosity of the dispersions. Due to the high aspect ratio of the CNCs, they present a relatively high viscosity, even at low volume fractions. The charge suppression measured with the zeta potential can also be seen in the viscosity of the aqueous CNCs dispersions which increases with increasing AIBA content up to 1 g/L as partial CNC aggregation occurs with increasing AIBA content. The shear thinning behavior observed at higher AIBA concentrations also suggests the formation of aggregates. At AIBA content of 2 g/L the effect on viscosity is different dependent on the concentration of CNCs. At 30 g/L CNC above 1 g/L AIBA zeta potential continues to decrease (see Figure 6-3) and thus the dispersion becomes more prone to aggregation and becomes more viscous. However at 10 g/L CNC the viscosity at 2 g/L AIBA is lower than at 1 g/L. Looking at the effect on zeta potential in Figure 6-3 it can be seen that in this case the increase in AIBA content does not have any influence on the zeta potential and thus it can be assumed that any additional AIBA is free in the aqueous phase. As a result this increases ionic strength of the medium and may explain the reduction in viscosity in this case. Based on these results it can clearly be seen that the degree of charge suppression and stability of the CNC dispersion is highly dependent on the relative ratio of the cationic initiator to the amount of CNCs and we therefore proceeded with a number of emulsion polymerization reactions, varying the relative quantities of these two materials.

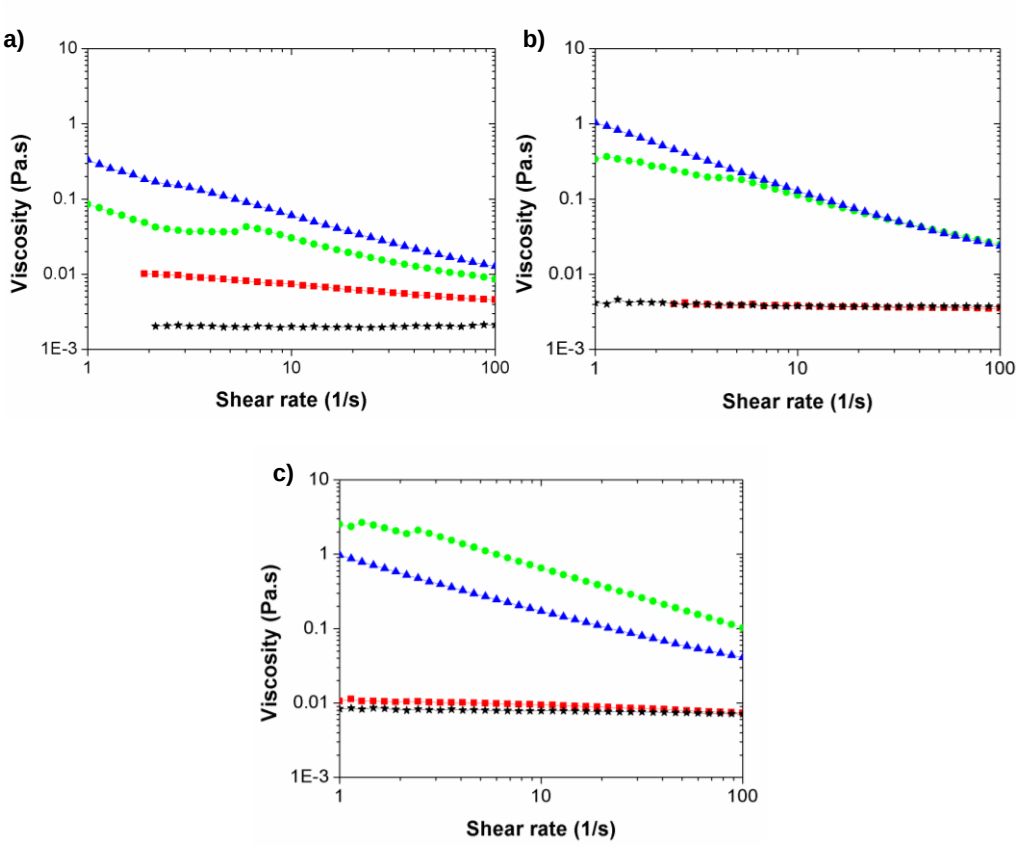

Figure 6-4: Viscosity of different solutions of cellulose nanocrystals with variation of 2,2′ -Azobis(2-methylpropionamidine) dihydrochloride with a) 10g/L of CNCs, b) 20g/L of CNCs and 30 g/L of CNCs (black ★correspond to no AIBA CNCs, red ■ to 0.5g/L of AIBA, blue ▲ to 1 g/L of AIBA, and green ● to 2g/L of AIBA)

6.3.2 Characteristics of the different latexes

Table 6-4 summarizes the results of the polymerizations based on the formulations given in Table 6-2. Figures III-22 to III-6, in Appendix III, give the TEM pictures of the latex dispersions and the particle size distributions determined by TEM. A first acrylic polymer latex, L1, was synthesized by batch emulsion polymerization using 20 wbm % (weight based on monomer) of CNCs as stabilizer with 1 wbm % of cationic initiator. For reference, this corresponds approximately to the system containing 20 g/L CNC and 1 g/L AIBA in the experiments shown in Figures 6-3 and 6-4. Full conversion (X>99.5%) was reached with 110 ppm of residual monomers and a limited amount of aggregated polymer (5.8 wt%, see Table 6-4). The small amount of aggregated polymer present is likely due to the high charge suppression of the anionic sulfate half ester groups of the CNCs by the AIBA that results in some partial coagulation between the armored latex particles. As large particles with a broad particle size distribution (PSD) were found, TEM was used to determine the PSD (Figure 6-5). The distribution was broad with an average particle size of 165 nm. The TEM image shown in Figure 6-5 suggests that the nanocrystals were indeed covering the particles with some free CNC. It should be noted that when no CNCs were added to the formulation (latex L0) stabilization occurred as a result of electrostatic interactions due to the use of the charged initiator.[57] However, particle size was high (420 nm, Figure 6-5) indicating that the presence of CNCs significantly influences the particle nucleation process.

Table 6-4: Results of the different polymerizations

	L0	L1	L2	L3	L4	L5	L6	L7	L8	L9	L10
CNCs (wbm %)	0	20	30	10	20	20	20	30	10	20	20
AIBA (wbm %)	0.5	1	1	1	2	0.5	0.25	0.5	0.5	0.5	0.5
SC (%, theoritical)	9.5	10.9	11.8	10.0	10.9	10.9	10.9	11.8	10	15.2	20
SC (%, experimental)	8.9	10.4	11	0	1.4	10.2	8.9	10.9	8.8	14.8	17.9
Coagulation (wt %)	0	5.8	7	100	87	3.1	3.8	1.9	16	2.6	10.8
Residual monomers (ppm)	250	110	170	/	/	110	400	280	210	190	226
Particle size per number (d_n, nm)	417	165	173	/	/	160	/	160	/	233	/
Particle size per weight (d_w, nm)	433	355	303	/	/	233	/	274	/	307	/
Polydispersity (d_w/d_n)	1.04	2.15	1.75	/	/	1.45	/	1.7	/	1.31	/
Zeta potential (mV)	42.1	-25.4	-27.4	/	/	-31	-29.3	-31.7	/	-30.1	/

/ not measured

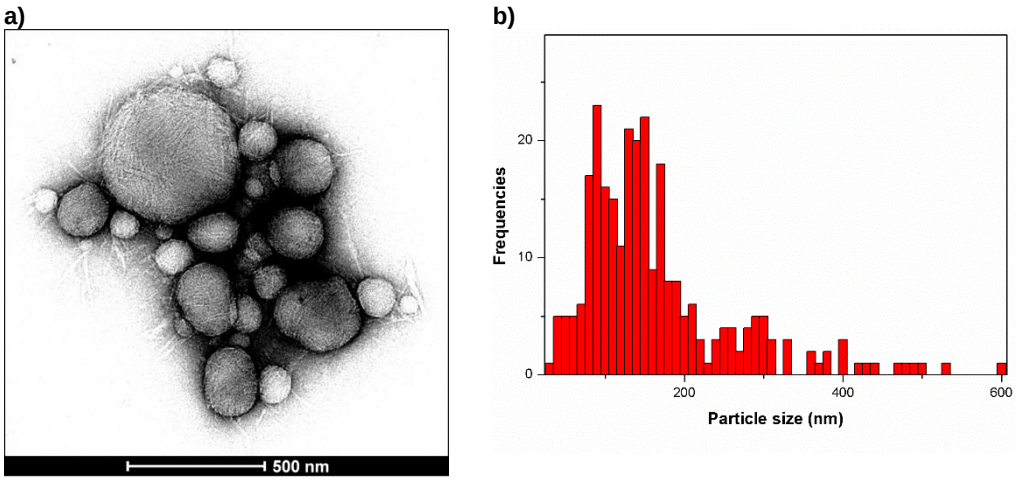

Figure 6-5: a) TEM image of particles from latex L1 (scale bar: 500 nm) and b) Particle size distribution

Taking this formulation as a reference, the initiator and CNCs concentrations were varied in order to gain an insight into the polymerization process. In latex L2, with 30 wbm% of CNCs and 1 wbm% of AIBA, due to the increase of viscosity of the system again some aggregation occurred (7 wt% coagulation). This may be linked to diffusion limitations of adsorption of the CNCs to the latex particle surface at higher CNC concentrations. However, the particle size distribution was narrower (Figure III-3). With a low concentration of CNCs (10 wbm%) in latexes L3 and L8, due to the large degree of charge suppression of the anionic sulfate half esters groups of the CNCs, a high amount of coagulation was observed during the reaction (respectively 100 and 16 wt%). In latex L4, the AIBA concentration was increased of to

2 wbm%, leading to a high amount of charge suppression and as such, due to the aggregation of CNCs, a high amount of coagulation took place during the reaction (87 wt%).

Thus, the stability of the latex is highly dependent on surface charge density of the CNCs. At an optimum concentration of AIBA, the hydrophilicity of the CNC particles is sufficiently reduced such that they adsorb to the surface of the latex particle without complete suppression of the surface charges that leads to high amounts of coagulum. As such latex L5 was synthesized containing lower amounts of AIBA (0.5 wbm%). In this case a stable latex was obtained with negligible aggregated polymer. Figures 6-6 confirmed the presence of CNCs at the surface of the particles. Further decrease of the initiator concentration to 0.25 wbm% (latex L6) led to an equally stable latex. However, in this case a large amount of free CNCs is noticeable on the TEM picture and the particle size distribution was broad (Figure III-6). This was due to a high residual charge on the CNCs which renders them strongly hydrophilic and prevents adsorption to the polymer-water interface. Similarly, with a high concentration of CNCs and a low concentration of AIBA (latex L7), a stable latex was formed. Particle size was small (160 nm) suggesting that the particles were stabilized by CNCs but in this case a large amount of free CNCs were also present in the water phase (Figure III-4). Solids content was successfully increased to 15 wt% (latex L9), however particle size distribution was broader (Figure III-5). Increasing to 20 wt% (latex L10) resulted in a significant increase of coagulum which may be related to the high viscosity of the system when increasing the amount of CNC. These results point to an optimum CNC/AIBA charge ratio of around 1 whereby at lower values significant aggregation/coagulation of the polymer occurs whereas at much higher values the

CNC does not adsorb to the polymer surface and the final product is effectively a blend of latex and free CNCs.

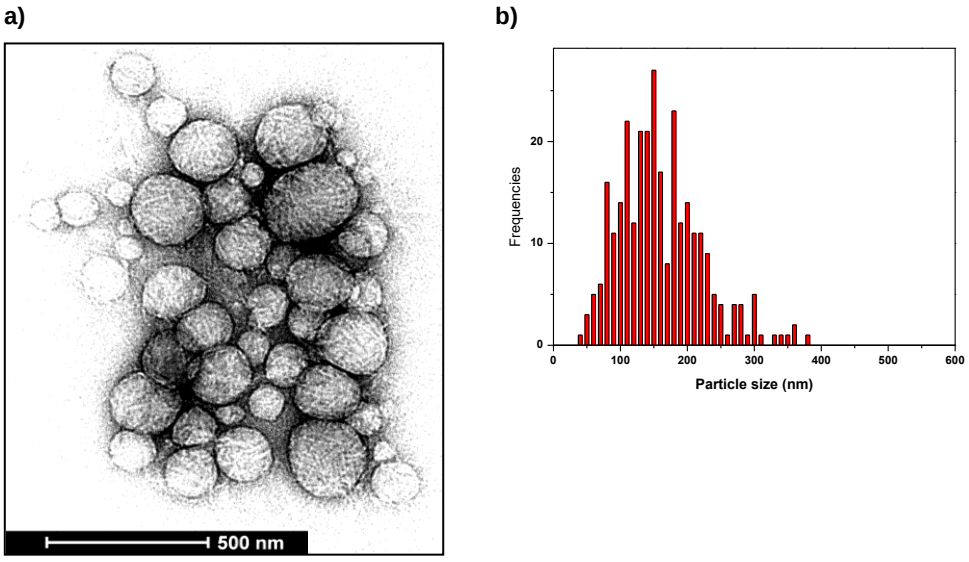

Figure 6-6: a) TEM image of particles from latex L5 (scale bar: 500 nm) and b) Particle size distribution

6.3.3 Films morphologies and properties

It has previously been reported that polymer colloids stabilized with inorganic particles are able to form coherent films that offer outstanding mechanical properties[28,58,59] and new functionalities[60]. Therefore, the ability to form films of the CNC armored latex particles synthesized above was checked. For latex L5, it was found that at 23 °C and 55% relative

humidity the film was transparent although it presented large cracks due to stress buildup in the drying film.[61–63] However, at 65 °C a homogeneous and transparent film was obtained (Figure 6-7).

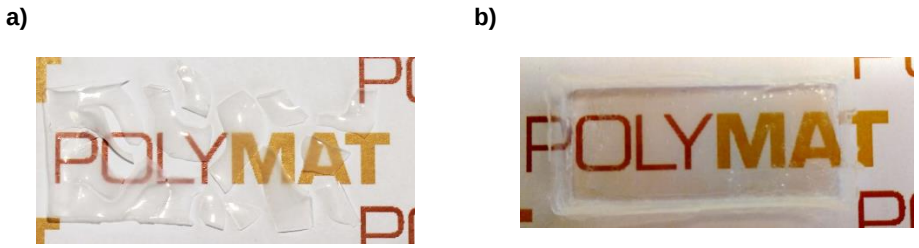

Figure 6-7: Films cast from latex L5 at 55% relative humidity and a) 23ºC and b) 65ºC

Figure 6-8 presents the AFM height images of the air-film interface as well as that of the cross-section of the film cast at 23 °C. It can be seen that the particles were covered by CNCs and presumably this hard shell hindered particle deformation, preventing the formation of a coherent film. White dots were visible in the image of the cross-section. These dots did not appear in the film cast from a latex devoid of CNCs (Figure 6-8 d)), which strongly suggests that they were aggregates of CNCs located at the boundaries where several particles joined. This indicates that even for this well stabilized latex a fraction of the CNCs remained dispersed in the water. The cross-section of the film cast at 65 °C and 55% relative humidity (Figure 6-9) was similar to that cast at 23 °C, but the fact that a coherent and transparent film was obtained

indicates that the polymer was able to overcome the resistance offered by the CNCs covering the polymer particles as has previously been reported for silica stabilized systems.[28]

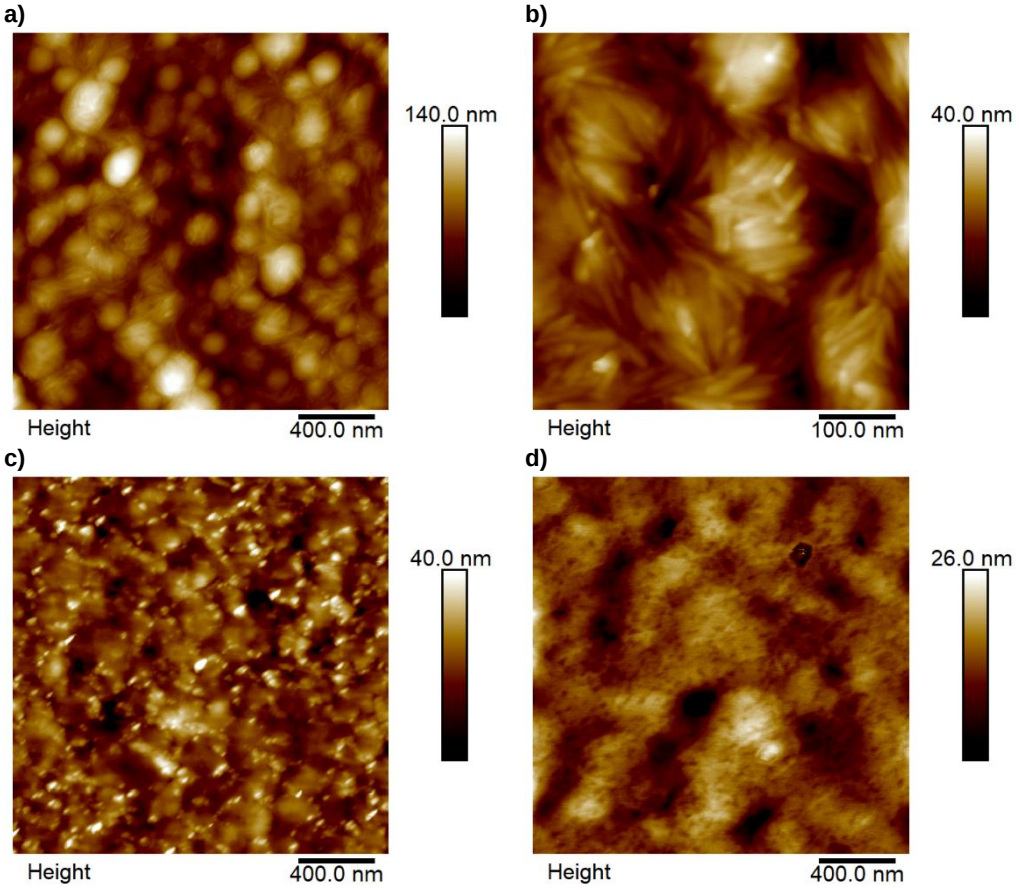

Figure 6-8: AFM height images of a) and b) the air-film interface, c) the cross-section of a dried film of latex L5 and d) the cross section of L0, all cast at 23 ºC and 55% relative humidity

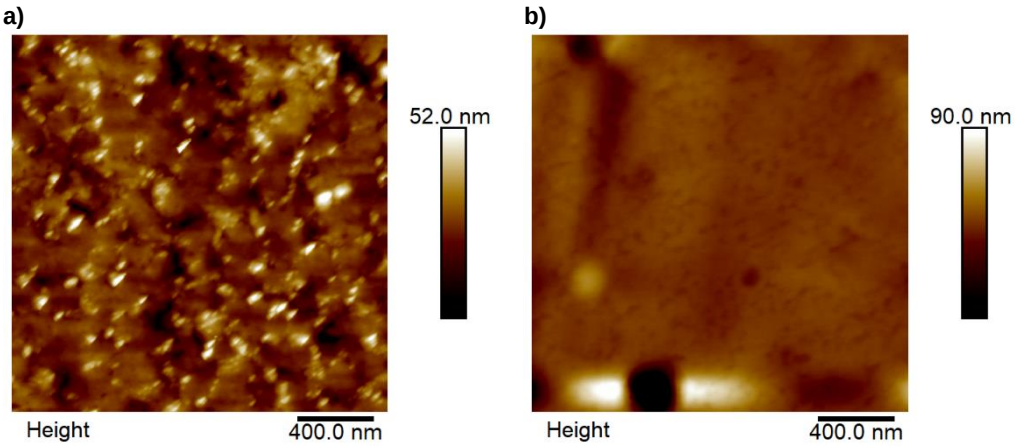

Figure 6-9: AFM height images of the cross-section of a dried film at 65 ºC and 55% relative humidity of a) L5 and b) L0

In order to allow film formation to occur at room temperature, different blends were prepared with the latexes L5 and L0 in various proportions. The characteristics of the blends (CNC content, zeta potential and T_g) is given in Table III-1 in Appendix III. In these blends, the small anionically charged CNC armored particles of L5 (with a zeta potential of -31 mV) can adsorb on the large cationic charged ones of L0 (with a zeta potential of +42.1 mV). This avoids segregation of particles by size during film formation leading to a good dispersion of the CNC stabilized particles in the film.[64–67] However, the colloidal stability of such blends which contain mixtures of oppositely charged particles also has to be taken in account. Indeed, blends with an amount of L0 superior to 33 % coagulated. In this case, as the cationic particles are in excess, addition of the anionic particles serves to connect particles together, leading

eventually to coagulation (see schematic in Scheme 6-2). With lower amounts of L0, stable mixtures were obtained which formed homogeneous films at 23 °C. Although L5 itself is not able to form a film at 23 °C, in the blends up to 66 wt% could be included whilst still forming homogeneous films without cracks at room temperature. Above this amount free CNC armored particles result in particle deformation being prevented (see schematic in Scheme 6-2).

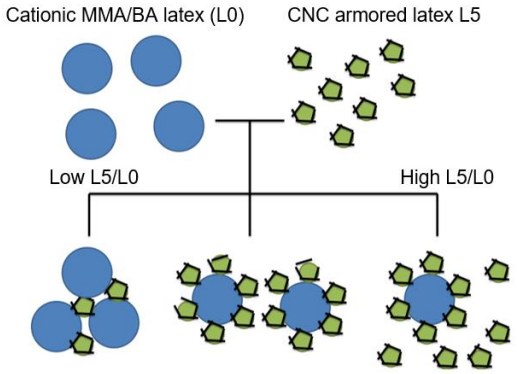

Scheme 6-2: Schematic view of the blends between L5 and L0

As a representative case, Figure 6-10 presents the AFM height images of the air-film interface, film-substrate interface and cross-section of a film from the blend L5:L0 - 1:1 dried at 23 °C and 55% relative humidity. Despite the difference of particles size (L5: 165 nm and L0: 417 nm) the two types of particles were homogeneously distributed in the film, without segregation of particles by sizes as a result of the electrostatic interactions between the

particles. Indeed, at the air-film interface and the film-surface interface, both particle types are visible.

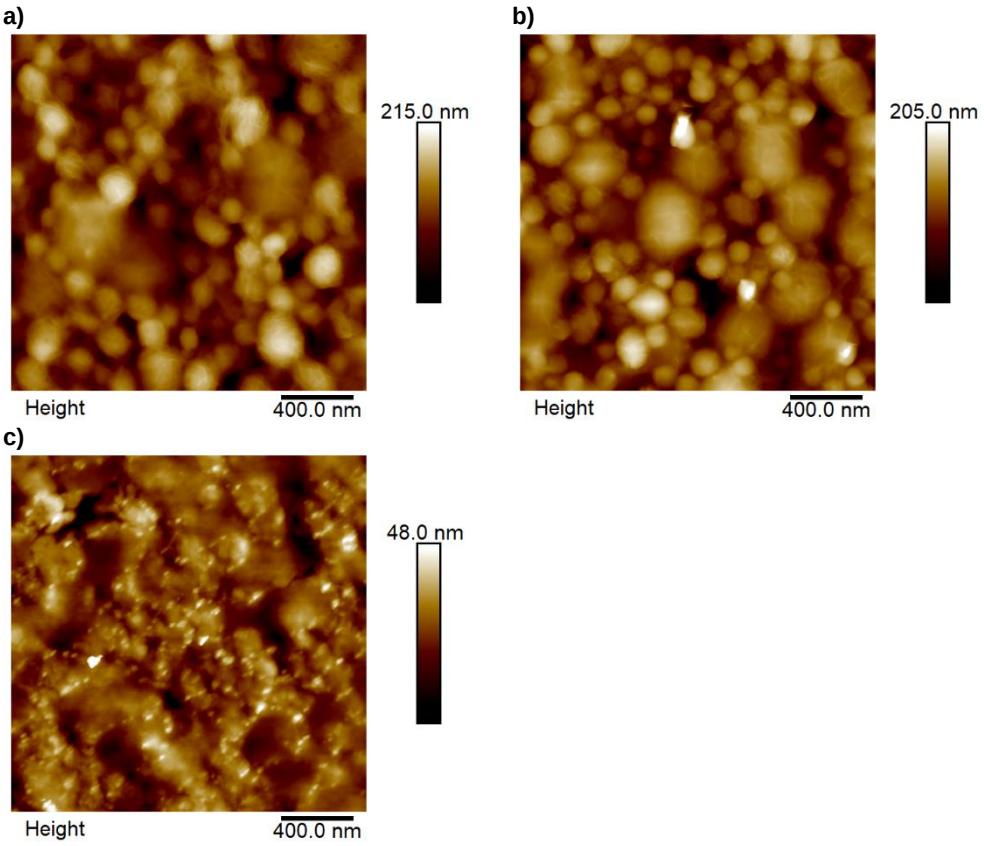

Figure 6-10: AFM height images of the a) air-film interface, b) film-substrate interface and c) cross-section of a dried film of the blend L5:L0 - 1:1 at 23 ºC and 55% relative humidity

A major interest of the CNC armored particles is their influence on the mechanical strength of the films. For example, films cast from pristine CNCs with similar properties as the ones used in this study have a Young's modulus of 2.1 GPa.[68] Therefore, films from latexes L5 and L0 and their blends were dried at 65 °C in Teflon molds for 24h and the mechanical properties measured. A thermogravimetric analysis was performed to confirm that all the water was removed from the films (see Figure III-7 in Appendix III). DSC of the dried films showed a difference in the glass transition of the latex containing CNCs (see Table III-1 and Figure III-8). There are two factors that may contribute to this observation. On the one hand it has previously been observed that glass transition temperature can be changed by the introduction of filler particles such as silica.[69–71] On the other hand, this may be related to a wide composition drift in the reaction due to the higher reactivity of MMA in the copolymerization[72] and the diffusion limitations of the BA to the particle. This results in a wide compositional polydispersity and can broaden the range of the T_g.

The results of the tensile tests are given in Figure 6-11 and Table 6-5. The film from latex L5 presented a high stiffness (40x the Young's modulus and 8x the stress at break of latex L0). However, the flexibility was excessively low due to the high amount of CNCs added to the polymer (20 wt%) and, furthermore, as previously mentioned such films cannot be formed at ambient temperature. When the proportion of L0 in the blend was increased, the Young's modulus decreased and the elongation at break and toughness increased in line with the decrease in the concentration of CNC in the system. With 6.66 wbp% of CNCs (namely the blend L5:L0 - 1:2) the highest toughness was reached with a relatively high Young's modulus whilst still forming a film at ambient temperature. It should be noted that for this blend (L5:L0 –

1:2) the Young`s modulus is an order of magnitude higher than the blank latex L0 in which the polymer has a composition typical of that of a film forming latex used in emulsion paints. For the blend L5:L0 – 2:1, which is also capable of forming a film at ambient temperature, the Young's modulus in excess of 1 GPa is unprecedented for latex polymers and demonstrates the potential of using CNC armored latex particles to produce high strength polymer films cast from aqueous dispersions.

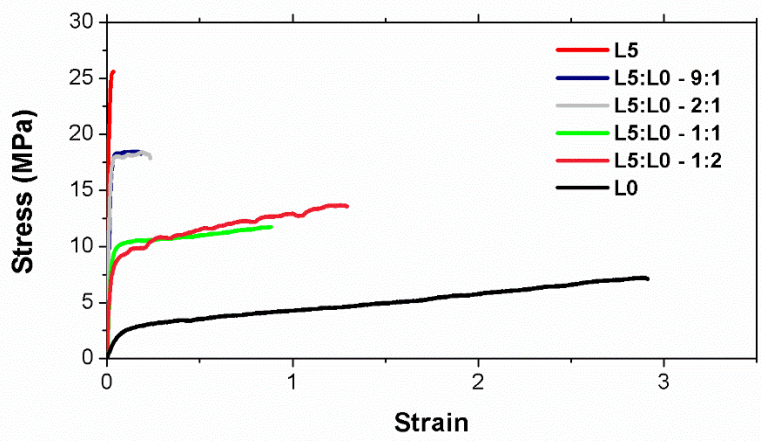

Figure 6-11: Stress-strain curves for latexes with low initiator concentration: L5 with CNCs and L0 without CNCs and the blends dried at 65 ºC and 55% relative humidity

Table 6-5: Tensile tests results for the latexes L5, L0 and the blends dried at 65 ºC and 55% relative humidity

	Young's modulus (MPa)	Elongation at break	Stress at break (MPa)	Toughness (MPa)
L5	1708 ± 320	0.03 ± 0.01	22.5 ± 10	2.9 ± 0.7
L5:L0 – 9:1	1220 ± 180	0.16 ± 0.07	18.4 ± 1.6	3.2 ± 0.3
L5:L0 – 2:1	1074 ± 72	0.23 ± 0.07	17.8 ± 1.9	4 ± 1.5
L5:L0 – 1:1	527 ± 70	0.879 ± 0.2	11.7 ± 0.2	9.4 ± 1.9
L5:L0 – 1:2	405 ± 38	1.28 ± 0.55	13.6 ± 2.5	14.9 ± 7.4
L0	39 ± 5	2.88 ± 0.11	7.2 ± 0.3	14.1 ± 0.7

6.4 Conclusions

CNCs represent one of the strongest natural materials known and when incorporated efficiently into a conventional polymer film can significantly increase its mechanical strength. In order to synthesize CNC armored latex particles for use as coatings, emulsion polymerization of an acrylic latex was conducted using a cationic initiator in the presence of CNCs. The electrostatic interactions between the anionic cellulose nanocrystals and the cationic initiator drove adsorption to the polymer/water interface and led to a formation of CNC armored latex particles. The relative amount of CNC to the cationic initiator was critical in the formation of stable latexes. Under suitable conditions a latex, with low particle size and high monomer

conversion could be obtained. A homogeneous and transparent film from the latex could be obtained at elevated temperature. However, the film was brittle due to the nature of the CNCs. Blending of the CNC armored latex with a conventional, cationically stabilized latex allowed for the possibility to obtain a film with outstanding mechanical properties yet capable of forming a film at room temperature, offering the potential future development of hard VOC-free coatings.

6.5 References

(1) Salas, C.; Nypelö, T.; Rodriguez-Abreu, C.; Carrillo, C.; Rojas, O. J. Nanocellulose properties and applications in colloids and interfaces *Curr. Opin. Colloid Interface Sci.* **2014**, *19*, 383–396.

(2) George, J.; Sabapathi, S. N. Cellulose nanocrystals: synthesis, functional properties, and applications. *Nanotechnol. Sci. Appl.* **2015**, *8*, 45–54.

(3) Reid, M. S.; Villalobos, M.; Cranston, E. D. Benchmarking Cellulose Nanocrystals: From the Laboratory to Industrial Production *Langmuir* **2017**, *33*, 1583–1598.

(4) Mathew, A. P.; Oksman, K.; Karim, Z.; Liu, P.; Khan, S. A.; Naseri, N. Process scale up and characterization of wood cellulose nanocrystals hydrolysed using bioethanol pilot plant *Ind. Crops Prod.* **2014**, *58*, 212–219.

(5) de Souza Filho, M. de sá M.; Nascimento, L. D.; Cassales, A. R.; do Nascimento, D. M.; Morais, J. P. S.; Rosa, M. de F. Extraction and characterization of nanocellulose structures from raw cotton linter *Carbohydr. Polym.* **2012**, *91*, 229–235.

(6) Martínez-Sanz, M.; Lopez-Rubio, A.; Lagaron, J. M. Optimization of the nanofabrication by acid hydrolysis of bacterial cellulose nanowhiskers *Carbohydr. Polym.* **2011**, *85*, 228–236.

(7) García, A.; Gandini, A.; Labidi, J.; Belgacem, N.; Bras, J. Industrial and crop wastes: A new source for nanocellulose biorefinery *Ind. Crops Prod.* **2016**, *93*, 26–38.

(8) Kim, N.; Herth, W.; Vuong, R.; Chanzy, H. The Cellulose System in the Cell Wall of Micrasterias *J. Struct. Biol.* **1996**, *117*, 195–203.

(9) Kalashnikova, I.; Bizot, H.; Bertoncini, P.; Cathala, B.; Capron, I. Cellulosic nanorods of various aspect ratios for oil in water Pickering emulsions *Soft Matter* **2013**, *9*, 952.

(10) Iguchi, M.; Yamanaka, S.; Budhiono, A. Bacterial cellulose - a masterpiece of nature's arts *J. Mater. Sci.* **2000**, *35*, 261–270.

(11) Chen, L.; Wang, Q.; Hirth, K.; Baez, C.; Agarwal, U. P.; Zhu, J. Y. Tailoring the yield and characteristics of wood cellulose nanocrystals (CNC) using concentrated acid hydrolysis *Cellulose* **2015**, *22*, 1753–1762.

(12) Bian, H.; Chen, L.; Wang, R.; Zhu, J. Green and Low-cost Production of Thermally Stable and Carboxylated Cellulose Nanocrystals and Nanofibrils Using Highly Recyclable Dicarboxylic Acids *J. Vis. Exp.* **2017**, *55079*.

(13) Brinchi, L.; Cotana, F.; Fortunati, E.; Kenny, J. M. Production of nanocrystalline cellulose from lignocellulosic biomass: Technology and applications *Carbohydr. Polym.* **2013**, *94*, 154–169.

(14) Kim, J. H.; Shim, B. S.; Kim, H. S.; Lee, Y. J.; Min, S. K.; Jang, D.; Abas, Z.; Kim, J. Review of nanocellulose for sustainable future materials *Int. J. Precis. Eng. Manuf. - Green Technol.* **2015**, *2*, 197–213.

(15) Moon, R. J.; Martini, A.; Nairn, J.; Simonsen, J.; Youngblood, J. Cellulose nanomaterials review: structure, properties and nanocomposites *Chem. Soc. Rev.* **2011**, *40*, 3941.

(16) Hamad, W. On the Development and Applications of Cellulosic Nanofibrillar and Nanocrystalline Materials *Can. J. Chem. Eng.* **2008**, *84*, 513–519.

(17) Hajji, P.; Cavaillé, J. Y.; Favier, V.; Gauthier, C.; Vigier, G. Tensile behavior of nanocomposites from latex and cellulose whiskers *Polym. Compos.* **1996**, *17*, 612–619.

(18) Favier, V.; Canova, G. R.; Cavaillé, J. Y.; Chanzy, H.; Dufresne, A.; Gauthier, C. Nanocomposite materials from latex and cellulose whiskers *Polym. Adv. Technol.* **1995**, *6*, 351–355.

(19) Xu, X.; Liu, F.; Jiang, L.; Zhu, J. Y.; Haagenson, D.; Wiesenborn, D. P. Cellulose

nanocrystals vs. Cellulose nanofibrils: A comparative study on their microstructures and effects as polymer reinforcing agents *ACS Appl. Mater. Interfaces* **2013**, *5*, 2999–3009.

(20) Dufresne, A. Cellulose nanomaterial reinforced polymer nanocomposites *Curr. Opin. Colloid Interface Sci.* **2017**, *29*, 1–8.

(21) Kaboorani, A.; Riedl, B.; Blanchet, P.; Fellin, M.; Hosseinaei, O.; Wang, S. Nanocrystalline cellulose (NCC): A renewable nano-material for polyvinyl acetate (PVA) adhesive *Eur. Polym. J.* **2012**, *48*, 1829–1837.

(22) Nagalakshmaiah, M.; Kissi, N. El; Mortha, G.; Dufresne, A. Structural investigation of cellulose nanocrystals extracted from chili leftover and their reinforcement in cariflex-IR rubber latex *Carbohydr. Polym.* **2015**, *136*, 945–954.

(23) Pu, Y.; Zhang, J.; Elder, T.; Deng, Y.; Gatenholm, P.; Ragauskas, A. J. Investigation into nanocellulosics versus acacia reinforced acrylic films *Compos. Part B Eng.* **2007**, *38*, 360–366.

(24) Bettaieb, F.; Khiari, R.; Dufresne, A.; Mhenni, M. F.; Belgacem, M. N. Mechanical and thermal properties of Posidonia oceanica cellulose nanocrystal reinforced polymer *Carbohydr. Polym.* **2015**, *123*, 99–104.

(25) Abitbol, T.; Prevo, B. G.; Galli, C.; Choudhary, S.; Corwin, J.; Villalpando, F.; Nguyen, L.; Villalobos, M.; Komarov, A.; Veldhuis, S. C.; Cranston, E. D. Comparison of Nanocrystalline Cellulose and Fumed Silica in Latex Coatings *Green Mater.* **2014**, *2*, 206–221.

(26) Pei, A.; Malho, J. M.; Ruokolainen, J.; Zhou, Q.; Berglund, L. A. Strong nanocomposite reinforcement effects in polyurethane elastomer with low volume fraction of cellulose nanocrystals *Macromolecules* **2011**, *44*, 4422–4427.

(27) Negrete-Herrera, N.; Putaux, J.-L.; David, L.; Haas, F. De; Bourgeat-Lami, E. Polymer/Laponite Composite Latexes: Particle Morphology, Film Microstructure, and Properties *Macromol. Rapid Commun.* **2007**, *28*, 1567–1573.

(28) González-Matheus, K.; Leal, G. P.; Asua, J. M. Film formation from Pickering stabilized waterborne polymer dispersions *Polymer* **2015**, *69*, 73–82.

(29) Vatansever, A.; Dogan, H.; Inan, T.; Sezer, S.; Sirkecioglu, A. Properties of na-montmorillonite and cellulose nanocrystal reinforced poly(butyl acrylate-co-methyl

methacrylate) nanocomposites *Polym. Eng. Sci.* **2015**, *55*, 2922–2928.

(30) Ramsden, W. Separation of Solids in the Surface-layers of Solutions and Suspensions (Observations on Surface-membranes, Bubbles, Emulsions, and Mechanical Coagulation). — Preliminary Account. *Proc. R. Soc. London* **1903**, *72*, 156–164.

(31) Pickering, S. U. CXCVI.—Emulsions *J. Chem. Soc. Trans.* **1907**, *91*, 2001–2021.

(32) Rohm, O.; Trommsdorff, E. Process for the polymerization of methyl methacrylate. US 2171765 A, 1939.

(33) Bon, S. A. F. F.; Colver, P. J. Pickering miniemulsion polymerization using laponite clay as a stabilizer *Langmuir* **2007**, *23*, 8316–8322.

(34) González-Matheus, K.; Leal, G. P.; Tollan, C.; Asua, J. M. High solids Pickering miniemulsion polymerization *Polymer* **2013**, *54*, 6314–6320.

(35) Schrade, A.; Landfester, K.; Ziener, U. Pickering-type stabilized nanoparticles by heterophase polymerization *Chem. Soc. Rev.* **2013**, *42*, 6823.

(36) Teixeira, R. F. A.; Mckenzie, H. S.; Boyd, A. A.; Bon, S. A. F. Pickering Emulsion Polymerization Using Laponite Clay as Stabilizer *Macromolecules* **2011**, *44*, 7415–7422.

(37) Colver, P. J.; Colard, C. A. L.; Bon, S. A. F. Multilayered Nanocomposite Polymer Colloids Using Emulsion Polymerization Stabilized by Solid Particles *J. Am. Chem. Soc.* **2008**, *130*, 16850–16851.

(38) Fielding, L. A.; Tonnar, J.; Armes, S. P. All-acrylic film-forming colloidal polymer/silica nanocomposite particles prepared by aqueous emulsion polymerization *Langmuir* **2011**, *27*, 11129–11144.

(39) Bourgeat-Lami, E.; Guimarães, T. R.; Pereira, A. M. C.; Alves, G. M.; Moreira, J. C.; Putaux, J.-L.; dos Santos, A. M. High Solids Content, Soap-Free, Film-Forming Latexes Stabilized by Laponite Clay Platelets *Macromol. Rapid Commun.* **2010**, *31*, 1874–1880.

(40) Dupin, D.; Schmidt, A.; Balmer, J. A.; Armes, S. P. Efficient synthesis of poly(2-vinylpyridine)-silica colloidal nanocomposite particles using a cationic azo initiator *Langmuir* **2007**, *23*, 11812–11818.

(41) Brunier, B.; Sheibat-Othman, N.; Chevalier, Y.; Bourgeat-Lami, E. Partitioning of Laponite Clay Platelets in Pickering Emulsion Polymerization *Langmuir* **2016**, *32*, 112–124.

(42) Kalashnikova, I.; Bizot, H.; Cathala, B.; Capron, I. New pickering emulsions stabilized by bacterial cellulose nanocrystals *Langmuir* **2011**, *27*, 7471–7479.

(43) Paximada, P.; Tsouko, E.; Kopsahelis, N.; Koutinas, A. A.; Mandala, I. Bacterial cellulose as stabilizer of o/w emulsions *Food Hydrocoll.* **2016**, *53*, 225–232.

(44) Kedzior, S. A.; Marway, H. S.; Cranston, E. D. Tailoring Cellulose Nanocrystal and Surfactant Behavior in Miniemulsion Polymerization *Macromolecules* **2017**, *50*, 2645–2655.

(45) Buffiere, J.; Balogh-Michels, Z.; Borrega, M.; Geiger, T.; Zimmermann, T.; Sixta, H. The chemical-free production of nanocelluloses from microcrystalline cellulose and their use as Pickering emulsion stabilizer *Carbohydr. Polym.* **2017**, *178*, 48–56.

(46) Zhai, X.; Lin, D.; Liu, D.; Yang, X. Emulsions stabilized by nanofibers from bacterial cellulose: New potential food-grade Pickering emulsions *Food Res. Int.* **2018**, *103*, 12–20.

(47) Fujisawa, S.; Togawa, E.; Kuroda, K. Facile Route to Transparent, Strong, and Thermally Stable Nanocellulose/Polymer Nanocomposites from an Aqueous Pickering Emulsion *Biomacromolecules* **2017**, *18*, 266–271.

(48) Werner, A.; Schmitt, V.; Sèbe, G.; Héroguez, V. Synthesis of surfactant-free micro- and nanolatexes from Pickering emulsions stabilized by acetylated cellulose nanocrystals *Polym. Chem.* **2017**, *8*, 6064–6072.

(49) Ben Mabrouk, A.; Rei Vilar, M.; Magnin, A.; Belgacem, M. N.; Boufi, S. Synthesis and characterization of cellulose whiskers/polymer nanocomposite dispersion by mini-emulsion polymerization *J. Colloid Interface Sci.* **2011**, *363*, 129–136.

(50) Kedzior, S. A.; Dubé, M. A.; Cranston, E. D. Cellulose Nanocrystals and Methyl Cellulose as Costabilizers for Nanocomposite Latexes with Double Morphology *ACS Sustain. Chem. Eng.* **2017**, *5*, 10509–10517.

(51) Grishkewich, N.; Mohammed, N.; Tang, J.; Tam, K. C. Recent advances in the application of cellulose nanocrystals *Curr. Opin. Colloid Interface Sci.* **2017**, *29*, 32–45.

(52) Werner, A.; Sèbe, G.; Heroguez, V. New Strategy to Elaborate Polymer Composites via Pickering Emulsion Polymerization of a large range of monomers *Polym. Chem.* **2018**, *9*, 5043–5050.

(53) Liu, L.; Hu, Z.; Sui, X.; Guo, J.; Cranston, E. D.; Mao, Z. Effect of Counterion Choice on the Stability of Cellulose Nanocrystal Pickering Emulsions *Ind. Eng. Chem. Res.* **2018**, *57*, 7169–7180.

(54) Biensan, M. Process for the preparation of polymer powders by suspension polymerization. US5,840,819, 1998.

(55) Zhang, Y.; Karimkhani, V.; Makowski, B. T.; Samaranayake, G.; Rowan, S. J. Nanoemulsions and Nanolatexes Stabilized by Hydrophobically Functionalized Cellulose Nanocrystals *Macromolecules* **2017**, *50*, 6032–6042.

(56) Asua, J. M. Challenges for industrialization of miniemulsion polymerization *Prog. Polym. Sci.* **2014**, *39*, 1797–1826.

(57) Faridi-Majidi, R.; Sharifi-Sanjani, N.; Agend, F. Encapsulation of magnetic nanoparticles with polystyrene via emulsifier-free miniemulsion polymerization *Thin Solid Films* **2006**, *515*, 368–374.

(58) Ruggerone, R.; Plummer, C. J. G.; Negrete Herrera, N.; Bourgeat-Lami, E.; Månson, J. A. E. Fracture mechanisms in polystyrene/laponite nanocomposites prepared by emulsion polymerization *Eng. Fract. Mech.* **2009**, *76*, 2846–2855.

(59) Bonnefond, A.; Mičušík, M.; Paulis, M.; Leiza, J. R.; Teixeira, R. F. A.; Bon, S. A. F. Morphology and properties of waterborne adhesives made from hybrid polyacrylic/montmorillonite clay colloidal dispersions showing improved tack and shear resistance *Colloid Polym. Sci.* **2013**, *291*, 167–180.

(60) González, E.; Bonnefond, A.; Barrado, M.; Casado Barrasa, A. M.; Asua, J. M.; Leiza, J. R. Photoactive self-cleaning polymer coatings by TiO2 nanoparticle Pickering miniemulsion polymerization *Chem. Eng. J.* **2015**, *281*, 209–217.

(61) Petersen, C.; Heldmann, C.; Johannsmann, D. Internal stresses during film formation of polymer latices *Langmuir* **1999**, *15*, 7745–7751.

(62) Tirumkudulu, M. S.; Russel, W. B. Cracking in drying latex films *Langmuir* **2005**, *21*, 4938–4948.

(63) Yow, H. N.; Beristain, I.; Goikoetxea, M.; Barandiaran, M. J.; Routh, A. F. Evolving stresses in latex films as a function of temperature *Langmuir* **2010**, *26*, 6335–6342.

(64) Tzitzinou, A.; Keddie, J. L.; Geurts, J. M.; Peters, A. C. I. A. I. A.; Satguru, R. Film formation of latex blends with bimodal particle size distributions: Consideration of particle deformability and continuity of the dispersed phase *Macromolecules* **2000**, *33*, 2695–2708.

(65) Grillet, A.-C.; Brunel, S.; Chevalier, Y.; Usoni, S.; Ansanay-Alex, V.; Allemand, J. Control of the morphology of waterborne nanocomposite films *Polym. Int.* **2004**, *53*, 569–575.

(66) López, A. B.; de la Cal, J. C.; Asua, J. M. Highly Hydrophobic Coatings from Waterborne Latexes *Langmuir* **2016**, *32*, 7459–7466.

(67) Schulz, M.; Keddie, J. L. A critical and quantitative review of the stratification of particles during the drying of colloidal films *Soft Matter* **2018**, *14*, 6181–6197.

(68) Bras, J.; Viet, D.; Bruzzese, C.; Dufresne, A. Correlation between stiffness of sheets prepared from cellulose whiskers and nanoparticles dimensions *Carbohydr. Polym.* **2011**, *84*, 211–215.

(69) Reid, C. G.; Greenberg, A. R. Influence of silica reinforcement upon the glass transition behavior of acrylic polymers *J. Appl. Polym. Sci.* **1990**, *39*, 995–1014.

(70) Howard, G. J.; Shanks, R. A. The influence of filler particles and polymer structure on the mobility of polymer molecules *J. Appl. Polym. Sci.* **1981**, *26*, 3099–3102.

(71) The Effect of Fillers on Polymer Properties AU - Peyser, P. *Polym. Plast. Technol. Eng.* **1978**, *10*, 117–129.

(72) Aerdts, A. M.; German, A. L.; van der Velden, G. P. M. Determination of the reactivity ratios, sequence distribution and stereoregularity of butyl acrylate-methyl methacrylate copolymers by means of proton and carbon-13 NMR *Magn. Reson. Chem.* **1994**, *32*, S80–S88.

Chapter 7. Linking film structure and mechanical strength in nanocomposite films formed from heterocoagulated dispersions of cellulose nanocrystals(CNC) and acrylic latexes

7.1 Introduction

In Chapter 6, the synthesis of cellulose nanocrystals anchored latex particles was described and it was shown that these hybrid particles led to reinforced films thanks to the CNCs dispersed in the polymer matrix. In this chapter, we describe the synthesis of hybrid particles of a meth(acrylic) polymer and CNCs by heterocoagulation processes based on interactions between particles of dissimilar natures. The heterocoagulation processes were controlled by electrostatic interactions of the anionic CNCs (due to the presence of sulfate half ester groups) with preformed cationically charged particles latexes.

Two distinct hybrid particle morphologies were obtained using cationically charged particles of different sizes. On one hand, when the latex particles were larger (d_p = 510 nm) than the length of CNCs, the CNCs adsorbed onto the polymer particle surface (Scheme 7-1). The adsorption of the CNCs on the cationic particles led to a similar particle morphology than in Chapter 6.

Scheme 7-1: Heterocoagulation process using large cationically charged particles and cellulose nanocrystals

On the other hand, when small polymer particles were used (namely under 30 nm radius), the polymer particles adsorbed onto the CNCs (Scheme 7-2). Adsorption of polymer particles onto the surface of inorganic materials has been used in the past to obtain core-shell particles with the polymer forming the shell.[1] However, as illustrated in Scheme 7-2, the expected morphology was not core-shell. This technique favors good dispersion of the inorganic material in the polymer matrix, which improves the mechanical properties.

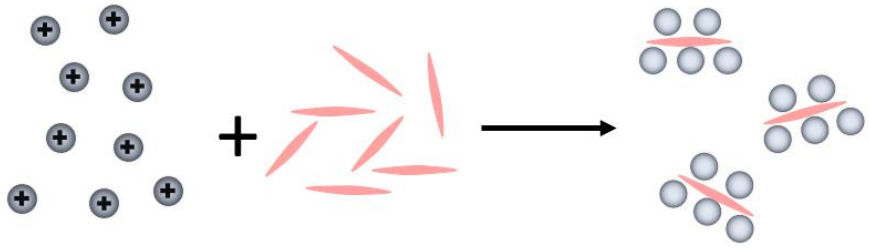

Scheme 7-2: Heterocoagulation process using small cationically charged particles and cellulose nanocrystals

For the sake of comparison, CNCs were blended with anionically charged latex particles (Scheme 7-3). As shown in Section 6.1, cellulose derivatives can directly be blended with an anionically charged particles latex at high solids content, improving the mechanical properties of the composite film.[2–4] However, films cast from such dispersions may result in phase separation of the two colloids and lead to poor physical properties of the film.[5,6]

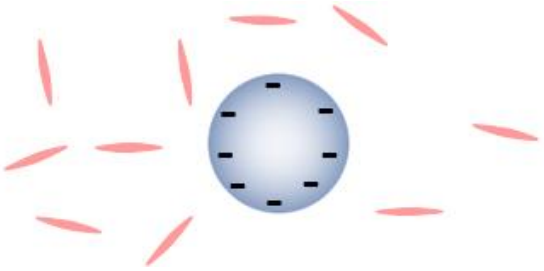

Scheme 7-3: Schematic view of a blend of CNCs with anionically charged particles latex

7.2 Experimental part

7.2.1 Materials

Methyl methacrylate (MMA, technical grade, Quimidroga) and butyl acrylate (BA, technical grade, Quimidroga)) were used as received. 2,2′-Azobis(2-methylpropionamidine) dihydrochloride (AIBA, 97%, Sigma-Aldrich) and potassium persulfate (KPS, Sigma-Aldrich) were used as thermal initiators. Dowfax 2A-1 (alkyldiphenyloxide disulfonate, Dow Chemical Co.), Emulan OG (BASF) and dodecyltrimethylammonium Bromide (DMAB, Sigma-Aldrich,

>99%) were used as surfactants. Sodium bicarbonate ($NaHCO_3$, Sigma-Aldrich, >99.5%) was used as received. GPC grade tetrahydrofuran (THF, Scharlau) was also used as received. Cellulose nanocrystals were provided by Alberta Innovates Technology Futures. Deionized water was used throughout the work.

7.2.2 Synthesis of the acrylic polymer latexes and hybrid preparation

A 35 wt % solids content latex (LLC: Latex with Large Cationically charged particles) stabilized by a cationic emulsifier (dodecyltrimethylammonium bromide, DMAB), was synthesized using a cationic initiator (2,2′-Azobis(2-methylpropionamidine) dihydrochloride, AIBA) by semi-continuous emulsion polymerization. The formulation used to prepare the latex is given in Table 7-1. The polymerization was carried out in a 1- L glass reactor equipped with a reflux condenser, an Ekato Mig impeller, sampling device and nitrogen inlet. The temperature of the reaction was 70 ºC and the agitation rate 180 rpm. The initial charge was a solution composed of 1 wt% of the total surfactant, 50% of the total water and all of the $NaHCO_3$. The initial charge was purged with nitrogen for 30 minutes. After reaching the desired temperature (70 ºC) the rest of the formulation was fed during 6 hours. Afterwards the latex was left to react in batch for another hour.

A 5 wt% solids content latex, (LSC: Latex with Small Cationically charged particles) was synthesized by semi-continuous emulsion polymerization. Particles were stabilized by the combination of the nonionic polymeric surfactant (Emulan OG) and the cations resulting from AIBA that was used as initiator. The formulation used to prepare the latex is given in Table 7-1. The polymerization was carried out in a 500- mL glass reactor equipped with a reflux condenser, a stainless steel anchor type stirrer, a sampling device and nitrogen inlet. The temperature reaction was 70 ºC and the agitation rate 180 rpm. An initial charge of a solution composed of the total amount of surfactant and water was added to the reactor together with 5 wt% of the total amount of monomers. The initial charge was purged with nitrogen for 30 minutes. After reaching the desired temperature (70 ºC), the initiator, previously dissolved in a minimum amount of water, was added as a shot. Five minutes after the addition of the initiator, the rest of the monomers was fed for 2 hours. Then, the latex was left to react batchwise during 2 hours.

A 35 wt% solids content latex (LA: Latex with Anionically charged particles) was synthesized by semi-continuous emulsion polymerization. Particles were stabilized by an anionic emulsifier, Dowfax 2A-1. The formulation used to prepare the latex is given in Table 7-1. The polymerization was carried out in a 1- L glass reactor equipped with a reflux condenser, a stainless steel anchor type stirrer, a sampling device and nitrogen inlet. The temperature reaction was 70 ºC and the agitation rate 180 rpm. The initial charge was a solution composed of 1% of the total surfactant, 50% of the total water and all of the $NaHCO_3$. The initial charge was purged with nitrogen for 30 minutes. After reaching the desired temperature (70 ºC), the

rest of the formulation was fed for 3 hours. Afterwards, the latex was left to react batchwise during 1 hour.

Finally, a 3 wt% dispersion of CNCs was prepared as follows: the freeze-dried CNCs were dispersed in water, and let under magnetic agitation for 15 min. Then, the dispersion was sonicated for 10 minutes in order to disperse the agglomerates. The latexes (previously diluted to 20 wt% for LLC and LA) were then blended with the 3 wt% dispersion of cellulose nanocrystals (in order to obtain a concentration of 20 wbp % of CNCs) under an agitation of 1000 rpm. Moreover, different amounts of cellulose nanocrystals (2.5, 5, 10 and 20 wbp %) were blended with the latexes LA and LSC in order to study the effect of the concentration of cellulose nanocrystals on film properties.

Table 7-1: Formulation of the latexes

Compounds	LLC (g)	LSC (g)	LA (g)
Water	617	332	616
DMAB	9.69	-	-
Emulan OG	-	3.8	-
Dowfax 2A-1	-	-	6.6
MMA	180	8.8	180
BA	180	8.8	180
AIBA	2.52	0.245	-
KPS	-	-	1.8
$NaHCO_3$	0.2	-	0.2

7.2.3 Characterization

The particle size of the final latexes and blends were measured by dynamic light scattering (DLS), Zeta potential was calculated from the measure of electrophoretic mobility of the latexes and the CNCs dispersion. The molecular weight distributions were determined by gel permeation chromatography (GPC). Particles morphology was determined by transmission electron microscopy (TEM). The film morphologies were studied by means of atomic force microscope (AFM). The mechanical properties of the films cast from the synthesized latexes and blends were determined by tensile test measurements. A detailed description of the characterization methods is provided in Appendix I.

7.3 Results and discussion

7.3.1 Interactions between CNCs and the latexes particles

The characteristics of the latexes synthesized by semi-batch emulsion polymerization are given in Table 7-2. Due to the different strategies used for polymerizations, the latexes presented different surface charges, particle sizes and molecular weights. Comparison between LLC and LSC shows that particle size was smaller for LSC likely due to the contribution of the non-ionic surfactant used (Emulan OG). There were also surprising results. On one hand, the larger particles (LLC) had a lower zeta potential (9.8 mV) than LSC (31.4 mV) even though LLC used a cationic surfactant and the amount of cationic initiator per unit of

surface area was higher than for LSC. The low zeta potential of LLC led to partial coagulation of the latex with storage time. The second surprising result was that the molecular weight of the polymer was lower for the latex with small particles (LSC), when the opposite is expected in emulsion polymerization for the case in which the radicals are produced in the aqueous phase. A possible explanation of these surprising results is that the radicals were not only produced in the aqueous phase. Although AIBA is completely soluble in water, it partitions between the aqueous and organic phases (the partition coefficient octanol-water is PoW=0.3,[7] which is similar to that of the n-propanol[8]). Therefore, a non-negligible fraction of radicals were generated in pairs within the polymer particles. This had two consequences. On one hand, the molecular weight is lower in the small particle because the radicals terminate rapidly.[9] On the other, some of the stabilizing moieties from the initiator became buried in the polymer particles, and the fraction that became buried was likely greater for the large particles. In addition, the positive charges of the initiator hindered the adsorption of the cationic surfactant leading to a low zeta potential.

These three latexes were then blended with a dispersion of cellulose nanocrystals to form hybrid particles. In order to obtain a blend with a relatively high solids concentration, a 3 wt% CNCs dispersion was used. Above this concentration, due to the high aspect ratio of the CNCs, the dispersion was too viscous and coagulation occurred during blending. As described in the experimental part, the latex LLC was added to the CNC dispersion under vigorous agitation. This ensured that the surface charges of the latex particles were rapidly masked by generation of the CNC armored structure (see Scheme 7-4a) and prevented aggregation between partially covered particles. When, alternatively, the CNC dispersion was added to the

latex, the blend coagulated instantaneously. In this case the CNCs acted as a flocculant (see Scheme 7-4b).[10]

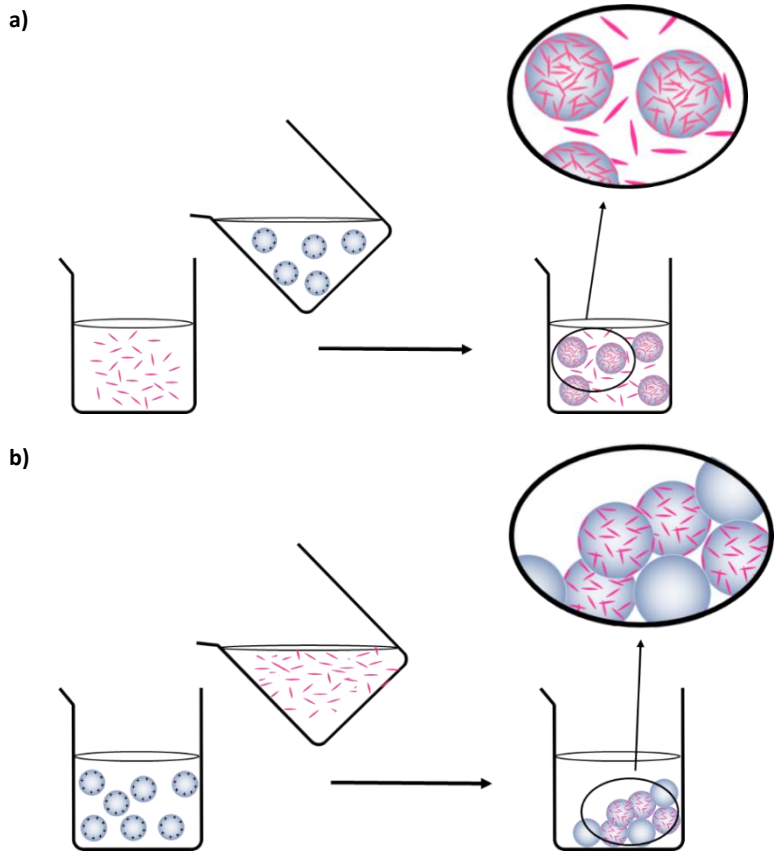

Scheme 7-4: Representation of a) addition of the cationic latex on CNC particles giving rise to CNC armored latex particles and b) addition of the CNC particles on the cationic latex leading to aggregation

Table 7-2 Characteristics of the blank latexes and blends

	Solids content (%)	Particle size (nm)	Mn (kg/mol)	Mw (kg/mol)	Đ	Zeta potential (mV)
CNCs dispersion	3	117	-	-	-	-39.4
LLC	20*	510	168.2	446.4	2.7	9.8
LLC – 20%CNC	13.2**	1500	-	-	-	-33.4
LSC	5.2	33	72.3	270.3	3.7	31.4
LSC – 20%CNC	4.5	7300	-	-	-	-17.5
LA	20*	112	166.2	678.0	4.1	-42.5
LA – 20%CNC	13.2**	115	-	-	-	-42.6

* After dilution

**After blending with a 3 wt% dispersion of CNCs

The zeta potential of the blends was monitored during the addition of LLC to the CNC dispersion (see Table 7-3). At all ratios, the zeta potential was close to the zeta potential of a pure CNC dispersion indicating a large excess of CNCs. The final blend presented a concentration of cellulose nanocrystals of 20 wbp% (weight based on polymer). Higher loadings of polymer were impossible to obtain due to coagulation while adding the latex to the CNCs dispersion. Particle size of the blend was measured by DLS. The particle size increased from 510 nm (pure polymer particle) to 1.5 µm in the blend (see Table 7-2) showing that some limited aggregation of the hybrid particles occurred. Figure 7-1 presents the particle morphology of LLC-20%CNC. These images confirm the adsorption of the CNCs onto the particles surface and the limited aggregation. However, these images show that a large fraction of CNCs was free in the system showing the limitation of this process.

Table 7-3: Evolution of zeta potential while adding LLC to the CNC dispersion

% polymer (wt)*	Zeta potential (mV)
20	-36.2
40	-34.3
60	-33.4
80	-33.4

*Weight based on CNC

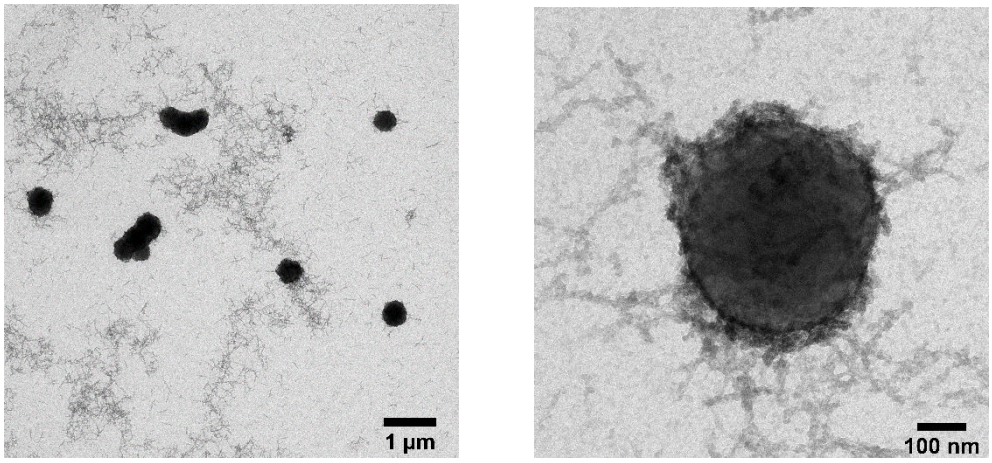

Figure 7-1: TEM images of the particle morphology of LLC-20%CNC

When using the latex LSC, the dispersion of CNCs was added dropwise to the latex LSC as the small latex particles adsorb onto the CNCs. If the blend is prepared by adding the polymer dispersion on the CNCs, flocculation occurs for a similar reason than in LLC.[10] In this case, the zeta potential decreased gradually during the addition of the CNC dispersion (Table 7-4) until eventually a negative potential was observed, suggesting an excess of CNCs. Particle size measurement of the blend showed that some aggregation of the hybrid particles occurred for these hybrid particles due to the interaction between cationically stabilized aggregates and the excess CNCs (Table 7-4).

Table 7-4: Evolution of zeta potential while adding the CNC dispersion to LSC

% CNC (wbp)	Zeta potential (mV)	Particle size (nm)
0	31.4	31.4
5	19.3	415
10	15.3	1600
15	11.4	4100
20	-17.5	7300

For the blend of anionic stabilized particles with CNCs, LA-20%CNC, the particle size of the polymer particles remained the same in the blend (Table 7-2). It has to be pointed out that the hydrodynamic volume of the pure CNCs measured by DLS was around 110 nm meaning that the addition of the CNCs should not affect the measurement of the particle size of the blend if the CNCs do not form any structure. The DLS measurements showed that there was no aggregation of the nanocrystals with the polymer particles due to the repulsive interactions between the two negatively charged constituents of the blend.

7.3.2 Film morphology and properties

Figure 7-2 presents the AFM height images of the morphology of a film cast from the blend LA-20%CNC at 23 ºC and 55% relative humidity. Also, a schematic representation of the cross-section of the film is included for better understanding. Some CNCs are present at the air-film interface and the film-substrate interface, as indicated by arrows. In the cross-section, large aggregates were visible; they were formed by depletion induced flocculation of the polymer particles by the CNCs, thus leading to phase separation. The action of CNCs as flocculating agents has previously been observed in mixtures of CNCs and certain species of bacteria.[11,12] These aggregates were not visible in the dispersed state because of the low solids content (13.3 wt%) but as the water evaporated during film formation, the depletion interactions become stronger, leading to phase separation.

Figure 7-3 presents the AFM height images of the air-film and film-substrate interfaces as well as that of the cross-sections of the film cast form the blend LLC-20%CNC at 23 ºC and 55% relative humidity. Also, a schematic representation of the cross-section of the film is included for better understanding. CNCs are present at both the air-film interface and film-substrate interface. These images, compared with the ones of LA-20%CNC, confirm that the CNCs were covering the particles as a result of the electrostatic interactions between the nanocrystals and the latex particles. In the cross-section, the boundaries of the particles were visible with the cellulose nanocrystals surrounding them, leading to a honeycomb structure of CNCs. In addition to the honeycomb like structure, aggregates of CNCs were present in the film. The black defects on the cross-section image (shown with the arrows) corresponded to

CNCs aggregates removed from the film with the knife during sample preparation. It has to be pointed out that the aggregates formed are small compared to the large fraction of free CNCs visible in Figure 7-1, meaning that some free CNCs formed part of the honeycomb structure.

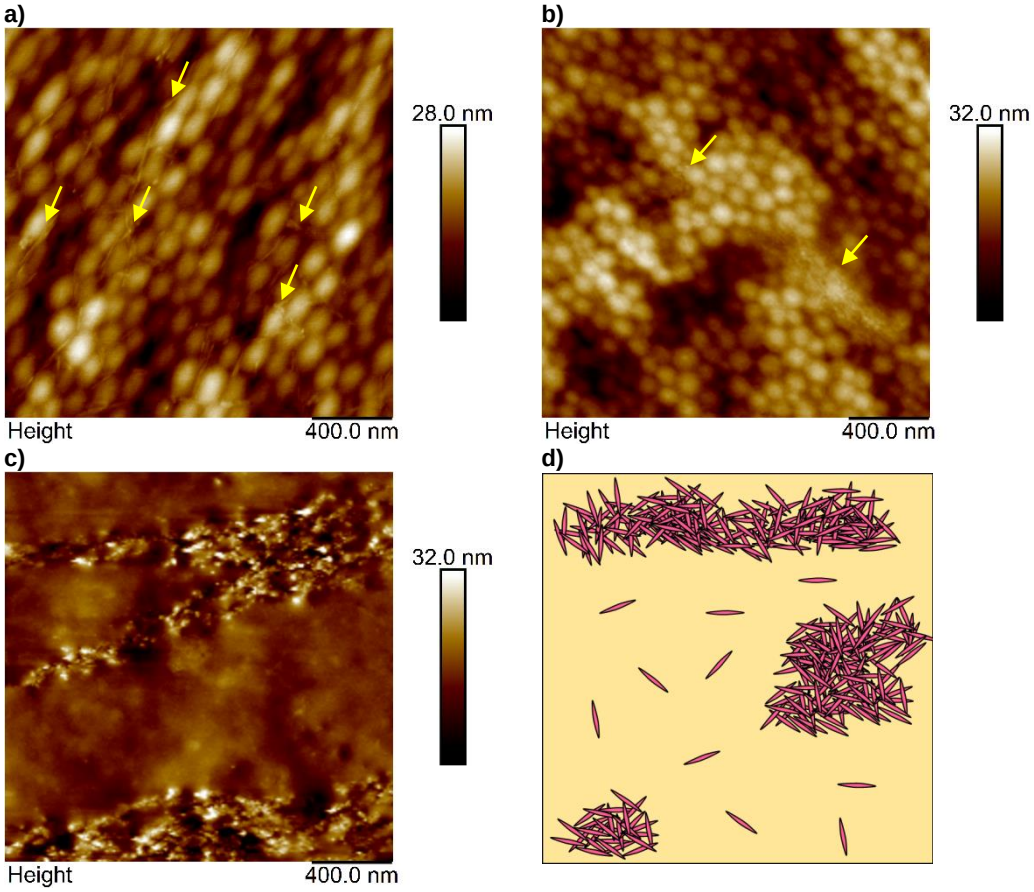

Figure 7-2: AFM height images of the a) air-film interface, b) substrate-film interface, c) cross-section and d) schematic representation of a film cast from the blend LA-20%CNC at 23 ºC and 55% relative humidity

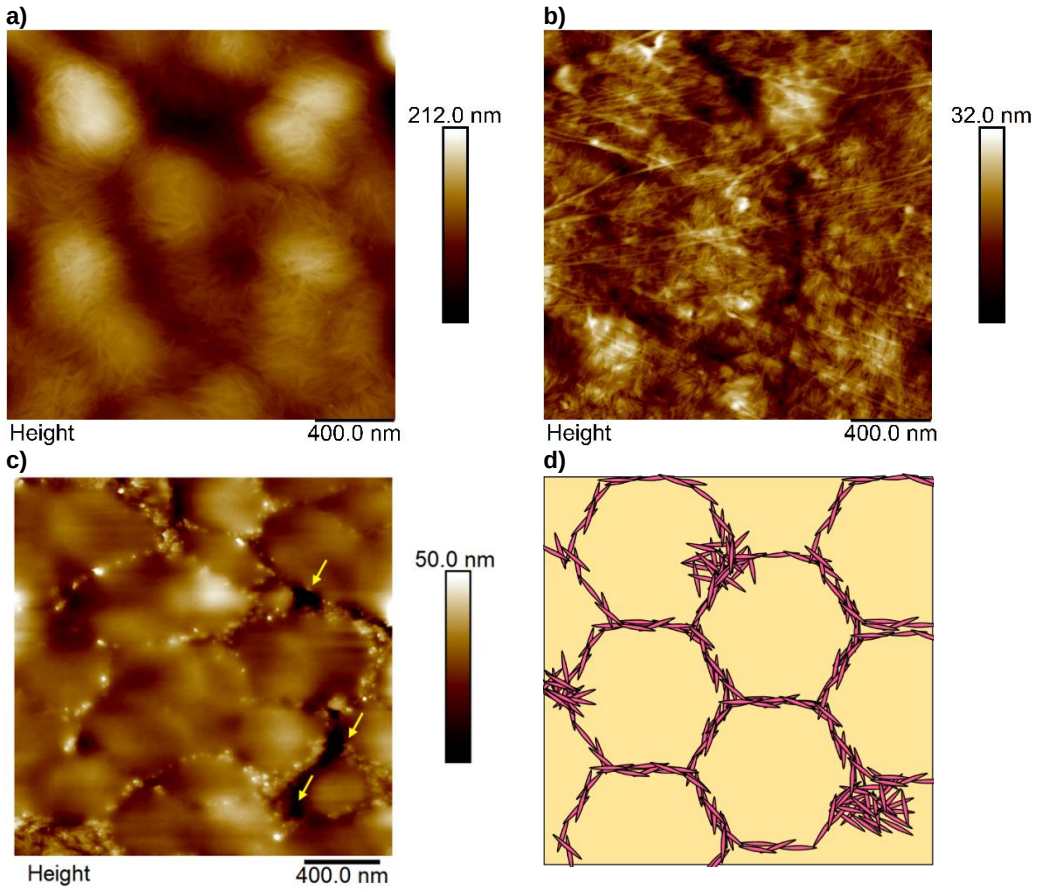

Figure 7-3: AFM height images of the a) air-film interface, b) substrate-film interface, c) cross-section and d) schematic representation of the cross-section of a film cast from the blend LLC-20%CNC at 23 ºC and 55% relative humidity

Figure 7-4 presents the AFM height images of the air-film and film-substrate interfaces as well as that of the cross-sections of the film cast from the blend LSC-20%CNC at 23 ºC and 55% relative humidity. A schematic representation of the cross-section of the film is included for better understanding. Films were immersed in water for 5 minutes before analysis to remove the excess of surfactant on the surface of the film. The film morphology was in agreement with the particle morphology. As the small cationically charged polymer particles adsorb on the CNCs surface, the CNCs were encapsulated by the polymer after film formation. This led to a homogenous dispersion of the CNCs in the polymer matrix as single crystals (whit dots on Figure 7-4 c). Although the CNCs looked aligned on the cross-section view, this is likely due to an artifact of the measurement due to tip displacement in the horizontal direction on the relatively soft polymer. At the interfaces of the film, CNCs were not visible as they were covered by polymer.

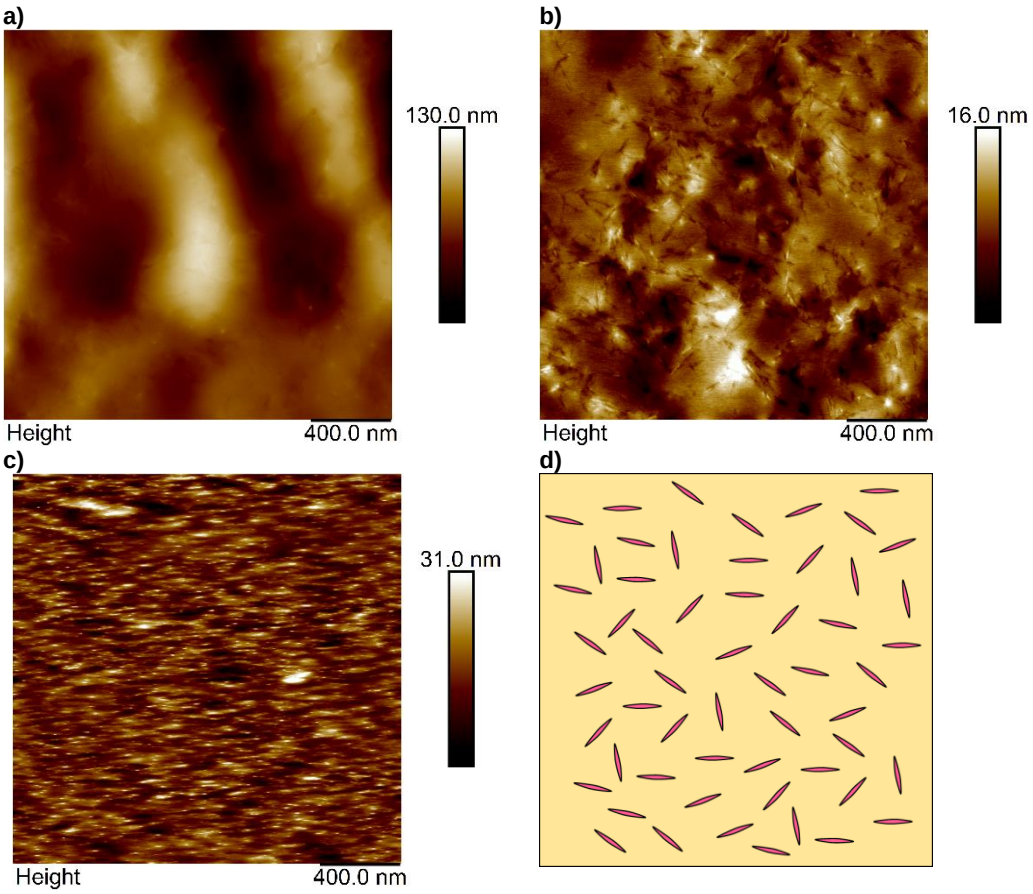

Figure 7-4: AFM height images of the a) air-film interface, b) substrate-film interface, c) cross-section and d) schematic representation of a film cast from the blend LSC-20%CNC at 23 ºC and 55% relative humidity

Figure 7-5 and Table 7-5 show the mechanical properties of films cast from the latexes and their corresponding blends at 23 ºC and 55% relative humidity. Comparing first the latexes alone without the addition of CNCs, LSC presented the longest elongation at break and smallest toughness of the three polymers. LA presented the highest toughness. This was due to the difference in molecular weights of the polymers (Table 7-2). Indeed, LSC showed the lowest molecular weight and LA the highest. The addition of the cellulose nanocrystals increased the Young's modulus in all blends, decreasing at the same time the elongation at break and the toughness of the films. This was due to the properties of the cellulose nanocrystals (high Young's modulus) and the high amount of nanocrystals added (20 wbp %) which increase hardness but decrease flexibility.

It is important to note that the extent to which the addition of CNCs affected the mechanical properties was very different depending on the particle morphology of the blends. In the case of LLC-20%CNC, Young's modulus increased by approximately 10 times and the yield stress of the material was considerably higher. For LA-20% CNC although the Young's modulus increased, the film had very low flexibility and ultimate tensile stress was considerably lower than for the latex alone. Similarly, for LSC-20%CNC the flexibility decreased strongly without any real increase in the yield stress of the material. These features can be related to the structure of the films. In the case of LSC-20%CNC the CNC particles were encapsulated and thus in the film there was no interaction between the individual CNC particles (Figure 7-4c and d). As a result, the CNCs acted as fillers (increase of strength and modulus but decrease of toughness and flexibility).[13,14] In the case of LA-20%CNC, the presence of aggregates of CNCs (Figure 7-2d) led to a brittle film with very poor cohesion between the nanocrystals after

film formation. Only in the case of LLC-20%CNC, where the CNCs were forming a honeycomb structure (Figure 7-2 d), the strength of the CNCs efficiently translated into strength of the nanocomposite.[15,16]

The hybrid particles obtained in Chapter 6 did not form a film at 23 ºC because they were hard. There were two main differences with respect the particles in this chapter. The first one was that in Chapter 6, batch emulsion polymerization was used compared to semi-batch polymerization here. Due to the difference in reactivity ratio between MMA and BA, a broader polymer composition distribution was obtained in batch emulsion polymerization leading to the formation of some MMA-rich hard polymer. The second difference is related to the link between the CNC and the polymer particles. In Chapter 6, the CNC was used as a Pickering agent to stabilize the particles and therefore it was strongly attached to the surface of the particles forming a hard shell that hindered film formation. However, in the case of LLC, the CNC were more loosely attached to the polymer particles or even not attached at all. This made the surface of the particles much more flexible and there were able to deform and form film. In conclusion, the heterocoagulation process presents some advantages compared to the method developed in Chapter 6, although surfactant is used.

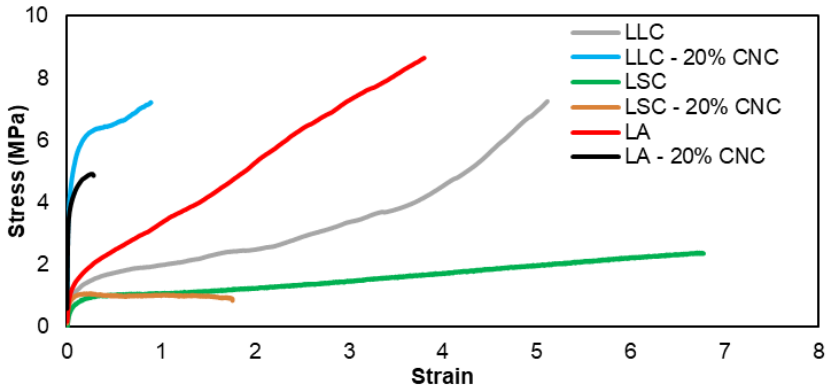

Figure 7-5: Stress-strain curves of films cast from the blank latexes and the blends at 23 ºC and 55% relative humidity

Table 7-5: Tensile tests results of films cast from the blank latexes and the blends at 23 ºC and 55% relative humidity

	Young's modulus (MPa)	Yield stress (MPa)	Elongation at break	Stress at break (MPa)	Toughness (MPa)
LLC	48 ± 6	1.90 ± 0.34	5.17 ± 0.79	7.5 ± 0.78	17.5 ± 3.6
LLC – 20% CNC	407 ± 33	5.24 ± 0.88	0.91 ± 15	7.2 ± 1.3	5.8 ± 0.5
LSC	7 ± 4	0.72 ± 0.17	8.06 ± 1.5	1.85 ± 0.34	9.27 ± 1.67
LSC – 20% CNC	47 ± 15	1.11 ± 0.1	1.78 ± 0.86	0.94 ± 0.09	2.06 ± 0.53
LA	37 ± 5	2.3 ± 0.65	3.81 ± 0.43	8.6 ± 1.2	20 ± 2.8
LA – 20% CNC	265 ± 15	4.11 ± 0.6	0.273 ± 0.04	4.9 ± 0.44	1.1 ± 0.26

In order to confirm the effect of particle morphology on the mechanical properties, the effect of the CNC content with the latexes LSC and LA was studied. This could not be performed with LLC because the blend coagulated with loadings of CNCs lower than 20 wbp %. The results are given in Figure 7-6 and Table 7-6 for LSC and in Figure 7-7 and Table 7-7 for LA. It can be seen that the films became stiffer with the increase in the concentration of CNCs. For LSC, the elongation at break remained constant from 2.5 to 10 wbp% CNCs and decreased by 2.5 times at 20 wbp% of CNCs. As the CNCs were encapsulated by the polymer they did not show connectivity between them in the final film which, as previously discussed, led to a limited reinforcement of the film. Above 10%, the presence of free CNCs, as shown by the negative zeta potential (see Table 7-4), results in aggregated domains of CNCs with poor cohesive strength and leads to a significant decrease in the flexibility of the film. In the case of anionically charged particles (LA), with 2.5% of CNC, the Young's modulus increased maintaining the elongation at break due to the homogeneous distribution of the CNCs through the film (Figure 7-7). Above this concentration of cellulose nanocrystals, the film hardened as the Young's modulus and stress at break increased, while the toughness and elongation at break decreased. As the concentration of CNCs increased, the aggregates formed due to the repulsive forces between the CNCs and the polymer particles (Figure 7-2 d) which increased the stiffness of the film. For both systems, a similar increase of Young's modulus was obtained with the increase of the amount of cellulose nanocrystals in the blends. These results are in line with the theories of mechanical properties of the incorporation of fillers in composite materials such as that proposed by Halpin-Ksaï (see equation 7-1).[13,14,17,18]

$$\frac{E_C}{E_m} = \frac{1 + AB\emptyset_f}{1 - B\emptyset_f} \quad \textbf{(7-1)}$$

$$B = \frac{\left(\frac{E_f}{E_m}\right) - 1}{\left(\frac{E_f}{E_m}\right) + A} \quad \textbf{(7-2)}$$

$$A = 2 \times \frac{L}{w} \quad \textbf{(7-3)}$$

whereE_C, E_m and E_f are the Young's moduli of the composite, the matrix and the filler, respectively,$\emptyset_f$ to the volume fraction of filler, *A* is a constant that reflects the geometry of the filler (the length, *L*, and the width, *w*, of the CNCs), B is a constant that takes into account the relative moduli of the continuous and dispersed phases.

The theoretical Young's moduli of the blends were calculated using. E_f =2.1 GPa[19], L= 134 nm and w = 8 nm[20] and compared to the experimental values (Figure 7-8). For LSC, the experimental data followed the theory as the nanocrystals were well-dispersed in the polymer matrix thanks to the particle morphology. When using the latex LA, the experimental data tent to deviate from the theory as the CNCs aggregated as shown in Figure 7.2.

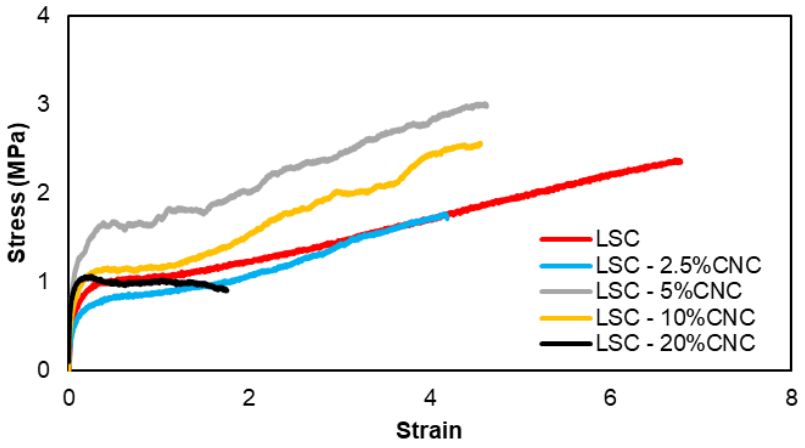

Figure 7-6: Stress-strain curves for films cast from the blends of the small cationically charged particles latex with cellulose nanocrystals at different concentrations at 23 ºC and 55% relative humidity

Table 7-6: Tensile tests results of films cast from the blends of the small cationically charged particles latex with cellulose nanocrystals at different concentrations at 23 ºC and 55% relative humidity

	Young's modulus (MPa)	Yield stress (MPa)	Elongation at break	Stress at break (MPa)	Toughness (MPa)
LSC	7 ± 4	0.72 ± 0.17	8.06 ± 1.5	1.85 ± 0.34	9.27 ± 1.67
LSC – 2.5% CNC	13 ± 6	0.73 ± 0.27	4.2 ± 2.2	1.77 ± 0.52	4.83 ± 3.12
LSC - 5% CNC	21 ± 2	1.22 ± 0.18	4.79 ± 0.88	2.13 ± 0.46	7.53 ± 1.86
LSC - 10% CNC	29 ± 4	1.32 ± 0.26	4.53 ± 0.95	2.53 ± 0.37	5.04 ± 1.39
LSC - 20% CNC	47 ± 15	1.78 ± 0.86	1.78 ± 0.86	0.94 ± 0.09	2.06 ± 0.53

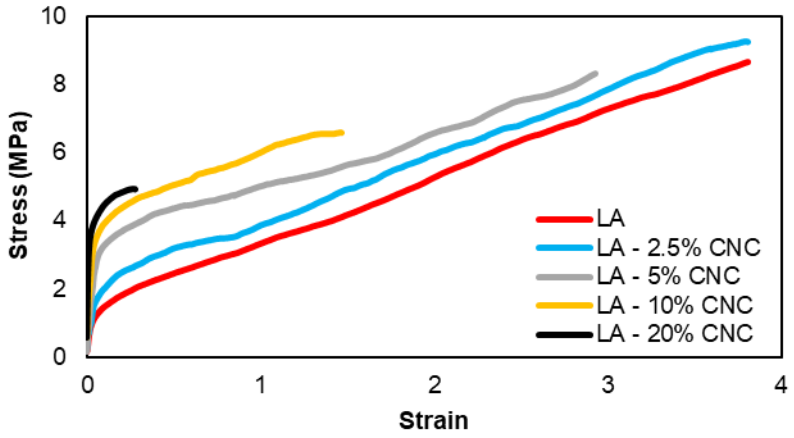

Figure 7-7: Stress-strain curves for blends from the anionically stabilized particles latex and cellulose nanocrystals at different concentrations

Table 7-7: Tensile tests results of the blends from the anionically stabilized particles latex and cellulose nanocrystals at different concentration

	Young's modulus (MPa)	Yield Stress (MPa)	Elongation at break	Stress at break (MPa)	Toughness (MPa)
LA	37 ± 5	2.3 ± 0.65	3.81 ± 0.43	8.6 ± 1.2	20 ± 2.8
LA - 2.5% CNC	48 ± 8	2.93 ± 0.43	3.8 ± 0.65	9.3 ± 2.9	22 ± 2.5
LA - 5% CNC	64 ± 9	3.69 ± 0.69	2.9 ± 0.32	8.3 ± 0.88	16.7 ± 3
LA - 10% CNC	89 ± 11	4.44 ± 0.55	1.5 ± 0.14	6.58 ± 0.79	7.9 ± 1.4
LA - 20% CNC	265 ± 15	4.11 ± 0.6	0.273 ± 0.04	4.9 ± 0.44	1.1 ± 0.26

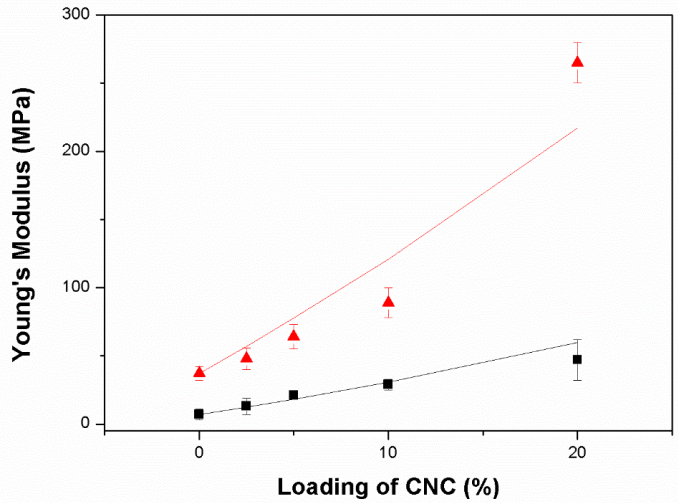

Figure 7-8: Evolution of the Young's modulus with the loading of CNCs, comparison between the experimental lines (scatter) and predicted data form the Halpin-Tsaï model for LSC (black, ■) and LA (red, ▲)

7.4 Conclusions

Hybrid particles obtained by heterocoagulation of P(MMA-*co*-BA) latexes with cellulose nanocrystals were studied. Two distinct hybrid particle morphologies were obtained using cationically polymer particles of different sizes. Cellulose nanocrystals adsorbed on polymer particles when their diameter was larger than the CNCs length. However, due to strong interactions between the CNCs and the cationically charged particles, a limiting amount of CNCs was adsorbed and a large fraction of CNCs remained free in the system. The film morphology of a film cast from this latex showed a honeycomb structure with some aggregates

of CNCs. When small polymer particles were used, they adsorbed on the CNCs leading to encapsulation of the CNCs. This led to the homogeneous distribution of single crystals into the polymer matrix after film casting. For comparison, an anionically charged particles latex was blended with the CNCs. Due to repulsive forces between the two components, the CNCs aggregated during film formation. The addition of the CNCs reinforced the films in all the cases due to their inherent mechanical strength. The film presenting a honeycomb structure gave the composite with the highest strength, thanks to the formation of a co-continuous structure. These results highlight the importance of initial particle morphology on the strength of nanocomposite materials. As film morphology is directly influenced by particle morphology it is essential to design nanocomposite materials in which upon film formation, the hard phase are in at least partial contact in order to maximize the strength of the film. However, flexibility of the final particles should be preserved to obtain films with a high toughness.

7.5 References

(1) Voorn, D. J.; Ming, W.; van Herk, A. M. Encapsulation of Platelets by Physical and Chemical Approaches *Macromol. Symp.* **2006**, *245–246*, 584–590.

(2) Favier, V.; Canova, G. R.; Cavaillé, J. Y.; Chanzy, H.; Dufresne, A.; Gauthier, C. Nanocomposite materials from latex and cellulose whiskers *Polym. Adv. Technol.* **1995**, *6*, 351–355.

(3) Vatansever, A.; Dogan, H.; Inan, T.; Sezer, S.; Sirkecioglu, A. Properties of na-montmorillonite and cellulose nanocrystal reinforced poly(butyl acrylate-co-methyl methacrylate) nanocomposites *Polym. Eng. Sci.* **2015**, *55*, 2922–2928.

(4) Nechyporchuk, O.; Pignon, F.; Botelho Do Rego, A. M.; Belgacem, M. N. Influence of ionic interactions between nanofibrillated cellulose and latex on the ensuing composite properties *Compos. Part B Eng.* **2015**, *85*, 188–195.

(5) Vandervorst, P.; Lei, C. H.; Lin, Y.; Dupont, O.; Dalton, A. B.; Sun, Y. P.; Keddie, J. L. The fine dispersion of functionalized carbon nanotubes in acrylic latex coatings *Prog. Org. Coatings* **2006**, *57*, 91–97.

(6) Tiarks, F.; Landfester, K.; Antonietti, M. Silica nanoparticles as surfactants and fillers for latexes made by miniemulsion polymerization *Langmuir* **2001**, *17*, 5775–5780.

(7) 2,2'-Azobis(2-methylpropionamidine)dihydrochloride - Vesta Intracon bv https://vestachem.com/chemicals/22-azobis2-methylpropionamidinedihydrochloride/ (accessed Mar 5, 2019).

(8) Sangster, J. Octanol Water Partition Coefficients of Simple Organic Compounds *J. Phys. Chem. Ref. Data* **1989**, *18*, 1111–1229.

(9) Autran, C.; de la Cal, J. C.; Asua, J. M. (Mini)emulsion Polymerization Kinetics Using Oil-Soluble Initiators *Macromolecules* **2007**, *40*, 6233–6238.

(10) Dickinson, E.; Eriksson, L. Particle flocculation by adsorbing polymers *Adv. Colloid Interface Sci.* **1991**, *34*, 1–29.

(11) Sun, X.; Danumah, C.; Liu, Y.; Boluk, Y. Flocculation of bacteria by depletion interactions due to rod-shaped cellulose nanocrystals *Chem. Eng. J.* **2012**, *198–199*, 476–481.

(12) Vandamme, D.; Eyley, S.; Van den Mooter, G.; Muylaert, K.; Thielemans, W. Highly charged cellulose-based nanocrystals as flocculants for harvesting Chlorella vulgaris *Bioresour. Technol.* **2015**, *194*, 270–275.

(13) Nielsen, L. E. Mechanical Properties of Particulate-Filled Systems *J. Compos. Mater.* **1967**, *1*, 100–119.

(14) Lawrence, E. N. Simple theory of stress-strain properties of filled polymers *J. Appl. Polym. Sci.* **1966**, *10*, 97–103.

(15) Negrete-Herrera, N.; Putaux, J.-L.; David, L.; Haas, F. De; Bourgeat-Lami, E. Polymer/Laponite Composite Latexes: Particle Morphology, Film Microstructure, and Properties *Macromol. Rapid Commun.* **2007**, *28*, 1567–1573.

(16) González-Matheus, K.; Leal, G. P.; Asua, J. M. Film formation from Pickering stabilized waterborne polymer dispersions *Polymer* **2015**, *69*, 73–82.

(17) Nielsen, L. E. Generalized equation for the elastic moduli of composite materials *J. Appl. Phys.* **1970**, *41*, 4626–4627.

(18) Affdl, J. C. H.; Kardos, J. L. The Halpin-Tsai equations: A review *Polym. Eng. Sci.* **1976**, *16*, 344–352.

(19) Bras, J.; Viet, D.; Bruzzese, C.; Dufresne, A. Correlation between stiffness of sheets prepared from cellulose whiskers and nanoparticles dimensions *Carbohydr. Polym.* **2011**, *84*, 211–215.

(20) Reid, M. S.; Villalobos, M.; Cranston, E. D. Benchmarking Cellulose Nanocrystals: From the Laboratory to Industrial Production *Langmuir* **2017**, *33*, 1583–1598.

Chapter 8. Conclusions

The main goal of this PhD thesis was to establish a link between particle morphology and film morphology in hybrid particles latexes. As film morphology affects films properties, this understanding would ultimately allow for control of the film properties through the polymerization process. This is a particularly important issue in the development of VOC free latexes designed to achieve good mechanical strength whilst having low minimum film formation temperature. Typically this can be achieved by the use of two polymers, a low T_g polymer for film formation and a high T_g polymer for stiffness, either obtained by blends of particles of different composition or by the use of heterogeneous particles. Hybrid particles are favored as they show great potential to overcome the drawbacks rising from the use of blends. Indeed, without careful selection of the polymers particles characteristics, phase separation can occur during film formation of latexes blend.

The strategy used to understand this problem was to study the film morphology and properties of a variety of polymer-polymer hybrid particles latexes. For each polymer-polymer system studied, different morphologies with near identical compositions and polymer microstructure (molecular weights, particle size, gel content, T_{gs}) were prepared. The different morphologies were obtained using both chemical and physical techniques. The chemical

techniques involve the polymerization of monomers by (mini)emulsion polymerization (Figure 8-1a). In this case, the morphology was controlled by varying the interfacial tension between the two polymers, and that of the polymers and the water through slight changes in the polymer compositions. In addition, core-shell particles were obtained through physical interactions of cellulose nanocrystals (CNCs) with the polymer in batch emulsion polymerization. This morphology was compared with particles formed by heterocoagulation of CNCs with a charged acrylic latex. This physical technique allowed us to obtain different particle morphologies with identical polymer composition by varying the size and the stabilization charges of the polymer particles (Figure 8-1b).

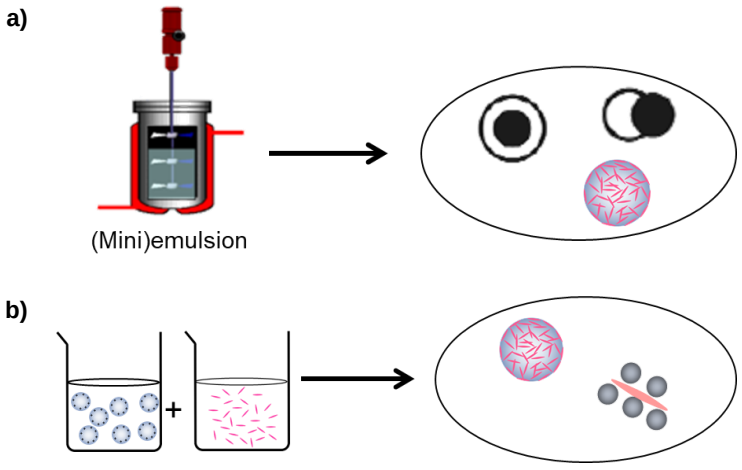

Figure 8-1: Strategies for synthesis of hybrid particles a) by chemical process and b) and physical process

We demonstrated by TEM and atomic force microscopy (AFM) imaging, that film morphology is directly influenced by the particle morphology. Thus, for hybrid particles with a hard seed polymer and a soft second stage polymer, the continuous phase of the film is formed of the soft polymer. Core-shell morphologies led to a honeycomb structure with a MFFT close to the T_g of the soft polymer (Figure 8-2a). Hemispherical morphologies led to the formation of small aggregates of hard polymers in the soft matrix during film formation which increases the MFFT of the film (Figure 8-2b). It was been demonstrated in Chapter 3 that particles containing a hard polymer on the outer part of the particles allowed film formation close to room temperature. Thanks to high driving forces for deformation of the soft polymer, particles could deform and hard segments were dispersed in the soft continuous phase (Figure 8-2c). In this case, the MFFT increased with the T_g of the hard polymer and its proportion in the hybrid particle. For CNC armored latex particles, as the hard polymer was at the outside of the particles, a honeycomb structure was also obtained (Figure 8-2d). In the contrary when small cationically charged polymer particles were adsorbed on the CNCs surface, the CNCs were dispersed as single crystals in the polymer matrix.

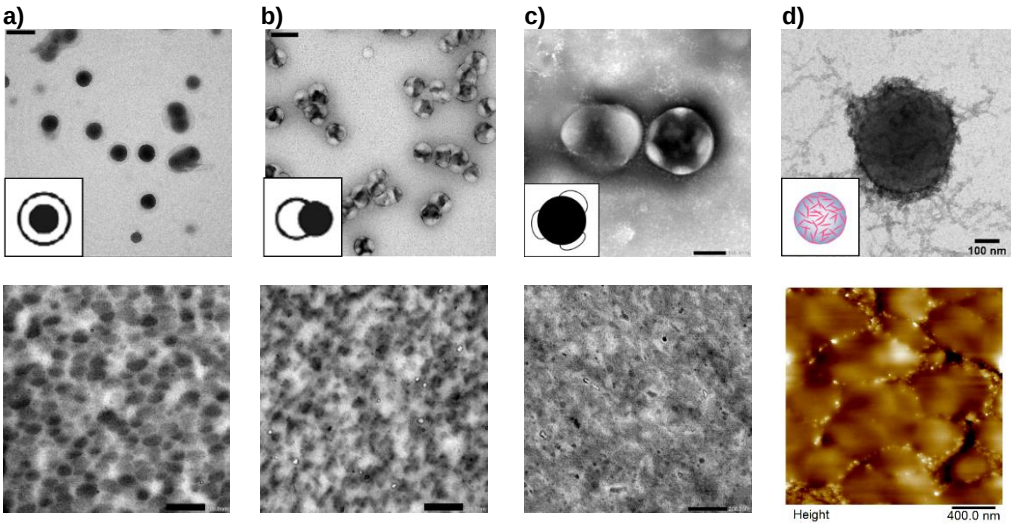

Figure 8-2: Effect of particle morphology on film structure extracted for a) and b) Chapter 2, c) Chapter 3 and d) Chapter 7

Tensile tests were performed for all the systems studied to determine the effect of film morphology on properties. The composition of the polymer phases has an important effect of the film properties. The honeycomb-like structure displayed by films cast from soft core-hard shell particles enhances the film stiffness as the continuous phase is formed of the hard polymer. When the continuous phase is soft (coming from soft-second stage polymer in core-shell particles, or multi hard lobes particles), the hard polymer is dispersed the soft continuous phase (spherical or segments hard domains), the film is reinforced compared to a pure soft film. Hemispherical morphologies led to higher film stiffness than hard core-soft shell ones.

Indeed, the formation of small aggregates of hard polymers increases the film stiffness (Figure 8-3). The heterocoagulation process gave the possibility to obtain hybrid particles from polymer and cellulose nanocrystals with different morphologies. Moreover, as the polymer can be synthesized by semi-batch polymerization in this process, the final film had higher flexibility and toughness than the hybrid formed by batch emulsion polymerization. For the CNC armored particles synthesized in situ, blending the obtained particles with a latex devoid of CNCs decreased the final loading CNCs, and films with high toughness were obtained. The ratio between the two polymers also affected the film properties. In Chapter 3, we demonstrated that a minimum loading of 20 wt% of hard phase is needed to have a significant improvement of the films toughness. If the hard polymer presented remarkable strength such as cellulose nanocrystals, a lower loading is required to obtain a reinforced hybrid polymer film.

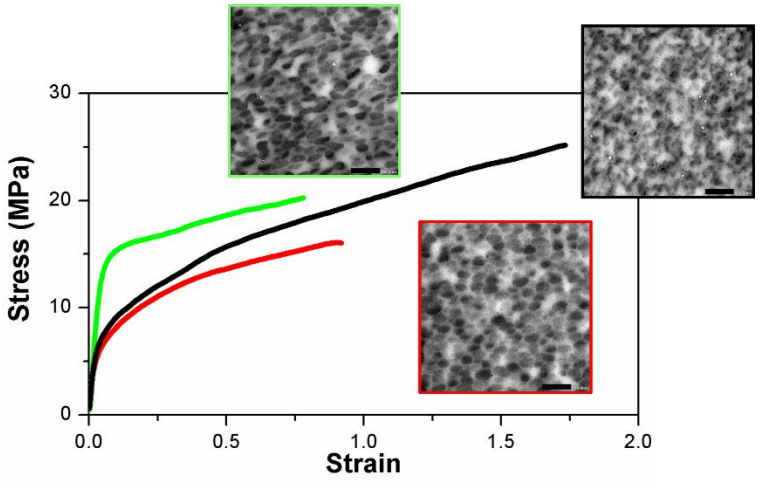

Figure 8-3: Effect of film structure on the film properties

We demonstrated by thermal treatment of the films that the film morphology strongly affects the properties of the film. This technique allowed us to compare different film morphologies with the same composition. Thermal treatment above the T_g of the hard phase encourage phase migration and the polymers segregate. The segregation leads to lower transparency and increase the stiffness of the film. However, phase migration could lead to the formation of a co-continuous structure if the compatibility of the polymers was high. In this case, the toughness of the film was enhanced compared to hard segments dispersed in the soft matrix (Figure 8-4).

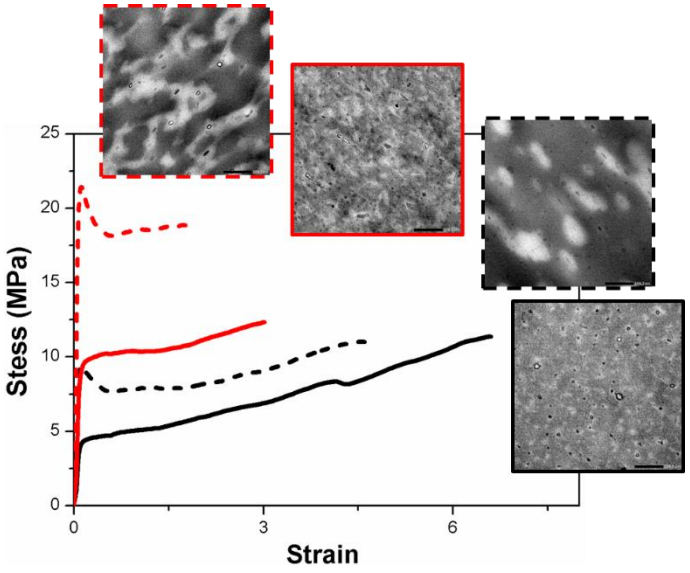

Figure 8-4: Effect of thermal treatment on film morphology and properties

Furthermore, we showed that, in addition to the particle morphology, two important parameters have to be taken in account for film formation: the drying conditions and the compatibility between the phases. As explained before, annealing of the films above the T_{gs} lead to different film morphologies and properties. If the phases show low compatibility they segregate during film formation. In Chapter 4, we demonstrated that the curing process of the alkyd resin in acrylic / alkyd hybrid particles had a large effect on the final film morphology. In this system, two parameters have to be taken in account. First, the curing was slow and

inhomogeneous through the film which led to extensive phase migration and the development of large, aggregated domains of the two polymer phases. Secondly, due to the partial miscibility of the uncured alkyd resin with the acrylic phase, as curing progresses phase separation was increasingly favored with high crosslinking leading to a strongly segregated structure which led to limited mechanical resistance in the bulk film (Figure 8-5).

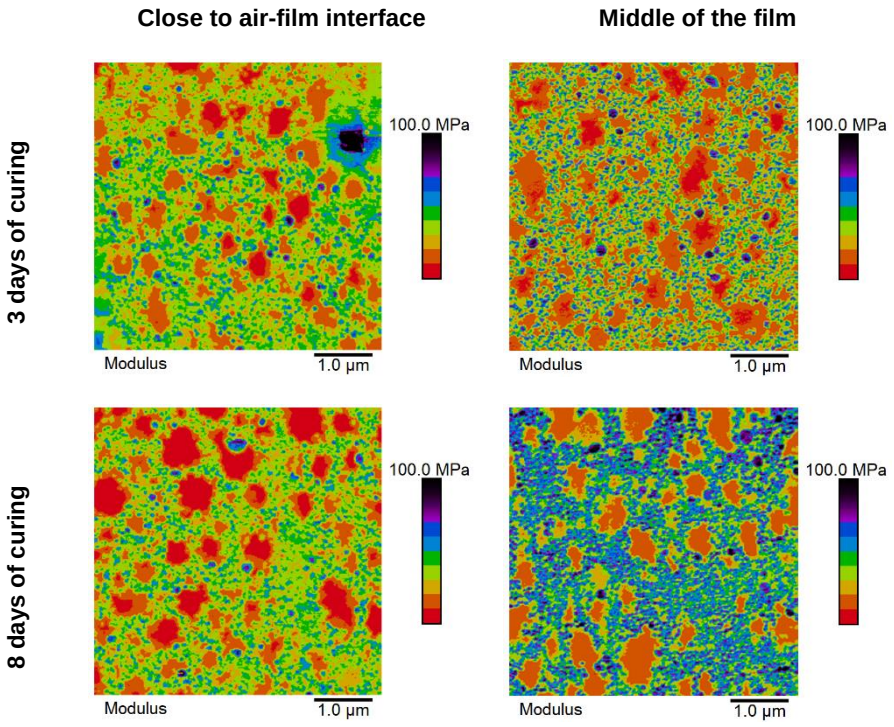

Figure 8-5: Evolution of film morphology in acrylic / alkyd hybrid particle latex film with 1 wt% of Mn based catalyst with curing of alkyd resin

In order to confirm the advantages of hybrid particles to the use of blends, we compared hybrid particles latexes with a blend of two latexes of same overall compositions in Chapters 2 and 5. We confirmed with these examples that hybrid particles lead to more homogeneous

films structure. However, depending on the composition and the size of the particles, and the ratio, different film morphologies and properties were obtained. In general, films from the latexes blends resulted in lower transparency and lower properties (high stiffness or flexibility depending on the composition) compared to the hybrid particles films dried in the same conditions (Figure 8-6).

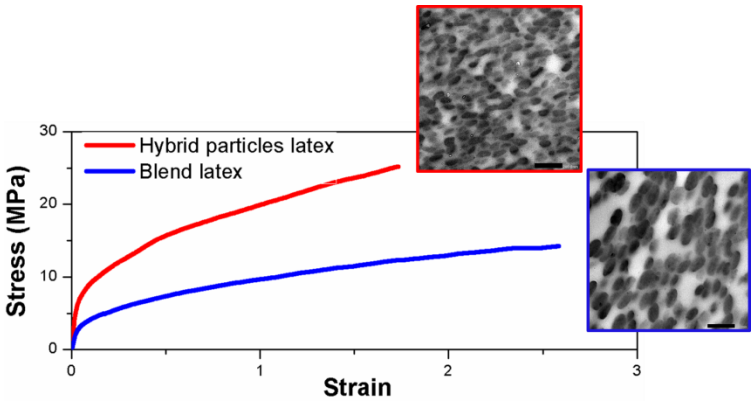

Figure 8-6: Comparison of film morphology and properties of a hybrid latex (red) and a blend of two latexes (blue)

The ultimate goal of this project is to use hybrid particles latexes as binder in coatings applications. It was observed that the morphologies of the paint films from acrylic / alkyd hybrid particles latexes were in agreement with the latexes films. Moreover, the trends shown in the properties of the formulated paints were similar to that of the latexes films. This is a significant

observation because it shows the knowledge generated within this thesis can be translated to commercial systems that use hybrid particles latexes as binders in coating formulations.

Overall, it can be concluded that the final properties of polymer films and coatings can be tailored in the reactor by carefully designed synthesis of hybrid latex particles and post-synthesis through thermal treatment of the dry polymer films. As mentioned above, the mechanical strength of the film depends on the internal film structure and to be able to control it offers a viable synthetic route to obtaining mechanically strong films from emulsion polymers.

List of publications and conference presentations

[1]

Parts of this thesis will be published soon. The list of papers that would be issued form this work is as follows (variation in the paper title might be possible):

Limousin, E.; Ballard, N.; Asua, J. M. The Influence of Particle Morphology on the Structure and Mechanical Properties of Films Cast from Hybrid Latexes. *Prog. Org. Coatings* **2019**, *129*, 69–76.

Limousin, E.; Ballard, N.; Asua, J. M. Soft Core-Hard Shell Latex Particles for Mechanically Strong VOC-Free Polymer Films. *J. Appl. Polym. Sci.* **2019**, 47608.

Limousin, E.; Ballard, N.; Asua, J. M. Synthesis of Cellulose Nanocrystal Armored Latex Particles for Mechanically Strong Nanocomposite Films. *Polym. Chem.* **2019**.

Limousin, E.; Martinez-Tong D. E., Ballard, N.; Asua, J. M. Cure dependent morphology of acrylic/alkyd hybrid latex coatings via nanomechanical mapping (under preparation)

Limousin, E.; Ballard, N.; Asua, J. M. Linking filnm structure and mechanical strength in nanocomposite films formed from heterocoagulated dispersions of cellulose nanocrystals(CNC) and acrylic latexes (under preparation)

Parts of this work have been presented in international conferences, as well in Industrial Liaison Program (ILP) Meetings.

Oral presentations

"Effect of particle morphology on film morphology and properties" E. Limousin, N. Ballard, J.C. de la Cal, J.M: Asua. POLYMAT, 15th Industrial Liaison Program (ILP) Meeting, UPV/EHU, Polymat, Donostia- San sebastian, Spain, 2015.

"Effect of particle morphology on film morphology and properties" E. Limousin, N. Ballard, J.C. de la Cal, J.M: Asua. POLYMAT, 16th Industrial Liaison Program (ILP) Meeting, UPV/EHU, Polymat, Donostia- San sebastian, Spain, 2016.

"Hybrid particles: an alternative to the use of VOCs" E. Limousin, N. Ballard, J.M: Asua. Graduate Research Symposium (GRS), Aranzazu, Spain, 2017.

"Effect of particle morphology on film morphology and properties" E. Limousin, N. Ballard, J.M: Asua. POLYMAT, 17th Industrial Liaison Program (ILP) Meeting, UPV/EHU, Polymat, Donostia- San sebastian, Spain, 2017.

"Effect of particle morphology on film morphology and properties" E. Limousin, N. Ballard, J.M: Asua. POLYMAT, 18th Industrial Liaison Program (ILP) Meeting, UPV/EHU, Polymat, Donostia- San sebastian, Spain, 2018.

Poster presentations

"Effet de la morphologie des particules dans un latex hybride polymère-polymère sur les propriétés du film" " E. Limousin, N. Ballard, J.C. de la Cal, J.M: Asua.Club emulsion, Pau, France, 2017.

"Incorporation of cellulose nanocrystals in acrylic latex films" E. Limousin, N. Ballard, J.C. de la Cal, J.M: Asua. Multifunctional, Hybrid and Nanomaterials, Lisbon, Portugal, 2017.

"Hybrid particles: an alternative to the use of VOCs" E. Limousin, N. Ballard, J.M: Asua. International Polymer Colloid Group (IPCG), Aranzazu, Spain, 2017.

"Scientific Photography Award" in 4th Scientific Photography Contest organized by Polymat Institute (March 2017).

Resumen y conclusiones

Uno de los mayores retos a los que se enfrenta la sociedad moderna es la reducción del cambio climático y el desarrollo de materiales sostenibles. Teniendo esto en cuenta, la producción de recubrimientos protectores y decorativos, que tradicionalmente estaba dominada por productos a base de disolventes, se está desplazando gradualmente hacia el uso de dispersiones en base acuosa. Tales recubrimientos implican la formación de un film que tiene necesita satisfacer varios requisitos aparentemente contradictorios con respecto a las propiedades mecánicas. Un ejemplo común es la necesidad de que los recubrimientos para exteriores sean capaces de formar un film a temperaturas relativamente bajas mientras que sean duros a la misma temperatura. Los recubrimientos a base de disolventes cumplen fácilmente estos requisitos. Igualar su rendimiento con recubrimientos en base acuosa no es sencillo y, a menudo, se deben agregar aditivos potencialmente tóxicos, como los agentes coalescentes, a la formulación. Los esfuerzos ahora se dedican a sintetizar látex que presentan buenas propiedades agregando un mínimo de aditivos. Una forma de hacerlo es mediante el uso de una combinación de dos látex con diferentes Tg. Un látex con una Tg baja para formar un film a baja temperatura y el otro con una Tg más alta para proveer dureza al film. Sin embargo, la mezcla produce films no homogéneos y sus propiedades se ven afectadas. Se puede obtener una distribución más uniforme de las dos fases en el film utilizando partículas poliméricas heterogéneas (también llamadas partículas híbridas). En este caso, dos polímeros diferentes están presentes en la misma partícula para combinar las

propiedades positivas de sus constituyentes. Aunque tales polímeros son típicamente incompatibles, su separación de fases durante la formación del film puede controlarse mediante reacciones de injerto.

La estrategia utilizada para comprender este problema fue estudiar la morfología del film y las propiedades de una variedad de látex de partículas híbridas polímero-polímero. Para cada sistema de polímero-polímero estudiado, se prepararon diferentes morfologías con composiciones y microestructura de polímero casi idénticas (pesos moleculares, tamaño de partícula, contenido de gel, Tgs). Las diferentes morfologías se consiguieron utilizando técnicas tanto químicas como físicas. Las técnicas químicas implican la polimerización de monómeros mediante polimerización en (mini)emulsión. En este caso, la morfología se controló variando la tensión interfacial entre los dos polímeros, y la de los polímeros y el agua a través de ligeros cambios en las composiciones de polímeros. Además, las partículas núcleo-corteza se obtuvieron a través de interacciones físicas de nano cristales de celulosa (CNC) con el polímero en la polimerización discontinua en emulsión. Esta morfología se comparó con partículas formadas por la heterocoagulación de los CNC con un látex acrílico cargado. Esta técnica física nos permitió obtener diferentes morfologías de partículas con una composición de polímeros idéntica variando el tamaño y las cargas de estabilización de las partículas de polímeros.

Demostramos mediante imágenes de TEM y microscopía de fuerza atómica (AFM), que la morfología del film está directamente influenciada por la morfología de las partículas. De este modo, para partículas híbridas con un polímero con un núcleo duro y un polímero de segunda etapa blando, la fase continua del film se forma gracias al polímero blando. Las morfologías del núcleo y la envoltura llevaron a una estructura de panal con una MFFT cerca de la Tg del polímero blando. Las morfologías hemisféricas condujeron a la formación de pequeños agregados de polímeros duros en la matriz blanda durante la formación del film, lo que aumenta la MFFT del film. Se demostró que las partículas que contienen un polímero duro en la parte exterior de las partículas permitieron la formación del film cerca de la temperatura ambiente. Gracias a las altas fuerzas motrices de deformación del polímero blando, las partículas podían deformarse y los segmentos duros se dispersaron en la fase continua blanda. En este caso, la MFFT aumentó con la Tg del polímero duro y su proporción en la partícula híbrida. Para las partículas de látex con CNC, como el polímero duro estaba en el exterior de las partículas, también se obtuvo una estructura de panal de abeja (Figura 8-2d). Por el contrario, cuando se adsorbieron pequeñas partículas de polímero con carga catiónica en la superficie de los CNC, los CNC se dispersaron como cristales simples en la matriz del polímero.

Se realizaron pruebas de tracción para todos los sistemas estudiados para determinar el efecto de la morfología del film en las propiedades. La composición de las fases del polímero tiene un efecto importante de las propiedades del film. La estructura similar a panal de abeja exhibida por los films moldeadas a partir de partículas de corteza dura y de núcleo

blando mejora la rigidez del film a medida que la fase continua se forma del polímero duro. Cuando la fase continua es blanda (proveniente del polímero de segunda etapa blanda en partículas núcleo-corteza, o partículas de multiples lóbulos duros), el polímero duro se dispersa en la fase continua blanda (dominios duros esféricos o segmentos), el film se refuerza en comparación con un film puro de fase blanda. Las morfologías hemisféricas condujeron a una mayor rigidez del film que las de corteza dura y de núcleo duro. De hecho, la formación de pequeños agregados de polímeros duros aumenta la rigidez del film. El proceso de heterocoagulación ofreció la posibilidad de obtener partículas híbridas de nanocristales de polímero y celulosa con diferentes morfologías. Además, como el polímero se puede sintetizar mediante polimerización en semicontinuo. En este proceso, el film final tuvo mayor flexibilidad y tenacidad que el híbrido formado por polimerización en emulsión discontinua. Para las partículas con CNC sintetizadas *in situ*, la mezcla de los films obtenidas con un látex sin CNC disminuyó la carga final de los CNC, y se obtuvieron films con alta tenacidad. La proporción entre los dos polímeros también afectó las propiedades del film. Demostramos que se necesita una carga mínima de 20% en peso de la fase dura para tener una mejora significativa de la resistencia del film. Si el polímero duro presenta una resistencia notable, como los nanocristales de celulosa, se requiere una carga más baja para obtener un film de polímero híbrido reforzado.

Demostramos mediante tratamiento térmico de los films que la morfología del film afecta fuertemente sus propiedades. Esta técnica nos permitió comparar diferentes morfologías de film con la misma composición. El tratamiento térmico superior a la Tg de la

fase dura favorece la migración de las fases y los polímeros se segregan. La segregación conduce a una menor transparencia y aumenta la rigidez del film. Sin embargo, la migración de fases podría llevar a la formación de una estructura co-continua si la compatibilidad de los polímeros fuera alta. En este caso, la resistencia del film se mejoró en comparación con los segmentos duros dispersos en la matriz blanda.

Demostramos que, además de la morfología de las partículas, se deben tener en cuenta dos parámetros importantes para la formación del film: las condiciones de secado y la compatibilidad entre las fases. Como se explicó anteriormente, el recocido de los films por encima de las Tgs conduce a diferentes morfologías y propiedades de los films. Si las fases muestran baja compatibilidad, se segregan durante la formación del film. Demostramos que el proceso de curado de la resina alquídica en partículas híbridas acrílicas / alquídicas tuvo un gran efecto en la morfología del film final. En este sistema, hay que tener en cuenta dos parámetros. Primero, el curado fue lento e inhomogéneo a través del film, lo que condujo a una extensa migración de fases y al desarrollo de grandes dominios agregados de las dos fases del polímero. En segundo lugar, debido a la miscibilidad parcial de la resina alquídica no curada con la fase acrílica, a medida que el curado progresaba, la separación de fases se favoreció cada vez más con una alta reticulación que llevó a una estructura fuertemente segregada que llevó a una resistencia mecánica limitada en el film.

Con el fin de confirmar las ventajas de las partículas híbridas al uso de mezclas, comparamos látex de partículas híbridas con una mezcla de dos látex de las mismas composiciones generales. Confirmamos con dos ejemplos que las partículas híbridas conducen a una estructura de films más homogénea. Sin embargo, dependiendo de la composición y el tamaño de las partículas, y la proporción, se obtuvieron diferentes morfologías y propiedades del film. En general, los films de las mezclas de látex resultaron en una menor transparencia y menores propiedades (alta rigidez o flexibilidad según la composición) en comparación con los films de partículas híbridas secadas en las mismas condiciones.

El objetivo final de este proyecto era utilizar partículas de látex híbrido como aglutinante en aplicaciones de recubrimientos. Se observó que las morfologías de los films de pintura a partir de látex de partículas híbridas acrílicas / alquídicas estaban de acuerdo con los films de látex. Además, las tendencias mostradas en las propiedades de las pinturas formuladas fueron similares a las de los films de látex. Esta es una observación importante porque muestra que el conocimiento generado dentro de esta tesis puede traducirse a sistemas comerciales que utilizan partículas de látex híbrido como aglutinante en formulaciones de recubrimiento.

En conclusión, se puede concluir que las propiedades finales de los films y recubrimientos de polímeros se pueden adaptar en el reactor mediante síntesis

cuidadosamente diseñada de partículas de látex híbrido y post-síntesis a través del tratamiento térmico de los films de polímero seco. Como se mencionó anteriormente, la resistencia mecánica del film depende de su estructura interna y para poder controlarla se ofrece una ruta sintética viable para obtener films mecánicamente fuertes a partir de polímeros en emulsión.

Appendix I. Characterization methods

I.1 Solids content and monomer conversion

Approximately 1mL of latex was withdrawn from the final latex, put in a pre-weight aluminium pan and immediately thereafter 0.1 mL of a 1% hydroquinone solution was added. The pan was dried in the oven at 60ºC until constant weight was achieved. The conversion was obtained gravimetrically and is given by:

$$X = \frac{\left(\frac{W_{dried\ sample}}{W_{sample}}\right) - \left(\frac{W_{non-polymeric\ solids}}{W_{total}}\right)}{\left(\frac{W_{monomers}}{W_{total}}\right)} \quad \text{(I.1)}$$

Residual monomers were measured by Gas Chromatography using Hewlett Packard GC system equipped with a Headspace sampler (HP7694E).

I.2 Coagulum amount

The amount of coagulum was measured by filtering the latex through a 85 μm nylon mesh and drying the retained amount. The results are presented as the weight of the coagulum with respect to the total weight of solids in the formulation.

I.3 Particle size and particle size distribution (PDS)

I.3.1. Dynamic Light Scattering (DLS)

Particle size was measured by Dynamic Light Scattering (DLS) using a Malvern Zetasizer Nano ZS. The equipment determines the particle size by measuring the rate of fluctuations in light intensity scattered by particles as they diffuse trough a fluid. Samples were prepared by diluting a fraction of the latex with deionized water. The analyses were carried out at 25ºC and each run consist in 1 minute of temperature equilibration followed by 3 size measurement per sample. An average is given as a final value.

I.3.2. Capillary hydrodynamic fractionation chromatography (CHDF)

To determine the particle size distribution of the latexes (PSD) Capillary Hydrodynamic Fractionation chromatography technique was used (CHDF-2000 from Matec Applied Science). It was operating at a flow rate of 1.4 mL/min and at 35ºC. The detector wavelength was 200 nm and the carrier fluid was 1X-GR500. The samples were diluted to 0.5 wt% using the carrier fluid and they were analyzed using Matec software v.2.3.

I.4 Differential scanning calorimetry

Glass transition temperatures (T_g) were measured by differential scanning calorimetry (DSC), (DSC Q2000, TA instruments) in modulated mode for Chapter 2 and 3 at a heating rate of 3 ºC/min with an amplitude of ± 2 ºC and a period of 60s. Samples were heated to the reaction temperature (70 ºC) for 1 min then cooled under the T_gs of the phases (namely -30ºC) ant two thermal scans were performed until 150ºC. For these measurements, the latexes were freeze-dried in order to dry them under the T_gs of both copolymers. In Chapter 6, Measurements were carried out in temperature range from -70 to 150 °C at a heating rate of 10 °C/min from polymer films. Two heating cycles were made and the T_{gs} were determined on the second heating.

I.5 Gel content

The gel content by definition is the fraction of polymer which is not soluble in common solvent such a tetrahydrofuran (THF). The gel fraction was determined by Soxhlet extraction. To measure the gel content glass fiber square pads (CEM) were used as backing. A few drops of latex were placed on the filter (filter weight, W_1) and dried overnight at room temperature. The filter together with the dried polymer was weighed (W_2) and a continuous extraction with THF under reflux in the Soxhlet for 24 hours was done afterwards (see Figure I-1). After this period of time, the wet filter was dried overnight and weighted (W_3). Gel content was calculated as the ratio between the weight of the insoluble polymer fraction and that of the initial sample as Equation (I.2) shows

$$\text{Gel content (\%)} = \frac{W_3 - W_1}{W_2 - W_1} x\ 100 \qquad \text{(I.2)}$$

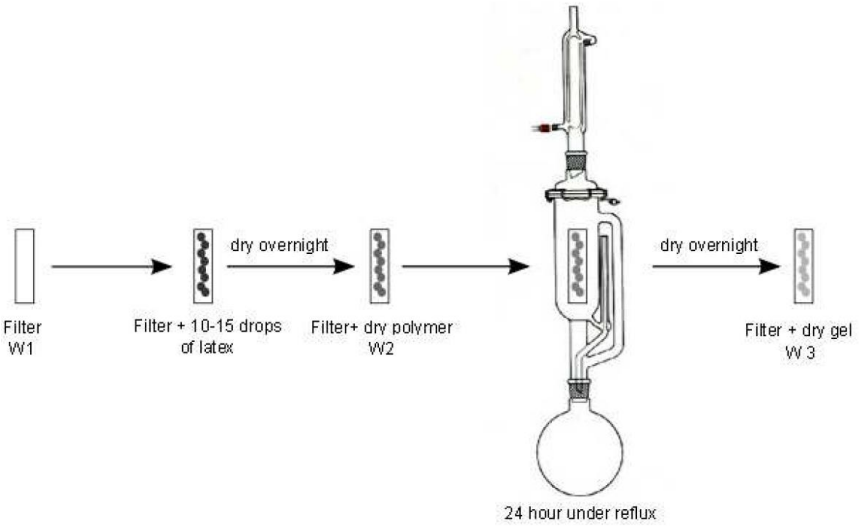

Figure I-1: Scheme of Soxhlet extraction method for gel content measurements

I.6 Molecular weight

The molecular weights of the soluble fraction of the polymers were determined by gel permeation chromatography (GPC). The soluble part of the polymers form the Soxhlet extraction was dried and redissolved in GPC grade THF at a concentration of roughly 1 mg/ml. Then it was filtered (polyamide Φ= 45 µm) before being injected into the GPC via an autosampler (Water 717). A pump (LC-20A, Shimadzu) controlled a THF flow of 1mL/min. The GPC was composed of a differential refractometer (Waters 2410) and three columns in series (Styragel HR2, HR4 and HR6, with pore sizes ranging from 10^2 to 10^6 Å). Measurements were

performed at 35 ºC. Molecular weights were determined using a calibration curve based on polystyrene standards.

I.7 Mass fraction of alkyd grafted on the acrylic polymer

The mass fraction of alkyd grafted to the acrylic polymer (resin degree of grafting: RDG) in the sol fraction were determined by Size Exclusion Chromatography (SEC). The SEC measurements were carried out with a LC-20AD Shimadzu pump fitted with a set of three fractionation columns (Waters Styragel HQ2, HQ4, HQ6) and two on-line detectors, a differential refractometer (DR) and a UV sensor (Waters) at 263 nm of wavelength. The RDG determination method was based on the fact that the acrylic polymer was not detected by the UV sensor at the wavelength of 263 nm. Therefore, the area of the UV-chromatogram of an acrylic/alkyd hybrid material was proportional to the resin concentration in the sol fraction of the sample. Figure I-2 presents the UV signal of an acrylic/alkyd hybrid material (continuous line) and that of the neat alkyd resin (dash line). The areas of the two chromatograms were normalized so that they represented the same total area, that is, the same alkyd concentration. The signal appearing at low elution time (V) (so high molecular weight) corresponded to the resin bounded to acrylic chains. Three areas can be distinguished in this Figure. Surface B represents the amount of alkyd grafted to high molecular weight acrylic polymer. This is a minimum value because some graft copolymer may remain in the white area. Surface A is another measurement of the amount of free alkyd resin that has been incorporated into the graft copolymer but as in the case of surface B may be an underestimation because of the

presence of some graft copolymer in the white region. Therefore, RDG estimated as A/A_{resin} or B/A_{resin} where A_{resin} is the area of the UV trace of the original resin (area below the dashed line in Figure I-2) is underestimated[1].

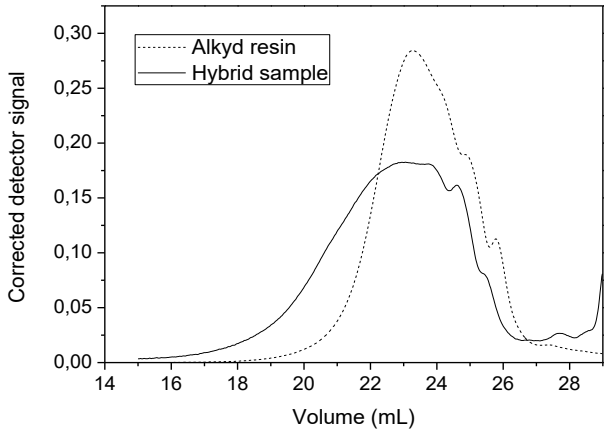

Figure I-2: UV chromatogram at 263 nm of a hybrid sample and of the alkyd resin S293

I.8 Double bonds content of alkyd resin

The double bond content of the alkyd resin in the latex particles was measured by comparison of the iodine value (IV) of the sample. Indeed, this characteristic is proportional to the content of double bonds. This technique consists in making react the unsatured double bonds with iodine monochloride. Then, non-reacted iodine monochloride react with potassium

iodide. The formed diiodine is titrated by a sodium thiosulfate solution[2]. The reactions occurring during the measurement are the following:

$$RCH=CHR' + ICl \rightarrow RCHI\text{-}CHClR' + ICl_{(remaining)} \quad (I.3)$$

$$ICl_{(remaining)} + KI \rightarrow I_2 + KCl \quad (I.4)$$

$$I_2 + 2\ Na_2S_2O_3 \rightarrow Na_2S_4O_6 + 2\ NaI \quad (I.5)$$

The iodine value is calculated with the following formula:

$$IV = \frac{Molecular\ weight\ of\ Iodine \times Volume\ of\ Na_2S_2O_3 \text{consumed} \times \text{Normality of } Na_2S_2O_6 \times 100 \times 10^{-3}}{weight\ of\ the\ sample\ use\ for\ analysis} \quad (I.6)$$

with the volume of $Na_2S_2O_3$ is the difference between the volume obtained for a blank measurement and the effective measurement.

I.9 Microscopic techniques

Particle and film morphologies were determined by transmission electron microscopy (TEM) using a Jeol TM-1400 Plus series 120kV electron microscope. The latexes were diluted with deionized water (0.05 wt%) placed on copper grids covered with Formvar R and dried at ambient temperature. Samples in Chapter 2 were stained with RuO_4 for 20 min. The films were

cryosectioned with a Leica EMUC6 cryoultramicrotome at -25ºC with a Diatome 45° diamond knife, and the observations were made in the microscope described above.

Atomic Force Microscopy (AFM) pictures were obtained using an atomic force microscope Bruker Nanoscope V Dimension Icon in PeakForce tapping mode with a silicon nitride cantilever equipped with a rotated super sharp silicon tip. The nominal resonant frequency of the cantilever was 55 kHz and the spring constant was 0.25 N/m.

I.10 Minimum Film Formation Temperature (MFFT)

The measurement of MFFT was carried out on a steel bar having a temperature gradient along it, with sensors that measure the temperature at different equidistant points. The temperature at the point of the bar at which the film became optically clear and also presented a clear cut made with a knife was defined as the MFFT.

I.11 Mechanical properties: tensile tests

Tensile stress-strain measurements were carried out from latex and paints films with a tensile testing machine (Stable Micro Systems Ltd., Godalming, UK) with a constant velocity of 5 mm/s, corresponding to an initial strain rate of ca. 0.33 s-1. The results reported were the average of 5-10 repeated measurements.

I.12 References

(1) Goikoetxea, M.; Minari, R. J.; Beristain, I.; Paulis, M.; Barandiaran, M. J.; Asua, J. M. Polymerization Kinetics and Microstructure of Waterborne Acrylic/Alkyd Nanocomposites Synthesized by Miniemulsion. *J. Polym. Sci. Part A Polym. Chem.* **2009**, *47* (19), 4871–4885.

(2) International, A. Official Methods of Analysis of AOAC International. Arlington 1984.

Appendix II. Supporting information for Chapter 4

II-1. AFM images

Figures S1 – S3 show a non-continuous topography, resembling a phase separated system. The darker areas have a mean depth in the range of 20 – 30 nm. At the bottom of these valleys we did not observe any structuring, *i.e.,* the bottoms are flat. The brighter areas of the AFM image have a mean height of about 10 – 20 nm and have a diameter close to the particle size. The topography images serve as a first indication that the hybrid latex films consists of different phases.

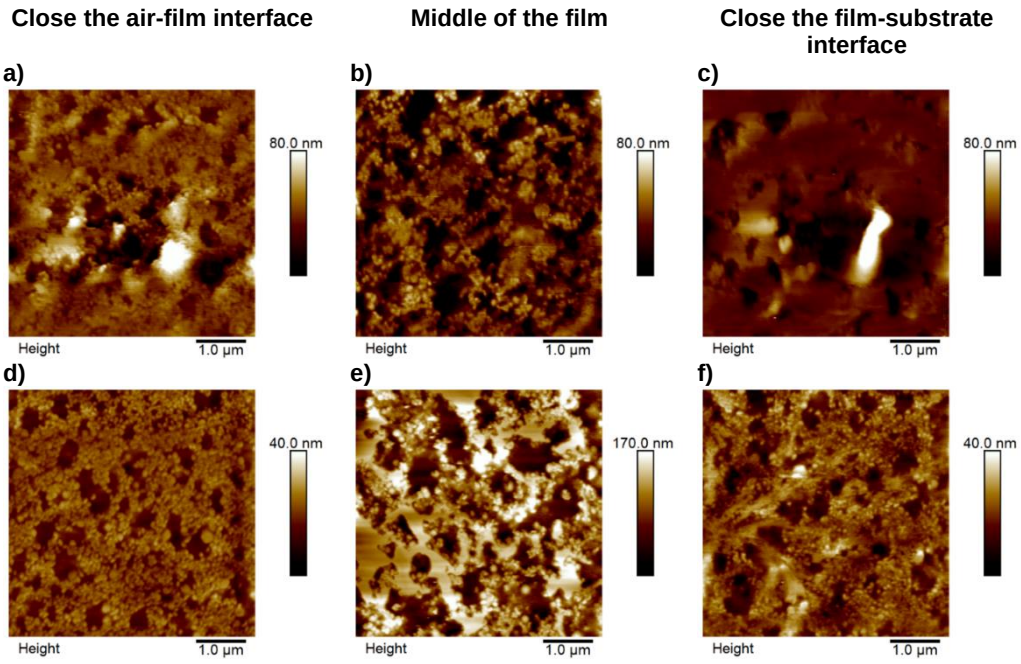

Figure II-1: AFM height images of the films with 1% of Mn-based catalyst abc) and 2% Mn-based catalyst def) after 1 day of curing at 23ºC and 55% relative humidity. For each system, the left image was performed close to air-film interface, the second in the middle of the film and the right image close to the film-substrate interface

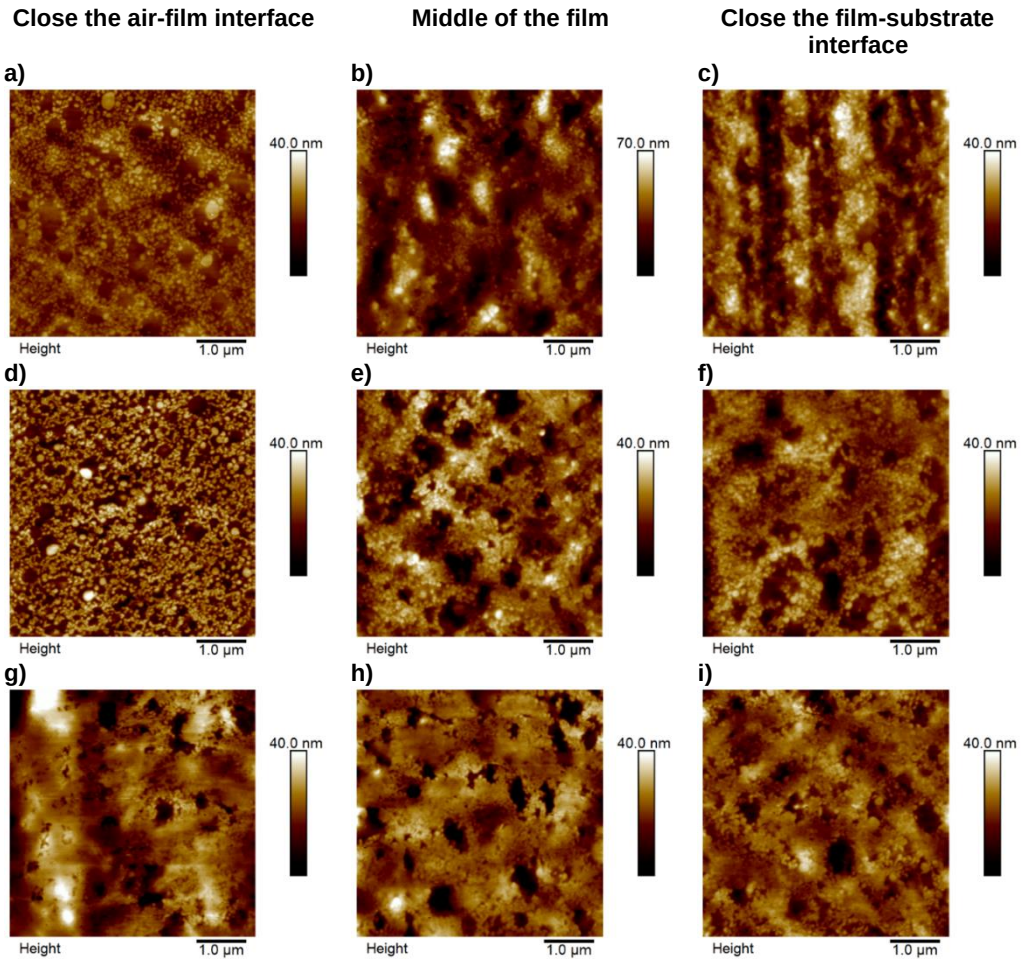

Figure II-2: AFM height images of the films with 0.25% of Mn-based catalyst abc),1% of Mn-based catalyst def) and 2% of Mn-based catalyst ghi) after 3 days of curing at 23ºC and 55% relative humidity. For each system, the left image was performed close to air-film interface, the second in the middle of the film and the right close to the film-substrate interface

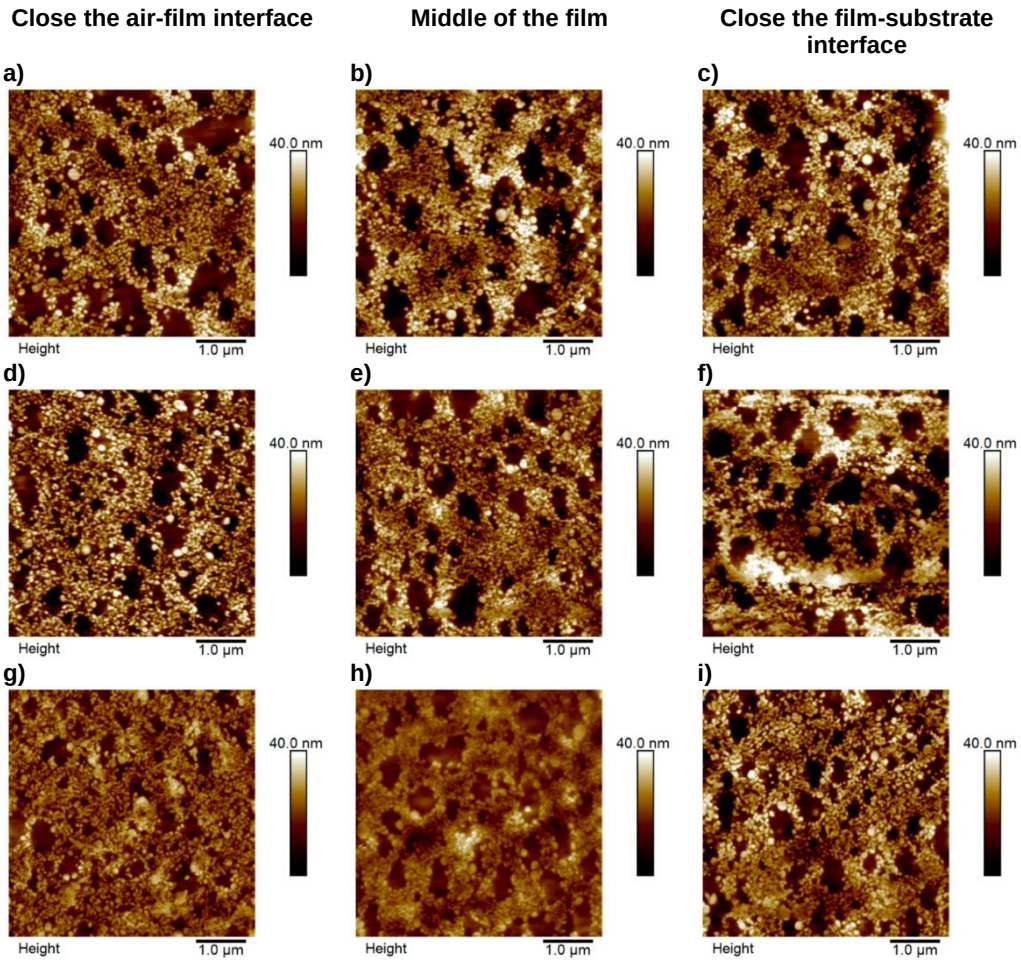

Figure II-3: AFM height images of the films with 0.25% of Mn-based catalyst abc),1% of Mn-based catalyst def) and 2% of Mn-based catalyst ghi) after 8 days of curing at 23ºC and 55% relative humidity. For each system, the left image was performed close to air-film interface, the second in the middle of the film and the right image close to the film-substrate interface

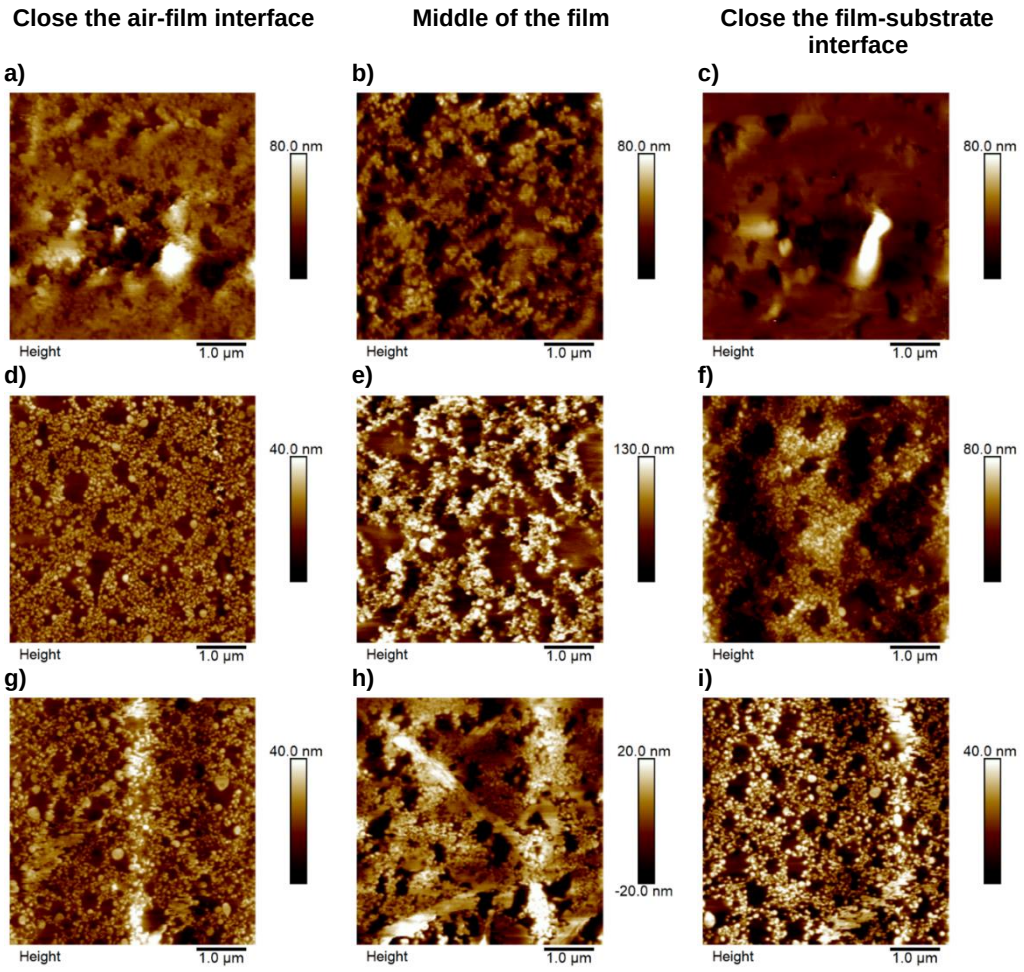

Figure II-4: AFM height images of the films with 1% Mn-based catalyst solely abc),and Zr-based catalyst def) and Ca-based catalyst ghi) after one day of curing at 23ºC and 55% relative humidity. For each system, the left image was performed close to air-film interface, the second in the middle of the film and the right image close to the film-substrate interface

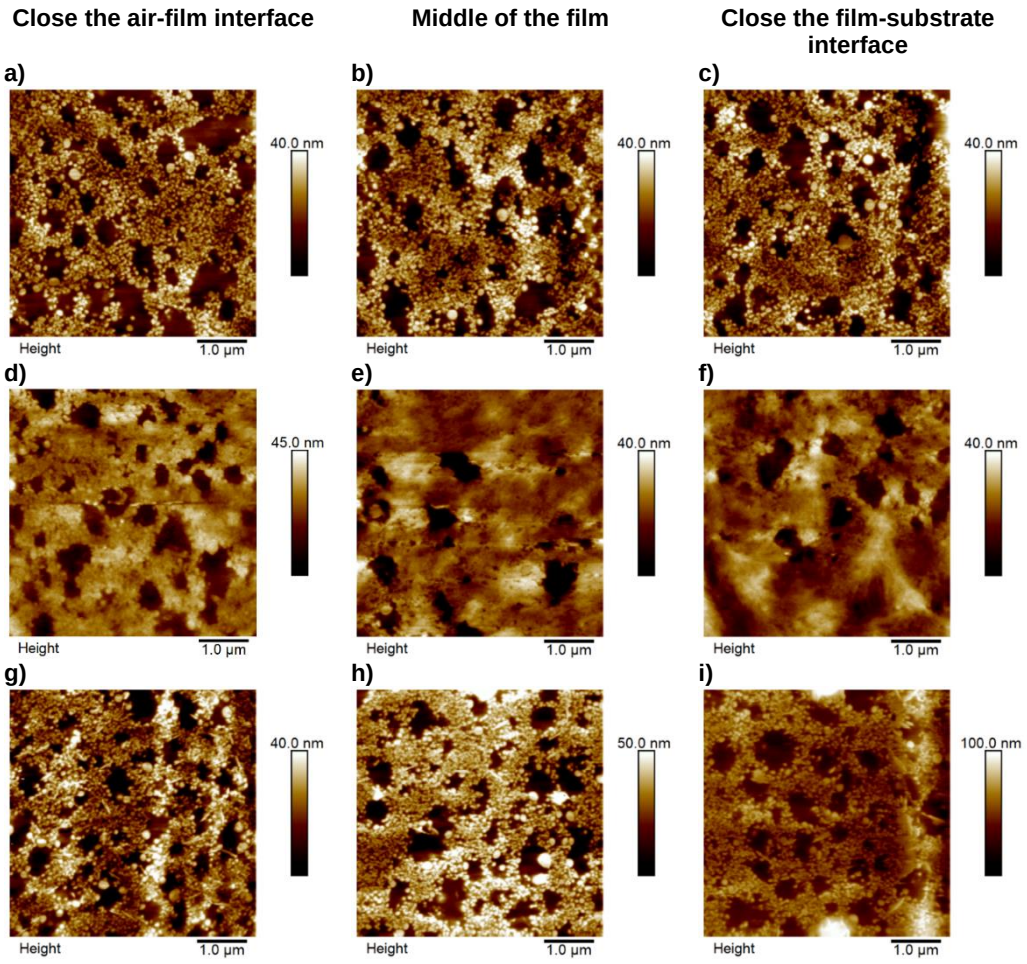

Figure II-5: AFM height images of the films with 1% Mn-based catalyst solely abc),and Zr-based catalyst def) and Ca-based catalyst ghi) after 8 days of curing at 23ºC and 55% relative humidity. For each system, the left image was performed close to air-film interface, the second in the middle of the film and the right image close to the film-substrate interface

II-2. Film of pure cured alkyd

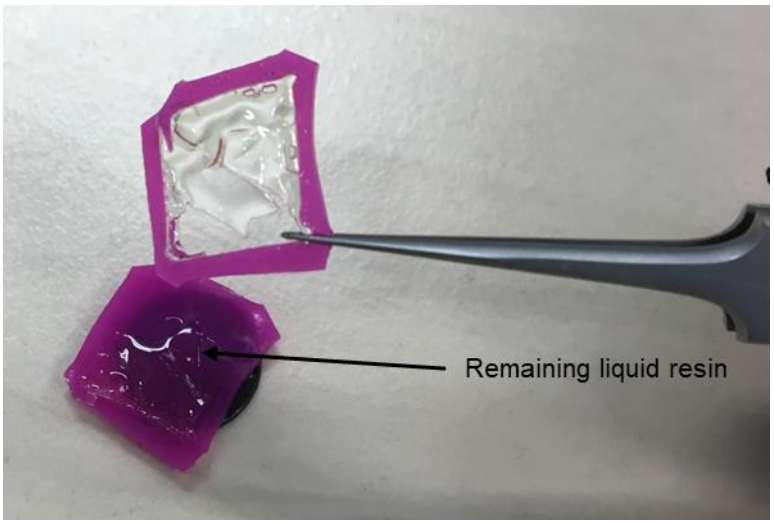

Figure II-6: Photo of an alkyd film with 1%of Mn-based catalyst after one week of curing.

Appendix III. Supporting information for Chapter 6

III-1. Zeta potential of solutions of CNCs with AIBA

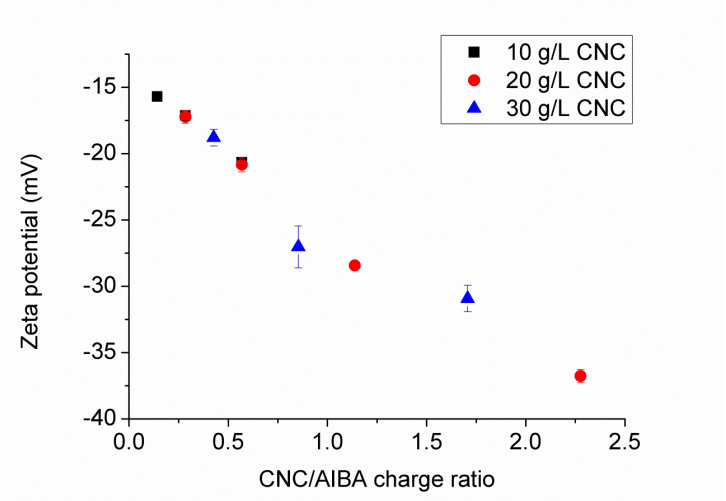

Figure III-1: Data from Figure 2 of the main manuscript showing the zeta potential of different solutions of cellulose nanocrystals with variation of 2,2′-Azobis(2-methylpropionamidine) dihydrochloride plotted as a function of CNC/AIBA charge ratio.

III-2. Latexes characteristics

a) **b)**

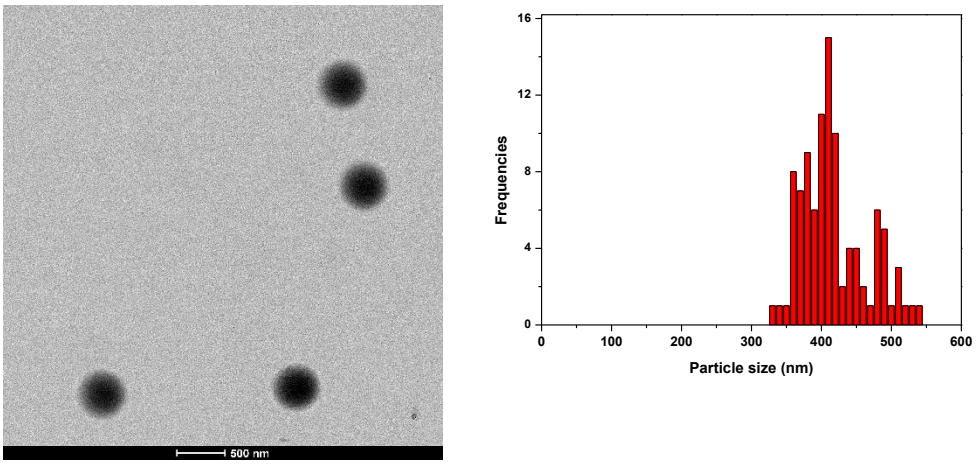

Figure III-2: a) TEM image of particles from latex L0 (scale bar: 500 nm) and b) Particle size distribution

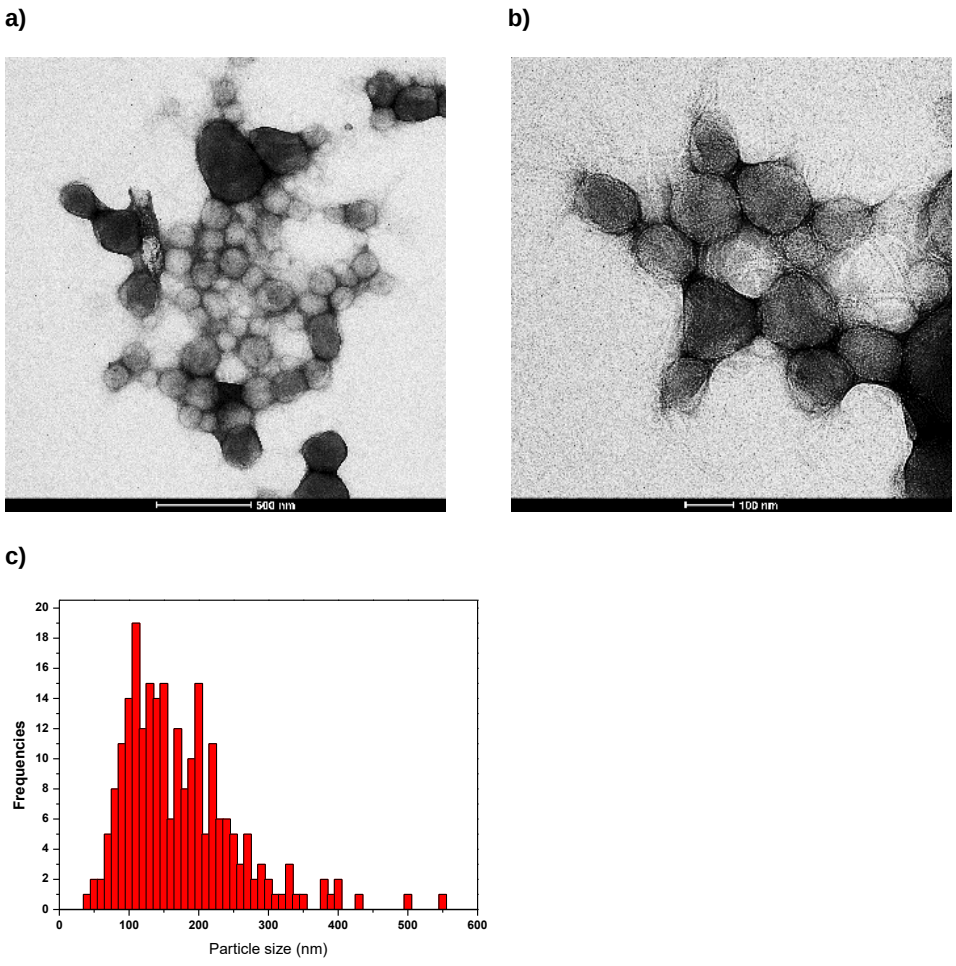

Figure III-3: TEM images of CNCs stabilized particles from latex L2 (scale bar: a): 500 nm, and b) 100 nm) and c) Particle size distribution

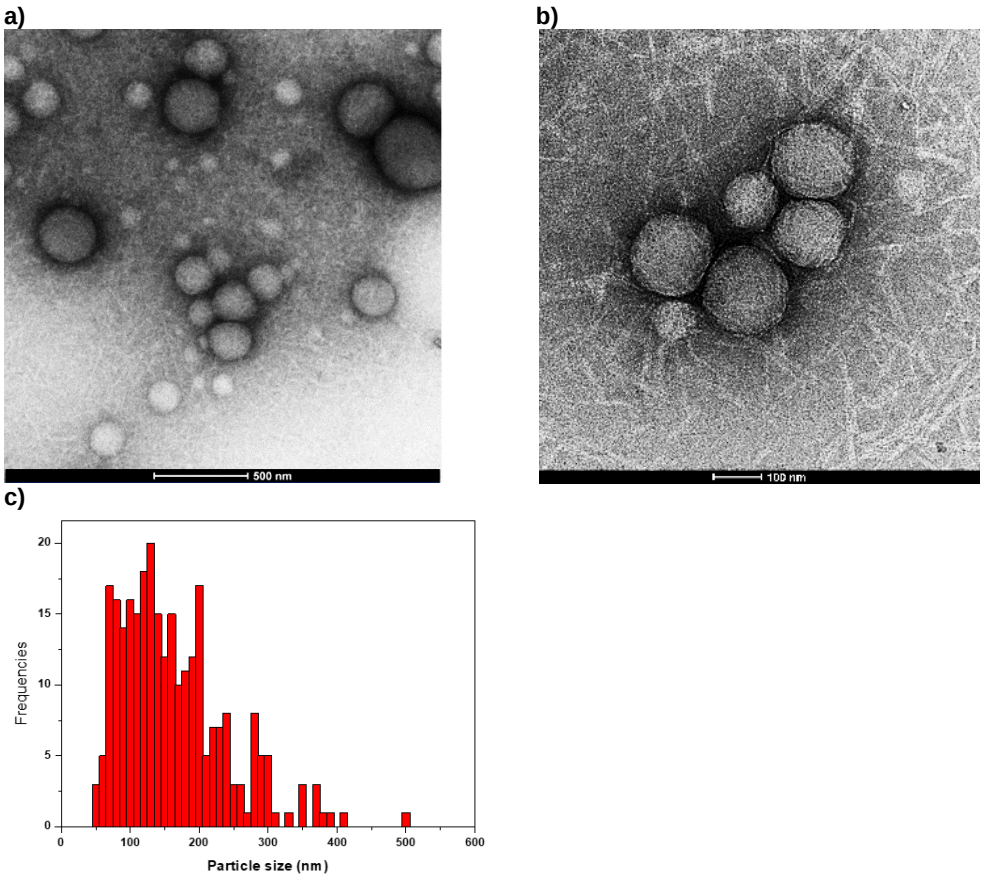

Figure III-4: TEM imagess of CNCs stabilized particles from latex L7 (scale bar: a): 500 nm, and b) 100 nm) and c) Particle size distribution

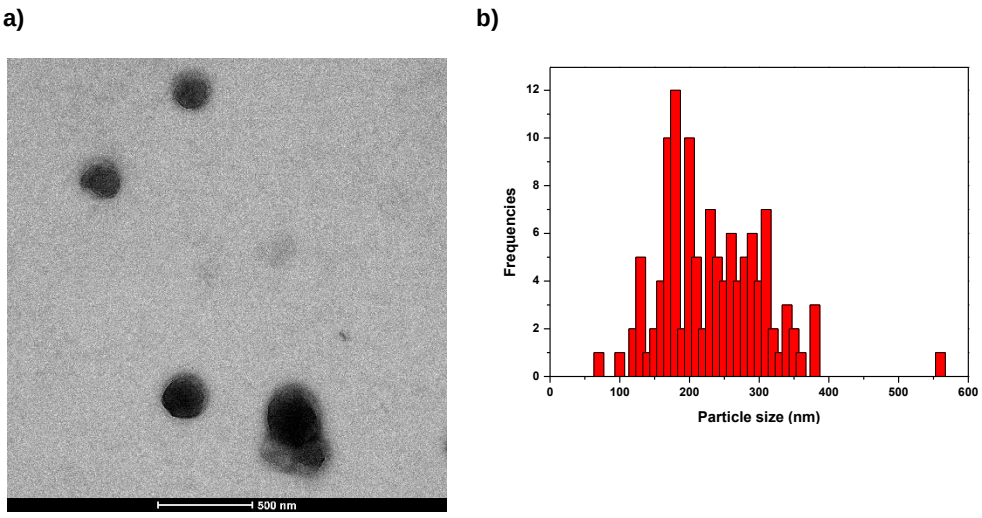

Figure III-5: a) TEM image of CNCs stabilized particles from latex L9 (scale bar: 500 nm) and b) Particle size distribution

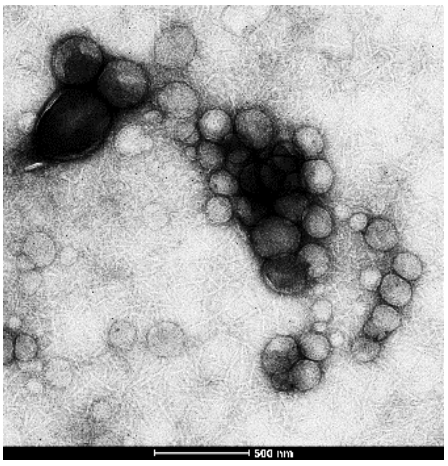

Figure III-6: TEM image of CNCs stabilized particles from latex L6 (scale bar: 500 nm)

Table III-1: Characteristics of the latexes and blends used

	L5	**L5:L0 9:1**	**L5:L0 2:1**	**L5:L0 1:1**	**L5:L0 1:2**	**L0**
CNCs (wbm %)	20	18	13.3	10	6.66	0
Particle size per number (d_n, nm)	160					417
Particle size per weight (d_w, nm)	233					433
Polydispersity (d_w/d_n)	1.45					1.04
Tg (ºC)	35	29	28	28	25	18
Zeta potential (mV)	-31	-32.5	-33	-29.7	-21.4	42.1

III-3. Film properties

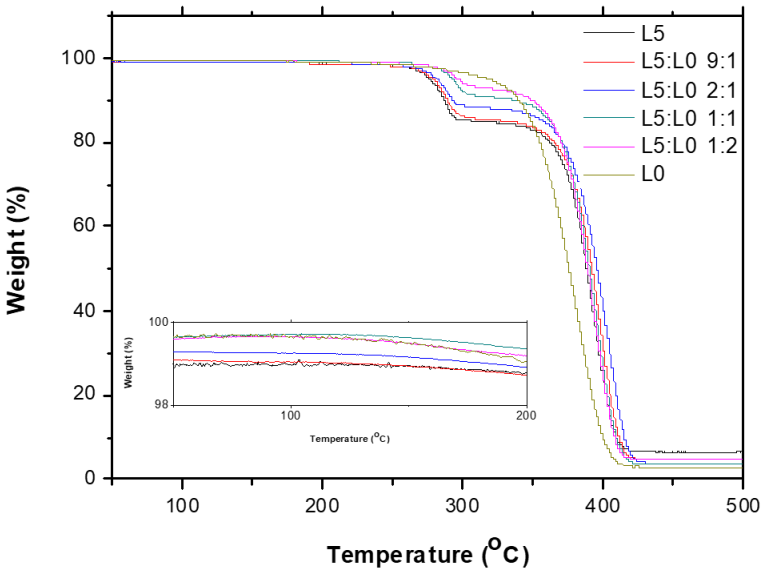

Figure III-7: Themogravimetric analysis curves of the films dried at 65 ºC for 24h

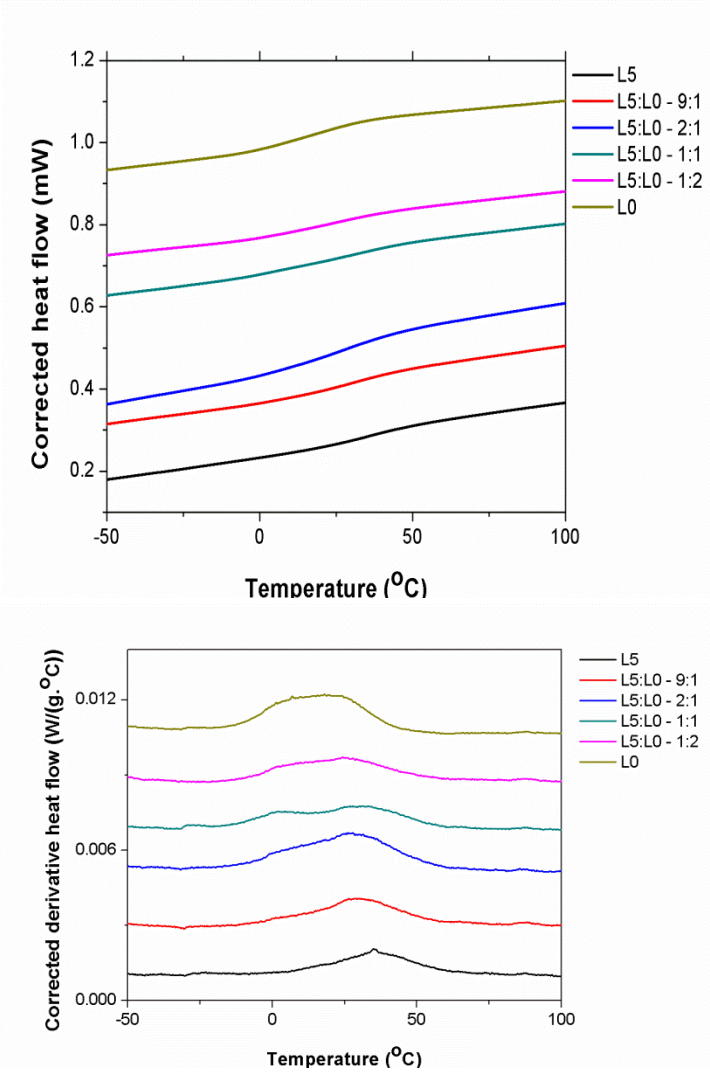

Figure III-8: DSC and first derivative showing the variation in glass transition temperature. for the films cast from latex L0 , L5 and their blends.

List of acronyms and abbreviations

μ	viscosity
A	interfacial area
AA	acrylic acid
AFM	atomic force microscopy
AIBA	2,2′-Azobis(2-methylpropionamidine) dihydrochloride
AIBN	azobisisobutyronitrile
AM	acrylamide
AsAc	ascorbic acid
BA	butyl acrylate
BCN	bacterial cellulose nanocrystals
BMA	butyl methacrylate
Ca	calcium
CeO_2	cerium oxide
CHDF	capillary hydrodynamic fractionation chromatography
CNCs	cellulose nanocrystals
cryo-TEM	cryogenic transmission electron microscopy
$Đ$	polydispersity index
D_0	diffusion coefficient
DG	degree of grafting
DLS	dynamic light scattering
DMAB	dodecyltrimethylammonium bromide
d_n	particle size per number
DSC	differential scanning calorimetry
DVB	divinylbenzene
d_w	particle size per weight

E	evaporation rate
F	force
F_{adh}	adhesion force
FCC	face centered cubic
FF7	disodium hydroxysulfinoacetate
fm	extent of mixing of polymer chains
G	shear rate
GC	gas chromatography
GPC	gel permeation chromatography
H	wet-thickness - dry thickness
HDC	hydrodynamic chromatography
HR-TEM	high-resolution transmission electron microscopy
I	inorganic material
k	boltzman constant
KOH	potassium hydroxide
KPS	potassium persulfate
LA	Blank latex with anionically charged particles
LLC	Blank latex with large cationically charged particles
LSC	Blank latex with small cationically charged particles
M	monomer
MFFT	minimum film formation temperature
MMA	methyl methacrylate
M_n	number average molecular weight
Mn	manganese
M_w	weight average molecular weight
$NaHCO_3$	sodium bicarbonate
Na-MMT	sodium montmorillonite
OsO_4	osmium tetroxide
P	polymer
Pa	Pascal

PBA	poly (butyl acrylate)
PDMS	polydimethylsiloxane
Pe	Peclet number
PET	polyethylene terephthalate
PF-QNM	peakforce - quantitative nanomechanical mapping
PMMA	poly(methyl methacrylate)
ppm	parts-per notation
PS	polystyrene
PSD	particle size distribution
PVC	pigment volume content
QDs	quantum dots
R	radius
RDB	resin double bonds
RDG	resin degree of grafting
RuO4	ruthenium tetroxide
S	styrene
SA	stearyl acrylate
SC	solids content
SDS	sodium dodecyl sulfate
SEM	scanning electron microscope
T	temperature
t_{diff}	time for diffusion
t_{evap}	time for evaporation
TBHP	tert-butyl hydroperoxide
TEM	transmission electron microscope
T_g	glass transition temperature
THF	tetrahydrofuran
TiO2	titanium dioxide
UV	Ultra visible
VOC	volatile organic compound

W	aqueous phase
wbm	weight based on monomer
wbop	weight based on oil phase
wbp	weight bases on polymer
wt	weight
X	conversion
Zr	zirconium
γ	interfacial tension